



# Journal of Engineering

ISSN 1726-4073



A Scientific Refereed Journal  
Published by College of  
Engineering University of  
Baghdad

January  
2014

Number 1  
Volume 20

ISSN 1726-4073

# مجلة الهندسة



مجلة علمية محكمة تصدرها  
كلية الهندسة - جامعة بغداد

العدد 1

المجلد 20

# ENGINEERING

College of Engineering

Baghdad University

Baghdad

## List of Contents

<b>English Section:</b>	<b>Page</b>
<b>Punching Shear Strength of Reinforced Concrete Flat Plates with Openings</b>	<b>1 – 20</b>
<i>Prof. Dr. Nazar K. Oukaili Thaar Saud Salman</i>	
<b>The Behavior of Gypseous Soil under Vertical Vibration Loading</b>	<b>21 – 30</b>
<i>Assist. Prof. Dr. Bushra AL-Busoda Maryam Mohammedsaeed Alahmar</i>	
<b>Influence of Some Additives on the Efficiency of Viscosity Index Improver for Base Lubricating Oils</b>	<b>31 – 41</b>
<i>Prof. Dr. Talib Bahjat Kashmoula Tiba Naif Jasim</i>	
<b>Effect of Nb addition on hardness and wear resist of Cu-Al-Ni shape memory alloy fabricated by powder metallurgy</b>	<b>42 – 49</b>
<i>Msc Raied Z. Alfay Asst prof. Ayad M. Takhakh Asst prof. Abdul Rahim K. Abid Ali</i>	
<b>Experimental And Numerical Investigation Of Creep Behavior In Isotropic Composites</b>	<b>50 – 61</b>
<i>Prof. Dr. Mohsin Jaber Jaweej Dr. Mohsin A. Abdulhussein Bashar kassim Zalzala</i>	
<b>Performance Evaluation of Small Scale Air-Conditioning System Using R22 and Alternative Refrigerants</b>	<b>62 – 77</b>
<i>Prof. Dr. Khalid Ahmed Al-Joudi Asst. Lect. Qusay Rasheed Abd Al-Amir</i>	
<b>Analytical Solution of Transient Heat Conduction through a Hollow Spherical Thermal Insulation Material of a Temperature Dependant Thermal Conductivity</b>	<b>78 – 97</b>
<i>Dr. Mishaal Abdulameer Abdulkareem</i>	

**A Developed Model for Selecting Optimum Locations of Water Harvesting Dams Using GIS Techniques** 98 – 113

*Dr. Prof. Rafa Hashim Al-Suhaili  
Raghad Hadi Hassan*

**Construction Time-Cost Optimization Modeling Using Ant Colony Optimization** 114 – 131

*Mohammed Nooruldeen Azeez  
Angham Alsaffar*

**Study of the Friction Stir Welding For A516 Low Carbon Steel** 132 – 150

*Prof. Dr. Qasim Mouhamed Doos  
Riyadh F. Farhan*





# Punching Shear Strength of Reinforced Concrete Flat Plates with Openings

Prof. Dr. Nazar K. Oukaili, University of Baghdad, dr\_nazar12000@yahoo.com  
Thaar Saud Salman, University of Wassit ,thaar20042000@yahoo.com

## ABSTRACT

Test results of six half-scale reinforced concrete flat plates connections with an opening in the vicinity of the column are reported. The test specimens represent a portion of a slab bounded by the lines of contraflexure around the column. The tests were designed to study the effect of openings on the punching shear behavior of the slab-column connections. The test parameters were the location and the size of the openings. One specimen had no opening and the remaining five had various arrangements of openings around the column. All specimens were cast with normal density concrete of approximately 30 MPa compressive strength. The openings in the specimens were square, with the sides parallel to the sides of the column. Three sizes of openings were used: the same size as the column (150 x 150 mm), 67 percent of the column size (100 x 100mm), and 150 percent of the column size (225x225mm). Due to the presence of the openings, the specimens showed a decrease in punching shear capacity ranged between 11.43% and 29.25% with respect to the control solid slab. Also, the stiffness decreased between 0.31% and 83.00%, depending on the size and location of these openings with respect to the column.

**KEYWORDS:** Flat plates, Openings, Slab-column connection, Punching shear, column.

## مقاومه القص الثاقب في البلاطات الخرسانيه المسلحه المسطحه والحاويه على فتحات

أ.د. نزار كامل العكيلي  
م.م. ثائر سعود سلمان

### الخلاصه

في هذا البحث تم مناقشته النتائج العمليه لسته بلاطات خرسانيه مسلحه لاكريميه حاويه على فتحات بالقرب من العمود. ان عينات الفحص تمثل جزء من بلاطه محاطه بخطوط انقلاب العزم حول العمود. ان الغرض من هذا البحث هو دراسته تأثير الفتحة على مقاومه القص الثاقب للبلاطات اللاكريميه. وكانت المتغيرات هي موقع وابعاد الفتحة بالنسبة للعمود. احد العينات لاتحتوي على فتحة اما الخمسه المتبقية فكانت تحتوي على ترتيب مختلف من الفتحات حول العمود. الفتحات كانت مربعه الشكل وبابعاد موازيه لابعاد العمود. تم استخدام ثلاث ابعاد للفتحات وهي: مساويه لابعاد العمود (150x150 ملم) و 67% من ابعاد العمود (100x100 ملم) و 150% من ابعاد العمود (225x225 ملم). نتيجة لوجود الفتحات في البلاطات تناقصت مقاومه القص الثاقب بين 11,43% الى 29,25% مقارنة مع بلاطه بدون فتحة كذلك قلت الصلاده بمقدار 0,31% الى 83% اعتمادا على ابعاد وموقع تلك الفتحات حول العمود.

الكلمات الرئيسية: البلاطات المسطحه، فتحات، الارتباط بين البلاطه والعمود، القص الثاقب، العمود

## 1. INTRODUCTION

Reinforced concrete flat plate structure is a widely used in low to medium-rise multistory buildings, it consists of a floor or a roof of a uniform thickness carried directly by prismatic columns. The drop panels, column capitals and spandrel beams are omitted.

Since 1950, flat plate slab has proved economical in tall apartment house construction (Ferguson, 1981), it is preferable in bridge decks and multi-storey structures such as office buildings and car parks for many reasons such as its simplicity and accelerating site operations in addition to its allowance for easy and flexible arrangement of columns, partitions and hence reduction of the overall height of tall buildings (McCormac, 2001).

The critical problem in the design of concrete flat plate is the concentration of shear stresses around the column-slab connection which can cause abrupt punching shear failure at loads far below the slab flexural strength. Punching shear failure of the slab is usually sudden and leads to a progressive collapse of the flat plate structures. The local and brittle nature of the punching shear failure in the form of column punching through the slab along a truncated cone is caused by a diagonal cracking around the column (Hong and Yew-Chang, 2003).

In flat plate floor systems there is often a need to install new services that required openings in the vicinity of columns. The openings are required mainly for sanitary reasons, ventilation, heating, air conditioning and electrical ducts. The existence of the opening takes away part of the volume of concrete responsible for resisting shear force and unbalanced moment, which in turn further reduces the punching shear capacity of the slab-column connection. The connection is therefore more vulnerable to brittle punching shear failure.

Over the past 100 years only a moderate amount of research has been conducted on punching shear strength of flat reinforced concrete slabs with openings in the vicinity of columns, in

comparison with other subjects matter in structural engineering. This is reflected in the codes of practice covering the design of such structural systems where the conservative nature of code predictions has been widely recognized (Guan, 2009). Moe (1961) conducted an investigation focused on the failure of reinforced concrete slabs and footings in shear, where a wide range of experiments were conducted on a variety of different slabs with openings adjacent to the columns. Hognestad et al. (1964) carried out further laboratory tests on slab- interior column connections with openings with particular emphasis on lightweight aggregate concrete slabs. Not until the mid 90's that studies on the punching shear behavior of slab-column connections with openings have regained researchers' attention (Guan, 2009). Various laboratory investigations have been conducted including openings in the vicinity of square columns by El-Salakawy et al.(1999), Teng et al.(2004), and Bompa and One (2010). However, these researches seem to be limited. The tests reported in this paper partially fill this void.

## 2. RESEARCH SIGNIFICANCE

In design and construction of reinforced concrete members, the shear failure should be prevented. Openings near the columns decrease the punching shear capacity of slab. Therefore, understanding the behavior of slabs with openings is important for developing safe design procedures.

## 3. TEST SPECIMENS

The test specimens were half-scale and represented interior columns connected to a slab bounded by the lines of contraflexure around the column. The dimensions of the specimen were defined by performing the analysis of a typical floor system consisting of three 4.25m bays in one direction and an infinite number of 4.25m bays in the other. The resulting test slabs were 70mm thick and had in-plane dimensions of 1000×1000 mm. the columns' cross sections were 150mm

square and the high of the columns above the slab was 200mm (**Fig.1**).

A total of six specimens (XXX, SF0, CF0, LF0, CC0, and CF1) were tested. The main parameters were the location and the size of the opening. All openings in the specimens were square with the sides, of length  $l$ , parallel to the sides of the column,  $c$ . Three sizes of openings were used: (150×150mm) with  $l/c=1$ , (100×100mm) with  $l/c=0.67$ , and (225×225) with  $l/c=1.5$ , where  $c$  is the length of the side of the column (**Fig. 2**).

The specimen designation can be explained as follows. The first letter indicates the size of the opening (C= column size= 150×150mm, S=smaller size=100×100mm, and L=larger size= 225×225mm). The second letter indicates the position of the opening around the column (F=front and C=corner), and the third letter indicates the distance  $D$  of the opening from the column face, divided by the thickness of the slab  $h$  ( $D/h=0$ , and 1). In case of a solid slab (without opening), the designation (XXX) is used. The entire characteristics and details of the tested specimens are listed in **Table 1**.

All specimens were supported on the (900×900mm) perimeter on the bottom of the slab. The top of the specimen represents the slab compression surface under vertical load. This is opposite to the situation in a real slab-column system where compression is on the bottom.

All specimens were reinforced by one bottom layer of (6mm in diameter) steel bars, spaced (75mm)  $c/c$  in each direction and arranged to give an average effective depth ( $d_{av}$ ) of (54mm). All column stubs were reinforced with four (12mm) longitudinal bars and (6mm) as transverse reinforcement (ties). The openings were not bordered with reinforcement as it used and requested by code design specifications. This condition was imposed in order to find out which is the quantum when bordering is passed over and the cut in slab is made on site without accounting the possible loss of strength in the control perimeter. The reinforcement details of the specimens are shown in **Fig. 1**.

The specimens were constructed using a normal density concrete with a compressive strength of approximately 30 MPa. The concrete was produced in the laboratory using normal portland cement, fine aggregate, and crushed coarse aggregate of 10 mm maximum nominal size. **Table 1** lists the final strengths based on the average values from the tests performed on at least three 150 x 300mm cylinders for each test specimen. The tensile strength of the concrete was determined by performing the split cylinder tests. The properties of the steel used in the reinforcing mats of the slabs are listed in **Table 2**.

#### 4. TEST PROCEDURE

All specimens were tested using the hydraulic testing frame (**Fig. 3**). Flat plate specimens were placed inside the testing frame so that support lines, point load and dial gauges were fixed in their correct locations. The specimens were then loaded centrally through the column stub with monotonically increasing load until failure. The load was applied slowly in increment of (3.5 kN) using a hydraulic jack of (1000 kN) capacity.

At each loading stage, the test measurements included the magnitude of the applied load, deflection of the slab at five locations(**Fig.4**), first crack width, and strain in compressive face of slab were recorded.

At the end of each test, the angle at which the shear cracks propagated away from the column face was measured and the crack pattern and mode of failure for each specimen were carefully examined.

#### 5. TEST RESULTS AND DISCUSSION

##### 5.1. General Behavior and Crack Patterns

Six specimens failed in a brittle sudden punching mode. Under loading, the first cracks (flexural) occurred at a load range of about (21.1% to 28.6%) of the ultimate punching capacity of the specimens. The cracks first started with diagonal cracks running from the corners of the column stub toward the slab edges on the tension side. As

the load was increased, circumferential cracks occurred at a location farther away from the column stub and developed gradually over the entire slab. At load of (54.9% to 63%) of the failure load of the specimens, the flexural cracks reached all the way out to the edges of the slabs. The first cracks generally reached the edges at a distance equal approximately 201 to 324 mm from the corners of the slab.

The formation of inclined shear cracks was visible inside the openings during testing of interior slab-column connections. These cracks developed at approximately (40-80%) of the failure load at an angle of approximately (26-53) degrees. The inclined shear cracks usually started from flexural cracks. Very often these flexural cracks first developed in the corner of the opening.

In Specimens **SF0**, **CF0**, and **LF0** (openings immediately adjacent to the face of the column), the first cracks started in the nearest corners of the opening to the column, and propagated to the edges of the slab. At load of (48%-59%) of the ultimate load, other cracks formed in the farthest corners of the opening, and propagated to the corners of the slab.

In Specimen **CC0** (opening immediately adjacent to the corner of the column), the first cracks initiated in the corner of the opening near the column. Other cracks formed in the opposite corner at approximately 40% of the failure load and migrated to the nearest corners of the slab.

In Specimen **CF1** (opening at distance of 70mm from the column face), the first cracks formed between the corners of the column and the closest corners of the opening, instead of developing from the column corners to the slab edges. At slightly larger load, other cracks started from the farthest corners of the opening and migrated to the corners of the slab. The inclined cracks that caused failure for this specimen did not start at the corner of the opening, but traveled approximately straight through the opening at mid-distance between the corners.

In general, signs of punching failure in specimens were evident in the formation of one major circumferential crack, away from the column face and the sudden and brittle punching of the column stub through the slab. While punching of the column stub through the slab at the compression face occurred at the face of the column.

The cracks pattern at the tension and compression face as well as inside the openings for all specimens after failure are shown in **Fig. 5 to 10**. In all specimens, the shear failure cone ranged on average from 154 to 191mm from the face of the column which corresponds  $2.86$  to  $3.54d$ , where  $d$  is the effective depth of the slab.

## 5.2. First Cracking and Ultimate Loads Results

In order to compare the test results of specimens with different compressive strength, the measured load of each specimen is normalized to the concrete compressive strength of the control Specimen **XXX** (35.69 MPa). The normalized load is obtained by multiplying the measured load by  $(35.69/f_c')^{1/2}$ . Where  $f_c'$  is concrete compressive strength of the individual specimen in MPa. This method, to compensate for the differences in a concrete strength, was adopted in the most previous researches conducting on punching shear strength of concrete flat plates (El-Salakawy et al. (1999), Harajli and Soudki (2003), Polak et al. (2003), Sharaf et al. (2006), Soudki et al. (2012))

The experimental results for cracking and ultimate loads of all specimens are given in **Table 3**. The test results show that, due to the openings existence, both the cracking and ultimate loads decreased in comparison with the reference Slab **XXX** (solid slab) depending on the sizes and locations of these openings.

The size of the opening has a significant effect on the capacity of the slab. For specimens with openings located directly next to the column, the normalized cracking and ultimate loads of Specimen **LF0** with larger opening (225×225mm) decreased by 47.87% and 29.25% respectively in comparison with the normalized cracking and

ultimate loads of Specimen **XXX**, while for Specimen **SF0** with smaller opening (100×100mm), the decreasing in the normalized cracking and ultimate loads are 14.15% and 12.42%, respectively. This means in other words, the bigger the opening size the larger the reduction in both normalized cracking and ultimate loads, as shown in **Fig. 11**. It can be seen that, the reductions in normalized cracking and ultimate loads are proportional to the ratio of the opening size to the column size. Additionally, with increasing the opening size there is more rapid increase in the reduction in the normalized cracking load, which is always larger than that in the normalized ultimate load especially when the opening size is greater than the column size.

The distance between the column edge and the opening influences the cracking and ultimate loads of the concrete flat plate. For Specimen **CF1** with a 150×150mm opening located at the distance of 70mm from the front edge of the column, both the normalized cracking and ultimate loads decreased by 13.5% with respect to the cracking and ultimate loads of Specimen **XXX**. For Specimen **CF0** with the same size opening located directly next to the column, the normalized cracking and ultimate loads are 23.28% and 19.65% smaller than those of solid Specimen **XXX**, respectively. **Fig. 12** shows that, the further the opening from the column face, the lower the reduction in both the normalized first cracking and ultimate loads.

The arrangement of the openings around the column also affects the cracking and ultimate loads of the slab. For specimen **CC0** where 150mm square opening is immediately adjacent to the corner of the column, there is the smallest influence of the opening on its punching shear capacity. The normalized first cracking load decreased by 13.22% and the normalized ultimate load decreases by 11.43%. This reduction in normalized loads is quite small comparing to specimen **CF0** with the same size opening located next to the front of the column. These results are expected because the opening at the corner of the column has a smaller effect on the area and the

inertia of the critical shear section than that opening at the front edge of the column.

### 5.3. Load-Deflection Response

**Figs.13 and 14** compare the normalized load-central deflection response of all six tested specimens. It is clear that, the deflection characteristics are similar for all slabs. In general, the normalized load- central deflection response can be divided into uncracked and cracked stages. The cracked stage can be divided into two substages: a preyield stage and a postyield stage. The preyield cracked stage is from the cracking load to the yield load. The postyield cracked stage extends from the yield to the punching failure load.

The behavior of the specimens with openings is compared to the behavior of specimen **XXX** (without an opening) at two load stages: a service load stage and the failure load stage. The serviceability limit is about 70-75% of the peak load (Tan and Zhao, 2004). In the presented discussion of deflections, the service loads are equal to 71.16 kN (70% of the peak load of control specimen **XXX**). The failure loads are equal to the recorded failure load, as listed in **Table 3**.

The influence of the size of the openings on normalized load- central deflection behavior is demonstrated in **Fig.13**, where the results for **SF0** (with a 100×100mm opening), **CF0**(with a 150×150mm opening), and **LF0**(with a 225×225mm opening) are compared with **XXX**, the control specimen without opening. The experimental results confirm that, the larger the opening the larger the reduction in slab stiffness or in other words, the larger the deflection at the same load level. However, the influence of the opening size on the recorded deflections at service stage is relatively small when the opening size is less than the column size as in specimen **SF0**, where the maximum measured deflection at normalized service load is 3.37% larger than that of control specimen. At failure, this percentage

increases to 32.18%. The effect of the opening becomes more significant when the opening size exceeds the column size as in specimens **LF0**, where the maximum recorded deflection at normalized service and failure loads are 83% and 83.23% respectively larger than those of specimen **XXX**.

**Fig.14** illustrates the effect of the opening location on normalized load- central deflection behavior, where the behavior of specimens with 150 mm square openings that constructed at different locations is compared with the behavior of the solid slab **XXX**. It can be seen that, there is a significant increase in the recorded deflection at normalized service load for specimen with front edge opening (**CF0**) about 30.63% over the control slab, while at failure this percentage becomes 57.47%. For two other specimens, the increases in the recorded deflections at normalized service load are relatively small, which are 0.31% and 7.50% for specimens **CC0** and **CF1**, respectively. At failure, these percentages become 23.06% (**CC0**) and 27.07% (**CF1**), as listed in **Table 4**.

#### 5.4. Cracking Behavior of Specimens

In general, slabs with openings have maximum crack width larger than the reference slab (**XXX**) during the same stage of loading. The existence of opening in concrete slab-column connection reduces the rigidity of the connection depending on the size and location of this opening and that reflects the increase in the crack width. This is illustrated in **Figs. 15 and 16**.

**Fig. 15** compares the crack behavior of specimens with openings immediately adjacent to the column front face with the crack behavior of specimen **XXX** to study the effect of the opening size. There is significant increase in the crack width with increasing the size of the opening as shown in **Fig. 15**. At load level of 71.16 kN that represents service load in solid slab **XXX** as mentioned previously, the maximum crack width measured in specimen with smaller opening size (**SF0**) is 66.48% over the solid slab. This percentage

increases to 296.35 % for specimen with larger opening size (**LF0**).

The influence of the opening location on the cracking behavior of specimens is shown in **Fig.16**. In specimen **CF0** with front face opening, the maximum crack width at normalized service load is 159.97% larger than the maximum crack width of specimen **XXX**. The increase in the maximum crack width at normalized service load becomes 108.55% when the opening is immediately adjacent to one of the column corners (**CC0**). In specimen with opening located away from the front column face (**CF1**), the maximum crack width increases about 72.21% over the solid slab at normalized service load.

At failure loads of specimens, the values of maximum crack width for specimens with openings are generally larger than that of solid control slab at the same load level and ranged between 71.82% and 296.99% over the control specimen **XXX**. However, the values of crack width beyond 0.41mm are not important because the slabs are out of the serviceability stage (Nilson et al., 2004).

#### 5.5. Concrete Compressive Strains

Concrete strains were measured using demec points where placed on the compression side of specimens to observe the strain level at punching. The position and direction of the demec points are shown **Fig. 17**. The test results show that, both the tangential and the radial strains at ultimate loads for each specimen were inversely proportional to the distance from the column stub. In addition, with increasing distance from the column stub there was a more rapid decrease in the radial strains, which were always smaller than the tangential strains.

**Figs. 18 and 19** show the relations between normalized load and maximum concrete compressive strains for the tested slabs. The maximum strain values for all specimens were recorded at line  $L_1$  (between two demec points) nearest to the column stub in tangential direction perpendicular to that passing through opening.



The figures show that specimens with openings have maximum concrete strains larger than of solid specimen at the same stage of loading depending on the location and size of the opening. In other words, the bigger the opening size the greater the maximum concrete strains and for specimens with same opening size, the closer the opening to the column front face the greater the maximum concrete strains.

## 6.SUMMARY AND CONCLUSIONS

The main conclusions can be summarized as follows:-

1. All specimens failed in punching shear mode.
2. The size of the opening affects the capacity of the flat plate. The ultimate strength of the flat plate with the larger opening decreased by 29.25% with respect to the ultimate strength of solid specimen. For the specimen with a smaller opening, the decrease in capacity was 12.42%.
3. The further the opening from the column, the higher the ultimate strength of the connection. For the specimen with opening at distance  $h$  (70mm) from the front face of the column, the shear capacity decreased by 13.47% from control one. For specimen with the opening next to the column, the decrease in capacity was 19.65%.
4. The opening located at the front of the column decreases the shear capacity of the flat plate more than the same size opening located at the corner of the column. The opening location adjacent to the front column face decreased the shear capacity by 19.65% from control one, while that adjacent to the column corner decreased the capacity by 11.43%.
5. The presence of openings in flat plates decreases the stiffness depending on the sizes and locations of these openings. For the specimen with the opening of the 1.5 size of the column, significant reduction in stiffness (83.00%) at service stage was observed, while for slabs with smaller openings, the reduction in stiffness was much smaller (0.31 to 30.63%).
6. Slabs with openings have maximum crack width larger than what observed in the reference slab during the same loading stage. The increase in maximum crack width at service load ranged between 66.48% to 296.35% with respect to solid specimen.
7. The existence of openings increases the strains in concrete on the compression face of the slabs. Generally, the bigger the opening size the greater the maximum concrete strains and for specimens with same opening size, the closer the opening to the column front face the greater the maximum concrete strains.

## REFERENCES

- Bompa, D.V., and One, T.,(2010) "**Behaviour of Symmetric Flat-Slab Connections with Openings in the Control Perimeter**", North University Of Baia Mare, Scientific Bulletin, Series D, Vol. XXIV, No.2, pp. 111-116.
- El-Salakawy, E. F., Polak, M.N., and Soliman, M.H.,(1999) "**Reinforced Concrete Slab-Column Edge Connection with Openings**", ACI Structural Journal, Vol. 96, No. 1, January, PP. 79-87.
- Ferguson, P.M., (1981) "**Rinforced Concrete Fundamentals**", 4<sup>th</sup> Edition, John Wiley & Sons, Inc., 694 pp.
- Guan, H., (2009) "**Prediction of Punching Shear Failure Behavior of Slab-Edge Column Connections with Varying Opening and Column Parameters**". Advances in Structural Engineering-An International Journal, vol. 12, No.1, PP. 19-36.
- Harajli, M.H. , Soudki, K.A.,(2003) "**Shear Strengthening of Interior Slab-Column Connections Using Carbon Fiber-Reinforced Polymer Sheets**", Journal of Composites for construction ,ASCE, Vol. 7, No. 2, pp. 145-153.

Hognestad, E., Elstner, R.C. and Hanson, J.A.,(1964) "**Shear Strength of Reinforced Structural Lightweight Aggregate Concrete Slabs**", ACI Structural Journal, Vol. 61, No. 6, June, pp. 643-656.

Hong, G. and Yew-Chang, L.,(2003) "**Failure Analysis of Column-slab Connections with Stud Shear Reinforcement**", Canadian Journal of Civil Engineering, Vol.30, pp.934-944.

McCormac, J.C.,(2001) "**Design of Reinforced Concrete**", 5<sup>th</sup> Edition, John Wiley & Sons, Inc., 738 pp.

Moe, J.,(1961) "**Shearing Strength of Reinforced Concrete Slabs and Footing under Concentrated Load**" Portland Cement Association Research and Development Laboratories Bulletin D47, April, 130 pp.

Nilson, A. H. , Darwin, D. and Dolan, C. W. ,(2004) "**Design of Concrete Structure**" McGraw-Hill Book Company, Thirteen Edition, 412 pp.

Polak, M.N., El-Salakawy, E. F., and Soudki, K.A.,(2003) "**New Shear Strengthening**

**Technique for Concrete Slab-Column Connections**", ACI Structural Journal, Vol. 100, No. 3, May, pp. 297-304.

Sharaf, M.H., Soudki, K.A., and Dusen, M.V.,(2006) "**CFRP Strengthening for Punching Shear of Interior Slab-Column Connections**", Journal of Composites for construction ,ASCE, Vol. 10, No. 5, pp. 410-418.

Soudki, K., El-Sayed, A.K., and Vanzwol, T.,(2012) "**Strengthening of Concrete Slab-Column Connections Using CFRP Strips**", Journal of King Saud University-Engineering Sciences, Vol.24, Issue 1, January, pp. 25-33.

Tan, K. G. And Zhao, H. ,(2004) "**Strengthening of Openings in One-Way Reinforced-Concrete Slabs Using Carbon Fiber-Reinforced Polymer Systems**", Journal of Composites for construction ,ASCE, Vol. 8, No. 5, pp. 393-402.

Teng, S., Cheong, H.K., Kuang, K.L., and Geng, J.Z.,(2004) "**Punching Shear Strength of Slabs with Openings and Supported on Rectangular Columns**", ACI Structural Journal, Vol. 101, No. 5, September, pp. 678-687.

**Table 1: Summary of Test Data**

Specimen designation	Opening size, mm	Opening location around column	Distance of opening from column, mm	Age of slab ( from casting to testing, days)	Compressive strength at time of slab testing $f'_c$ (MPa)	Splitting tensile strength $f_t$ at time of slab testing (MPa)
XXX	N/A	N/A	N/A	90	35.69	3.61
SF0	100×100	Front	0	95	37.10	3.50
CF0	150×150	Front	0	103	34.13	3.44
LF0	225×225	Front	0	108	32.83	3.01
CC0	150×150	Corner	0	109	36.27	3.29
CF1	150×150	Front	70	110	36.50	3.37

Note: N/A not applicable

**Table 2: Properties of Steel Reinforcement**

Nominal diameter (mm)	Measured diameter (mm)	Yield Stress $f_y$ (MPa)	Ultimate Strength $f_u$ (MPa)
6	5.83	598	657
12	11.87	648	721

**Table 3: Cracking and Ultimate Loads of Test Specimens**

specimen	Experimental load, kN		* Normalized load, kN		% decrease in first cracking load with respect to Control slab (XXX)	% decrease in ultimate load with respect to Control slab (XXX)
	First cracking load, $P_{cr}$	Ultimate loads, $P_u$	First cracking load, $P_{ncr}$	Ultimate loads, $P_{nu}$		
XXX	29.04	101.65	29.04	101.65	0	0
SF0	25.41	90.76	24.93	89.02	14.15	12.42
CF0	21.78	79.87	22.28	81.68	23.28	19.65
LF0	14.52	68.98	15.14	71.92	47.87	29.25
CC0	25.41	90.76	25.20	90.76	13.22	11.43
CF1	25.41	88.94	25.13	88.95	13.46	13.47

\* Normalized load = experimental load  $\times \sqrt{(35.69/f'_c)}$ .

**Table 4: Central Deflections of Tested Specimens at Normalized Service and Ultimate Loads**

specimen	Deflection at normalized service load $\Delta_{ns}$ (mm),	% Increase in deflection*	ultimate load of individual specimen(kN)	Deflection at normalized ultimate load $\Delta_{nu}$ (mm)	Deflection of control specimen (XXX) at ultimate load of individual specimen $\Delta_{nuc}$ (mm)	% Increase in deflection at ultimate load**
XXX	6.53	0.00	101.65	15.91	15.91	0.00
SF0	6.75	3.37	89.02	14.46	10.94	32.18
CF0	8.53	30.63	81.68	13.81	8.77	57.47
LF0	11.95	83.00	71.92	12.24	6.68	83.23
CC0	6.55	0.31	90.76	13.98	11.36	23.06
CF1	7.02	7.50	88.95	13.33	10.49	27.07

$$* \frac{\Delta_{ns} - \Delta_{ns(control)}}{\Delta_{ns(control)}} \times 100\%$$

$$** \frac{\Delta_{nu} - \Delta_{nuc}}{\Delta_{nuc}} \times 100\%$$

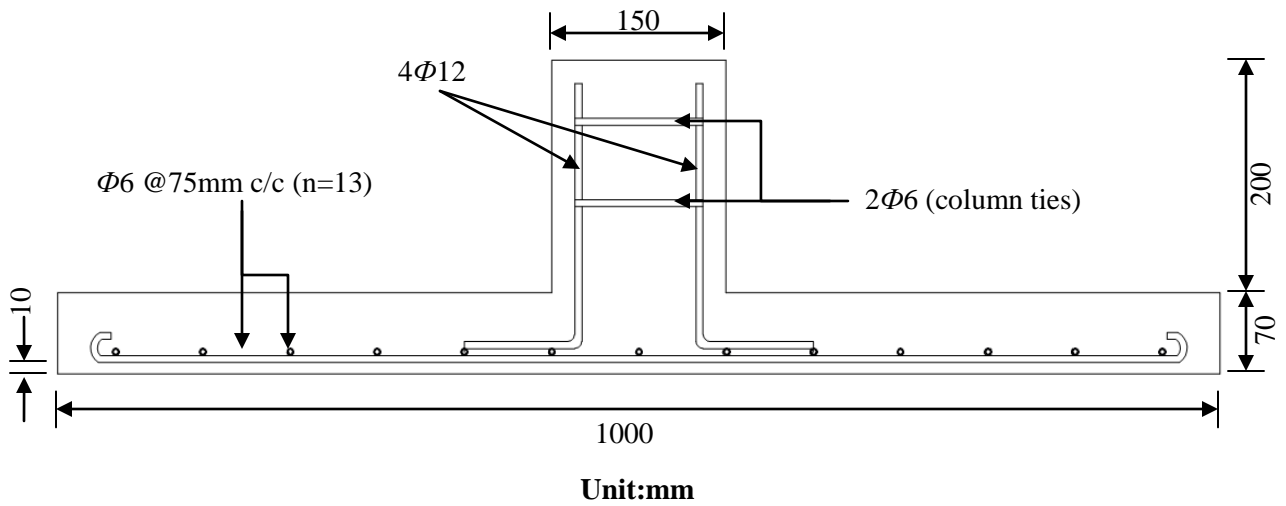


**Fig. 1: Details of Half-Scale Model Slab**

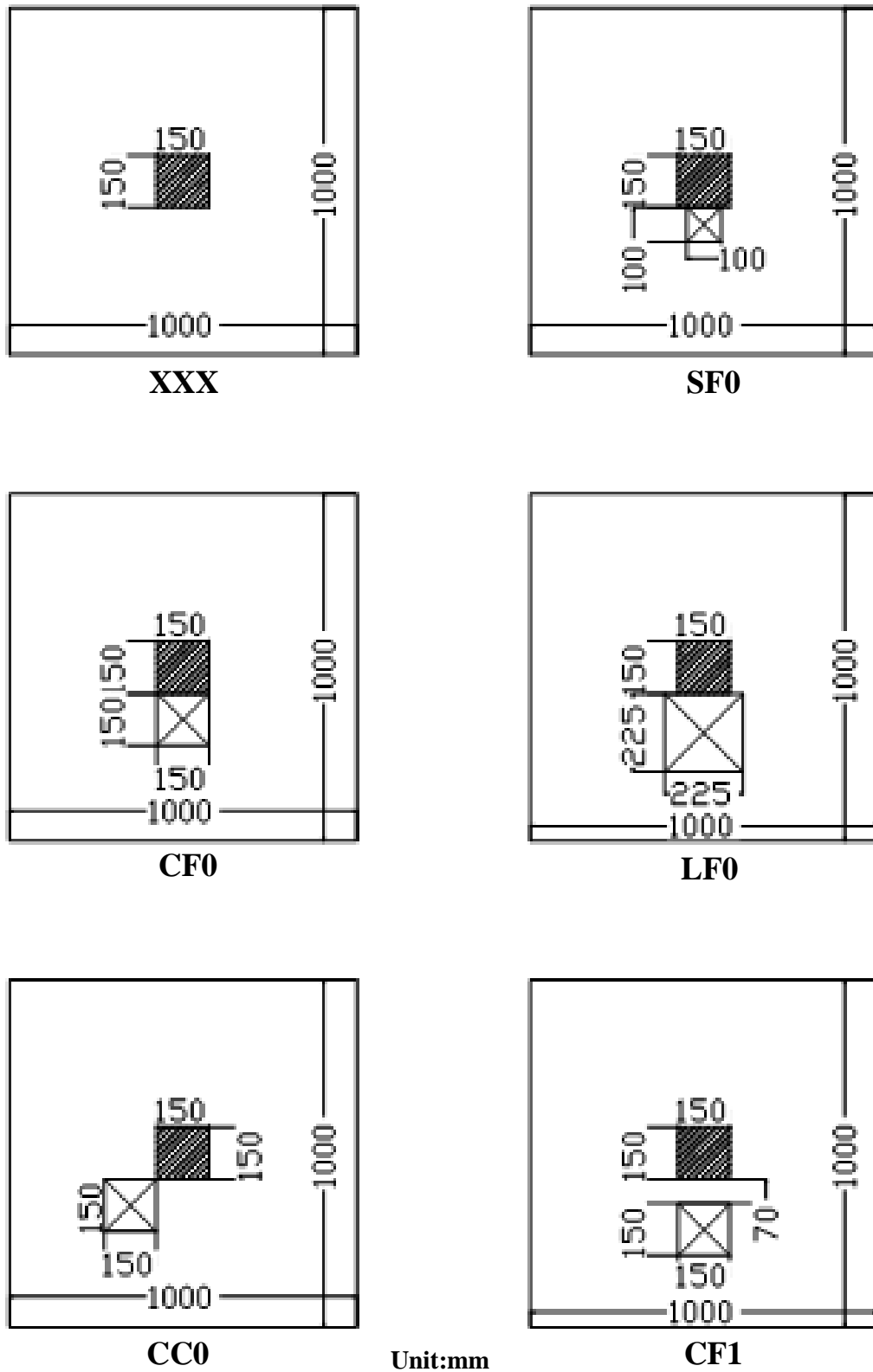


Fig. 2: Plan View of Test Specimens



(a) Specimen inside the Testing Frame



(b) Supporting Ring Beams

Fig.3: Testing Frame

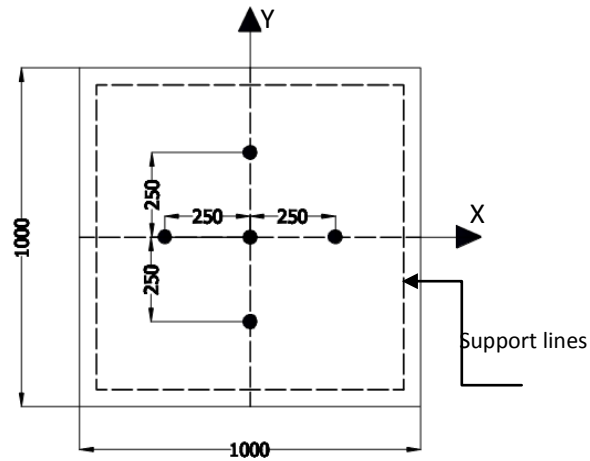


Fig. 4: Arrangement of the Dial Gages

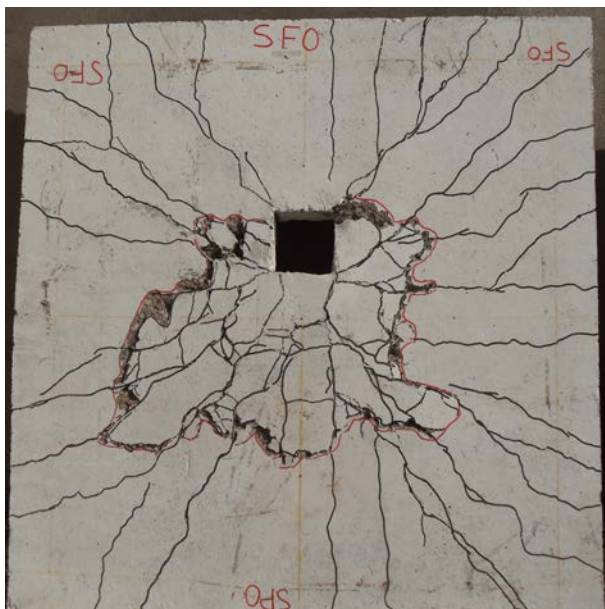


(a) Tension face

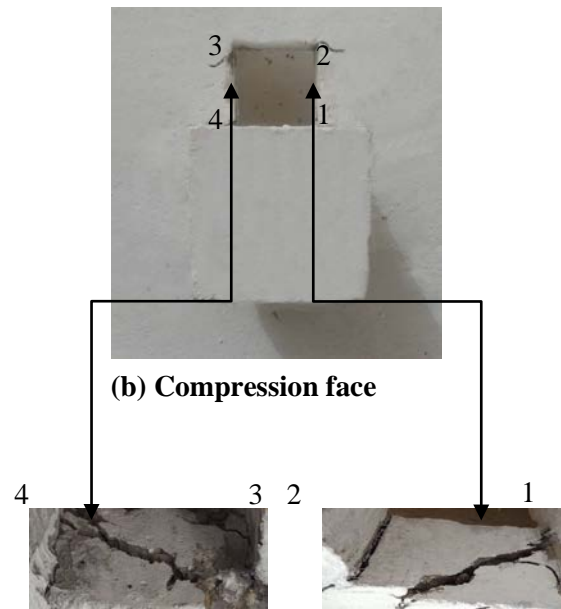


(b) Compression face

**Fig.5: Cracks Pattern for Specimen XXX (Solid Slab) after Failure.**



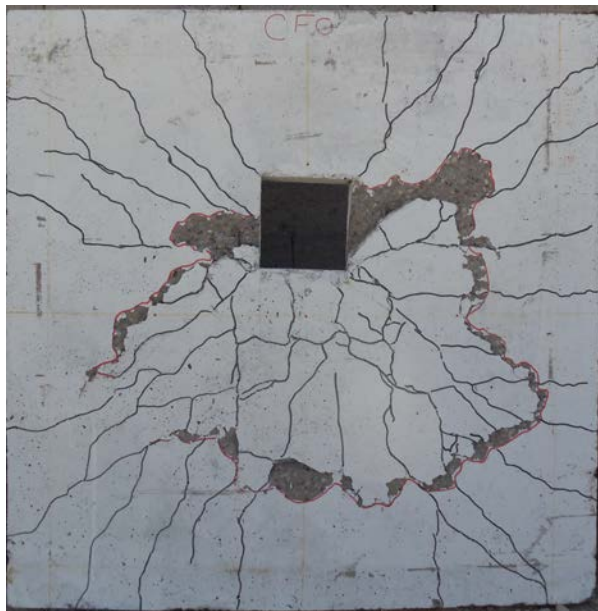
(a) Tension face



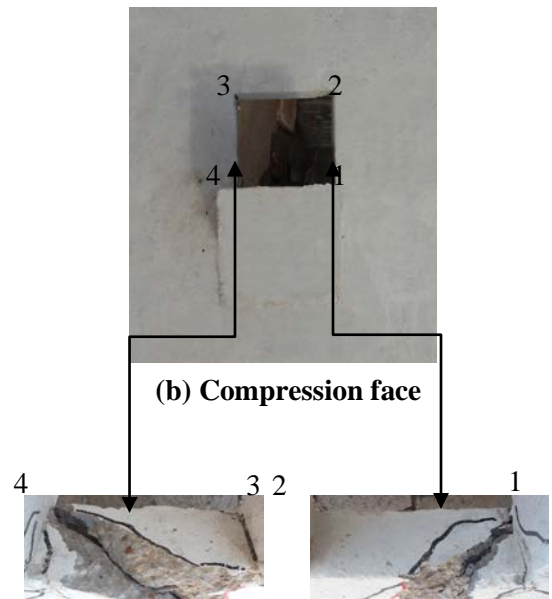
(b) Compression face

(c) Inside the opening

**Fig.6: Cracks Pattern for Specimen SF0 (100×100 mm Opening Size) after Failure.**



(a) Tension face

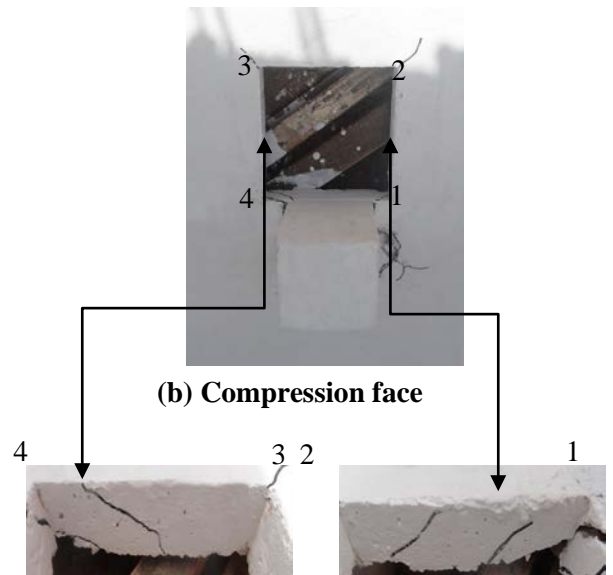


(c) Inside the opening

Fig.7: Cracks Pattern for Specimen CF0 (150×150 mm Opening Size) after Failure.

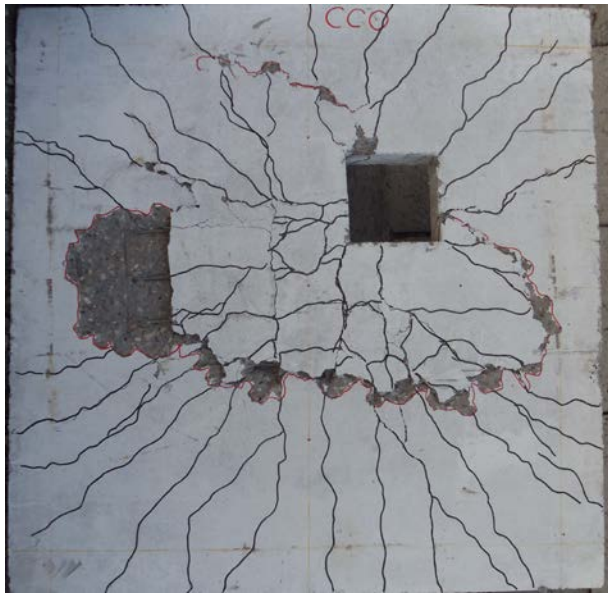


(a) Tension face

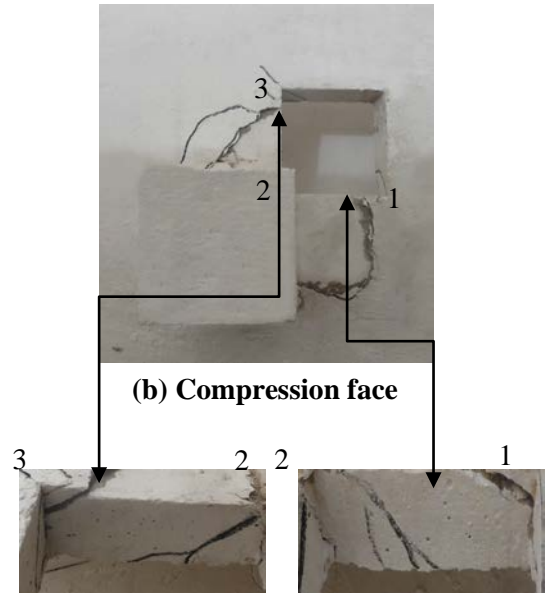


(c) Inside the opening

Fig.8: Cracks Pattern for Specimen LF0 (225×225 mm Opening Size) after failure.



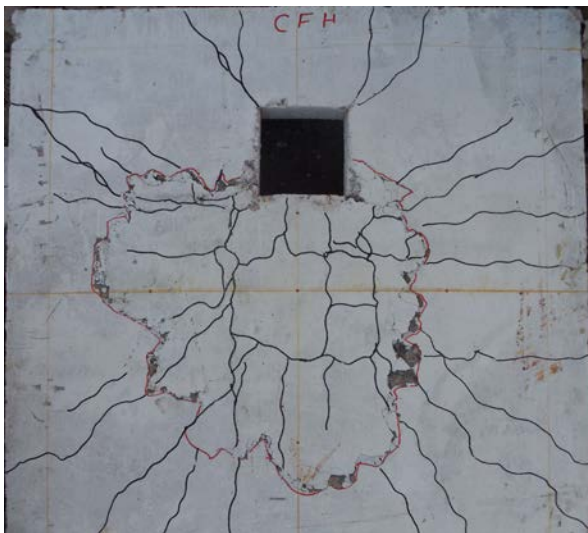
(a) Tension face



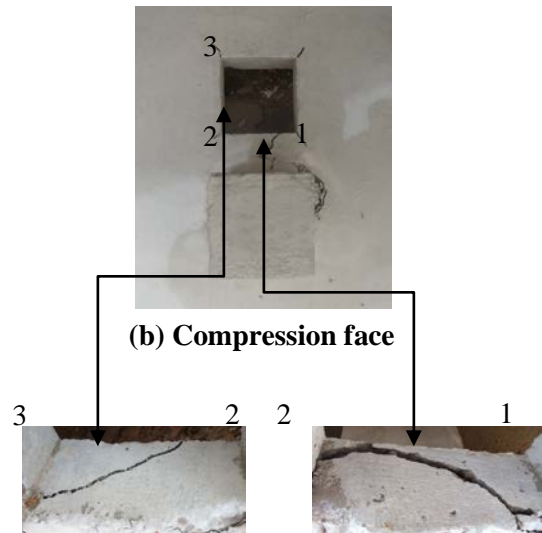
(b) Compression face

(c) Inside the opening

**Fig.9: Cracks Pattern for Specimen CC0 (150×150 mm Opening Size) after Failure.**



(a) Tension face



(b) Compression face

(c) Inside the opening

**Fig.10: Cracks Pattern for Specimen CF1 (150×150 mm Opening Size) after Failure.**

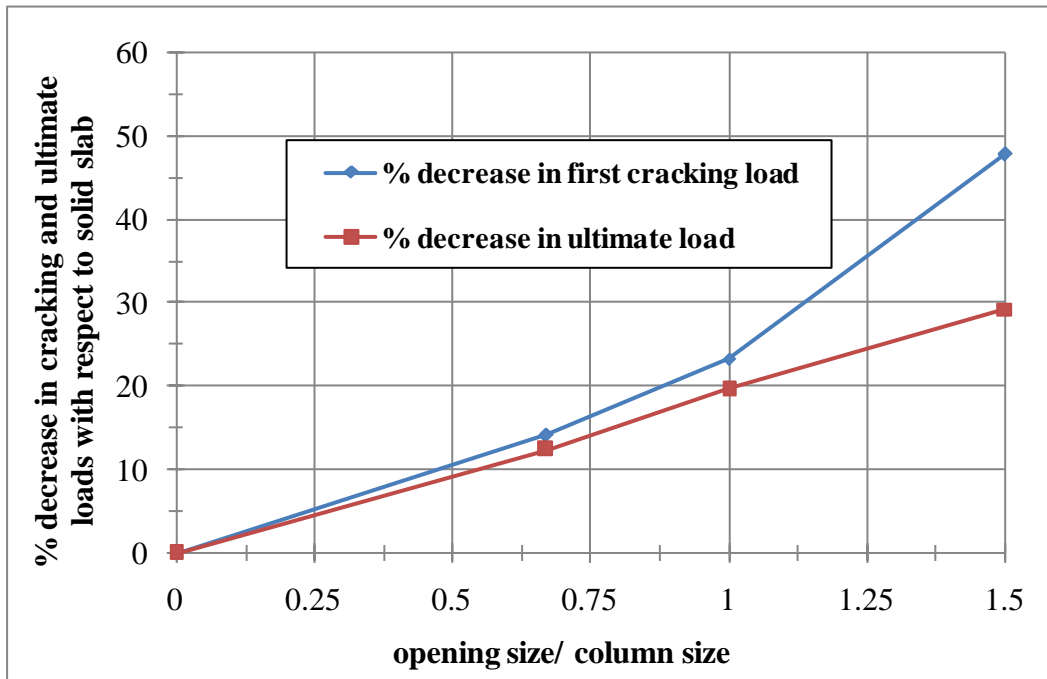


Fig. 11: Effect of Increasing (Opening Size/ Column Size) on the First Cracking and Ultimate Loads of the Specimens

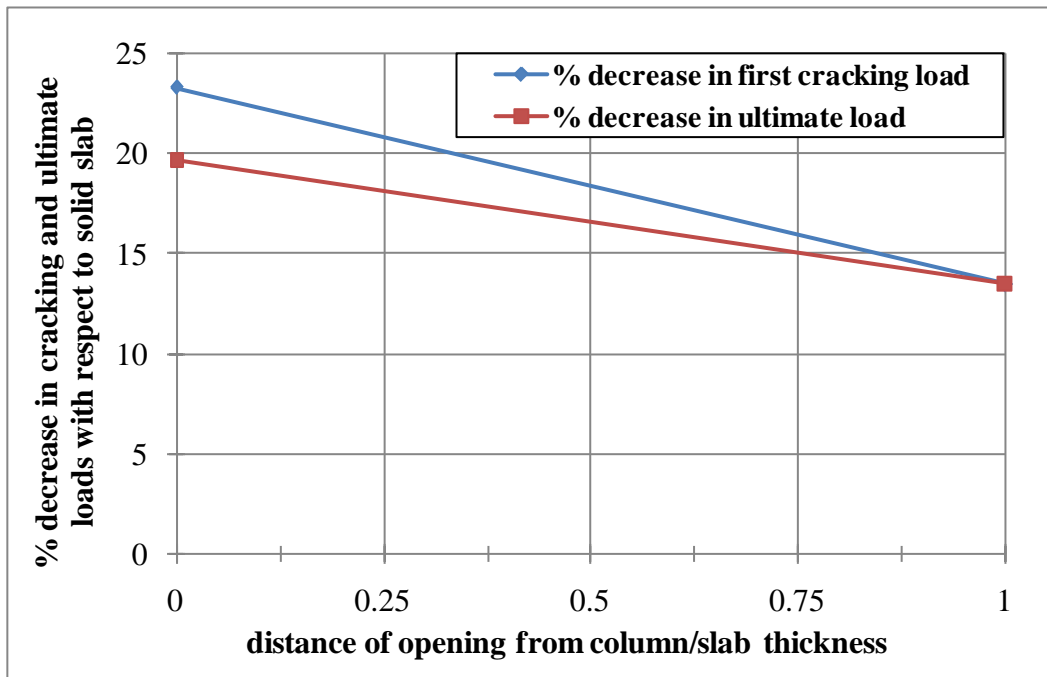


Fig. 12: Effect of Increasing (Distance of Opening from Column/ Slab Thickness) On the First Cracking and Ultimate Loads of the Specimens

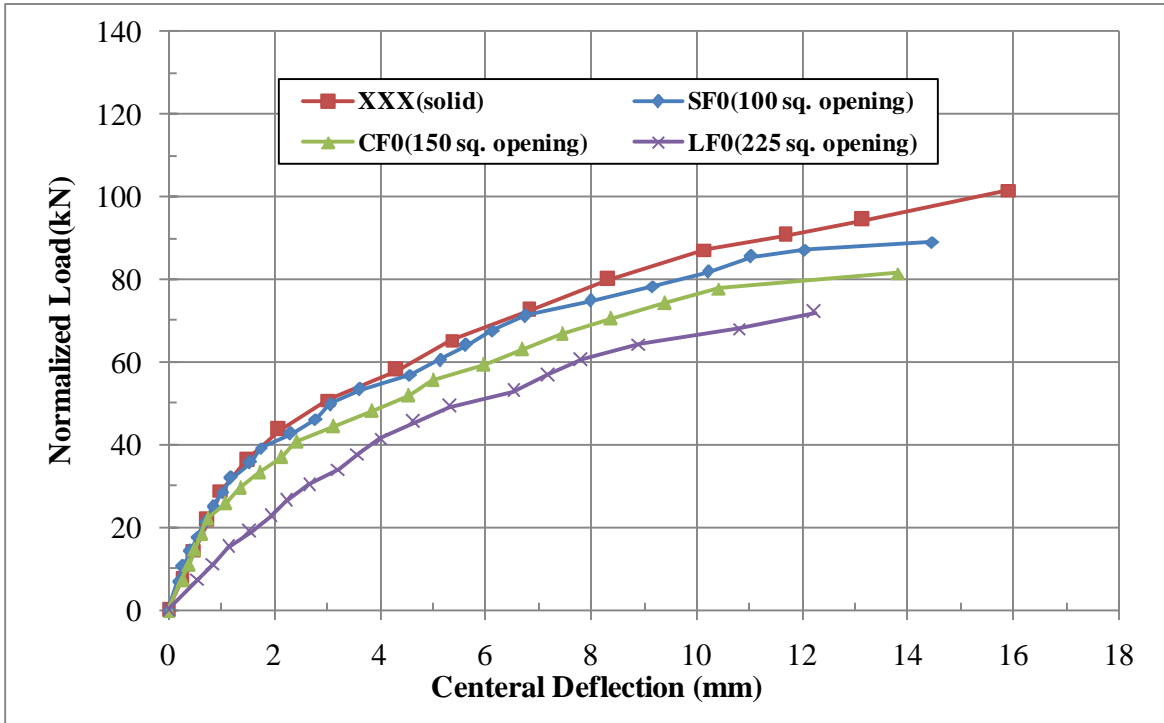


Fig. 13: Influence of the Size of Opening on the Normalized Load-Central Deflection Behavior of Specimens

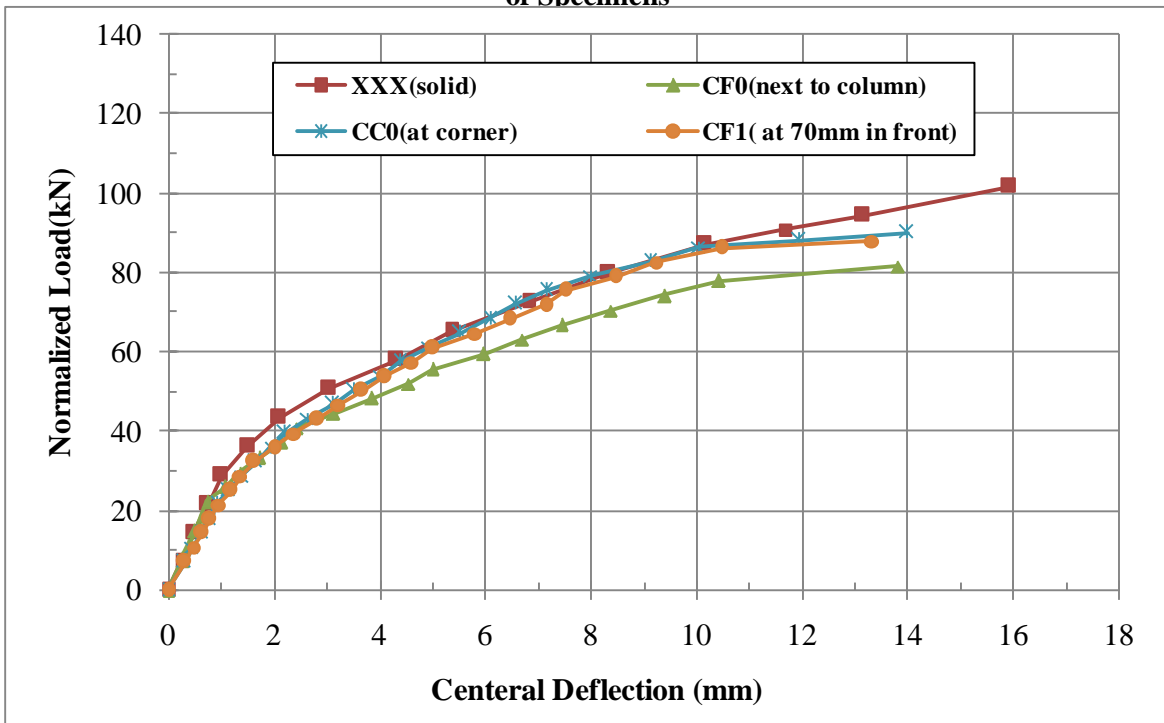


Fig. 14: Influence of the Location of Opening on the Normalized Load-Central Deflection Behavior of Specimens

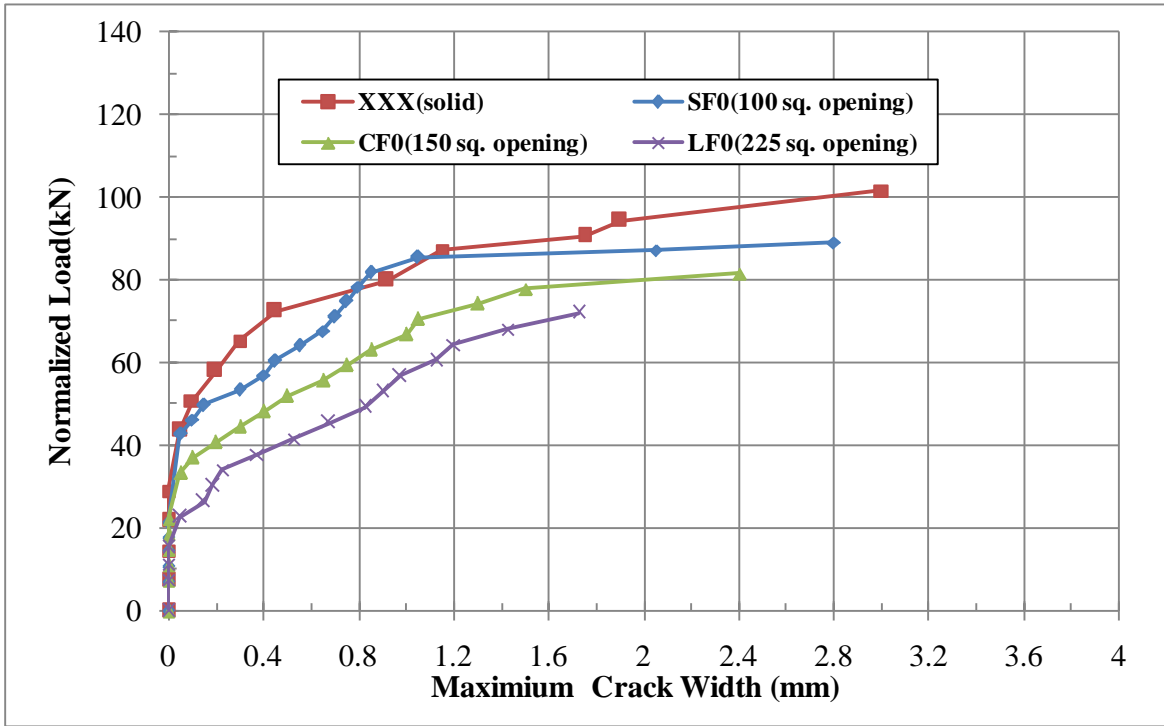


Fig. 15: Influence of the Size of Opening on the Cracking Behavior of Specimens

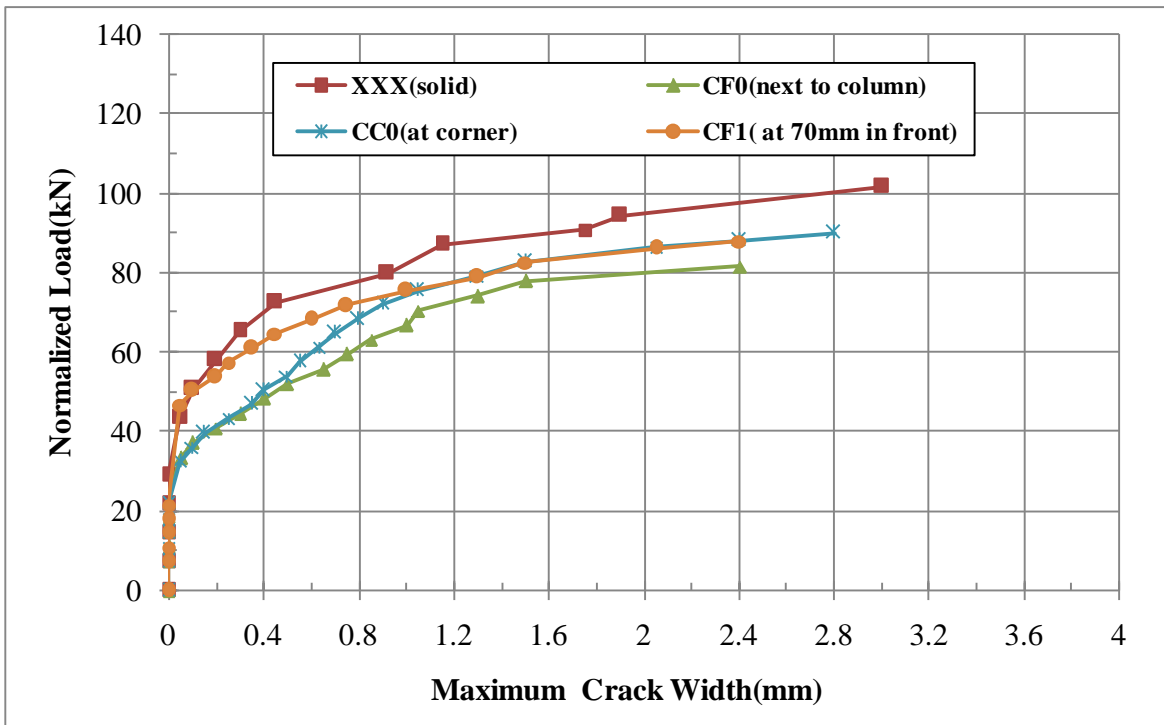


Fig. 16: Influence of the Location of Opening on the Cracking Behavior of Specimens

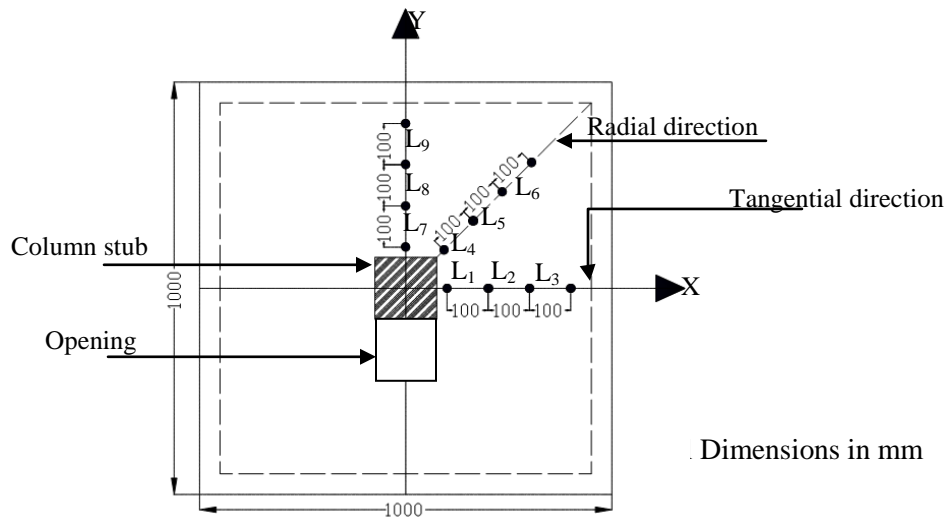


Fig.17: Demec Points Locations and Direction

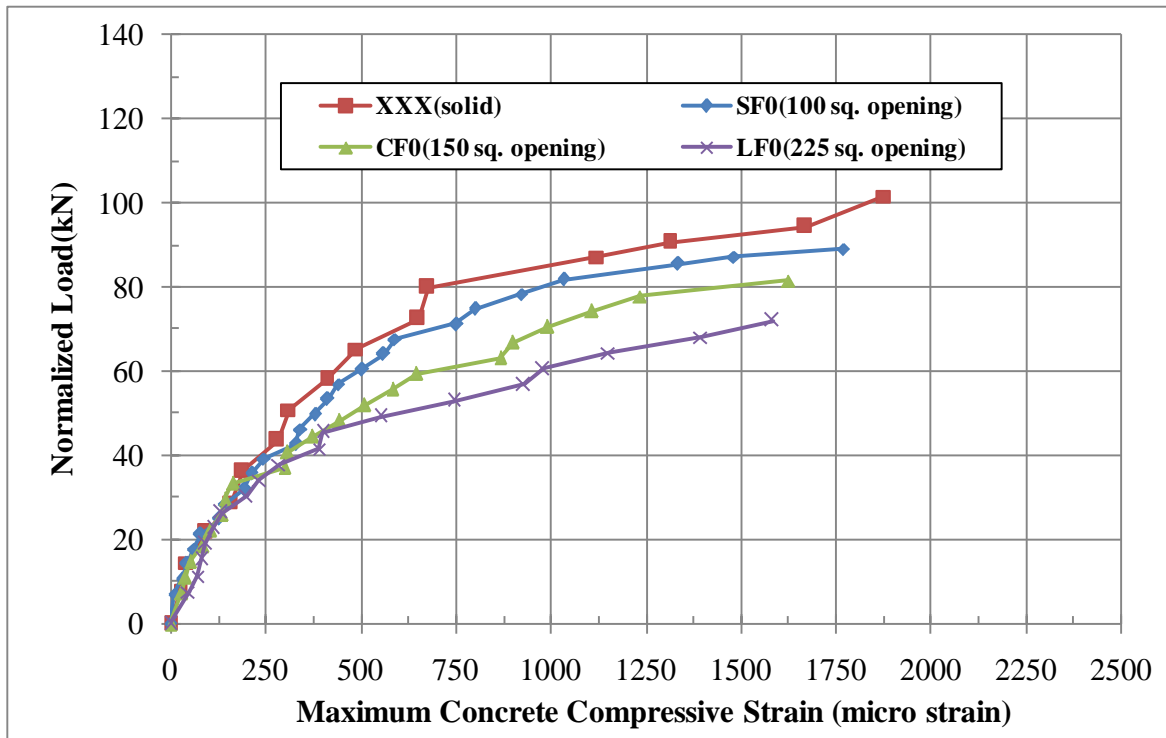


Fig. 18: Influence of the Size of Opening on the Maximum Concrete Compressive Strain

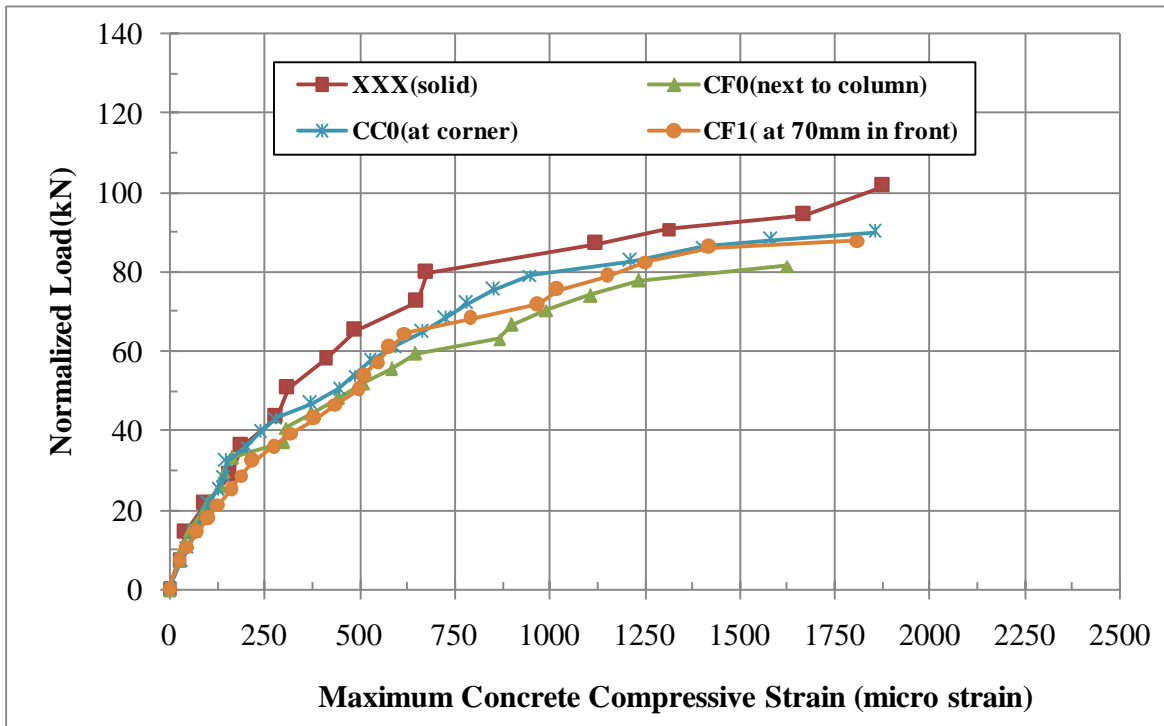


Fig. 19: Influence of the Location of Opening on the Maximum Concrete Compressive Strain

## The Behavior of Gypseous Soil under Vertical Vibration Loading

Assist.Prof. Dr.Bushra AL-Busoda  
albusoda@yahoo.com

Maryam Mohammedsaeed Alahmar  
mmsi\_88@yahoo.com

### ABSTRACT

The dynamic response of foundation rest on collapsible soil in dry and soaked states is studied through wide experimental programmed. Gypseous soil from Tikrit governorate area was obtained and subjected to various physical and chemical analysis to determine its properties. Steel rectangular footing (400x200x20) mm is manufactured. The machine is fitted to the footing, then the model machine foundation is placed centrally over the prepared soil layer in steel container (1200x 1000x1000)mm with proper care to maintain the center of gravity of whole system lie in the same vertical line with container. Then, the footing is subjected to vertical harmonic loading using a rotating mass type mechanical oscillator to simulate different dynamic loads. The effect of soaking and eccentric mass was investigated. The results showed that the amplitude of displacement in dry state is greater than its value at soaked state, while the resonant frequency in the soaked state is greater than in dry state. Also, the results showed that for specific frequency ,an increasing in eccentric mass leads to increase in amplitude of displacement. Moreover, an increasing in resonant frequency can be absorved when eccentric mass is increased.

**KEY WORDS:** Machine foundation, collapsible soil, dynamic response, harmonic loading

### تصرف التربة الجبسية تحت تأثير الحمل الاهتزازي العمودي

الاستاذ المساعد الدكتور بشرى البوسوده  
مريم محمد سعيد الاحمر

### الخلاصه

لقد تم دراسة الاستجابة الديناميكية للاسس مستنده على تربه انهياريه في الحاله الجافة والرطبة من خلال برنامج عملي واسع. التربه التي اجريت عليها الفحوص هي تربه جبسيه اخذت من محافظة تكريت، حيث اجريت عليها الفحوص الفيزيائيه والكيميائيه لايجاد خصائصها. تم تصنيع اساس حديدي مستطيل الشكل بابعاد (400\*200\*20) ملم. تم تثبيت الاله على هذا الاساس، بعد ذلك تم وضع النموذج (الاساس والآلة) مركزيا على طبقات التربه المحضره في حاويه حديديه بابعاد (1200\*1000\*1000) ملم مع الاخذ بنظر الاعتبار ان يكون مركز ثقل النظام ومركز الحاويه يقعون على خط عمودي واحد، بعد لك تم تعريض الاساس الى حمل توافقي باستخدام مذبذب ميكانيكي وذلك من اجل محاكاة احمال ديناميكيه مختلفه. لقد أظهرت النتائج أن سعة النزوح في الحاله الجافة أكبر من قيمتها في الحاله المغموره، في حين أن تردد الرنين في الحاله المغموره أكبر من الحاله الجافة. أيضا، أظهرت النتائج انه لتردد محدد، ان زيادة في الكتلة الغير مركزيه ر يؤدي إلى زيادة في سعة النزوح. كذلك لقد تم ملاحظة زيادة في تردد الرنين بزيادة الكتله الغير مركزيه.

الكلمات الرئيسية : اساس ماكنه، تربه انهياريه، الاستجابة الديناميكيه، الحمل المتناسق

## INTRODUCTION

The gypseous soil is one type of the collapsible soils, it covers wide areas in Iraq. This soil has high bearing capacity in dry state, but it subsides (collapses) upon saturation due to loss of cementation and particle bonding. Therefore, structures supported on unstable soil should be guarded against such danger.

A large number of studies have examined the behavior of collapsible soil in Iraq. The accuracy of these studies depend on manufacturing of test set and sampling techniques and has traditionally relied on routine tests under static condition. However, there is currently lack of knowledge in understanding of the behavior of collapsible soil under dynamic loading. With increases in development, particularly of electrical stations ,factories, roads and other transportation links dynamic loading is often critical. To date this has often been dealt with as a quasi static problem. However, this fails to fully replicate dynamic loadings experience under real environments. Therefore, it is important to study the response of this soil under dynamic loading.

## BACKGROUND

Geotechnical engineers Frequently come across two types of problem in relation to analysis and design of foundations namely (i) foundations subjected to static loads and(ii) foundations subjected to dynamics loads. The characteristics feature of static load is that for given structure the load carried by the foundation at any given time is constant in magnitude and direction. While the characteristics feature of dynamic load is that it varies with time. Purely dynamic loads do not occur in nature. Loads always in combinations of static and dynamic. loads **Saran(2007)**.

The main causes of dynamic loads on soils, foundations and structures are due to one of the following:

1. Impact load (pile driving in construction operations),

2.Harmonic excitation (machine foundation), and

3.Acceleration-time history (Earthquake).

The nature of each of these loads is quite different from another.

There are aspects that should be taken into account in the criteria for satisfactory action of foundation under dynamic load:

1. No resonance should occur; the natural frequency of the machine-foundation- soil system should not coincide with the operating frequency of the machine. Generally, a zone of resonance is defined and the natural frequency of the system should lie outside this zone (**Saran,2006**) .The frequency ratio ( $r$ ) (defined as the ratio of operating frequency to natural frequency) should be :

i. In reciprocating machines (IS:2975 pt I-1982)

for important machines :  
 $r > 2.0$  and  $r < 0.5$

for ordinary machines :  
 $r > 1.5$  and  $r < 0.6$

ii. In impact machines (IS:2975 pt II-1980)

$r > 1.5$  and  $r < 0.4$

iii. In rotary machines (IS:2975 pt III-1992)

$r > 1.25$  and  $r < 0.8$

2. The amplitudes of motion at operating frequencies should not exceed the limiting amplitudes specified by the manufacturer(**Prakash and Puri , 2006**).

3.The vibrations must not annoy the persons working in the shops or damp the other precision machines (**Prakash and Puri ,2006**).

4.Foundation block should be structurally adequate to carry the loads (**Rao, 2011**).



5. The combined center of gravity (CG) of machine and foundation and the center of contact area (with the soil) should lie on the same vertical line as far as possible (Rao, 2011), so that the bearing capacity of all the system will increase.

6. Where possible, the foundation should be planned in such a manner as to permit a subsequent alteration of natural frequency by changing the base area or mass of the foundation as may subsequently be found necessary (Arora, 1997).

7. The ground-water level should be as low as possible, and it should be at least deep by one-fourth of the width of foundation below the base plane, (Arora, 1997).

8. Machine foundations should be separated from adjacent building components by means of expansion joints (Arora, 1997).

9. Machine foundation should be taken to a level lower than the level of the foundations of adjacent buildings (Arora, 1997), so that the wave transmitted through soil will not cause damage to the adjacent foundation.

**Mandal and Baidya (2003)**, studied experimentally the dynamic response of a foundation subjected to vibration in vertical mode on dry sand. The tests were carried out in two different pits in the field; one with rigid base and the other with a large depth simulating the half space. The damping factor and stiffness are calculated from the test results and corresponding to governing equation of motion using single degree of freedom. mass-spring-dashpot model, the solution for the displacement is obtained.

**Moreschi and Farzam (2005)** studied the application of the harmonic analysis resonant frequencies of individual structural members in large steam-turbine generator foundations. They proposed a methodology for the accurate determination of the local structural vibration properties.

**Prakash and Puri (2006)**, studied the methods of analysis for determining the response of foundation subjected to harmonic excitation. Analogy based on the elastic- half space solutions were used, and soil stiffness considered frequency independent for design of machine foundations. They found that the embedment of a foundation strongly influences its dynamic response.

## EXPERIMENTAL PROGRAM

The soil of this investigation was taken from Tikrit Governorate, north of Iraq, has been implemented for the testing program; Table (1) shows the physical and chemical properties of the soil.

## APPARATUSES OF MODEL

The apparatuses of model includes as follow:

- a. Steel box with dimension (1200x100x100)mm
- b. Mechanical oscillator
- c. Piezoelectric accelerometer
- d. Piezoelectric- vibration pickup
- e. Digital storage oscilloscope
- f. Variable frequency drive
- g. Vibration meter
- h. R.S interface cable
- i. Digital tachometer
- j. Computer device

## PLACEMENT OF SOIL

The density of the gypseous soils used through the experiments was controlled by means of the raining technique. This technique included raining of the soil through different heights of drop that gives different placing densities. Many investigators used this technique, (Lee, et al, 1973), (Sanjeev, 2007), and (Denver,

1983). The relations between height of drop, placement density, void ratio and relative density of gypseous soils is shown in Figures (1). It was decided to employ density (14.0) kN/m<sup>3</sup> of gypseous soils, which corresponds to height of drop (35) cm .

## PREPARATION AND TESTS PROCEDURE

The required amount of the gypseous soil (clean and passing sieve no.4) is placed into the steel container in sixteen layers with a uniform field density using the raining technique. The surface was leveled and checked by a bubble ruler (balance). The model machine foundation is placed centrally over the prepared gypseous soil layers. Proper care is taken to maintain the center of gravity of whole system and the footing to lie in the same vertical line with center of gravity of the container.

For the test under soaked condition, the steel box left for (24) hours to ensure that all soil was completely soaked, and in the second day the model machine foundation is placed, then the test was began. In this investigation, three different eccentric settings ( $m_e = 55, 75, \text{ and } 105$  gm) are used to simulate three different dynamic force level. The oscillator is then run slowly through a motor using speed control unit (Variable frequency drive) to avoid sudden application of high magnitude dynamic load. Thus the foundation is subjected to vibration in the vertical direction. the dynamic response and the waveform produced by mechanical oscillator are measured and recorded at the same time using two transducers which are placed previously on top of the footing. To obtain a foundation response and locate the resonant peak correctly, the displacement amplitudes are noted at a frequency interval approximately of 5 to 25 Hz. A sufficient time between two successive measurements has been given to reach equilibrium, which facilitates accurate measurement of frequency and the corresponding displacement amplitude.

## RESULTS AND DISCUSSION

The main object of this test in this research is to determine the dynamic response of the gypseous soil under the effect of harmonic vertical mode of vibration. The dynamic system is the soil medium through which wave propagate outward from the source of industrial vibrations. the input signal of the system is the impulse response of the ground at the place of installation of machine foundation. The output signal is the dynamic response of location of interest situated on the surface of the foundation receiving vibration, this response in this study investigated as displacement. And to make a clear image of the gypseous soil behavior under this mode of vibration the dry soil is tested as well soaked under different eccentric settings. The curves of the displacement amplitude of vibration with respect to changes in the frequency of the oscillator is plotted for each force level. The results of these test are shown in the figure (2). it can be seen that an increase in the value of ( $m_e$ ) leads to (i) decrease in resonant frequency. (ii) increase in resonant displacement amplitude. These differences come from the fact that different forces cause different strain levels below the foundation .see figure (2).

A series of forced vertical vibration test was conducted on gypseous soil under different dynamic force level and soaked condition. The results of the these tests showed that the displacement response of the foundation on dry gypseous soil is more than that on soaked one. Also it showed increasing in resonant frequency clearly, if it compares with the same dynamic force level in dry state. when gypseous soil soaked with water it suffers high compressibility due to dissolution of gypsum and loss of cementation and particle bounding, this could explain the small displacement amplitude of soaked gypseous soil in comparison of dry one. see figure(3). the relationship of eccentric mass with maximum displacement amplitude



and resonant frequency is shown in the figures (4) and (5) respectively.

## CONCLUSION

The following conclusions are drawn:

1. The displacement response of the foundation resting on dry gypseous soil is more than that on the soaked gypseous soil, while the resonant frequency is increased when gypseous soil is soaked with water.

2. An increasing in eccentric mass lead to an increasing in amplitude of displacement for the specific frequency and decreasing in resonant frequency.

## REFERENCE

Arora, K. R. (1997). "Soil Mechanics and Foundation Engineering". 4th ed., Delhi Standard Publishers Distributors, India.

Daghigh, Y., (1993), "Numerical Simulation of Dynamic Behaviour of an Earth Dam during Seismic Loading", Ph.D., Thesis, Delft University of Technology, Netherlands.

Denver, H. et al, (1983) "Reinforcement of Cohesionless Soil by PVC-Grid", Improvement of Ground", Proc. of the Eighth European Conference on Soil Mech and Found Eng, Vol.2, PP.481-489.

Lee, K. L., Adams, B. D., and Vagneron, J. M. J., (1973) "Reinforced Earth Retaining Walls", journal Soil Mech. Found. Div., Pro, ASCE, Vol.9, No.Sm10, PP.745-763.

Mandal, A. and Baidya, D. K. (2003): "The Influence of Rigid Boundary on the Dynamic Response of the Foundation: An Experimental Investigation". Electronic Journal of Geotechnical Engineering, Vol. 8, Bundle B.

Moreschi, M. L., Farzam, F. (2005). "Determination of Local Structural Vibration Properties For the Design of Machine Foundations". Proceeding, 2005 Structures Congress and the 2005 Forensic Engineering Symp.: Part of Metropolis and Beyond, ASCE, Reston, PP. 1161-1169.

Prakash, S. and Puri, V.K. (2006): "Foundation for Vibrating Machine". Special Issue, April-May 2006, Journal of Structural Engineering, SERC, Madras, India, [http://yoga10.org/Documents/SPVKPSER\\_Cpaper.pdf](http://yoga10.org/Documents/SPVKPSER_Cpaper.pdf).

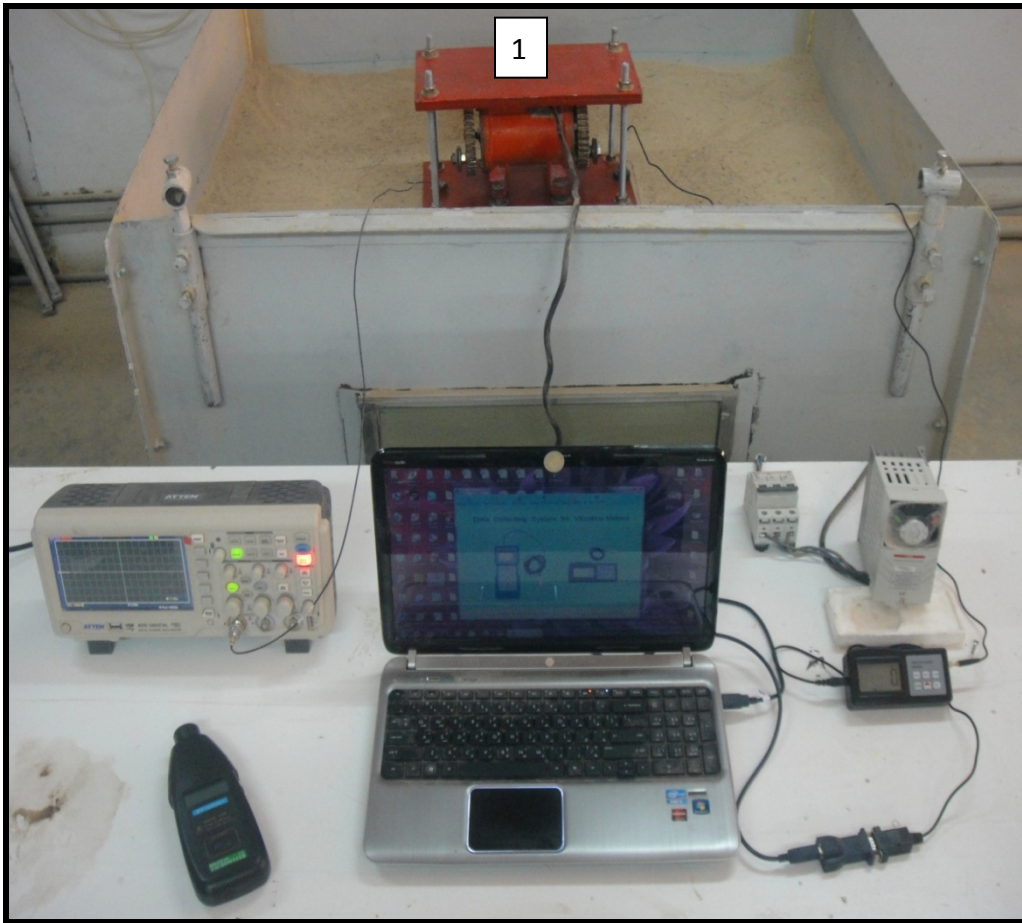
Rao, K., N. S. V. (2011). "Foundation Design Theory and Practice". a book, university Malaysia Sabah, Malaysia.

Sanjeev, M., (2007) "Effect of Wall Thickness on Plugging of Open Ended Steel Pipe Piles in Sand", ASCE, [Vislhttp://www.ascelibrary.org](http://www.ascelibrary.org).

Saran, S. (2006): "Soil Dynamic and Machine Foundation". Suneel Galgotia for Galgotia Publications.

**Table (1). Physical and Chemical Properties of Gypseous Soil**

Soil classification	SP-SM
Liquid Limit (L.L %)	21
Plastic Limit (P.L %)	19.6
Plasticity Index (IP)	1.4
Maximum Dry density( $\text{kN/m}^3$ )	14.8
Minimum Dry Density ( $\text{kN/m}^3$ )	11
Specific Gravity (Gs)	2.43
TSS %	42.02
Gypsum content %	43.10
SO <sub>3</sub> %	19.8
PH	8.5



**Plate(1)General View of Vibration Test Setup**

- 1-Mechanical oscillator**
- 2- Piezoelectric accelerometer**
- 3. Piezoelectric- vibration pickup**
- 4. Digital storage oscilloscope**
- 5. Variable frequency drive**
- 6. Vibration meter**
- 7.R.S interface cable**
- 8. Digital tachometer**
- 9.Computer device.**
- 10.Container.**

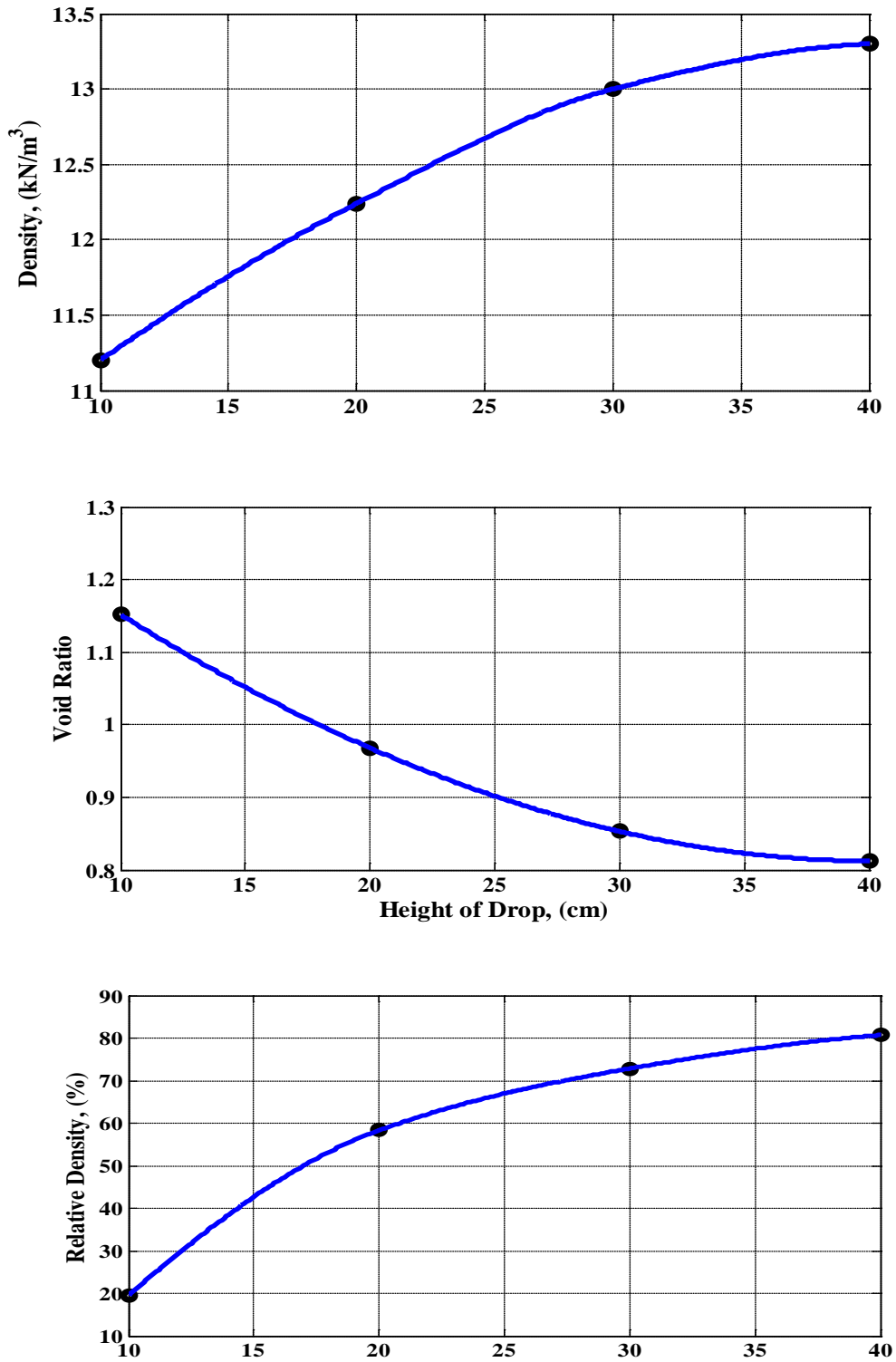
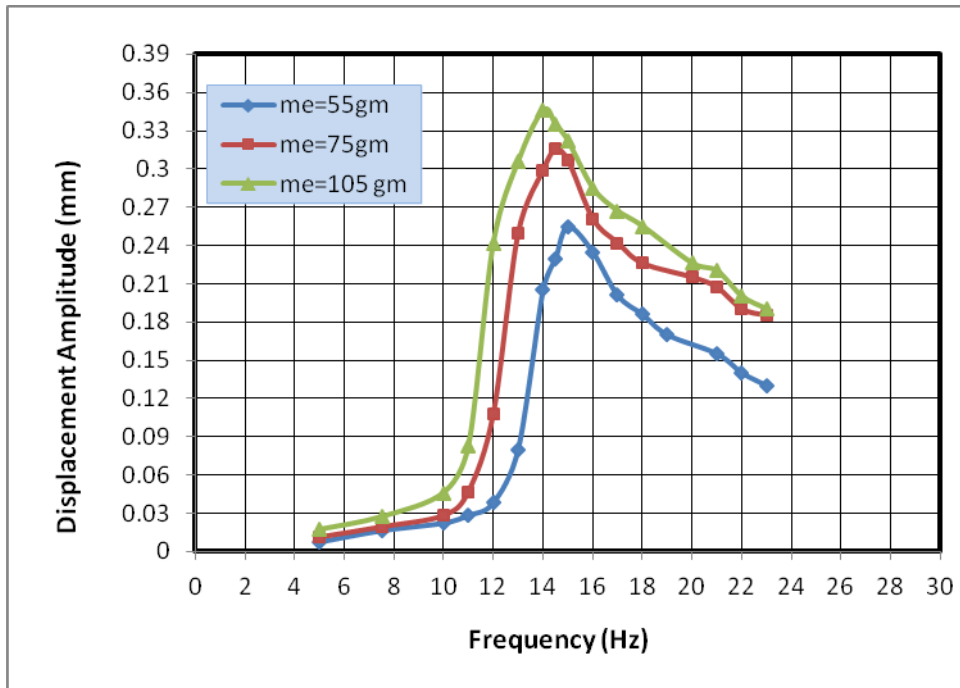
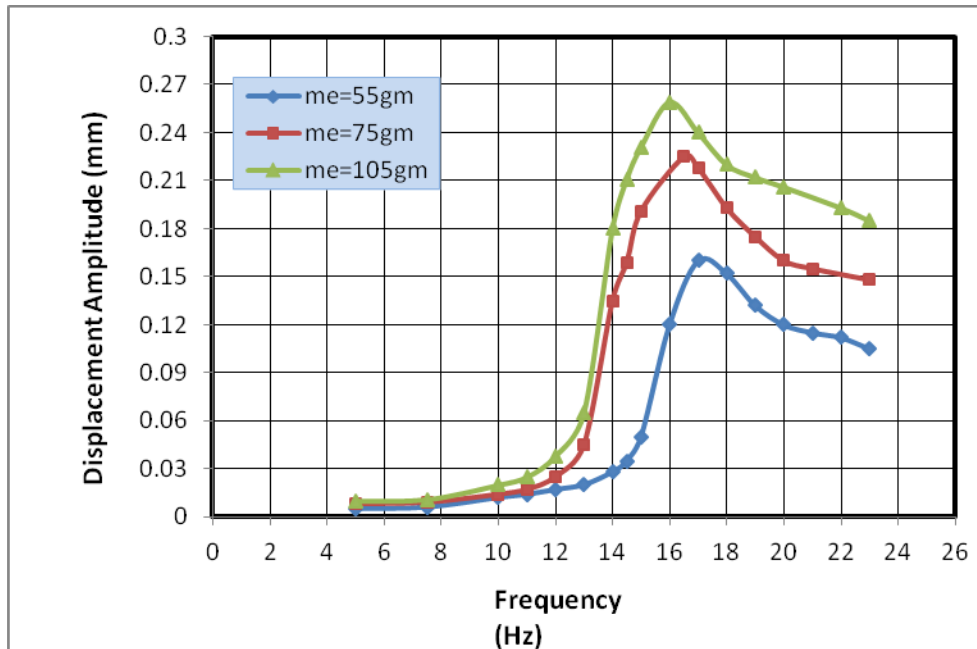


Fig. (1) Density Calibration Curves for Gypseous Soil By Raining Technique.



**Fig. (2) Variations of Displacement Amplitude with Frequency for Different Values of ( $m_e$ ) Dry State**



**Fig. (3) Variations of Displacement Amplitude with Frequency for Different Values of ( $m_e$ ), soaked State.**

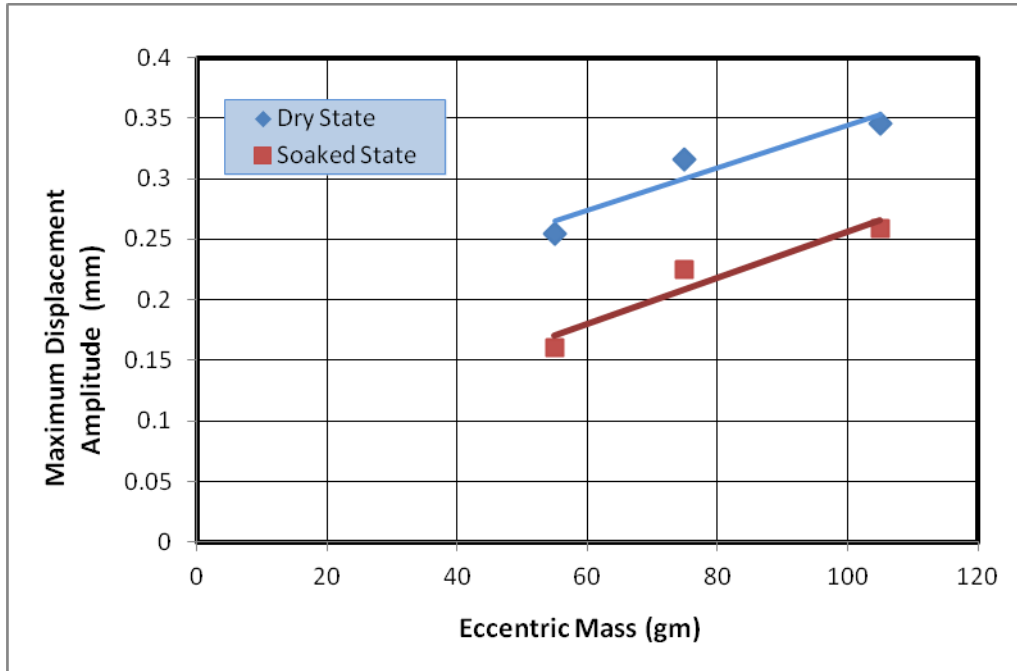


Fig.(4)The Maximum Displacement Amplitude and Eccentric Mass Relationship

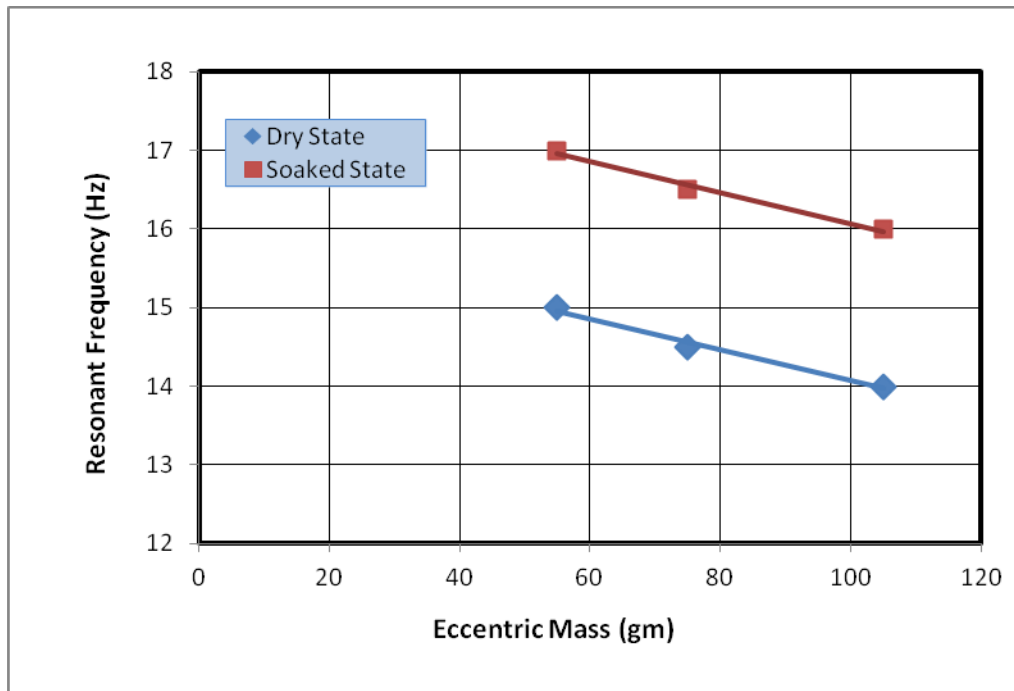


Fig.(5)The Resonant Frequency and Eccentric Mass Relationship



## Influence of Some Additives on the Efficiency of Viscosity Index Improver for Base Lubricating Oils

Prof. Dr. Talib Bahjat Kashmoula  
Tiba Naif Jasim

E-mail: [taiba208@yahoo.com](mailto:taiba208@yahoo.com)

Chemical Engineering Department, Collage of Engineering, Alnahrain University, Baghdad, Iraq

### ABSTRACT

The effects of three different additives formulations namely Lubrizol 21001, HiTEC 8722B and HiTEC 340 on the efficiency of VII namely OCP of three base lubricating oils namely 40 stock and 60 stock and 150 stock at four temperatures 40, 60, 80 and 100°C were investigated. The efficiency of OCP is decreased when blended with 4 and 8 wt% of Lubrizol 21001 for all the three base oil types. But it is increased when adding 4 wt% and 8 wt% of H-8722B in 40 stock. While for 60 stock and 150 stock the OCP efficiency decreased by adding 4 and 8 wt% of H-8722B. In the other hand, it is decreased with a high percentage by adding 4 and 8 wt% of H-340 for 60 stock and 150 stock and for 40 stock it is increased by adding 4 wt% of H-340 and decreased with insignificant percentage when adding 8 wt%. Finally, a number of VI correlations have been obtained depending on the results predicted in this study. These correlations represent the functional relationships between the VI and the concentration of OCP for three types of base lubricating oil and for each type of additives.

**Keywords:** Lubricating oil, Kinematic Viscosity, Viscosity Index, Viscosity Index Improver, Additives, Temperatures.

### تأثير بعض المضافات على كفاءة مؤشر محسن اللزوجة لزيوت التزييت الأساس

أ.د. طالب بهجت كشمولة

طبيبة نايف جاسم

قسم الهندسة الكيمياء، كلية الهندسة، جامعة النهرين، بغداد، العراق

### الخلاصة

في هذا البحث تمت دراسة تأثير ثلاثة أنواع من المضافات المستحصلة من مصفى الدورة في بغداد والتي هي Lubrizol 21001 و HiTEC 8722B و HiTEC 340 على كفاءة محسن مؤشر اللزوجة من نوع Olefin Copolymer والذي يستخدم لزيوت التزييت الأساس الثلاثة المستحصلة أيضا من مصفى الدورة والتي هي 40 stock و 60 stock و 150 stock. وتمت الدراسة عند أربع درجات حرارة هي 40 و 60 و 80 و 100 °م. وجد إن كفاءة محسن مؤشر اللزوجة (OCP) تقل بمعدل تصاعدي عند خلط 4 و 8 wt% من المضاف Lubrizol 21001 لأنواع زيوت التزييت الثلاث. ولكن هذه الكفاءة تتحسن بإضافة 4 wt% و 8 wt% من المضاف HiTEC 8722B عند خلطه مع الزيت 40 stock. بينما للنوعين 60 و 150 stock فإن كفاءة OCP تقل عند كلا التركيزين 4 و 8 wt%. لوحظ إنه عند خلط المضاف HiTEC 340 وبكلا التركيزين 4 و 8 wt% فإن كفاءة محسن مؤشر اللزوجة تنخفض بمقدار كبير للنوعين 60 و 150 stock. بينما عند خلطه مع الزيت 40 stock وبتركيز 4 wt% فإن الكفاءة تزداد بينما تقل عند خلطه بتركيز 8 wt%. أيضا تم إيجاد عدة معادلات تربط بين مؤشر اللزوجة وبتركيز محسن مؤشر اللزوجة لكل نوع من زيوت التزييت الثلاث ولكل نوع من المضافات الثلاثة المستخدمة.

كلمات رئيسية: زيوت التزييت، اللزوجة الكينماتيكية، مؤشر اللزوجة، محسن مؤشر اللزوجة، مضافات، درجات حرارة.

## 1. INTRODUCTION:

Lubricant may serve many purposes such as conducting the heat of friction away from the bearings, serving as a seal to exclude undesirable substances from the area being lubricated, acting as a carrier for rust preventive, anti-friction agents, extreme pressure additives and other properties. However, their primary purpose is in general to lubricate, i.e., to reduce friction (Zuidema, 1959). Lubricating oil additives are normally used in low concentrations from a fraction of a one percent to five percent or may be more. Their purposes may be to impart extreme pressure characteristics, reduce pour point, improve the viscosity index, reduce bearing corrosion, reduce or eliminate foaming and so on (Hobson, 1984). The selection of right additive or of the most suitable combination of additives depends on the specific use of the oil (Brouwer, 1966).

The most important property of lubricating oil is its kinematic viscosity, which is a measure of its internal friction or ability to flow and largely determines its suitability for any particular application (Brouwer, 1966).

The kinematic viscosity of an oil decreases with rising in temperature but to varying degree depending on the type of crude oil from which it is derived and the refining treatment to which it has been subjected. The relationship between viscosity and temperature is the significance for lubricating oils since most oils have to operate over a range of temperatures. There are many ways of expressing this relationship but the one firmly established in the petroleum industry is viscosity index (VI) system, even though it is an arbitrary system and more fundamental methods have been suggested (Bill Hires, 1993).

## 2. MATERIALS:

In this study, the experimental work will be carried out on Iraqi paraffinic oils which have three types of base-stocks that were obtained from Al-Daura Refinery, namely 40, 60 and 150 stock. These types of base stocks were processed as base lubricating oil without additives. The lightest one is 40 stock with °API gravity of 34.976, the middle type is 60 stock which have °API gravity of 29.24 and 150 stock is the heaviest type with

°API gravity of 23.90 (measured in the Research and Quality Control Laboratory, 2012).

Olefin Copolymer (OCP) of type PVC-100 XA is a VII (solute) for base lubricating oil (solvent). OCP is a polymer composed of two or more different monomer. The OCPs have unknown structure, different companies are producing them.

This type of VII is designed to provide a careful balance of thickening power, low-temperature fluidity, shear stability and high-temperature viscosity (McCrum, 1997).

Three types of additives (Lubrizol 21001, HiTEC 8722B and HiTEC 340) were obtained from Al-Daura Refinery. Lubrizol 21001 is a multipurpose additive for otto engine. The recommended dosage is 10.8% by weight. This additive when formulated with the appropriate base stocks and VII will meet the requirements of ACEA A3/B4-04(2004), API SL, API CF, and Volkswagen VW50101 (2005) (Research and Quality Control Laboratory, 2012).

HiTEC 8722B is a multipurpose additive for diesel engine. It provides efficient additive solutions according to API, ACEA and OEMs heavy-duty diesel requirements. This additive has been designed to offer cost optimized formulations and delivers a number of customer benefits. Its package approval is supported by complete engine test data. The recommended dosage is 7.8% by weight. And it allows the use of a wide range of base oils and VIIs (Afton Company, HiTEC-8722B).

HiTEC 340 is an economic automotive gear oil additive. It is used for axles and transmissions. It provides robust performance in automotive applications, cost savings at all treat-rates, extensive history of trouble-free performance and suitable for unharmed drain. The recommended dosage is 4% by weight and its treat-rates may vary depending on base oil type (Afton Company, HiTEC-340).

## 3. EXPERIMENTAL WORK:

The composition of each mixture was prepared as weight percentage for more accuracy than mole percentage. Mixing process was made by stirring and heating to about 50-60°C at the same time to ensure thorough mixing.



Viscosity measurements were taken immediately, after preparing the mixture to avoid deposit formation or vaporizing the light ends. All these measurements were taken at the atmospheric pressure.

The following mixtures were prepared in this study:

**1) Binary Mixtures:**

There were four types of binary mixtures, as follows:

- a) Binary mixtures of each type of oil-stock (40, 60 and 150 stock) with 0-10 wt% of OCP.
- b) Binary mixtures of each type of oil-stock (40, 60 and 150 stock) with 0-10 wt% of Lubrizol 21001.
- c) Binary mixtures of each type of oil-stock (40, 60 and 150 stock) with 0-10 wt% of H-8722B.
- d) Binary mixtures of each type of oil-stock (40, 60 and 150 stock) with 0-10 wt% of H-340.

**2) Ternary Mixtures:**

These ternary mixtures were prepared as follows:

- a) 40 stock:
  1. 40 stock with 4 and 8 wt% of Lubrizol 21001 with 2-8 wt% of OCP.
  2. 40 stock with 4 and 8 wt% of H-8722B with 2-8 wt% of OCP.
  3. 40 stock with 4 and 8 wt% of H-340 with 2-8 wt% of OCP.
- b) 60 stock:
  1. 60 stock with 4 and 8 wt% of Lubrizol 21001 with 2-8 wt% of OCP.
  2. 60 stock with 4 and 8 wt% of H-8722B with 2-8 wt% of OCP.
  3. 60 stock with 4 and 8 wt% of H-340 with 2-8 wt% of OCP.
- c) 150 stock:
  1. 150 stock with 4 and 8 wt% of Lubrizol 21001 with 2-8 wt% of OCP.

2. 150 stock with 4 and 8 wt% of H-8722B with 2-8 wt% of OCP.

3. 150 stock with 4 and 8 wt% of H-340 with 2-8 wt% of OCP.

Cannon Fenske Routine Viscometers (the glass capillary type) with different sizes were used for measuring the time of the solvent (base oil) ( $t_0$ ) and time of mixtures ( $t$ ) which are used in calculating the kinematic viscosity of transparent Newtonian liquids according to the Standard Test Method for Kinematic Viscosity of Transparent and Opaque Liquids (ASTM D 445-03).

Times measured are used to calculate the kinematic viscosity using the following equation:

$$v = t \times f \quad (1)$$

Where:  $v$  is the kinematic viscosity ( $\text{mm}^2/\text{s}$ ),  $t$  is the measured time (s) and  $f$  is the viscometer factor.

The VI as mentioned before is an arbitrary scale for comparing the rates of viscosity changes of lubricating oil with temperature. The VI scale was set up by the SAE. The temperatures chosen arbitrarily for reference are 40 and 100°C.

#### 4. RESULTS AND DISCUSSION:

The effect of temperature on the VI of the three types of base lubricating oil was measured. Table 1 shows the values of VI which are obtained from the kinematic viscosities and the SAE VI scale at the two reference temperatures 40 and 100°C.

Blends from the three types of base stocks with different concentrations of OCP with a range of 0-10 wt% were prepared. Those blends give a significance increase in the kinematic viscosity and VI as the weight percent of OCP increase. This is because OCP composed of long and flexible polymer molecules that interact with the base stocks and this interaction leads to increase the resistance to flow (Canter, 2011).

The concentration of OCP must be limited, because the additional effects may then arise from intermolecular forces and entanglements between chains. Therefore, OCP is excellent in economical efficiency, because it exhibits the effect even if it is added in a small amount (Kaneshige, 2009).

It is noticed that the increase in OCP concentration, which blended with the base oils, will improve the VI as shown in Figure 1. It affects 40 stock by 154%, 60 stock by 90% and 150 stock by 57%, by adding 10 wt% of OCP.

Also, the improving in VI will be with a decreasing rate as the concentration of OCP increased.

In the other hand, the three types of additives (Lubrizol 21001, HiTEC 8722B, and HiTEC 340) will blend with the three types of base oil in a concentration range of 0-10 wt% and temperature range of 40-100°C. And their effects on the kinematic viscosity and VI were different as shown in Figures 2, 3 and 4.

For Lubrizol 21001, it has been found that the enhancement in the VI for 40 stock is more pronounced than for 60 and 150 stock as sketched in Figure 2. The increasing in VI is about 35%, 10% and 8% for 40, 60 and 150 stock, respectively when adding 10 wt% of Lubrizol 21001. Also it has been noticed that the rate of improvement in the VI for 40 stock is in a range of 7.5-10%, while it is 2% for 60 stock and 1.1-2.2% for 150 stock with every 2 wt% added of Lubrizol 21001.

For the second type of additives which is H-8722B, it has been found that the improving in the VI for 40 stock is very noticeable more than for 60 and 150 stock as shown in Figure 3. The increasing in VI is about 22%, 5% and 2% for 40, 60 and 150 stock, respectively when adding 10 wt% of H-8722B. So it recommended using such additive with light oil types like 40 stock because of its insignificance effect on both 60 and 150 stock.

While for the third type of additives which is H-340, it can be seen from Figure 4 that the maximum VI is obtained at different concentrations of H-340. These concentrations are 2 wt% for 40 stock and 150 stock whereas 2, 4 and 6 wt% for 60 stock.

These concentrations are very helpful in selecting the base oil type and the recommended dosage of H-340 for producing effective and economic automotive gear oil. Such behavior of additive on the VI was also obtained by using the PIB and PBR with the base oil types (Tanveer, 2006).

But in order to study the influence of the three additives on the efficiency of OCP, two sets of mixtures from a base stock, OCP and an additive were prepared with an additive concentration of 4 wt% in the first set and 8 wt% in the second with the three types of base stocks (40, 60 and 150 stock) and OCP concentration range of 2-8 wt%.

The effect of Lubrizol 21001 on the VI is sketched in Figures 5, 6 and 7. It can be shown

that at a specific concentration of Lubrizol 21001, when blended with the three types of base oil, the VI will be improved with the increasing of OCP concentration.

Also it can be noticed that at all OCP concentrations the VI will be decreased as the concentration of Lubrizol 21001 increased.

The efficiency of OCP is performed by measuring the VI of blends before and after adding Lubrizol 21001. For 40 and 150 stock, the decreasing rate of OCP efficiency is calculated to be about 7% and 10% by adding 4 and 8 wt% of Lubrizol 21001, respectively. While the decreasing rate of the efficiency is obtained to be about 10% and 16% when 60 stock is blended with 4 and 8 wt% of Lubrizol 21001, respectively. So it is not preferred to use Lubrizol 21001 as lubricating oil additive in the presence of OCP because it lowers the VI as well as the efficiency of the VII.

For H-8722B its effect is drawn in Figures 8, 9 and 10. It can be indicated that the VI is improved with increasing OCP concentration at the two concentrations of H-8722B because this additive is composed of long and flexible polymer molecules that interact with the base oil and OCP. This interaction will cause greater volume and the base oil produces a proportionally greater thickening effect which in turn raises the VI of the oil (Shawn, 2002). In the other hand at all OCP concentrations the VI will be decreased as the concentration of H-8722B increased.

With respect to the efficiency of OCP, the 60 stock showed the same behavior as in adding Lubrizol 21001 by having the highest decreasing rate for the OCP efficiency which was about 7% and 14% by adding 4 and 8 wt% of H-8722B, respectively. While for 150 stock the decreasing rate is obtained to be about 2% by adding 4 wt% and being 4% by adding 8 wt% of H-8722B.

It is interesting to know that for 40 stock the efficiency is increased by 5% when adding 4 wt% and it increased by insignificant value when adding 8 wt% of H-8722B so it is better to use H-8722B as lubricating oil additive in the presence of OCP by adding 4 wt% or less.

Finally, the VI Figures from 11, 12 and 13 showed the effect of H-340 on the three base oil types and OCP.

It can be noticed that the VI is improved with increasing OCP concentration at the two concentrations of H-340. And at all OCP



concentrations the VI will be decreased as the concentration of H-340 increased.

As for the efficiency of OCP, this additive would strongly decrease the OCP efficiency of the 60 stock, the decreasing rate for the OCP which was about 37% and 28% by adding 4 and 8 wt% of H-340, respectively. While for 150 stock the decreasing rate is obtained to be about 10% by adding 4 wt% and being about 14% by adding 8 wt% of H-340.

It is a coincidence that for 40 stock the efficiency at 4 wt% of H-340 is increased just like in H-8722B which it was by about 5% and it also decreased when adding 8 wt% of H-340. So it is better to use H-340 as lubricating oil additive in the presence of OCP by adding 4 wt% or less.

### 5. CORRELATIONS FOR VI

A number of VI correlations have been obtained in this section using the regression analysis and depending on the results which presented in the previous section of this study.

The functional relationships are between the VI and the concentration of OCP for three types of base lubricating oil and for each type of additives.

From Table 2 three correlations between VI and the OCP concentration where obtained as shown below:

For 40 stock:

$$VI = -1.9821C_{OCP}^2 + 35.493C_{OCP} + 109.71 \quad (2)$$

For 60 stock:

$$VI = 9C_{OCP} + 102 \quad (3)$$

For 150 stock:

$$VI = 4.7571C_{OCP} + 94.381 \quad (4)$$

For Lubrizol 21001 it has been noticed that the correlations at 4 wt% of this additive is different from the correlations of 8 wt%. From Tables 3 and 4 the functional relationships were obtained as follows:

a. At 4 wt% of Lubrizol 21001:

For 40 stock:

$$VI = -2.0625C_{OCP}^2 + 31.875C_{OCP} + 121.25 \quad (5)$$

For 60 stock:

$$VI = 6.4C_{OCP} + 102 \quad (6)$$

For 150 stock:

$$VI = 3.151C_{OCP} + 97 \quad (7)$$

b. At 8 wt% of Lubrizol 21001:

For 40 stock:

$$VI = -0.875C_{OCP}^2 + 17.65C_{OCP} + 142.5 \quad (8)$$

For 60 stock:

$$VI = 4.5C_{OCP} + 96.5 \quad (9)$$

For 150 stock:

$$VI = 2.65C_{OCP} + 96.5 \quad (10)$$

Also for H-8722B the functional relationships were obtained using the regression analysis depending on Tables 5 and 6. The correlations are given below:

a. At 4 wt% of H-8722B:

For 40 stock:

$$VI = -0.5625C_{OCP}^2 + 18.275C_{OCP} + 107.75 \quad (11)$$

For 60 stock:

$$VI = 6.85C_{OCP} + 92.5 \quad (12)$$

For 150 stock:

$$VI = 4.1C_{OCP} + 87.5 \quad (13)$$

b. At 8 wt% of H-8722B:

For 40 stock:

$$VI = 10.95C_{OCP} + 117.5 \quad (14)$$

For 60 stock:

$$VI = 4.5C_{OCP} + 93 \quad (15)$$

For 150 stock:

$$VI = 3.6C_{OCP} + 86.5 \quad (16)$$

For H-340 the correlations at 4 wt% of this additive is different from the correlations of 8 wt%. These functional relationships were obtained depending on Tables 7 and 8 as follows:

a. At 4 wt% of H-340:

For 40 stock:

$$VI = 11.8C_{OCP} + 111 \quad (17)$$

For 60 stock:

$$VI = 1.35C_{OCP} + 95.5 \quad (18)$$

For 150 stock:

$$VI = 1.9C_{OCP} + 92 \quad (19)$$

b. At 8 wt% of H-340:

For 40 stock:

$$VI = 9.9C_{OCP} + 109.5 \quad (20)$$

For 60 stock:

$$VI = C_{OCP} + 95.5 \quad (21)$$

For 150 stock:

$$VI = 1.5C_{OCP} + 91.5 \quad (22)$$

For the correlations above the error percentage is in the range of 2-3%. These functional relationships are applicable only for this set of blends and it can be applied usefully for determining the VI values at any OCP concentration or vice versa.

## 6. CONCLUSIONS:

From the proposed study, the following conclusions have been extracted:

1. The kinematic viscosity and viscosity index of the light oil (40 stock) is affected more than the medium oil (60 stock) and the heavy oil (150 stock) and this can be attributed to the fact that the rate of change with temperature depends largely on the type of base oil.
2. The kinematic viscosity of the mixtures prepared from base oil, viscosity index improver and additives will decrease with increasing temperature as their resistance to flow will decrease.
3. The used additives (Lubrizol 21001, H-8722B and H-340) are packages contain a polymeric chain behaves as a viscosity index improver. So when those additives are blended with only the base oil the viscosity index will increase slightly and this is recommended in monograde oils. While when those additives are blended with the base oil and with a viscosity index improver like OCP, the obtained oil will be a multigrade oil.
4. The viscosity index for both 40 and 150 stock when blended with 2 wt% of H-340 additive will increase by about 4% and at higher concentrations it will decrease. While for 60 stock at 2, 4 and 6 wt% of H-340 the viscosity index will increase negligibly and then decrease at higher concentrations.
5. The efficiency of OCP (VII) is decreased with an increasing rate when blended with 4 and 8 wt% of Lubrizol 21001 for all the three base oil types.
6. The efficiency of OCP is increased by 5% when adding 4 wt% of H-8722B in 40 stock and increase by insignificant value when adding 8 wt%. For 60 stock the OCP efficiency decreased by a rate of about 7% and 14% by adding 4 and 8 wt% of H-8722B, respectively. While for 150 stock the efficiency of OCP decreased the decreasing rate is obtained to be about 2% by adding 4 wt% and being 4% by adding 8 wt% of H-8722B. So it is better to use this additive with lubricating oil in the presence of OCP by adding 4 wt% or less.
7. H-340 would strongly decrease the efficiency of OCP for 60 stock, the decreasing rate was about 37% and 28% by adding 4 and 8 wt% of H-340, respectively. For 150 stock the decreasing rate is obtained to be about 10% by adding 4 wt% and being about 14% by adding 8 wt% of H-340. While for 40 stock the efficiency at 4 wt% of H-340 is increased by about 5% and decreased insignificantly when adding 8 wt% of H-340. It is recommended to use H-340 as lubricating oil



additive in the presence of OCP by adding 4 wt% or less.

- 8. Many correlations were obtained for the VI with respect to the concentration of OCP. And it has been found that there is no unified correlation can represent this system as whole.

**7. REFERENCES:**

An American National Standard, "Standard Test Method for Kinematic Viscosity of Transparent and Opaque Liquids", D445-03, Part 71, 1990.

Bill Hires, "How to Select a Lubricating Oil for Farm Engines", October, 1993.

Brouwer, L.E.J., "The Petroleum Handbook", 5<sup>th</sup> Edition, pp. 116-235, 1966.

Canter N., "Viscosity Index Improvers", September, 2011. <http://www.STLE.ORG>

HiTEC-8722B\_PDS.pdf, 2011. <http://www.aftonchemical.com>

HiTEC-340\_PDS.pdf, 2011. <http://www.aftonchemical.com>

Hobson, G.D., "Modern Petroleum Technology", 5<sup>th</sup> Edition, Applied Science Publishers Ltd., London, 1984.

Kaneshige R., Matsuda A., Ikeda S., Okada K. and Kawasaki M., "Viscosity Modifier of Lubricating Oil for Power Transmission system and Lubricating Oil Composition for Power Transmission System", 22 January 2009. <http://www.freshpatents.com>

McCrum, N.G., C.P. Buckley and C.B. Bucknall, "Principles of Polymer Engineering", 2<sup>nd</sup> Ed., New York, 1997.

Shawn D., Tsai H. and Orban j., "Lubricants Base stock and Additive Effects on Diesel Engine Emissions", National Renewable Energy Laboratory, 2002.

Tanveer, Sabiha and Ram Prasad, Indian Journal of Chemical Technology, Vol.13, pp. 398-403, July, 2006.

Zuidema, H.H., "The Performance of Lubricating Oils", 2<sup>nd</sup> Edition, 1959.

**8. Tables and Figures:**

**Table 1 VI of Base Lubricating Oil**

Base Lubricating oil type	VI
40 stock	106
60 stock	97
150 stock	90

**Table 2 VI Values of Base Oil Blended with OCP**

OCP wt%	VI of 40 stock	VI of 60 stock	VI of 150 stock
0	106	97	90
2	178	119	105
4	223	143	117
6	248	162	126
8	262	176	133
10	270	185	138

**Table 3 VI Values of Base Oil and 4 wt% of Lubrizol 21001 with Different Concentrations of OCP at Different Temperatures**

OCP wt%	VI of 40 stock	VI of 60 stock	VI of 150 stock
2	176	114	103
4	218	128	110
6	236	142	116
8	245	152	122

**Table 4. VI Values of Base Oil and 8 wt% of Lubrizol 21001 with Different Concentrations of OCP at Different Temperatures**

OCP wt%	VI of 40 stock	VI of 60 stock	VI of 150 stock
2	174	106	101
4	200	113	108
6	216	125	113
8	228	132	117

**Table 5. VI Values of Base Oil and 4 wt% of H-8722B with Different Concentrations of OCP at Different Temperatures**

OCP wt%	VI of 40 stock	VI of 60 stock	VI of 150 stock
2	141	108	97
4	175	118	102
6	194	132	112
8	219	149	121

**Table 6. VI Values of Base Oil and 8 wt% of H-8722B with Different Concentrations of OCP at Different Temperatures**

OCP wt%	VI of 40 stock	VI of 60 stock	VI of 150 stock
2	139	100	95
4	163	114	99
6	181	120	108
8	206	128	116

**Table 7. VI Values of Base Oil and 4 wt% of H-340 with Different Concentrations of OCP at Different Temperatures**

OCP wt%	VI of 40 stock	VI of 60 stock	VI of 150 stock
2	134	99	96
4	161	100	99
6	178	103	103
8	207	107	107

**Table 8. VI Values of Base Oil and 8 wt% of H-340 with Different Concentrations of OCP at Different Temperatures**

OCP wt%	VI of 40 stock	VI of 60 stock	VI of 150 stock
2	131	98	95
4	147	99	97
6	168	101	100
8	190	104	104

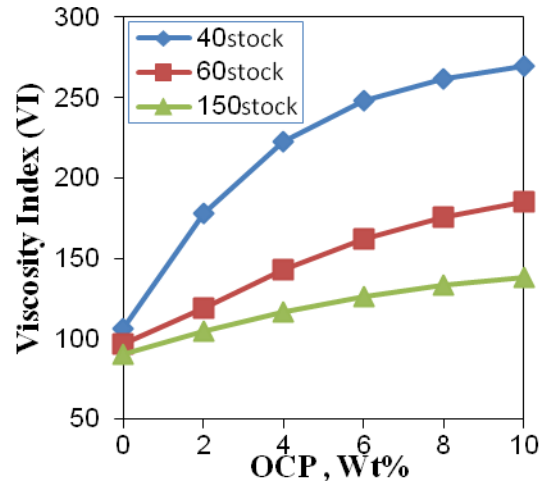


**Fig. 1 Effect of OCP on VI of the Three Types of Base Lubricating Oil**

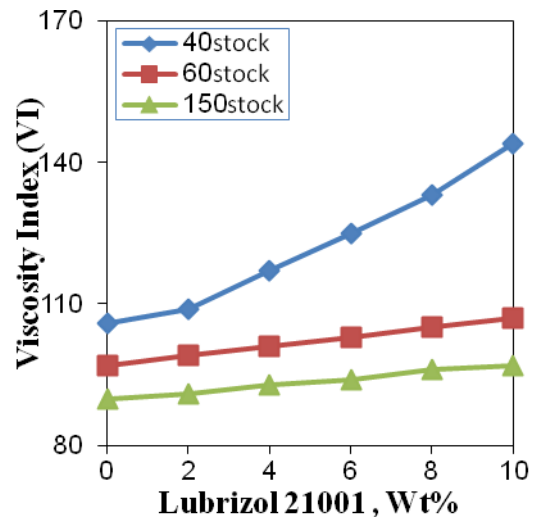


**Fig. 2 Effect of Lubrizol 21001 on VI of the Three Types of Base Lubricating Oil**

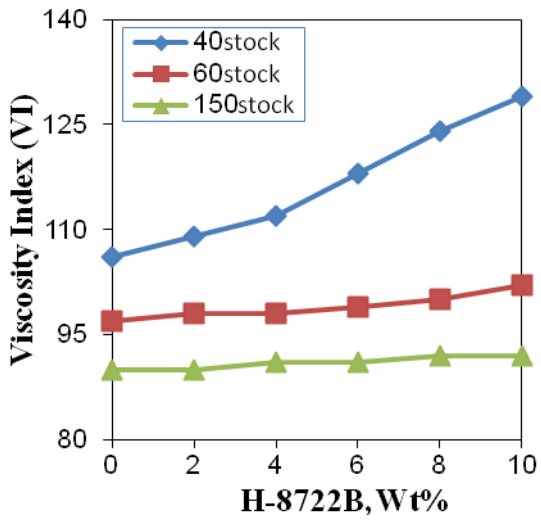


Fig. 3 Effect of H-8722B on VI of the Three Types of Base Lubricating Oil

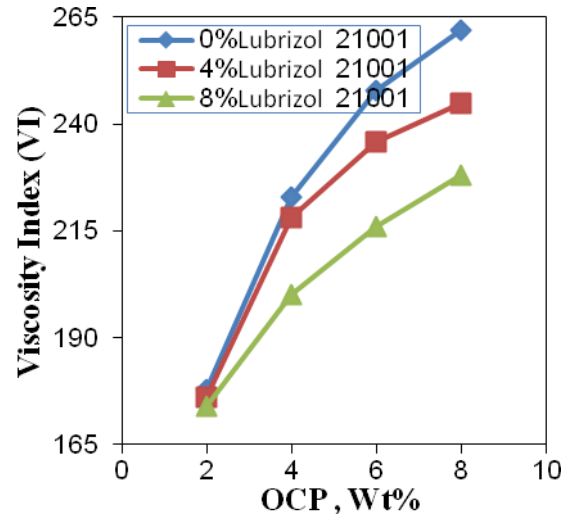


Fig. 5 Effect of OCP on VI of 40 stock + 0, 4 and 8 wt% of Lubrizol 21001

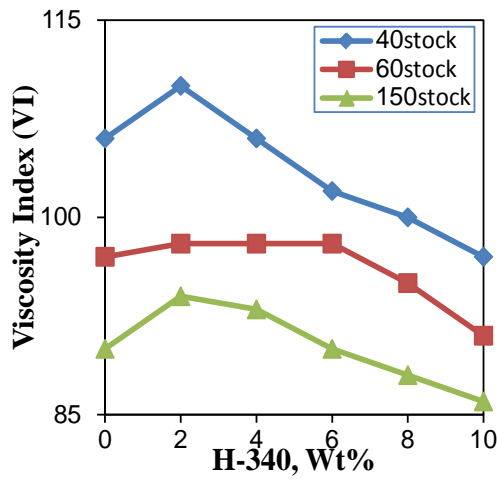


Fig. 4 Effect of H-340 on VI of the Three Types of Base Lubricating Oil

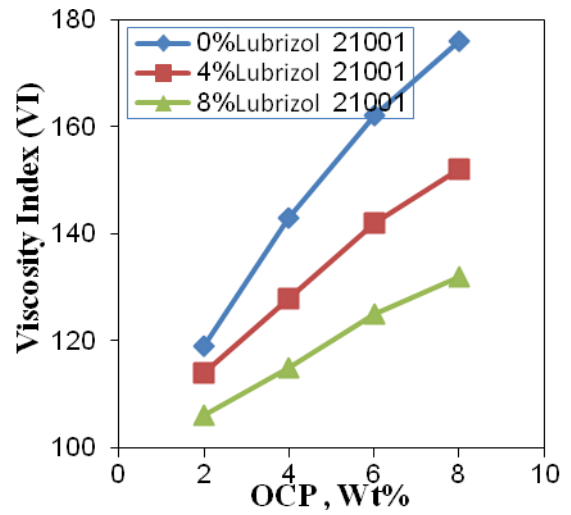


Fig.6 Effect of OCP on VI of 60 stock + 0, 4 and 8 wt% of Lubrizol 21001

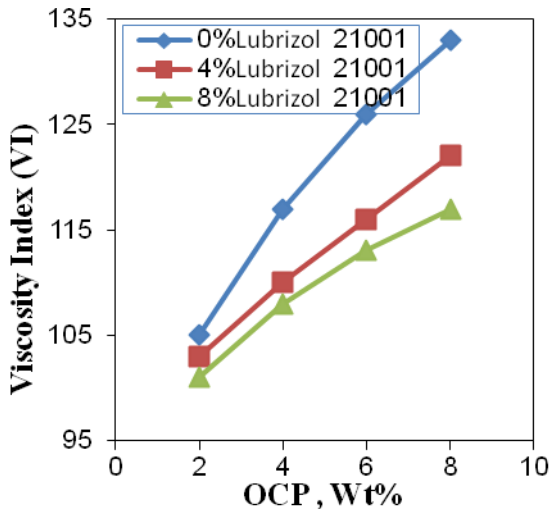


Fig. 7 Effect of OCP on VI of 150 stock + 0, 4 and 8 wt% of Lubrizol 21001

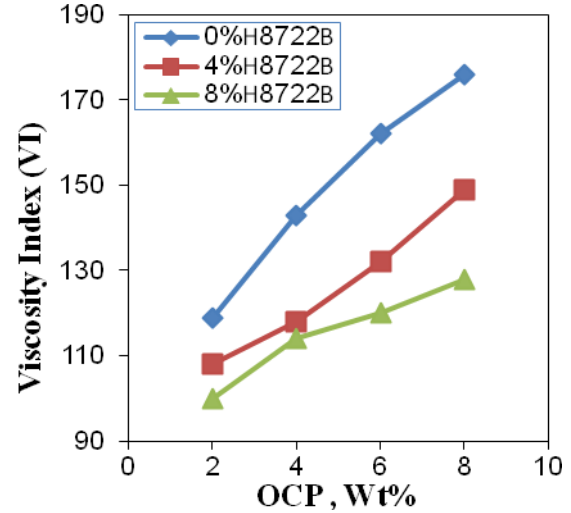


Fig. 9 Effect of OCP on VI of 60 stock + 0, 4 and 8 wt% of H-8722B

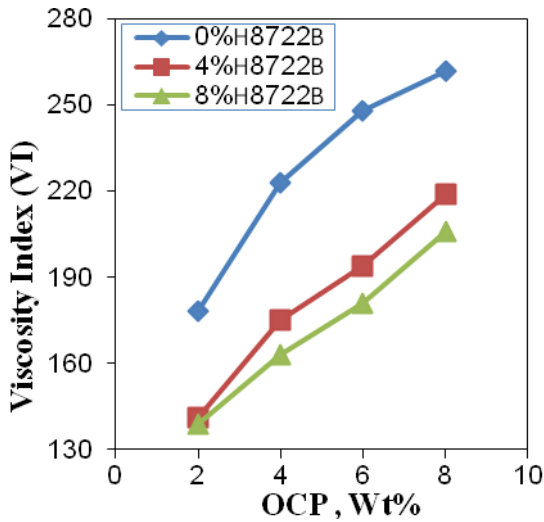


Fig. 8 Effect of OCP on VI of 40 stock + 0, 4 and 8 wt% of H-8722B

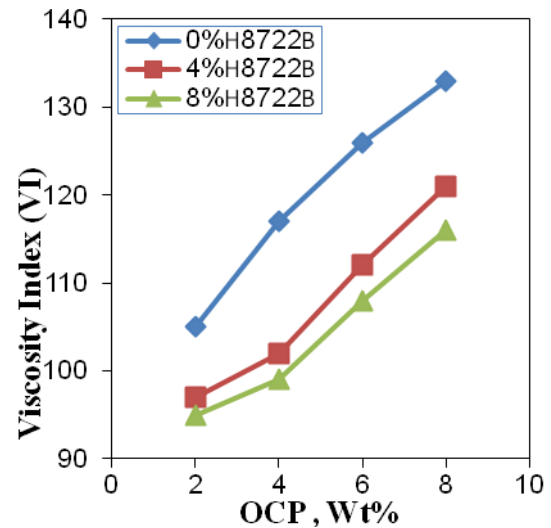


Fig.10 Effect of OCP on VI of 150 stock + 0, 4 and 8 wt% of H-8722B

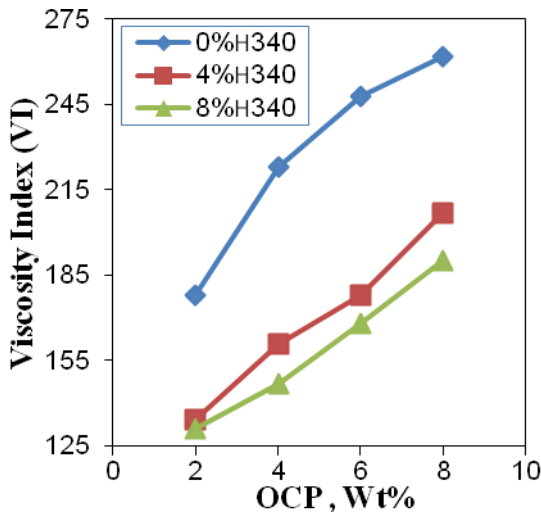


Fig. 11 Effect of OCP on VI of 40 stock + 4 and 8 wt% of H-340

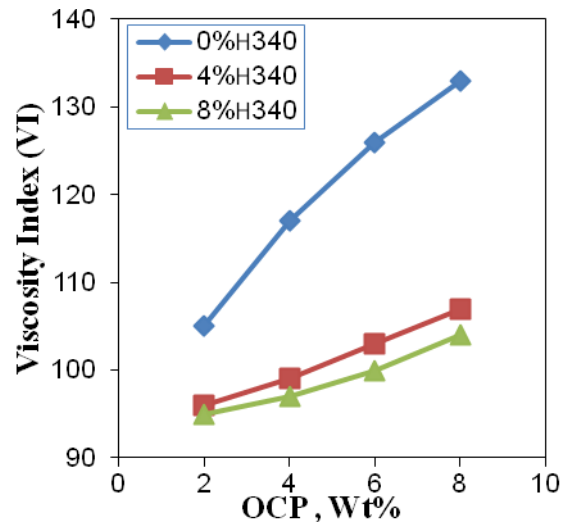


Fig. 13 Effect of OCP on VI of 150 stock + 4 and 8 wt% of H-340

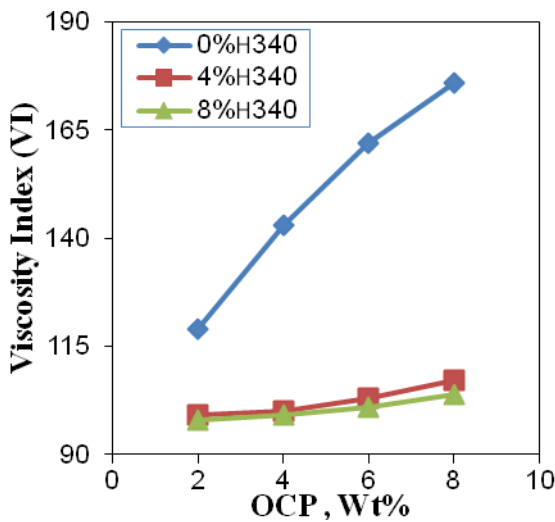


Fig. 12. Effect of OCP on VI of 60 stock + 4 and 8 wt% of H-340

### Notations and Abbreviations

- C<sub>OCP</sub> Concentration of Olefin Copolymer, g/cm<sup>3</sup>
- ACE European Automobile Manufacturers Association
- API American Petroleum Institute
- OCP Olefin Copolymer
- OEM Original Element Manufacturer
- PBR Poly Butadiene Rubber
- PIB Polyisobutylene
- SAE Society of Automotive Engineers
- VI Viscosity Index
- VII Viscosity Index Improver

## Effect of Nb Addition on Hardness and Wear Resist of Cu-Al-Ni Shape Memory Alloy Fabricated By Powder Metallurgy

M-sc. Raied Z. Alfay  
Collage of Engineering  
Al-Nahrain university  
raiedzewar@yahoo.com

Asst prof. Ayad M. Takhakh  
Collage of Engineering  
Al-Nahrain university  
ayadtakak@yahoo.com

Asst prof. Abdul Rahim K. Abid Ali  
Collage of Engineering  
Al-Nahrain university  
abidalieng@yahoo.com

### ABSTRACT

Cu-Al-Ni shape memory alloy specimens has been fabricated using powder metallurgy technique with tube furnace and vacuum sintering environment , three range of Nb powder weight percentage (0.3,0.6,0.9)% has been added. Micro hardness and sliding wear resist has been tested followed by X-ray diffraction, scanning electron microscope (SEM) and energy dispersive X-ray spectroscopy (EDX) for micro structure observation. The experimental test for the samples has showed that the increase of Nb powder weight percentage in the master alloy has a significant effect on increasing the hardness and decreasing the wear resist therefore it will enhance the mechanical properties for this alloy.

**KEYWORDS :** Shape Memory Alloy, Cu-Al-Ni, Nb Addition , Hardness, Wear Resist .

### تأثير اضافة عنصر النايبيوم Nb على الصلادة ومقاومة البلاء الاحتكاكي لسبيكة Cu-Al-Ni ذات خاصية تذكر الشكل المصنعة بتكنولوجيا المساحيق

أ.م. د. عبد الرحيم كاظم عبد علي  
قسم الهندسة الميكانيكية - جامعة النهرين

أ.م. د. اياد مراد طخاخ  
قسم الهندسة الميكانيكية - جامعة النهرين

الماجستير : راند زيور جميل  
قسم الهندسة الميكانيكية - جامعة النهرين

### الخلاصة

سبائك ذات قابلية التذكر للشكل Cu-Al-Ni قد تم تصنيعها باستخدام تكنولوجيا المساحيق وباستخدام الخواء كمحيط واقى في اثناء عملية التلبيد ، ثلاثة مستويات للنسب الوزنية لعنصر النايبيوم Nb وهي (0.3 ، 0.6 ، 0.9) تمت اضافتها الى السبيكة الرئيسية . اختبار الصلادة الدقيقة ومقاومة البلاء الاحتكاكي تمت لجميع العينات والحقت بفحص مطياف الاشعة السينية . وتم استعمال المجهر الالكتروني SEM مع مطياف الاشعة السينية EDX لغرض معاينة البنية المجهرية للعينات . النتائج العملية اظهرت ان زيادة النسبة المئوية الوزنية المضافة من عنصر النايبيوم Nb الى السبيكة الرئيسية له تأثير كبير في زيادة الصلادة الدقيقة وزيادة مقاومة السبيكة للبلاء الاحتكاكي والتي بالتالي تؤدي الى تحسين في الخواص الميكانيكية للسبيكة الرئيسية .

الكلمات الرئيسية : سبيكة ذاكرة للشكل ، نحاس - المنيوم - نيكل ، اضافة عنصر النايبيوم Nb، الصلادة ، مقاومة البلاء الاحتكاكي.

## I INTRODUCTION

Shape memory alloys (SMA's) are metals, which exhibit two very unique properties, pseudo-elasticity, and the shape memory effect. Arne Olander first observed these unusual properties in 1938 but not until the 1960's were any serious research advances made in the field of shape memory alloys [1]. The most effective and widely used alloys include NiTi (Nickel - Titanium), CuZnAl, and CuAlNi [2].

The two unique properties described above are made possible through a solid state phase change that is a molecular rearrangement, which occurs in the shape memory alloy. Typically when one thinks of a phase change, a solid to liquid or liquid to gas change is the first idea that comes to mind. A solid state phase change is similar in that a molecular rearrangement is occurring, but the molecules remain closely packed so that the substance remains a solid. In most shape memory alloys, a temperature change of only 10° C is necessary to initiate this phase change. The two phases, which occur in shape memory alloys, are Martensite, and Austenite.

As shown in **Fig.1** The unusual properties mentioned above are being applied to a wide variety of applications in a number of different fields [3].

The shape memory and pseudoelastic characteristics coupled with the bio- compatibility of NiTi make them an attractive candidate for medical applications. The combination of these unique characteristics has led to the development of various applications such as stents, filters, and orthodontic wires.

Also Shape memory alloys have been used in automobiles for applications ranging from impact absorption to sensing and actuation. In addition to the aerospace, transportation and medical industries, there are many other fields and applications that incorporate SMAs.

## II. EXPERIMENTAL PROCEDURES

Copper powder with 99.9% purity (-325 mesh), nickel powder with 99.9% purity(-325 mesh)

aluminum powder with 99.9%purity (-325mesh) , and Niobium powder with 99.9%purity(-325 mesh) respectively were imported from *SkySpring Nanomaterials, Inc. USA* and used to prepare samples of the master alloy ( without addition ) with a composition of 83% Cu 13%AL and 4% Ni and for the samples with Nb additives of 0.3,0.6 and 0.9% waight percentage which was taken from the copper percentage .These powders were weighed accordingly and placed into cylindrical containers which were then mixed in a horizontal barrel mixer as shown in **Fig.2** .

The container was filled with only 50% of powder [4] and 1% of acetone (by volume ) was added in order to increase the segregation and prevent the separation of the components ( since there is a difference in the densities ). Alumina balls for assisting the segregation has not been used in order to prevent the milling process and contamination of powder , the speed of rotating drum was set to 75 rpm and the time of mixing was 6 hour .

Samples from powder were prepared in the same die with a cross section of 11 mm in diameter and approximately 17 mm length in average as shown in fig. 3. The samples were pressed at (650) Mpa in a 100 ton Hydraulic computerized press Machine , with a displacement rate of 0.01 inch/min and a holding time of 2 minutes, Between these limits, samples were defect-free and had sufficient green strength for handling.

**Fig.3** shows samples from each composition after sintering in an electrical tube furnace supplied with a quartz tube and vacuum equipment

According to the try and error to find the suitable time and sintering procedure and standing on the phase diagram of ternary Cu-Al-Ni , in order to get a fine samples without cracks or defect ,Two stage sintering has been implemented since there is difference in melting point of the alloy components and to prevent the appearance of liquid phase sintering.

The first stage is to sinter the sample at 500°C for 1 hour and followed by the second stage which is raising the temperature to 850 °C with soaking time of 5 hour then leaving the sintered sample to cool in furnace. A heating rate of 20°C/min was maintained for the first stage and 15°C for the second stage. The vacuum pressure was always allowed to reach  $3 \times 10^{-6}$  bar before sintering and during the whole sintering process and cooling. The dual stage vacuum pump is allowed to run for the entire sintering time to suck the harmful gases which will be produced during the diffusing of particles which might effect the sintering efficiency.

After sintering , all sample have been quenched to get  $\beta$  phase which is AlCu<sub>3</sub> (martensite ) by heating the sintered sample to 800 °C and holding it at this temperature for 1 hour then rapidly quenched into iced water . After the quenching process, an ageing heat treatment is implemented to stabilize the  $\beta$  phase by heating the sample to 100°C and holding at this temperature for 2 hour [5].

The quenching and ageing process was also implemented in vacuum atmosphere to prevent the oxidation [6].

X- ray diffraction was implemented for the master alloy ( without additives) and for the sample with the Nb alloyed element for the three range weight percentage samples.

Scanning electron microscope (SEM) and Energy dispersive X-ray spectroscopies (EDS) have been used to observe the microstructure and the alloying element distribution along the structure. Vickers micro hardness testing with a 1000 gram load (HV 1) has been carried out on all samples with a holding time of 20 second.

More than three values of hardness for each sample have been taken to get the mean value represents hardness. The wear properties of the specimens were investigated using a pin-on-disc sliding wear device, a loading mass of 250 gram and a rotating speed of disc is set to 500 RPM. the pin was located at a radial distance of 100 mm from the rotating axis , for each 5 minute sample has been

taken out, cleaned and weighted with 0.0001 g accuracy balance. Six readings have been taken for each case to plot the mass loss against the sliding distance curve.

### III. RESULTS AND DISCUSSION

**Fig. 6 (a ,b ,c ,d)** shows four x-ray charts for master , 0.3Nb ,0.6Nb,0.9Nb additive samples respectively the result peaks was compared with the standard cards with the possible known phases which will be appear.

All samples have shown the martensitic phase after Nb addition and quenching which indicate the existence of the shape effect and no effect of Nb addition to the martensitic phase.

**Fig.7 (a,b,c and d)** shows SEM pictures of the microstructures of master, 0.3Nb,0.6Nb and 0.9 Nb respectively and showing the alloying element distribution .

The gray particles in **Fig.7( b ,c and d)** represent the Nb particles , the black particles represent the empty pore and the base is the structure .so it is quite obvious that the Nb addition was good distributed in the structures which indicate the successful mixing method and procedure.

As shown in **Fig. 8** and **Fig.9 (a , b)** EDS results for the alloyed sample is showing the existence of Nb in zone 1 which is confirm that this is a Nb particle and shows for zone 2 the existence of the Cu-Al-Ni concentration similar to the specified amount of mixture .

In **Fig. 10** Vickers micro hardness shows the differences between the master alloy and the three weight percentage of Nb additives samples, As it is seen there is a linear increment in HV result with the increasing the weight percentage of Nb which result to alloy enhancement with the addition of Nb particle to the structure, while In **Fig.11** mass loss for master and the alloyed samples has been determined.

Sliding wear resistance results indicate that there is a significant improvement in reducing mass loss

for the samples with additive Ta particles with the master alloy which has addition weight percentage more than 1% will be increasing more weight loss against the sliding wear for this alloy ,This might be due to the strong attractive between the Nb particles and the structure which has been verified by the increment of hardness followed by the enhancement in increasing the sliding wear resistance

## V. CONICLUSIONS

- 1-Using different Nb powder weight percentage will not effect on x-ray diffraction results or the shape memory effect.
- 2-Increasing Nb weight percentage will:
  - (a) Increase hardness.
  - (b) Increase sliding wear resistance for the shape memory alloy.
- 3- Increasing Nb weight percentage than 1% will still Increases the sliding wear resist for this aloy .

## ACKNOWLEDGEMENTS

The authors would like to acknowledge: (Al-Nahrain University – mechanical engineering dep. Labs), (central organization of standardization and quality control) and (state company for inspection and engineering rehabilitation) Baghdad –Iraq and school of metallurgy in university of Tehran, Tehran-Islamic republic of Iran. For the provision of facilities.

## REFERENCES

- Yong-Hua Zhang , Jie Yang , and Yan Song "Analysis and testing of shape memory alloy-driven bio robotic fish fins with multi propulsion modes " pp1 Journal of Bionic Engineering (2008).
- Cimprić Darjan "Shape memory alloys" seminar pp1 13. januar 2007
- Mel Schwartz "Encyclopedia of materials, parts and finishes" second edition, ASM handbooks 2002 by CRC Press LLC
- R. Hogg "Mixing and Segregation in Powders Evaluation, Mechanisms and Processes" KONA Powder and Particle Journal No.27(2009). pp9

- Sara Casciati "thermal treatment optimization for cu-based shape memory alloys" School of Architecture – University of Catania

Proceedings of the First International Conference on Self-Healing Materials, Netherland 18-20 April (2007) pp3

- G. S. Upadhyaya "powder metallurgy technology" Department of Materials and Metallurgical Engineering Indian Institute of Technology, Kanpur, India pp71 (2002)

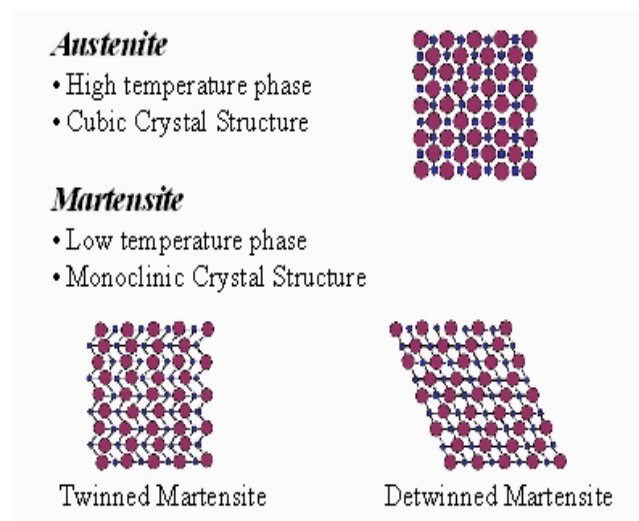


Fig 1: Phases of a shape memory alloy [3]



Fig 2: Horizontal barrel mixer



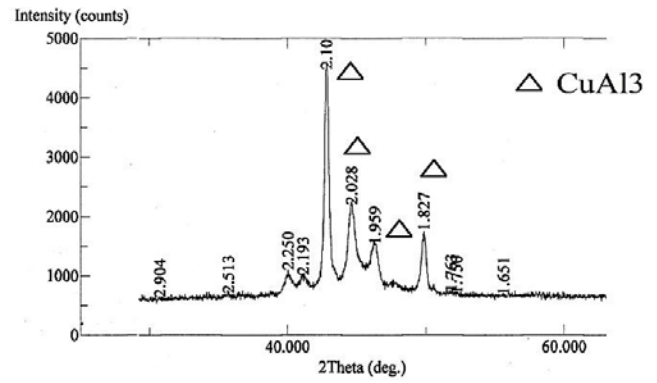
Fig. 3: Sintered samples



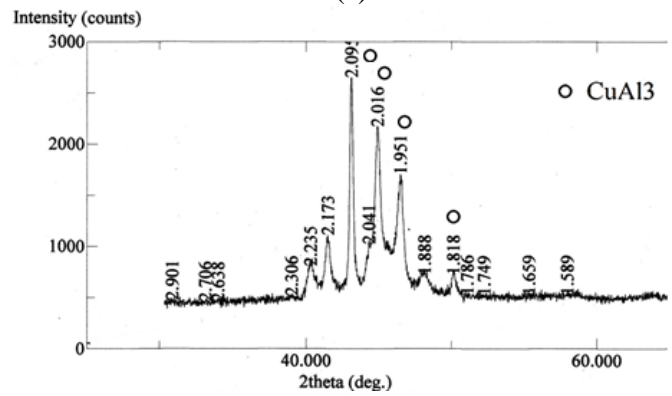
Fig. 4: Tube furnace



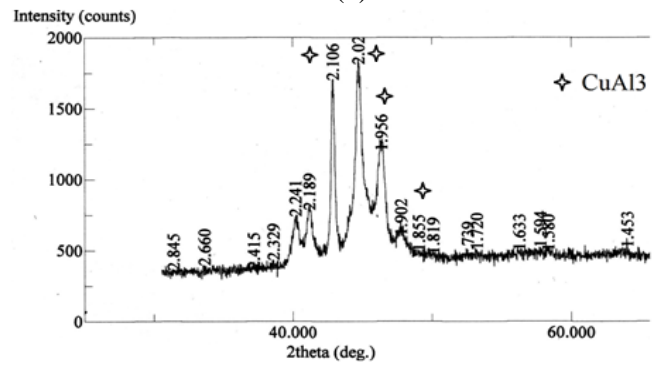
Fig. 5: Vacuum equipment for sintering process



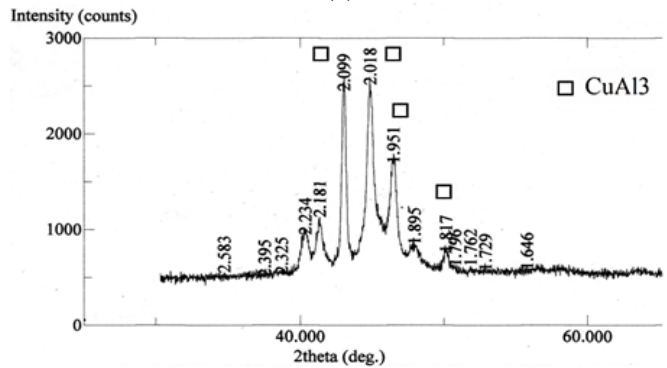
(a)



(b)



(c)



(d)

Fig. 6 (a, b, c, d) X-ray diffractions

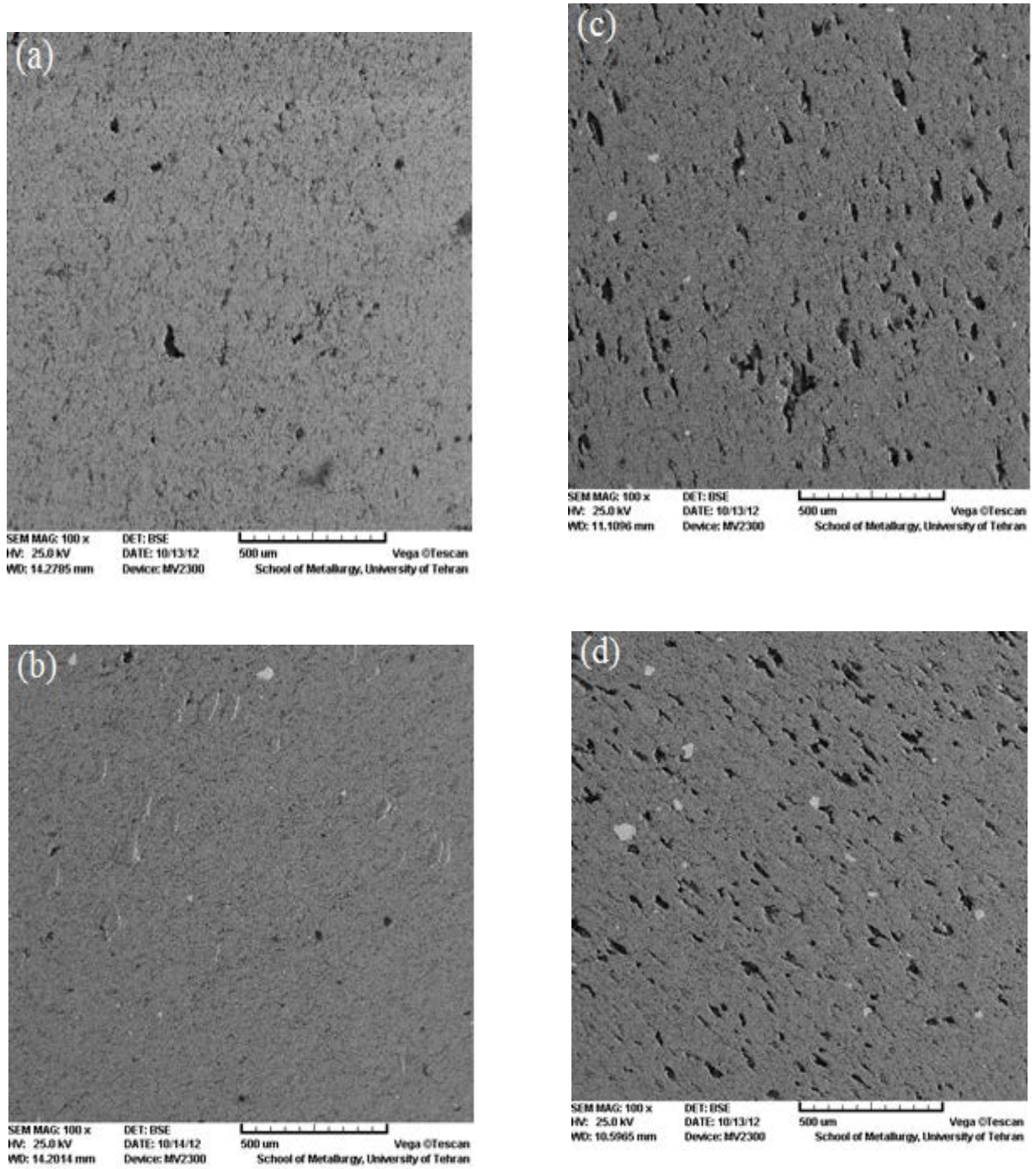
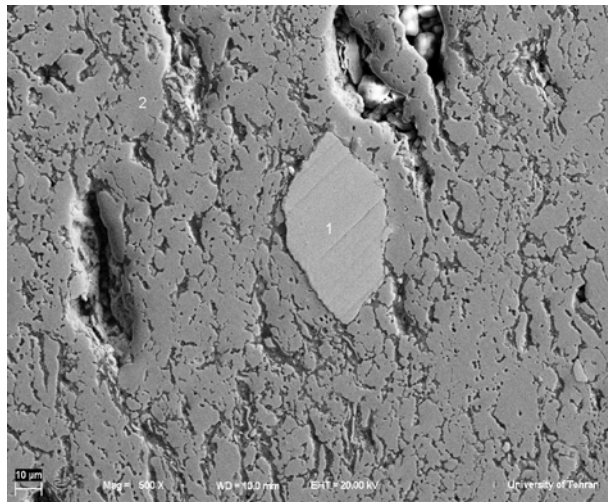
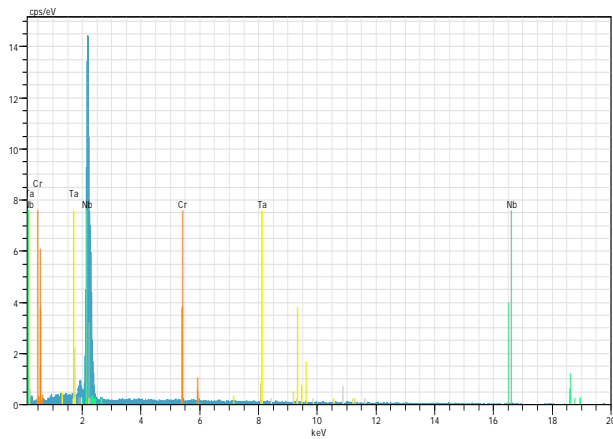


Fig. 7 (a,b,c,d) SEM Pictures with 500X magnification



**Fig.8 Nb Particle reviled by FESEM**



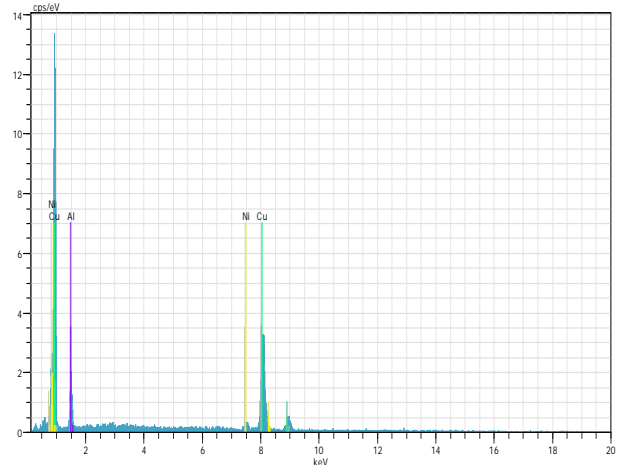
**N-1** Date:10/13/2012 11:35:45 PMHV:20.0kV Puls th.:4.17kcps

El	AN	Series	unn. C [wt.%]	norm. C [wt.%]	Atom. C [at.%]	Error [wt.%]
----	----	--------	---------------	----------------	----------------	--------------

Nb	41	L-series	122.72	98.64	99.07	4.6
Ta	73	L-series	1.46	1.18	0.61	0.2
Cr	24	K-series	0.23	0.18	0.33	0.1

Total: 124.41 100.00 100.00

**Fig. 9 (a) EDS results for zone 1**



**N-2** Date:10/13/2012 11:36:30 PMHV:20.0kV Puls th.:3.39kcps

El	AN	Series	unn. C [wt.%]	norm. C [wt.%]	Atom. C [at.%]	Error [wt.%]
----	----	--------	---------------	----------------	----------------	--------------

Cu	29	K-series	71.57	84.99	74.22	2.4
Al	13	K-series	8.78	10.43	21.45	0.6
Ni	28	K-series	3.85	4.58	4.33	0.3

Total: 84.20 100.00 100.00

**Fig. 9 (b) EDS results for zone 2**

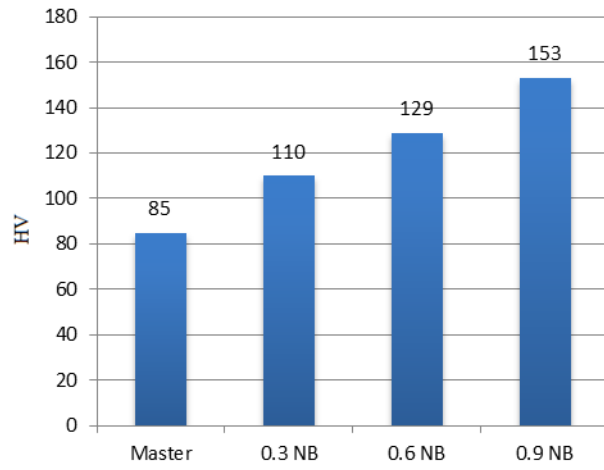


Fig. 10 Vickers micro hardness (HV 1)

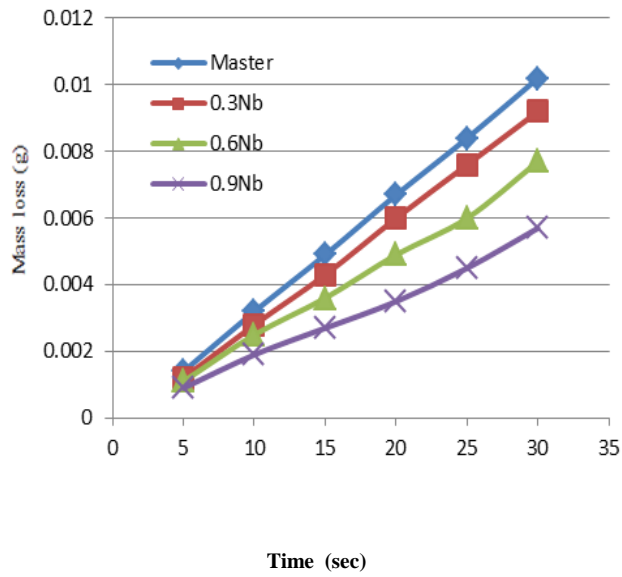


Fig. 11 wear test results



## Experimental and Numerical Investigation of Creep Behavior In Isotropic Composites

**Prof. Dr. Mohsin Jaber Jaweej**  
Al-Nahrain University  
College of Engineering  
Mechanical Engineering Dep  
[mohsinjj@yahoo.com](mailto:mohsinjj@yahoo.com)

**Dr. Mohsin A. Abdulhussein**  
University of Baghdad  
College of Engineering  
Mechanical Engineering Dep  
[mohsinabdullah@yahoo.com](mailto:mohsinabdullah@yahoo.com)

**Bashar kassim Zalzala**  
University of Baghdad  
College of Engineering  
Mechanical Engineering Dep  
[Bashar.zalzala@yahoo.com](mailto:Bashar.zalzala@yahoo.com)

### ABSTRACT

Creep testing is an important part of the characterization of composite materials. It is crucial to determine long-term deflection levels and time-to-failure for these advanced materials. The work is carried out to investigate creep behavior on isotropic composite columns. Isotropy property was obtained by making a new type of composite made from a paste of particles of carbon fibers mixed with epoxy resin and E-glass particles mixed with epoxy resin. This type of manufacturing process can be called the compression mold composite or the squeeze mold composite. Experimental work was carried out with changing the fiber concentration (30, 40 and 50% mass fraction), cross section shape, and type of composite. The creep results showed that the higher the fiber concentration, the more the creep resistance. Type of fiber plays a very critical role, where carbon/epoxy composite showed much higher creep resistance and also showed much higher modulus of elasticity than the E-glass/epoxy composite. Specimen shape factor noticed to play a very small role. However, square cross sectional area showed slightly higher resistance for creep than the rectangular cross sectional area. This difference is not critical and can be ignored. F.E.M simulation with ANSYS Inc. software was implied and results were compatible with the experimental work with a maximum discrepancy of (17.24%).

**KEYWORDS:** isotropic composite, creep, mass fraction, squeeze mold composite, ANSYS, fibers.

### بحث عملي ونظري حول سلوك ظاهرة الزحف في المواد المركبة الايزوتروبية

أ.د. محسن جبر جويج      م.د. محسن عبد الله عبد الحسين      مهندس بشار قاسم زلزلة

#### الخلاصة:

ان اختبار الزحف هو احد اهم الفحوصات في وصف المواد المركبة، انه ضروري وحاسم لايجاد الاستطالة على مدى الزمن والوقت المطلوب حتى تفشل فيه هذه المواد. في هذا البحث تم توجيه الطاقات للبحث والتحليل في ظاهرة الزحف على مواد مركبة ذات خواص ايزوتروبية ، ان الخاصية الايزوتروبية تم تحقيقها بصنع مركب جديد النوع مصنوع من عجينة من خليط دقائق الالياف الكاربونية ممزوجة مع الايبوكسي و دقائق الياف الزجاج ممزوجة مع الايبوكسي. هذا النوع من التصنيع يمكن ان يطلق عليه اسم " مركب قالب الضغط" او " مركب قالب الحشر". الجزء العملي من البحث قد تناول هذه الظاهرة مع الاخذ بنظر الاعتبار عدة امور، منها، تغيير نسب الدقائق الوزنية (30,40,50) %، شكل مقطع العينة، ونوع دقائق الالياف المستخدمة. ان نتائج البحث في اختبار الزحف قد بينت ان زيادة نسب تركيز الدقائق تؤدي الى زيادة واضحة في مقاومة المركب للزحف. ايضاً تم ملاحظة الاختلاف الواضح بين نوعية الالياف المستخدمة فمثلاً الياف الكاربون كانت ذات مقاومة اعلى بكثير من نظيرتها الياف الزجاج ، اما بالنسبة لشكل المقطع فقد تبين انه لا يلعب دوراً خطيراً وان العينات ذات المقطع المربع والمستطيل كانت نتائجها متطابقة تقريباً والاختلاف بينهما بسيط جداً ويمكن اهماله تم عمل

نمزدج لجميع العينات التي تم فحصها عملياً باستخدام التحليل العددي (F.E.M) وذلك باستخدام برنامج ال (ANSYS) وقد اظهرت النتائج تطابق كبير بين النتائج العملية وبين ما تم ايجاده نظرياً بهذا البرنامج بنسبة خطأ اعلاها (17.24%).

الكلمات المرشدة: مركب ايزتروبي، الزحف، النسب الوزنية، مركب قالب الحشر، الياف

## 1. INTRODUCTION

### 1.1 General

A composite is a structural material which consists of combining two or more constituents. The constituents are combined at a macroscopic level and are not soluble in each other. One constituent is called the reinforcing phase and the one in which is embedded is called the matrix. The reinforcing phase material may be in the form of fibers, particles or flakes. [1]

Creep is the time-dependent deformation which accompanies the application of stress to a material. At room temperatures, apart from the low-melting-point metals such as lead, most metallic materials show only very small creep rates which can be ignored. With increase in temperature, however, the creep rate also increases and above approximately  $0.4 T$ , where  $T$ , is the melting point on the Kelvin scale, creep becomes significant. In high-temperature engineering situations related to gas turbine engines, furnaces and steam turbines, etc., deformation caused by creep can be significant and must be taken into account [ 2 ]. However, for polymers and composites, heat is not an important factor and creep can occur. [ 3 ] The study case here is isotropic squeezed composite under creep for one hour to study effect of fiber concentration, type of specimen cross section area and type of fiber particles on the behavior of creep. Houshyar et al (2004) [4] studied the effect of continuous fiber concentration on the behavior of creep and for about the same test time in this research, their results came compatible to the ones obtained in this research regarding the fiber concentration part.

Many composite materials are being used today in all sorts of industries such as golf equipments, fishing equipments, car industry, electrical isolators, airplanes and aerospace industry

### 1.1 Research Objectives:

The aim of this work is to investigate the creep behavior of isotropic composite materials by studying the change in design parameters, loading, material properties, shape factor, mass fraction, and to achieve the above objective, the following steps are followed:

- 1.Experimental study will be achieved by constructing a creep test to the isotropic CFRP and GFRP composite by applying constant load for short period of time and for values of (2000, 2500 and 3000) N to study the creep behavior for different design parameters.
- 2.Finite element analysis is required using ANSYS software for the creep test simulation.

## 2. CREEP THEORY

### 2.1 The creep test:

The creep test is usually carried out at a constant temperature and under constant load conditions rather than at constant stress conditions. This is acceptable because it is more representative of service conditions. A creep device such as that shown in **fig. 1** is used for this purpose. Each end of the specimen is screwed into the specimen holder, the load is applied by adding weights to the arm and readings are taken at periodic intervals of extension against time, the equipment is often housed in a temperature-controlled room. [2]

### 2.2 Phenomenology of creep:

The results from the creep tests are plotted in graphical form to produce a typical curve as shown in **Fig.2**. After the initial extension OA which is produced as soon as the test load is



applied, and which is not part of the creep process proper (but which nevertheless should not be ignored), the curve can be divided into three stages. In the first or primary stage AB, the movement of dislocations is very rapid. In the secondary stage BC, the work-hardening process of “dislocation pile-up” and “entanglement” are balanced by the recovery processes of “dislocation climb” and “cross-slip”. The third or tertiary stage CD coincides with the formation of internal voids within the specimen and this leads to “necking”, causing the stress to increase and rapid failure to result. [2]

### 2.3 Creep Theory

An empirical equation called the Arrhenius-type rate model is used to describe the creep in composite materials

$$\epsilon_{ss}^0 = \epsilon_{min}^0 = B\sigma^n \exp\left(\frac{Q}{RT}\right) \quad \text{Eq. (1)}$$

Where  $n$  is the stress exponent,  $Q$  is the activation energy for creep,  $R$  is the universal gas constant and  $T$  is the absolute temperature in Kelvin, to determine the various constants in Eq. (1) a series of isothermal tests are required. [2]. The isothermal creep test (which is the case of this research) implies that the temperature is to be constant at all times but the stress is not, meaning a three stresses at least must be applied on the test specimens at same constant temperature, this will lead to a change in the Arrhenius-type formula, where the creep law now becomes:

$$\epsilon_{ss}^0 = \epsilon_{min}^0 = B\sigma^n \quad \text{Eq. (2)}$$

This equation can be linearized by taking logarithms of both sides such that:

$$\log \epsilon_{ss}^0 = \log \epsilon_{min}^0 = \log B + n \log \sigma \quad \text{Eq. (3)}$$

Log-log plots of  $\epsilon_{ss}^0 = \epsilon_{min}^0$  versus  $\sigma$  often results in a bilinear relation in which the slope,

$n$ , at low stresses is equal to one indicating pure diffusion Fig. 3 [9].

## 3. EXPERIMENTAL WORK

### 3.1 materials:

The materials used in this research are:

1. Carbon particles (from chopped carbon fibers) reinforced epoxy resin.
2. Fiberglass (E-glass) particles (from chopped E-glass fibers) reinforced epoxy resin

Typical properties of fibers and resin used are listed in table 1

### 3.2 Compression mold or Squeeze mold method:

Rather than laying up fiber in sheets and impregnating it with resin like the typical fiber manufacturing, compression molding Composite uses a paste of fibers mixed with resin that is squeezed out to make almost any shape. Since the fibers aren't oriented in any particular direction, the finished part is strong all around, having the isotropic property while remaining light. Lamborghini and Callaway (car manufacturers) teamed up together to develop this method on 2010. But since this is a new method that needs special tools and machines which does not exist in Iraq, a simpler and basic method was conducted to manufacture the test specimens; a method that was conducted after long time of trials and errors, the problem was to be able of finding a method to manufacture any shape with perfect smoothness, no gaps as possible and with the fastest time possible. The mold used to manufacture the specimen was made of wood with smooth surfaces inside. It is also known that creep at high stresses results in  $n$  greater than one which indicates a power law creep [5]

The following procedure explains how the mold must be made and used:

- The mold must be taped and oiled with car oils; the tape makes the surface of

the specimen extremely smooth and also to be insulating layer between the mold and the specimen, while the car oil makes the operation of removing the specimen from the mold very easy.

- The cover of the mold must be closed after step (no. 1) from all direction leaving the narrow side opened, where the paste is to be compressed through this part as shown in **fig.5**
- After the calculations of fiber to matrix ratio are completed and the paste is ready, the paste is to be injected through the narrow part of the mold with a stick with continuous compression of the paste as shown in **fig. 6**, once the paste is all inside the mold, a small piece of wood with the same width and thickness of the opened side and with specified length is to be placed and then hammered to close the gap and compress the paste inside the mold.

### 3.3 Tensile test:

The tensile test specimens were manufactured according to ASTM D 3039 [6] (**fig.7** and **fig.8**). Young's modulus were obtained from the tensile test and listed in **table 2** , to be used as input data in ANSYS software.

### 3.4 Poisson's ratio:

Poissons ratio was measured for each tensile specimen and calculated, see **table 3**, these results are to be used as input data in ANSYS software.

### 3.5 Creep testing device

Since there was no creep device available in the nearby universities to be used for this specific study, where high load could be applied and the grips to be jaws and not hooks, a creep device was manufactured specially for this research. The device of test was designed then manufactured Similar to another model (MT 040). The model was designed for small specimens, therefore the device was to be taken in consideration the big sizes and strength of the tested specimens. Therefore a bigger size and a stronger device was manufactured not only to

## Experimental and numerical investigation of creep behavior in isotropic composites

test creep but to be adjustable to work as a buckling device as well if needed, and to have the ability of applying loads of (up to 3000 N). All the parts of device were manufactured from carbon steel No. 45 to withstand the high loads. The schematic drawing for the device is shown in **fig. 1**, the weights of the device and digital dial gauge were calibrated in the ministry of planning / central system for calibration

### 3.6 Testing Procedure:

#### 3.6.1 Creep specimens

Creep test specimen were manufactured according to ASTM D-638 [ 7 ] , but with different thickness, because one of the main objects of this research is to study the effect of cross sectional area shape on the creep test, In ASTM D 2990 [ 8 ] , (the standard for creep test) stated that "test specimens may be made by injection or compression molding with any particular shape if the object of test is to obtain design data" which is the case here, so the exact specimen details were used from the ASTM standard taking in consideration the same ratio between each length.

Test specimen was made with the following factors:

1. Two cross sectional area shape ( square) and ( rectangular) with maintaining the same effective area
2. Two Types of composites
  - Carbon particles / epoxy resin
  - E-glass particles / epoxy resin
3. Three different mass fraction (30 – 40 – 50) % wt/wt and for the two composites.

The Creep specimen dimensions are listed in **table 4** and shown in **fig. 9**

The specimens were compressed using a wooden mold as shown in **fig. 10**

Steps of manufacturing the creep specimens (letters represents steps in **fig. 10**



More details of manufacturing the creep specimen can be found in Ref. [10]

### 3.6.2 Conditioning

Test specimens were conditioned at 25 C<sup>0</sup> for (48) hours after manufacturing and then it was preconditioned in the test environment for (48) hours prior to testing as recommended in ASTM D-2990.

### 3.6.3 Final Specimens

The creep test specimens were all labeled and were ready to be tested. There were (36) specimens manufactured overall for the creep test, (18) specimens for each composite (**fig. 12** and **fig.13**)

### 3.6.4 Testing

- The conditioned specimen was mounted by the device grips and carefully aligned so that no eccentric misalignment would cause bending, each side of grips was screwed with the same amount so that the specimen is to be tightened at the entire surface to avoid slipping
- The digital dial gauge was adjusted and set to Zero.
- The full load was applied within a period not to exceed 5 seconds
- The timer was lunched at the start of the loading.
- Since the test is less than (1000) hours then the intervals were taken for each 5 minutes, to take readings of deformation for period of (60) minutes according to ASTM D-2990.
- A special document was created for each specimen to record exact data such as temperature, relative humidity, specimen dimensions, specimen weight; deflection with time, all these data was recorded prior to the testing process except for the deflection data, where all these data is required according to the ASTM D 2990.

- Once the period of test was completed, the load was removed rapidly and smoothly, the dial gauge and timer were shut off
- Calculations of other factors and graphing were employed for the final results.

### 3.7 Calculations of the creep constants and factors

Once the creep test process is completed for all specimens, the creep factors and constants was calculated and listed in **table 5**

## 4. RESULTS AND DISCUSSIONS

### 4.1 Experimental Results

When all Creep data were obtained, a graphical plot was drawn for each case of square shape compared to the rectangular shape, and each percentage compared to the other, and finally compared at three loads. The following graphs show the creep curves for this study, where it represent a creep curve at a secondary stage as planned from the beginning. Since the employed creep equation is only valid for secondary creep, and this was done by applying high stresses above the elastic limit, where this action leads to skipping the primary stage and jump straight to the secondary creep. There were two types of graphs plotted. One for a certain percentage at the three loads, and other one for one load with three percentages. Two of the graphs that represent a plot of a certain percentage at three loads are presented. Figures that represented a certain percentage at three loads (six graphs) (such as **fig 14** and **fig. 15**) showed graphical results of creep of both carbon particles reinforced epoxy and E-glass particles reinforced epoxy at three different loads in each figure, and with two cross sectional areas. The straight line represents the square shaped cross section specimen while the dotted line represents the rectangular shaped cross section specimen. It is shown when the mass fraction of composite increases, the composite tends to be more creep resistant in an obvious way. However the slope of the curves are not

increasing in a steady behavior, meaning, each curve is increasing with different slope and the distance between curve and another are not constant in two cases only. For example the curves distance from each other (the amount of increase in creep resistance) are increasing almost identically in all six graphs except of one of them, this could be because of the method of curve fitting used to draw the graphs, other possible reason might be due to the environmental effect, where the specimens were tested at a little different temperature and relative humidity, but in general, the creep resistance was increased clearly with the increasing of the mass fraction. On the other hand, the behavior of the two different shapes was noticed to be negligible. The curves show that no critical difference was found between the two different shapes and are almost identical, as for the curves that are not identical, this is because of the curve fitting, where the amount of displacement that was gathered from both shapes was almost the same, but in different intervals. Meaning, for example, at 10 minutes a square shape specimen might have a displacement of 0.15 mm where the rectangular specimen has 0.18 mm of displacement, but when the final extension is reached at 60 minutes the square shaped specimen might have 0.3 mm displacement while the rectangular shaped specimen extension is 0.31 mm. It is obvious that the total extension is what matters. In this case it is not critical difference between both shapes. But, due to the different intervals, the curve fitting was different in some cases which gave a misleading idea that there is a critical different between both shapes, but in reality there aren't any different that can be taken in consideration. Also, graphs of the three percentages at a certain load was plotted as those shown in **fig.16** and **fig.17** which represented a certain load for the three mass fraction percentages (six graphs also) showed graphical results of creep for both carbon particles reinforced epoxy and E-glass particles reinforced epoxy at three different percentages in each figure. Each figure represents creep resistant at one load with three different mass fraction percentages. It is shown that with the

increase of mass fraction the composite tends to be more creep resistance. The property of creep resistance from each percentage to another in the same composite is contrast. Fiberglass (E-glass) composites show constant increase in each percentage, that is almost increasing the same from one percentage of mass fraction to another. While in carbon composites, it is shown that the increasing in creep resistance from (40%) mass fraction to (50%) is twice of that from (30%) to (40%) mass fraction, this is because of the density of these fibers. E-glass fibers has a density of  $2 \text{ gr/cm}^3$ , and very low surface area as noticed with the manufacturing process. While carbon fibers have a density of  $1.55 \text{ gr/cm}^3$  and very high surface area which was obvious when the specimens were manufactured. In other words, changing the mass fraction for e-glass composite makes a little difference in volume fraction while carbon fiber composites make a noticed difference in volume fraction. That is because of the density and surface area as mentioned above. This was noticed also when tensile test was made for the specimens, e-glass composites showed less improvement in modulus of elasticity than the carbon particles composite, where the modulus was improving strongly, which explain the reason of this behavior in the graphs above.

#### 4.2 F.E.M (ANSYS) Results:

The specimen was meshed using SOLID186, a higher order 3-D 20-node solid element that exhibits quadratic displacement behavior [ 11 ]. Meshing was very fine, exactly (291904) nodes or (205235) elements.

**Figures 18** and **19** are samples of the numerical solution that was obtained using ANSYS software. Where **fig.18** represents a square shaped specimen, while **fig.19** represents a rectangular shaped specimen.

It is noticed that the creep strain is expanding from low level at edges to high level at the middle of the specimen, which support the experimental work, where the highest creep strain in ANSYS is at the same part of the specimen that was assumed in the experimental



work, which is the gauge length. All creep specimens in ANSYS showed the same creep strain distribution behavior in both square and rectangular specimens which supports the discussion earlier that is; both square and rectangular specimens had almost the same creep strain for the same composite at the same load. This means that the load distribution is the same in all specimens and hence no difference between the two specimens can be noticed at the same stress distribution, same volume and same materials that is made of. This will leave the only reason that was explained earlier in the experimental results which is the curve fitting issue; on the other hand ANSYS results also showed that there is no critical difference in creep strain between both square and rectangular specimens for the same composite at the same conditions. But, if results are to be compared for slight differences, then the square shaped specimen showed a slightly higher resistance to creep than the rectangular shaped specimen.

Discrepancy between Experimental and F.E.M solution (ANSYS) was between (0 – 17.24) % Maximum. This discrepancy can be due to many different factors, such as environment. Humidity for example plays a critical role in experimental work and continuously changing, while ANSYS software doesn't take it in consideration and even if it has been taken as a factor it would be constant and not changing. Other reason is may be due to the method of specimen fixing, in reality the specimen might have a slight misalignment or very small amount of slipping that can't be seen, while this type of problems doesn't exist in ANSYS.

## 5. – CONCLUSIONS

1. The creep results showed that when the mass fraction increases, the creep resistance increases. This means that mass fraction plays a critical role in the mechanical properties of the material. For example, a (30%) wt/wt mass fraction of carbon fiber particles reinforced epoxy at 2000 N showed a creep strain of (0.38%), then fiber concentration was increased to (40% wt/wt)

and the creep strain reduced to (0.26%), while a (50%) wt/wt showed a creep strain of (0.21%)

2. Type of fiber plays a very critical role, where Carbon fibers showed much higher creep resistance and also showed much higher modulus of elasticity than the E-glass fibers. Therefore when it comes to strength and higher creep resistance, carbon fiber is most recommended, but E-glass is not that bad when the cost factor is to be taken in consideration, where the carbon fibers cost 4 times more than the E-glass fibers for the same amount.
3. Specimen shape factor is noticed to play a very small role, square cross-sectional area showed slightly higher resistance for creep than the rectangular cross-sectional area. This difference is not critical and can be ignored. For example, a (40%) wt/wt CFRP square shaped at 2500 N specimen showed a creep strain of (0.59%) while the rectangular shape of the same type of specimen showed a creep strain of (0.62%).
4. In general it was found that the creep resistance increased in CFRP from [30% to 40%] by (34.17%), and increased from [30% to 50%] by (49.74%). As for the GFRP, the creep resistance increased from [30% to 40%] by (13.01%), and increased from [30% to 50%] by (28.79%).

## 6. REFERENCES

- Autar K. Kaw, “ Mechanics of Composite materials”, 2nd edition, CRC London, Washington [2004]
- Hearn E.J “Mechanics of Materials”,(Vol. 2), 3rd edition, Butterworth Heinemann, [1997]
- R.C Hibbeler, “Mechanics of Materials”, 8th edition, Pearson, [2011]
- Houshyar et al, “Tensile creep behaviour of polypropylene fibre reinforced polypropylene composites”, Elsevier, [2004]
- University of Washington, Creep course and lecture,  
<http://courses.washington.edu/me354a/chap8.pdf>
- ASTM D 3039/D 3039M : Standard Test Method for Tensile properties of Polymer Matrix Composite Materials [2006]
- ASTM D 638: Standard Test Method for Tensile Properties of Plastics, [2000]
- ASTM D 2990: Standard Test Methods for Tensile, Compressive, and Flexural Creep and Creep- Rupture of Plastics, [2001]
- J. Rösler, H. Harders, M. Bäker, “Mechanical Behavior of engineering Materials (Metals, Ceramics, Polymers, and Composites)”, Springer [2007]
- Bashar K. Zalzal, “Theoretical and experimental investigations of creep and buckling effects on composite materials”, M.Sc. Thesis, University of Baghdad.
- ANSYS theory reference manual

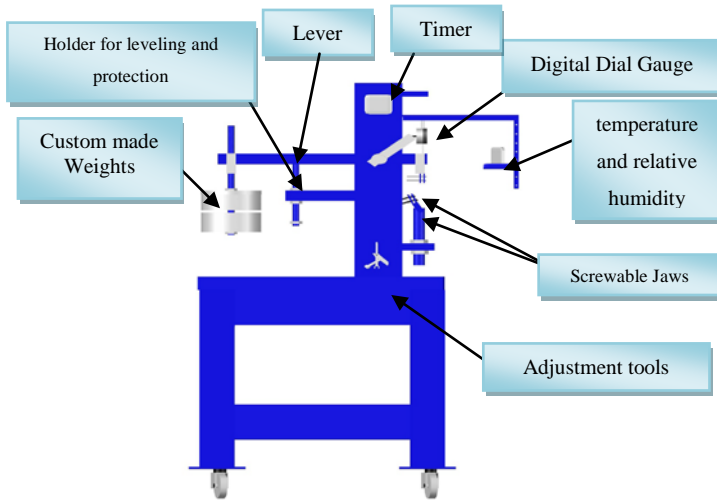


Fig.1 - Creep device.

Table 1: Typical properties of fibers and resin used in this research.

Item	E	Density	$\sigma_{ult}$
CFRP	150 – 180 GPa	1.55gr./cm <sup>3</sup>	4137 MPa
GFRP	72.40 GPa	2 g/cm <sup>3</sup>	3447 MPa
Epoxy	-	1.1 ± 0.05	≥ 25 MPa

CFRP: Carbon fiber (particles) Reinforced Epoxy

GFRP: Glass fiber (particles) Reinforced epoxy

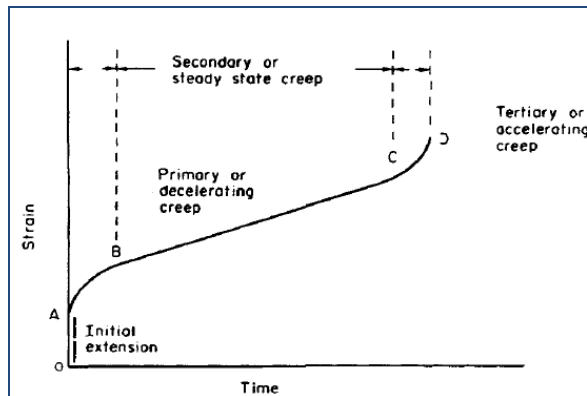


Fig.2 - Typical Creep Curve. [2].

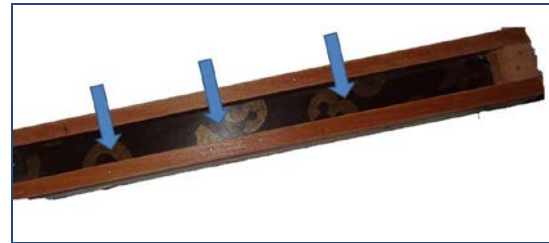


Fig.4 – The mold.



Fig.5 - (The process of enclosing the mold).

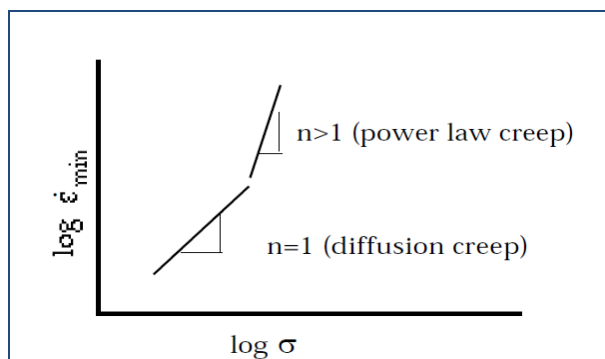


Fig.3 - Log-log plot of  $\epsilon_{min}^0$  versus  $\sigma$ .



Fig.6 – The injection process.

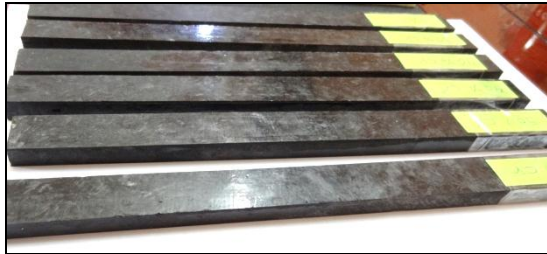


Fig.7 – CFRP tensile specimens

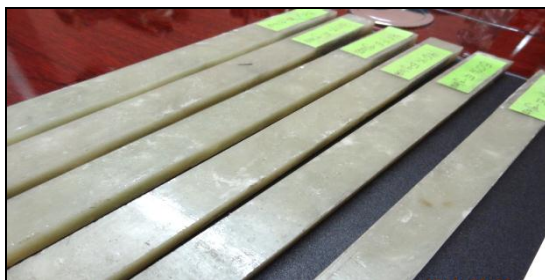


Fig.8 – GFRP tensile specimens

Table 2 – Young’s modulus for Composites

Item	Young’s modulus ( Gpa)
30 % CFRP wt/wt	13.3
40 % CFRP wt/wt	18.3
50 % CFRP wt/wt	23.3
30 % GFRP wt/wt	4.6
40 % GFRP wt/wt	7.46
50 % GFRP wt/wt	10

Table 3 – Poisson’s ratio for Composites

Item	Poisson’s ratio
30 % CFRP wt/wt	$\nu = 0.229$
40 % CFRP wt/wt	$\nu = 0.211$
50 % CFRP wt/wt	$\nu = 0.207$
30 % GFRP wt/wt	$\nu = 0.262$
40 % GFRP wt/wt	$\nu = 0.256$
50 % GFRP wt/wt	$\nu = 0.2$

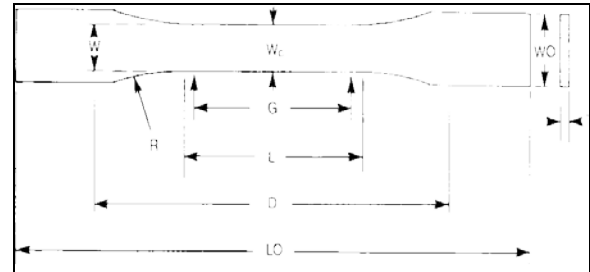


Fig.9 – Dimensions of creep specimen

Table 4 – Creep specimen dimensions

Symbol	Value
W—Width of narrow section	10 mm for square shape 14.28 mm for rectangular shape
L—Length of narrow section	38 mm
WO—Width overall,	15 mm for square shape 20 mm for rectangular shape
LO—Length overall	100 mm
G—Gage length	34 mm
D—Distance between grips	69 mm
T	10 mm for square shape 7 mm for rectangular shape

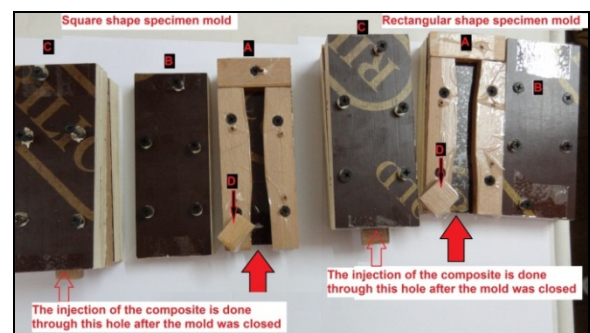


Fig.10 – Creep specimens mold shape and Procedure

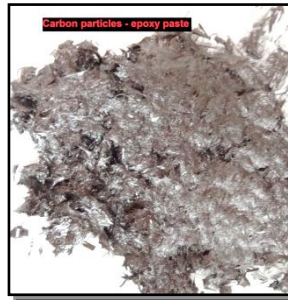


Fig.11 – Carbon/epoxy paste AND E-glass/ Epoxy paste.



Fig.12 – Carbon/epoxy Creep specimens



Fig.13 - E-glass/epoxy Creep specimens.

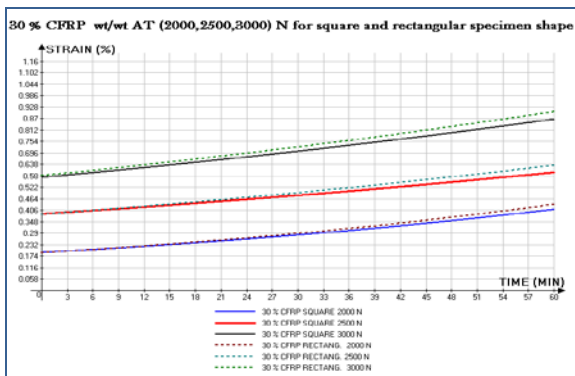


Fig.14 - Plot of 30% CFRP at three loads.

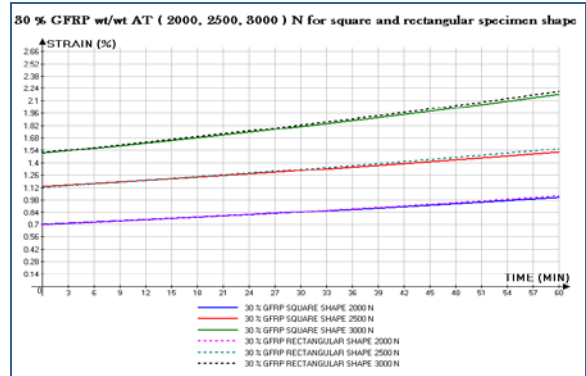


Fig.15 - Plot of 30% GFRP at three loads.

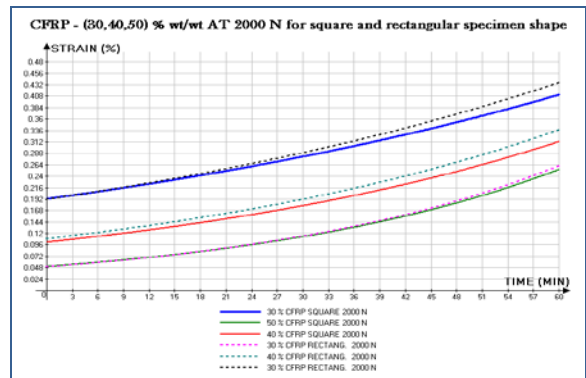


Fig.16 - Plot of 2000 N load for all three CFRP percentages.

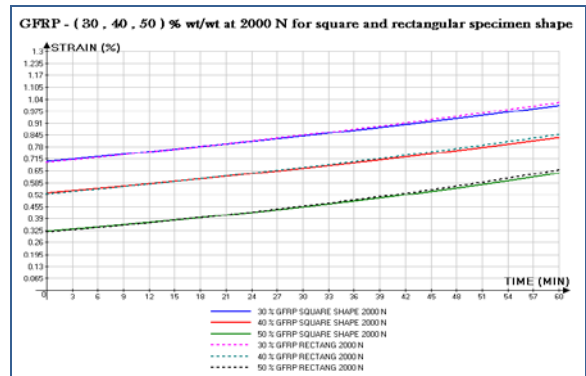
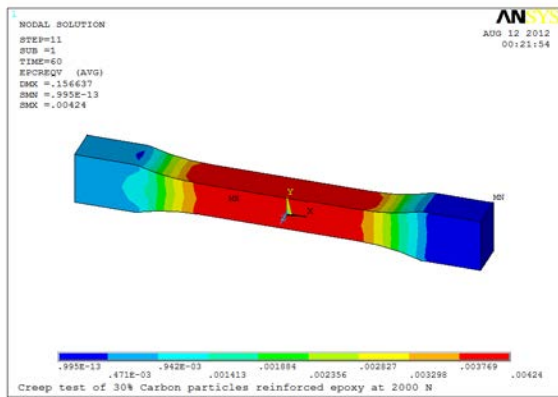
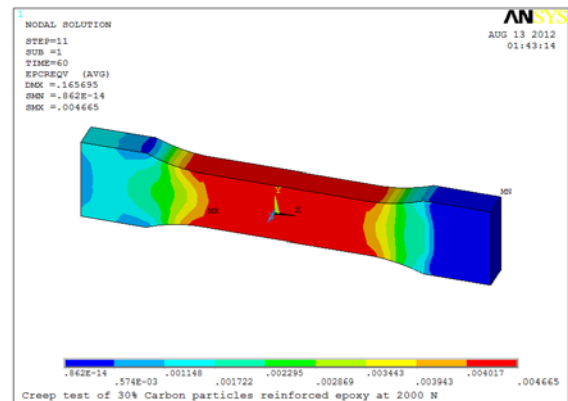


Fig.17 - Plot of 2000 N load for all three GFRP percentages.



**Fig.18** - Creep test of 30% Square Carbon/epoxy at 2000 N



**Fig.19** - Creep test of 30% rectangular Carbon/epoxy at 2000 N

**Table 5** – Creep constants

Item	n	B
30 % CFRP SQU.	1.98	$1.67 \times 10^{-07}$
30 % CFRP REC.	1.86	$2.39 \times 10^{-07}$
40 % CFRP SQU.	1.73	$3.53 \times 10^{-07}$
40 % CFRP REC.	1.57	$5.71 \times 10^{-07}$
50 % CFRP SQU.	1.41	$9.22 \times 10^{-07}$
50 % CFRP REC.	1.27	$1.40 \times 10^{-07}$
30 % GFRP SQU.	1.94	$1.88 \times 10^{-07}$
30 % GFRP REC.	1.89	$2.18 \times 10^{-07}$
40 % GFRP SQU.	2.3	$6.41 \times 10^{-08}$
40 % GFRP REC.	2.22	$6.41 \times 10^{-08}$
50 % GFRP SQU.	2.62	$6.41 \times 10^{-08}$
50 % GFRP REC.	2.5	$6.41 \times 10^{-08}$



## Performance Evaluation of Small Scale Air-Conditioning System Using R22 and Alternative Refrigerants

**Prof. Dr. Khalid Ahmed Al-Joudi**  
Department of Mechanical Engineering  
College of Engineering  
Baghdad University  
Email:Khalid47joudi@yahoo.com

**Asst. Lect. Qusay Rasheed Abd Al-Amir**  
Department of Mechanical Engineering  
College of Engineering  
Baghdad University  
Email:Qusay1972@gmail.com

### ABSTRACT:

A mathematical model has been formulated to predict the influence of high outdoor air temperature on the performance of small scale air - conditioning system using R22 and alternative refrigerants R290, R407C, R410A. All refrigerants were investigated in the cooling mode operation. The mathematical model results have been validated with experimental data extracted from split type air conditioner of 2 TR capacity. This entailed the construction of an experimental test rig which consists of four main parts. They are, the refrigeration system, psychrometric test facility, measuring instrumentation, and auxiliary systems. The conditioned air was maintained at 25 °C dry bulb and 19 °C wet bulb for all tests. The outdoor ambient air temperature was varied from 35 °C to 55 °C in 5 °C increments. The study showed that R290 is the better replacement for R22 when the air conditioning system works under high ambient temperature. It has better performance as a drop in refrigerant. R407C has the closest performance to R22, followed by R410A.

**KEYWORDS:** Numerical and experimental refrigeration cycle performance; Mathematical model; Small air conditioner; Alternative refrigerants at high ambient temperature.

### تقييم أداء منظومة تكييف هواء صغيرة الحجم باستخدام R22 وموائع بديلة

م.م. قصي رشيد عبد الامير  
قسم الهندسة الميكانيكية  
جامعة بابل

أ.د. خالد أحمد الجودي  
قسم الهندسة الميكانيكية  
جامعة بغداد

### الخلاصة :

تم بناء نموذج رياضي يحاكي تأثير ارتفاع درجة حرارة الهواء الخارجي على الأداء التشغيلي لمكيف هواء صغير السعة يعمل بمائع التثليج R22 و بدائله R290, R407C, R410A و بطور التبريد. قورنت نتائج النموذج رياضي لهذه الدراسة بنتائج عملية من مكيف هواء مُنفصل سعة 2 طن تبريد. استلزم ذلك بناء جهاز اختبار تجريبي يتكون من أربعة أجزاء وهي نظام التثليج وحجرات الاختبار البيئية ومعدات القياس و أجهزة السيطرة على درجات الحرارة . تم تثبيت درجة حرارة الهواء الداخلية عند 25 °م بصللة جافة و 19 °م بصللة رطبة. بينما تغيرت درجات حرارة الهواء الخارجية من 35 °م إلى 55 °م بزيادات مقدارها 5 °م كل مرة. أثبتت الدراسة أنّ مائع التثليج R290 هو البديل الأفضل إلى مائع التثليج R22 عندما يعمل نظام التكييف تحت درجات حرارة بيئية عالية. كان مائع التثليج R407C اقرب أداءاً إلى المائع R22 و يأتي بعده R410A.

الكلمات الرئيسية: دراسة عددية و تجريبية لدورة التثليج، نموذج رياضي، مكيف هواء صغير السعة ، موائع بديلة عند ظروف بيئية قاسية.

## 1. INTRODUCTION

Many mathematical models have been proposed in the past for modeling refrigeration systems. These models can be classified as steady state and transient simulations. Steady state simulations are commonly used for performance prediction and product design. In other words, vapor compression systems are rated and designed using steady state performance evaluations. Rice et al. (1981) used steady state simulation to explore optimization of conventional air-to-air heat pumps. The model was used to calculate the maximum coefficient of performance that can be attained, both with components that are presently available and with improved ones, for a range of heat exchanger sizes. Another model to predict the steady state performance of an air to air heat pump model was developed by Fisher and Rice (1983). This model is known as the ORNL heat pump model. The model was written using Fortran-IV computer program. In medium temperature refrigeration systems, Spatz et al. (2004) evaluated the performance of R22 with its potential alternatives of R410A, R404A, and R290. The results show that R410A is an efficient and environmentally acceptable option to replace R22 in medium temperature applications. According to Cabello et al.(2005), a simplified steady-state model of a single stage vapor compression plant was presented based on empirical and parametrical correlations. This model has been validated by experimental data obtained from a test bench using refrigerants R134a, R407C and R22. In 2007, Techarungpaisan et al. proposed a steady state simulation model to predict the performance of a small split type air conditioner with an integrated water heater. This model was also used to predict system parameters of interest such as hot water temperature, condenser exit air temperature, evaporator exit air temperature, mass flow rate of refrigerant, heat rejection in condenser and cooling capacity of the system.

In addition to the above, other models have been proposed as simulation tools for vapor compression refrigeration cycles such as VapCyc, and CYCLE-D. Richardson et al. (2004) presented VapCyc, which is a steady state simulation tool for the modeling and optimization of vapor

compression refrigeration system and its components. The simulation limits the user to the basic four component system. The simulation consists of a set of independent variables, such as system charge, component model numbers and component independent variables, and results in a set of dependent system variables, such as COP, capacity, weight and volume. Another simulation tool called CYCLE-D offered by the National Institute of Standards and Technology (NIST) for the theoretical analysis of a vapor compression system was used by Domanski et al. (2005). The goal of their results was to assess the impact of the evaporator performance on the COP for different refrigerants.

In this model, a comparative performance of R22 and its alternatives R290, R407C and R410A were determined theoretically in an attempt to examine the possibility of substituting R22 in residential air conditioners used in summer hot arid climate.

## 2-MATHEMATICAL MODELING

The refrigeration cycle consists of four major components; a rotary compressor running at constant speed, a finned-tube condenser coil, an evaporator coil, and capillary tubes. These components are connected by pipes which may be surrounded by insulation. Other components such as a filter-dries and an accumulator are neglected in this analysis due to their relatively small influence on the performance of the system (Jin and Spitler 2002). These components form a complete refrigeration cycle. In order to simulate the cycle, all models are interconnected with each other to form the complete model. The thermodynamic properties of R22 and the alternative refrigerants are calculated using the Engineering Equation Solver (EES) software (Klein 2006). These properties are calculated from the equation of state (EOS). The cycle presented in **Fig.1** is representative of a single-stage, vapor compression refrigeration cycle.

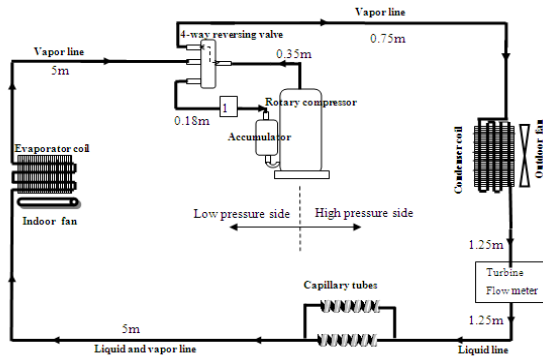


Fig.1 Schematic diagram of a split type A/C system

The pressure-enthalpy diagram for an actual system with state points is shown in Fig.2. It is noted that due to pressure drop across both the suction line and discharge line, the suction pressure ( $P_1$ ) is slightly lower than the evaporator pressure ( $P_e$ ), while the discharge pressure ( $P_2$ ) is higher than the condenser pressure ( $P_c$ ).

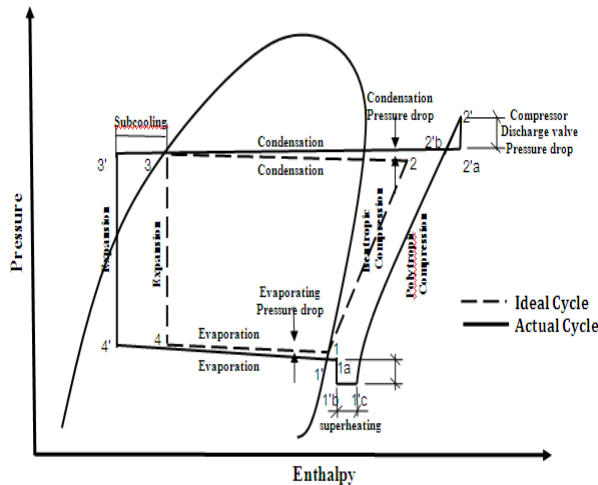


Fig.2 Ideal and real refrigeration cycles.

### 2.1 Modeling of Rotary Compressors

The following assumptions for the rotary compressor are made:

1. Compressor operates at steady state conditions.
2. Compression process is assumed polytropic.

3. Changes in kinetic and potential energies are negligible.
4. Compressor motor and mechanical efficiency are taken to be 78% and 92.5%, respectively (Wakabayashi et al. 1982).
5. The temperature of the gas along with the shell is constant.
6. Pressure drop across the discharge valve is isenthalpic.
7. The flow through the compressor is homogeneous and one dimensional.
8. The oil effects on the refrigerant properties are neglected.

In an actual compression process, the entropy increases as the irreversibilities of the process increase. Therefore, the compression process in the compressor is normally polytropic. The power of compressor is calculated according to the following equation (Winandy 2002):

$$W_{co} = \dot{m}_r \cdot P_1 \cdot v_1 \cdot \frac{n}{n-1} \left[ \left( \frac{P_2}{P_1} \right)^{\frac{n-1}{n}} - 1 \right] \quad (1)$$

The theoretical power ( $w_{co}$ ) can also be calculated in terms of the enthalpy change of refrigerant across the compressor, as follows:

$$W_{co} = \frac{W_{is}}{\eta_{is}} = \dot{m}_r \cdot (H_2 - H_1) \quad (2)$$

The power input to the compressor is determined as;

$$W_i = \frac{W_{co}}{\eta_{ov}} \quad (3)$$

The overall compressor efficiency determines the actual amount of electrical energy required to drive the compressor. This efficiency is calculated by Cho and Jung (2010), and Sakaino et al. (1984) as;

$$\eta_{ov} = \eta_{in} \eta_{me} \eta_{mo} \quad (4)$$

The values of efficiencies  $\eta_{mo}$  and  $\eta_{me}$  are taken as 0.78 and 0.925 respectively (Duprez et. al. 2007),

whereas the indicated efficiency  $\eta_i$  is calculated as (Ding and Zhang 2001):

$$\eta_{in} = \frac{\eta_v}{1 + 1.5 \Delta P_d \left( \frac{P_d}{P_s} \right)^{\frac{1}{n}} \cdot v_s / (H_d - H_s)} \quad (5)$$

The volumetric efficiency  $\eta_v$  of the compressor is calculated from the well known equation:

$$\eta_v = 1 + C - C \left( \frac{P_d}{P_s} \right)^{\frac{1}{n}} \quad (6)$$

It is well known that the rotary compressors have high clearance volumetric efficiencies due to the small clearance volume and corresponding low re-expansion losses of residual gas (Winandy et. al. 2002). In Eq.6, the clearance volume is taken at C=5%. The polytropic index n is given as;

$$n = \frac{\ln \left( \frac{P_d}{P_s} \right)}{\ln \left( \frac{v_s}{v_d} \right)} \quad (7)$$

$\Delta P_d$  in Eq.5, is given by Ding and Zhang (2001) as;

$$\Delta P_d = 25(T_d - 273.15)^{-1.01} \cdot 10^{-0.15 \frac{P_d}{P_s}} \quad (8)$$

At steady state, the mass flow rate of refrigerant is assumed to be the same throughout the system and equal to the mass flow rate through the compressor (Blanco et al. 2012). Most compressors operate at a fixed displacement rate. Therefore, the refrigerant mass flow rate will be a function of the suction specific volume as ;

$$\dot{m}_r = \frac{\eta_v \cdot V_d \cdot N}{v_1} \quad (9)$$

The theoretical displacement volume of the compressor ( $V_d$ ) is calculated from the difference in volume between the roller diameter and cylinder diameter as follows (ASHRAE Handbook 2010);

$$V_d = \frac{\pi \cdot L_{cy} \cdot (D_c^2 - D_r^2)}{4} \quad (10)$$

Where:  $D_c$  and  $D_r$  are the diameters of the cylinder and rolling piston respectively, and  $L_{cy}$  the length or height of the cylinder.

In the compressor, the heat is transferred during the compression cycle due to the temperature difference between the cylinder walls and the refrigerant gas  $Q_{su}$ , on one hand, and between the shell and the ambient  $Q_S$  on the other hand. It is difficult to study the heat transfer phenomena inside the rotary compressor since it requires knowledge of the internal dimensions and many factors concerning re-expansion of residual gas, mass of return flow, oil and gas leakage and so on. For these reasons, the heat transfer from the shell to the ambient is only considered in this study as in other works (Kim and Bullard (2001), Winkler (2009)). When the compressor shell temperature has reached a steady value, the rate of heat transfer from the refrigerant to the shell is equivalent to the rate of the heat transfer from the shell to the ambient. The heat transfer from the compressor shell can be obtained by applying the first law of thermodynamics across the compressor shell using the following equation for the steady state flow, neglecting the potential and kinetic energies (Duprez et. al., 2007).

$$Q_S = \dot{W}_i - \dot{m}_r (H_d - H_s) \quad (11)$$

## 2.2 Modeling of Finned Tube Condensers

On the refrigerant side, the condenser is divided into three heat transfer regions, a vapor phase de-superheating region, a two-phase condensing region and a liquid phase subcooling region. Among these three regions, de-superheating and subcooling occupy relatively a small portion. The de-superheating uses about 5 percent of the condensing surface area and subcooling uses 5 to 10 percent (Wang, 2000). The rest of the condenser area undergoes condensation at constant pressure and temperature. **Fig.3** shows a schematic diagram of the heat transfer processes through the condenser.

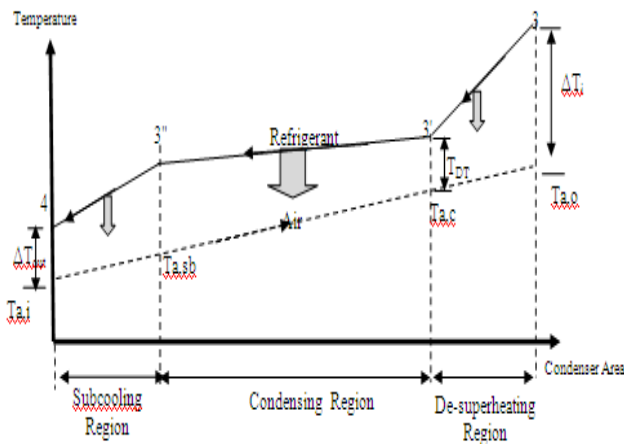


**Fig.3** Temperature profile in the condenser

The following assumptions are made in this study;

- 1-One dimensional steady flow,
- 2-Thermodynamic equilibrium between the liquid and vapor (separated flow),
- 3-The condenser coils are assumed to be one dry path.
- 4-In the two phase region, the flow is assumed to be annular flow.
- 5-The air side heat transfer coefficient is constant over the whole condenser.
- 6-The air and refrigerant flow directions are in counter flow configuration.
- 7-The heat transfer and pressure drop effects are considered in the condenser tubes and they are neglected in bends.

The heat rejected from each region can be determined by evaluating the enthalpies at the inlets and outlets.

$$Q_{c,d} = \dot{m}_r (H_3 - H_{3'}) \tag{12}$$

$$Q_{c,t} = \dot{m}_r (H_{3'} - H_{3''}) \tag{13}$$

$$Q_{c,sb} = \dot{m}_r (H_{3''} - H_4) \tag{14}$$

The effectiveness – number of transfer units ( $\epsilon$  - NTU ) method is utilized to find the heat transfer for each region in the heat exchanger, using the temperature difference between the air and refrigerant sides as:

$$Q_{c,d} = \epsilon_d C_{\min} (T_3 - T_{a,c}) \tag{15}$$

$$Q_{c,t} = \epsilon_t C_{\min} (T_{3'} - T_{a,sc}) \tag{16}$$

$$Q_{c,sb} = \epsilon_s C_{\min} (T_{3''} - T_{a,i}) \tag{17}$$

The condenser effectiveness ( $\epsilon$ ) is defined as the ratio between actual heat transfer rate to maximum heat transfer rate:

$$\epsilon = \frac{Q_a}{Q_m} \tag{18}$$

The effectiveness of cross flow heat exchanger with unmixed fluid is a function of the specific heat ratio ( $C_{\min} / C_{\max}$ ) and the number of transfer units ( Incropera and DeWitt, 1990 ).

For single phase region

$$\epsilon = 1 - \exp \left\{ \frac{NTU^{0.22}}{C_{\min} / C_{\max}} \left[ \exp((-C_{\min} / C_{\max}) * NTU^{0.78}) - 1 \right] \right\} \tag{19}$$

For two phase region

$$\epsilon = 1 - \exp(- NTU) \tag{20}$$

Where the number of transfer units is calculated for each region to determine the heat transfer rate. This parameter is defined as follows:

$$NTU = \frac{U A}{C_{\min}} \tag{21}$$

Where  $C_{\min} = \min(C_m, C_{um})$ , the refrigerant is modeled as mixed fluid and the air is modeled as unmixed fluid

$$C_m = \dot{m}_r C_{p_r} \tag{22}$$

$$C_{um} = \dot{m}_a C_{p_a}$$

The UA value denotes the overall thermal conductance of any region in the condenser in

$W/^{\circ}C$ . The overall thermal conductance is computed as:

$$\frac{1}{UA} = \frac{1}{h_r A_{t,i}} + \frac{\delta_t}{k_t A_{t,m}} + \frac{1}{h_{f, A_{t,o}}} + \frac{1}{\eta_o h_a A_o} \quad (23)$$

By neglecting the very small resistances of the tube wall and the thermal contact resistance, the overall thermal conductance reduce to;

$$\frac{1}{UA} = \frac{1}{h_r A_{t,i}} + \frac{1}{\eta_o h_a A_o} \quad (24)$$

In single-phase region (liquid or vapor), the forced convection heat transfer coefficient of the refrigerant side for a smooth tube was determined using the Dittus-Boelter equation (Incropera and DeWitt, 1990)

$$h_{r,s} = 0.023 \cdot Re^{0.8} \cdot Pr^a \frac{k_r}{D_i} \quad (25)$$

For liquid phase: (a=0.3)

$$Re_L = \frac{G \cdot d_i}{\mu_L}, \quad Pr_L = \frac{Cp_L \mu_L}{k_L} \quad (26)$$

For vapor phase( a=0.4)

$$Re_v = \frac{G \cdot d_i}{\mu_v}, \quad Pr_v = \frac{Cp_v \mu_v}{k_v} \quad (27)$$

In the two phase region, the condensation heat transfer coefficient correlations by Shah (1979) was employed. This correlation is calculated as a function of the vapor quality. It can be written as follows:

$$h_{r,t} = h_l \left[ (1-x)^{0.8} + \frac{3.8 x^{0.76} (1-x)^{0.04}}{P_{re}^{0.38}} \right] \quad (28)$$

Where the liquid heat transfer coefficient,  $h_l$ , is calculated using the Dittus-Boelter equation and  $P_{re}$  is the reduced pressure of refrigerant ( $P_{re} = P_{sa}/P_{cr}$ ). Furthermore, the average convection heat transfer coefficient in the condenser and evaporator is obtained by integrating local values over the length of the two phase region. The vapor quality of the

refrigerant is assumed to be linear throughout the length. Therefore, the integration is performed over the range of refrigerant vapor quality. The average condensing heat transfer coefficient,  $h_{av,t}$ , is thus given by:

$$h_{av,t} = \frac{1}{x_o - x_i} \int_{x_{in}}^{x_{out}} h_{r,t}(x) dx \quad (29)$$

Where  $x_i$  and  $x_o$  are vapor quality of refrigerant at the inlet and outlet of the condenser ( $x_i=1$  and  $x_o=0$ ).

The air side heat transfer coefficient for dry surfaces is based on the work of McQuiston (1981) and is calculated by the correlation :

$$h_{c,a} = \frac{J Cp_a G_m}{Pr^{2/3}} \quad 3000 < Re < 15000 \quad (30)$$

The dry fin efficiency for a thin insulated tip with uniform rectangular section is based on the Schmidt method as described by Incropera and DeWitt (1990).

$$\eta_f = \frac{\tanh(ml)}{ml} \quad (31)$$

The parameters  $m$  and  $l$  are defined as:

$$m = \sqrt{\frac{2 h_a}{k_f \delta_f}} \quad (32)$$

$$l = r_e \varphi = r_e \left[ \left( \frac{r_e}{r_0} - 1 \right) \left[ 1 + 0.35 \log \left( \frac{r_e}{r_0} \right) \right] \right] \quad (33)$$

Where  $r_e$  is equivalent radius, and  $r_o$  is the outer radius of the fin. The equivalent radius parameter is given by the equation.

$$\frac{r_e}{r_0} = 1.28 \psi (\beta - 0.2)^{1/2} \quad (34)$$

$$\psi = \frac{S_t}{2r_0} \quad (35)$$

$$\beta = \frac{S_L}{S_t} \quad \beta \geq 1 \quad (36)$$

Where:  $S_L$  and  $S_t$  are longitudinal and transverse pitch, respectively.  $S_L$  is always selected to be greater than or equal to  $S_t$ . Finally, the overall heat transfer rate for the entire condenser is the sum of the heat transfer rates for the three regions

$$Q_c = Q_{de} + \sum_{i=1}^n Q_{t,i} + Q_{sb} \quad (37)$$

Where  $n$  is number of condensing region segments.

### 2.3 Adiabatic Capillary Tube Modeling

The capillary tube is a constant area expansion device used widely in small scale air conditioner systems. The refrigerant flow inside the capillary tube can be divided into the single phase and two-phase regions. Fig.4 shows a schematic diagram of the straight capillary tube connecting the outlet of the condenser and the inlet of the evaporator.

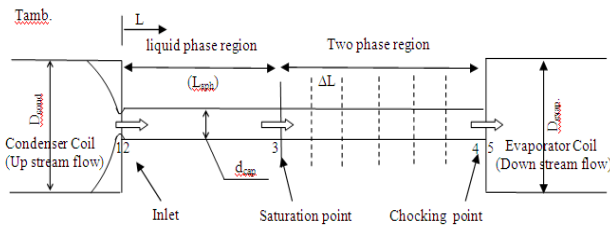


Fig.4 Schematic diagram of a capillary tube

The following assumptions are made:

- 1.The capillary tube operates at steady state.
- 2.Single and two phase flow analysis are considered.
- 3.A subcooled liquid state enters the capillary tube .
- 4.The flow of refrigerant inside the capillary tube is one dimensional, homogenous and adiabatic.
- 5.Changes in kinetic and potential energies are negligible.
- 6.The capillary tube is a straight and horizontal tube with a constant cross-sectional area.

The geometrical parameters and input conditions to the capillary tube model are inner diameter, temperature and pressure of the subcooled liquid refrigerant, and thermophysical properties of refrigerant. Results of the capillary tube model are the pressure and temperature at capillary tube exit and the capillary choking length.

By applying the Bernoulli equation between points 1 and 2, the minor pressure drop at the entrance is calculated by Sinpi boon and Wongwises (2002);

$$P_1 - P_2 = (1 + k) \frac{\rho V^2}{2} \quad (38)$$

Where  $k$  is the entrance loss factor. References are not in agreement about its value. The value of  $k=0.5$  is used here as given by Chen (2008).

In the single phase region (points 2→3), the pressure at point 2 decreases linearly until the saturation pressure at point 3 according to the following equation (Munson and Young 2010).

$$P_2 - P_3 = f_s \frac{L_{c.s}}{d_{ca}} \frac{\rho V^2}{2} \quad (39)$$

By applying the steady flow energy equation for the single phase liquid region in the capillary tube with negligible work and heat exchange, we get:

$$H_2 = H_3 = H_{sc} \quad (40)$$

Applying the steady flow energy equation for each element lying in the two phase region, between sections 3 and 4:

$$H_3 + \frac{V_3^2}{2} = H_f + x H_{fg} + \frac{G^2}{2} (v_f + x.v_{fg})^2 \quad (41)$$

Eq.41 is quadratic in the quality  $x$ . It is given with other details and the choking length by Sukkarin and Somchai, 2011.

### 2.4 Modeling of a Direct Expansion Evaporator

The analysis for the evaporator model is similar to that of the condenser, but is assumed to contain two heat transfer regions on the refrigerant

side, namely a two phase evaporating region and a single phase superheated region. In addition, the air side cooling region is divided into two sections which are dry and wet. **Fig.5** shows the refrigerant flow through the evaporator.

The following assumptions are made for the evaporator model:

1. Fin edges are adiabatic
2. Fin efficiency is assumed to be 90%
3. The degree of superheating at the evaporator is assumed to be 6 °C.
4. Dehumidification occurs on the air side at the entrance of two phase region.
5. Heat transfer and pressure drop effects due to bends are neglected.

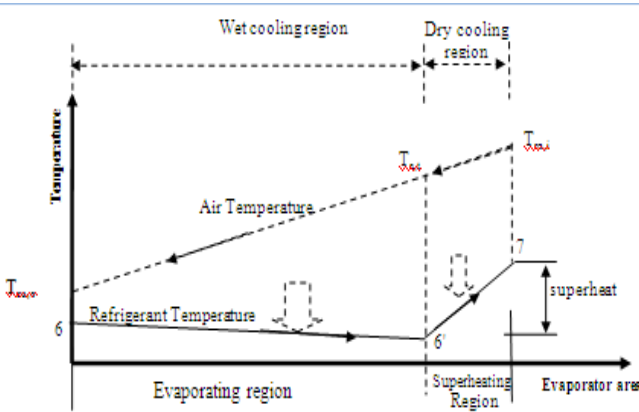


**Fig.5** Temperature diagram in an evaporator coil

The heat gain by the refrigerant side in the two phase and superheated regions are given by the formulae ;

$$Q_{e,t} = \dot{m}_r (H_6 - H_6) = \varepsilon_t^* C_{\min,t} (T_{a,t} - T_6) \quad (42)$$

$$Q_{e,sp} = \dot{m}_r (H_7 - H_6) = \varepsilon_{e,sp} C_{\min} (T_{ro,i} - T_6) \quad (43)$$

Where  $H_6$ ,  $H_7$  and  $H_6$  are refrigerant enthalpies at the locations in **Fig.5**. The modified heat

exchanger effectiveness  $\varepsilon_t^*$  is given by Harms et al (2002) as;

$$\varepsilon_t^* = 1 - \exp \left( -\frac{UA^*}{m_a C_{p_a}} \right) \quad (44)$$

Where  $UA^*$  is the overall heat transfer coefficient for the wet cooling region.

The overall thermal conductance of the wet region of the evaporator coil is computed as

$$\frac{1}{UA^*} = \frac{1}{h_r A_{t,in}} + \frac{1}{h_l A_0} + \frac{1}{h_{a,w} \eta_{o,w} A_0} \quad (45)$$

McQuiston and Tree (1973) assumed a linear relationship between the humidity ratio of the saturated air at the wet surface, and the surface temperature. These parameters are determined as follows:

$$h_l = \frac{k_{wa}}{\delta_{wa}} \quad (46)$$

$$h_{a,w} = h_{a,dry} \left\{ 1 + \frac{H_{fg,w} (w_a - w_w)}{L_e C_{p_a} (T_a - T_w)} \right\} \quad (47)$$

$$H_{fg,w} = \left( -2 * 10^{-5} T_w^3 + 0.0012 T_w^2 - 2.3804 T_w + 2501.6 \right) * 10^3 \quad (48)$$

The moist air properties are obtained using relations given by Joudi,1991.

As in the condenser model, the Dittus-Boelter equation is used to compute the refrigerant side heat transfer coefficient in the single phase region:

$$h_{r,s} = 0.023 . \text{Re}^{0.8} . \text{Pr}^{0.4} \frac{k_r}{D_i} \quad (25)$$

Whereas, the evaporating heat transfer coefficient in the two-phase region ( $h_{r,t}$ ) is calculated as (Domanski and David, 1985) ;

$$h_{r,t} = 3.22 . X_t^{-0.3} h_{r,s} \quad (49)$$

The above correlation is applicable for annular flow at qualities from 10 percent to 90 percent.

The forced convection heat transfer coefficient on the air side of flat finned tube heat exchangers ( $h_{a,dry}$ ) is calculated by the correlation proposed by Briggs and Yong, 1962.

$$h_{a,dry} = 0.134 \frac{k_a}{D_0} Re_a^{0.681} Pr_a^{0.333} \left(\frac{Z}{Y}\right)^{0.2} \left(\frac{Z}{t}\right)^{0.1134} \quad (50)$$

The evaporator cooling capacity is the sum of the combination of heat gains by the refrigerant side in the two phase and superheated regions and can be expressed as:

$$Q_e = \sum_{i=1}^n Q_{e,i} + Q_{e,sp} \quad (51)$$

## 2.5 System Pressure Drop

Pressure drop in the system consist of pressure drops in the main components of the system and connecting pipes. Conventional equations are used with full details given by Al-Amir 2013.

## 3. SOLUTION PROCEDURE

The Engineering Equation Solver (EES) software is used in this work for computer programming. The computer program of the actual cycle is more complex when compared to the ideal cycle program and consists of a main program and a number of procedures. These procedures are coupled with the main program by call commands. The main program contains system equations and call statements for all the preceding procedures. Basic inputs are required to the main program to simulate the actual vapor refrigeration cycle performance. These inputs are the physical dimensions of the components and operating conditions for cycle. The output parameters of the system simulation model are the cycle state points, cooling capacity, heat rejection from the condenser, refrigerant pressure drops, consumed power, and the coefficient of performance. To plot the steady state characteristic performance of the actual refrigeration cycle on a p-h diagram, pressure and enthalpy data are taken from the simulation results.

For each refrigerant, five different settings of outdoor air temperature into the condenser were considered. The EES software is used to plot data on a p-h diagram.

## 4. EXPERIMENTAL WORK

The experimental test rig is shown in **Fig. 6**.

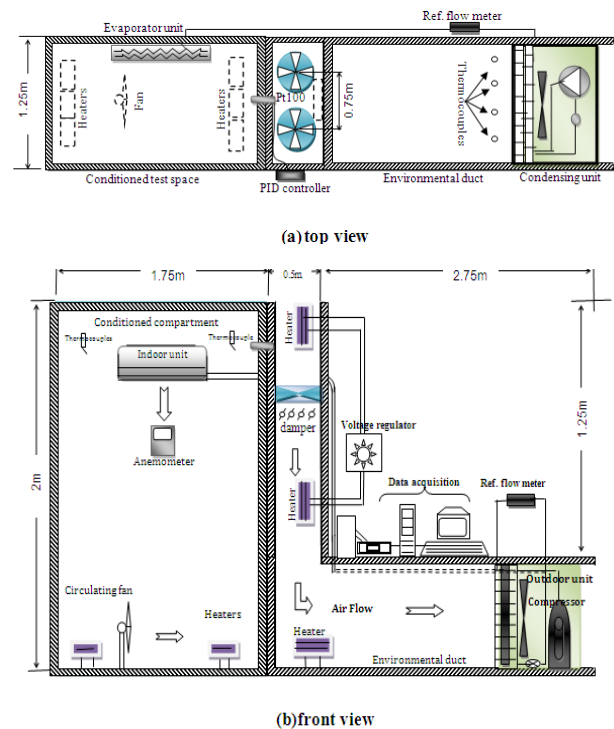


**Fig.6** A schematic diagram of the experimental test rig with dimension of conditioned compartment and environmental duct a)top view b) front view

It consists of four main parts which are the refrigeration system, the psychrometric apparatus, measuring instrumentation, and auxiliary systems. Split type air conditioners with a 2 TR nominal cooling capacity model EL-26ITERH manufactured by Denka company were tested experimentally. This system required to replace the compressor for R410A refrigerant due to its higher operating pressures. The psychrometric apparatus consists of two sections, which are the indoor conditioned compartment and the outdoor environmental duct. These sections were locally constructed and their conditions were maintained

according to the ASHRAE standard 37-2009 for testing unitary air conditioners and heat pumps. The dry and wet bulb air temperatures for the interior are 27 °C/19 °C and outdoor ambient are 35 °C/24 °C. The evaporator unit was mounted at a height of 1.75 m. Six electric heaters, 1200 W each, were placed inside the condition compartment for the heat load. They are controlled by a Solid State Relay (SSR) to maintain the air temperature inside the compartment at 25 °C throughout the test period. The environmental duct has an L shape and includes two circulation fans with dampers, which drive the air through the thermally insulated environmental duct. Three electric resistance heaters, 1200 W each, are located inside the duct for controlling the temperature of the air across the condensing unit. All the components such as system units, fans, electric heaters and voltage regulator are connected to a power supply. A sample of systematic test runs is summarized in Table 1.

**Table 1** Experimental runs at optimum charge under various outdoor air temperature

The instrumentation required for testing are divided into refrigerant and air sides. Refrigerant side measurements include the thermocouples type-K with a range of -50 to 250 °C and an accuracy of ± (0.4 % + 0.5 °C), pressure transducers with a range of 0-10 bar or 0-40 bar and an accuracy of ±1% of full scale, turbine flow meter with a range of 0.02-1.2 m<sup>3</sup>/h and an accuracy of ±0.58 of the reading. Whereas, air side measurements include thermocouples type-T with a range of -270 to 400 °C and an accuracy of ± 0.3 °C, and collection vane type anemometer with a range of 0.4 - 30 m/s and an accuracy of ± 3 % full scale. All measurements were calibrated before their use.

**5. RESULTS AND DISCUSSION**

**Fig.7** shows influence of outdoor air temperature on the compressor discharge temperature. Clearly, increasing the outdoor air temperatures increases the compressor discharge temperature. It is noted from the same figure that discharge temperature of the R22 is higher by about

21-23<sup>0</sup>C than that of R290 at outdoor temperature ranging from 35 °C to 55 °C.

**Fig.8** shows the effects of outdoor air temperature on power consumption of compressor when the system operates in the cooling mode. The compressor power consumption increases with increasing outdoor air temperature from 35 °C to 55 °C with a constant 25 °C inside the conditioned compartment. This is because the compressor power is affected by two factors, the refrigerant mass flow rate and the compression ratio. The power consumption increased from 2.365 kW to 2.84 kW for R22, 2.04 kW to 2.65 kW for R290, 2.47 kW to 2.93 kW for R407C, 2.74 kW to 3.32 kW for R410A for the same outdoor temperature range. Also, the power consumption increases with increased outdoor air temperature due to the rise in the temperature difference (lift) between the environmental duct and conditioned compartment.

The system has high cooling capacities at the standard rating conditions (35 °C outdoor air temperature), but lose capacity as the outdoor air

Ref. Type	Charge Level(gram)	No. of Run	Optimum Charge(g)	Outdoor Temp(C)	No. of Run
R22	1500	2	R22 (2000g)	35	2
	1600	2			
	1700	2		40	2
	1800	2			
	1900	2		45	2
	2000	2			
	2100	2		50	2
	2200	2			
2300	2	55	2		
R290	200	2	R290 (900 g)	35	2
	300	2			
	400	2		40	2
	500	2			
	600	2		45	2
	700	2			
	800	2		50	2
	900	2			
	1000	2		55	2
	1100	2			
R407C	1500	2	R407C (1900 g)	35	2
	1600	2			
	1700	2		40	2
	1800	2			
	1900	2		45	2
	2000	2			
	2100	2		50	2
	2200	2			
2300	2	55	2		
R410A	1800	2	R410A (2800 g)	35	2
	2000	2			
	2200	2		40	2
	2400	2			
	2600	2		45	2
	2800	2			
	3000	2		50	2
	3200	2			
				55	2

temperature increases as shown in **Fig.9** . The

cooling capacity of R410A has a higher value, at the standard test condition, than the other refrigerants. This is because of the high volumetric refrigerating capacity, which is defined as the cooling capacity per unit vapor volume at the exit of the evaporator in  $\text{kJ}/\text{m}^3$ . Moreover, the mass flow rate of R410A is higher than the other refrigerants at this condition. When the outdoor air temperature increases to  $55^\circ\text{C}$ , the cooling capacity of R410A drops faster than the other refrigerants because of its low critical temperature ( $72.5^\circ\text{C}$ ). Theoretical results for 2 TR system using R410A is higher by about 3.82 % than that of R22 while it is lower for the alternative refrigerants R407C and R290 by about 1.66 % and 4.63 % than that of R22, respectively.

**Fig.10** indicates that the lower the outdoor air temperature, the higher is the COP. As the outdoor temperature increases, the COP values decrease for all refrigerants. With increasing outdoor temperature, the COP of system charged with R410A drops much more than that of the same system charged with other refrigerants. Which means, the COP of R410A system is more sensitive to changes in outdoor temperature. On the other hand, the system charged with R290 has the highest COP among the selected refrigerants at standard conditions. The COP of R407C seems to be similar to R22, as expected. At maximum outdoor air temperature ( $55^\circ\text{C}$ ), the coefficient of performance is maximum for R290 and minimum for R410A.

## 6. VALIDATION OF THE THEORETICAL MODEL WITH EXPERIMENTAL DATA

The normal way of validation of a theoretical model is by comparison with experimental results at the same operating conditions. The deviations between the two results are calculated by the following formulas;

$$\text{Relative deviation } (x \%) = \frac{(x_{\text{theoretical}} - x_{\text{experimental}})}{x_{\text{experimental}}} \times 100 \quad (52)$$

$$\text{Average deviation. } (x_{\text{av}} \%) = \frac{1}{n} \sum_{i=1}^n \left[ \frac{(x_{i,\text{theoretical}} - x_{i,\text{experimental}})}{x_{i,\text{experimental}}} \times 100 \right] \dots\dots(53)$$

**Fig.11** shows the comparison between calculated and measured compressor discharge temperatures for outdoor air temperatures of  $35^\circ\text{C}$ ,  $40^\circ\text{C}$ ,  $45^\circ\text{C}$ ,  $50^\circ\text{C}$  and  $55^\circ\text{C}$ . **Fig.(11)** include 40 experimental data points, 10 data points for each refrigerant. The compressor discharge temperature calculations agree well with experimental measurements. All the points are within -3.198% and +4.4% .

A comparison of calculated and measured compressor work with different outdoor air temperatures is shown in **Fig.12**. The measured results, lie within a maximum deviation of 6.92% and a minimum deviation of -4.07 % .

Good agreement is observed between the calculated and measured cooling capacity at different outdoor air temperatures as shown in **Fig.13**. The maximum deviation in the system is +11.7%. All the theoretical values are higher than the experimental values for all four refrigerants.

The calculations of the coefficient of performance for the actual cycle lead to good results, as illustrated in **Fig. 14**. For R22, the average deviation in the coefficient of performance was 3.68% and minimum deviation of -3.38%. The theoretical predictions for COP values are higher than the experimental values for the actual cycle.

The actual cycle diagrams (**Figs. 15 to 18**) clearly show the effect of outdoor temperature at a relatively constant evaporator temperature. Pressure drops across suction line and discharge valve of compressor are very clear and the minor pressure drops inside the condenser and evaporator are obvious. These characteristics are, of course, not present in the assumptions for the ideal cycles.

## 7. CONCLUSIONS

1. At standard rating conditions, the cooling capacity for R410A was highest among the investigated refrigerants.
2. The compressor discharge temperature increase with increasing outdoor air temperatures. R22 refrigerant has higher discharge temperature than the other refrigerants.

3. The system charged with R290 has the best COP than the other refrigerants.
4. The comparison shows that the power consumption of R410A and R407C are higher by about 15.8-16.9% and 4.4-3.17%, respectively and R290 lower by about 13.7-6.7% as compared to R22 under same operating conditions. Test results demonstrate that R290 is a good alternative to replace R22 in air conditioners from the standpoint of energy efficiency.
5. The results also show that the COP values decrease for all investigated refrigerants, as the outdoor temperature increases. The COP for 2 TR system using R410A is found to be the lowest among the four refrigerants at high outdoor air temperature. Therefore, R410A is not a good choice for air conditioner in high outdoor air temperature.

## REFERENCES

- Al-Amir Q. R., 2013," Experimental assessment and numerical simulation of the performance of small scale air-conditioning systems using alternative refrigerants to R-22" University of Baghdad, PhD thesis.
- ASHRAE. 2009, ANSI/ASHRAE 37-2009," Methods of Testing for Rating Electrically Driven Unitary Air Conditioning and Heat Pump Equipment", American Society of Heating, Refrigeration, and Air-Conditioning Engineers, Inc.
- ASHRAE Handbook of Fundamental, 2010, American society for Heating, Refrigeration and Air Conditioning Engineers, Inc., New York, Chapter 6.
- Blanco D., Nagano K., Morimoto M., 2012" Steady state vapor compression refrigeration cycle simulation for a monovalent inverter-driven water-to-water heat pump with a desuperheater for low energy houses" International journal of refrigeration, 35, 1833- 1847.
- Briggs, D.E. and Yong, 1962," Convection heat transfer and pressure drop of air flowing across triangular pitch banks of finned tubes", 5<sup>th</sup> AICHE/ASME.
- Cabello R., Navarro J., Torrella E., 2005, " Simplified steady-state modelling of a single stage vapor compression plant. Model development and validation" Applied Thermal Engineering 25, 1740–1752.
- Chang Y., Wang C., 1997, "A Generalized Heat Transfer Correlation for Louver Fin Geometry", *International Journal of Heat and Mass Transfer*, Vol.40, pp. 533-544.
- Chen W., 2008," A comparative study on the performance and environmental characteristics of R-410A and R-22 residential air conditioners", Applied Thermal Engineering , Vol. 28, 1-7.
- Cho I. S and Jung J.Y., 2010," Lubrication characteristics of a rotary compressor used for refrigeration and air-conditioning systems ", Journal of Mechanical Science and Technology 24 (4), 851-856.
- Ding G., Hu H., Huang X., Deng B., Gao Y., 2009," Experimental investigation and correlation of two-phase frictional pressure drop of R410A–oil mixture flow boiling in a 5mm micro fin tube" International Journal of Refrigeration. 32, ,150 –161.
- Ding G.L., Zhang C.L., 2001, "Simulation and Optimization of Refrigeration and Air Conditioning Appliances, Science Press, Beijing. Quoted by Zhou (2010).
- Domanski, P.A., and David A. D., 1985," Simulation of a Heat Pump Operating with a Non azeotropic Mixture, ASHRAE Technical Data Bulletin" Advances in Non azeotropic Mixture Refrigerants for Heat Pumps, Vol.1, No.9, pp. 81, ASHRAE, Inc., Atlanta, GA.
- Domanski P. A., Yashar D., Kim M., 2005, " Performance of a finned-tube evaporator optimized for different refrigerants and its effect on system efficiency ", International Journal of Refrigeration 28, 820–827.
- Duprez, M.E., Dumont E., Frere M., 2007," Modeling of reciprocating and scroll compressors", International Journal of Refrigeration, 30, 5, 873-886.
- Fisher S.K., Rice C.K., 1983, "A steady-state computer design model for air to air heat pumps", Oak Ridge National Laboratory, Oak Ridge, Tennessee, U.S.A.
- Harms T. M., Braun J. E., and Groll E. A., 2002 "The Impact Of Modeling Complexity And Two-Phase Flow Parameters On The Accuracy Of System Modeling For Unitary Air Conditioners" , International Refrigeration and Air Conditioning Conference. Paper 569.



Incropera F., DeWitt D., 1990, "Fundamentals of Heat and Mass Transfer", third ed., John Wiley & Sons Inc., New Jersey, USA.

Jin H., and Spitler J.D., 2002. "A Parameter Estimation Based Model of Water-To-Water Heat Pumps for use in Energy Calculation Programs", ASHRAE Transactions, 108(1), pp. 3-17.

خالد احمد الجودي، 1991. مبادئ هندسة تكييف الهواء و التثليج، الطبعة الثانية، كلية الهندسة، جامعة البصرة.

Kim M.H., Bullard C.W., 2001, " A Simple Approach to Performance Analysis of Alternative Refrigerant Rolling Piston Type Rotary Compressors", MSc thesis, University of Illinois at Urbana Champaign.

Klein S.A., 2006, Engineering Equation Solver commercial version V8.914 .

McQuiston F. C., 1981, "Finned tube heat exchangers: state of the art for the air side", ASHRAE Trans., Vol.87, Part1, 1077-1085.

McQuiston F. C., Tree D. R., 1973, "Optimum space envelopes of the finned tube heat transfer surface," ASHAE Transactions, Vol.79, Pt. 2.

Munson B. R., Young D. F., 2010, " Fundamentals of Fluid Mechanics" Fourth edition, John Wiley & Sons. Inc. USA.

Rice C.K., Fisher S.K., Jackson W.L., Ellison R.D.,1981, "Design optimization and the limits of steady state heating efficiency for conventional single speed air source heat pumps", Oak Ridge National Laboratory, Oak Ridge, Tennessee ,U.S.A.

Richardson D. H., Aute V., Winkler J., and Radermacher, R. , 2004, " Numerical Challenges in Simulation of a Generalized Vapor Compression Refrigeration System." 2004 International Refrigeration and Air Conditioning Conference. Purdue University.

Sakaino K., Muramatsu S., Shida S., Ohinata O., 1984, " Some Approaches Towards a High Efficient Rotary Compressor, " International Compressor Engineering Conference, Purdue University.

Shah MM. , 1979, "A general correlation for heat transfer during lm condensation inside pipes". International Journal Heat and Mass Transfer, 22:547-56.

Sinpiboon J. , Wongwises S., 2002," Numerical investigation of refrigerant flow through non-adiabatic

capillary tubes" Applied Thermal Engineering , 22, 2015–2032.

Spatz M. W., 2004, "Replacement for HCFC-22 in air conditioning and heat pump system".

Sukkarin C., Somchai W., 2011," A comparison of flow characteristics of refrigerants flowing through adiabatic straight and helical capillary tubes" International Communications in Heat and Mass Transfer 38, 398–404.

Techarungpaisan P., Theerakulpisut S., Priprem S., 2007, "Modeling of a split type air conditioner with integrated water heater", Energy Conversion Management, 48, 1222-1237.

Wakabayashi H., Yuuda J., Aizawa T., Yamamura M., 1982," Analysis of Performance in a Rotary Compressor" International Compressor Engineering Conference, Paper 385.

Wang S. K. , 2000, " Handbook of air conditioning and refrigeration" Second Edition, chapter 10 page 26.

Winandy E., Saavedra O. C. , Lebrun J., 2002, "Simplified modelling of an open-type reciprocating compressor" Int. J. Therm. Sci. 41, 183–192.

Winkler J. M. ,2009," Development of a component based simulation tool for the steady state and transient analysis of vapor compression systems", PhD Thesis, University of Maryland, College Park

## NOMENCLATURE

$A$	Area ( $m^2$ )
$C_p$	Specific heat at constant pressure ( $J/kg \cdot ^\circ C$ )
$C_v$	Specific heat at constant volume ( $J/kg \cdot ^\circ C$ )
$d_{ca}$	Capillary tube diameter(m)
$D_h$	Hydraulic diameter (m)
$f_s$	Friction factor
$G$	Mass flux ( $kg/s \cdot m^2$ )
$h$	heat transfer coefficient ( $W/m^2 \cdot ^\circ C$ )
$H$	Enthalpy( $kJ/kg$ )
$J$	Colburn J factor
$k$	Thermal conductivity ( $W/m \cdot K$ )
$K$	Entrance loss factor
$k_t$	thermal conductivity of wall tube ( $W/m \cdot K$ )
$Le$	Lewis number
$\dot{m}$	mass flow rate( $kg/s$ )
$n$	Polytropic index

$n_f$	number of fins
$n_{ro}$	number of rows.
$n_{tu}$	number of tube
$N$	Number of cycles per minute(N=3600)
$Nu$	Nusselt number
$P$	Pressure (kPa)
$Pr$	Prandtl number
$P_{re}$	Reduce pressure
$Q$	Heat (kW)
$Re$	Reynolds number
$S_L$	Longitudinal pitch (m)
$S_t$	Tangential pitch (m)
$T$	Temperature (K)
$U$	Overall heat transfer coefficient ( $W/m^2K$ )
$v_1$	Specific volume at the comp. suc. ( $m^3/kg$ )
$V_d$	Displacement Volume of the compressor ( $m^3$ )
$W$	Compressor power (kW)
$x$	Quality
$X_{tt}$	Lockhart Martinelli parameter

r	refrigerant
s	suction
S	Shell
t	Tangential
v	vapor

**ABBREVIATIONS**

COP	Coefficient Of Performance
EES	Engineering Equation Solver
GWP	Global Warming Potential
HC	Hydrocarbon
HCFC	Hydro chlorofluorecarbon
HFC	Hydro fluorocarbon
PID	Proportional Integral Derivative
TR	Tone of Refrigeration

**Greek Symbols**

$\gamma$	Adiabatic index
$\varepsilon$	Effectiveness
$\varepsilon_v$	Void fraction
$\Delta P_d$	Pressure drop across the discharge valve
$\eta_0$	Efficiency
$\mu$	Dynamic viscosity ( $kg/m \cdot s$ )
$\nu$	Kinematic viscosity( $m^2/s$ )
$\rho$	Density ( $kg/m^3$ )
$\Phi_{Lt}$	Two phase liquid multipliers
$\Phi_{vt}$	Two phase vapor multipliers
$\delta_f$	Fin thickness(mm)
$\delta_t$	Wall thickness of the tube ( $\delta_t=0.5mm$ ).
$\sigma$	Surface tension ( $N/m$ )
$\Delta h$	Enthalpy change ( $kJ/kg$ )
$X_{tt}$	Lockhart Martinelli parameter

**SUBSCRIPTS**

c	condenser
co	compressor
d	discharge
e	evaporator
i	input
l	liquid

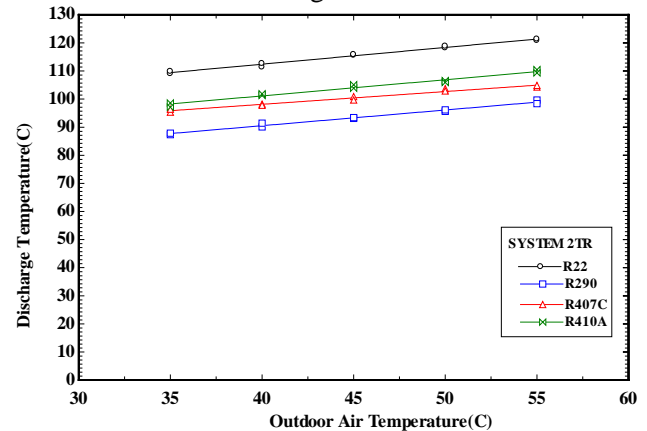


**Fig. 7** The effect of the outdoor air temperatures on discharge temperature.

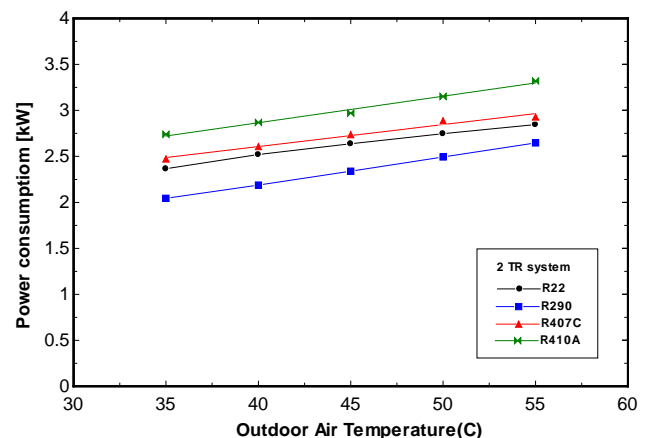


**Fig. 8** The effect of the outdoor air temperatures on compressor power consumption

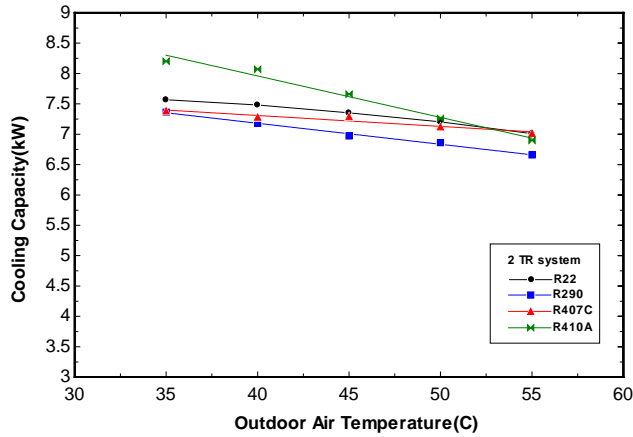


Fig. 9 The effect of the outdoor air temperatures on evaporator cooling capacity .

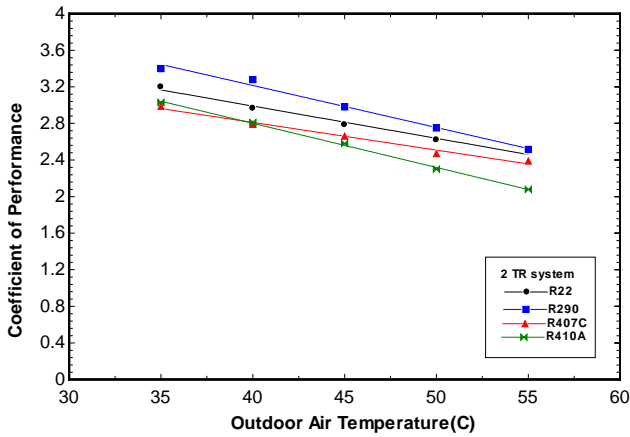


Fig. 10 The effect of the outdoor air temperatures on COP of system.

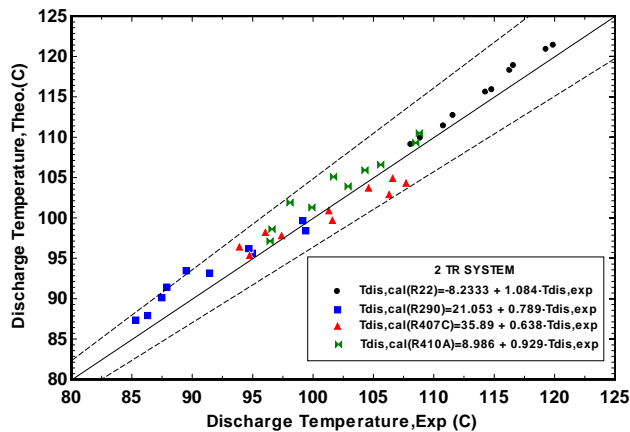


Fig.11 Comparison between theoretical and experimental compressor discharge temperatures system working with R22 and its alternative.

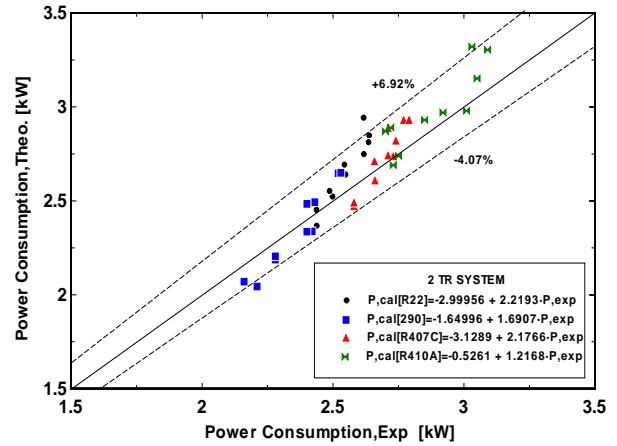


Fig.12 Comparison between calculated and measured compressor power consumption for system working with R22 and its alternative.

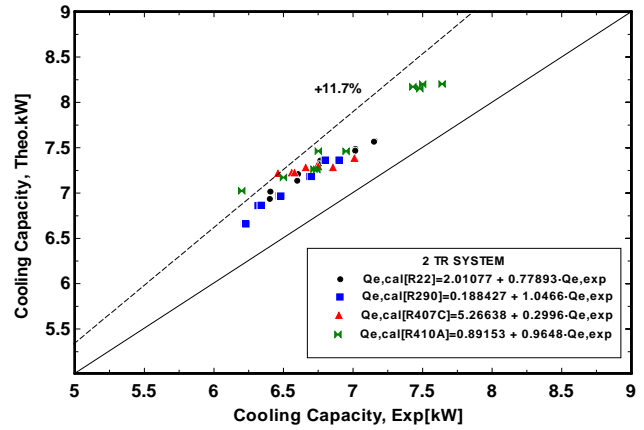


Fig.13 Comparison between theoretical and experimental cooling capacity for system working with R22 and its alternative.

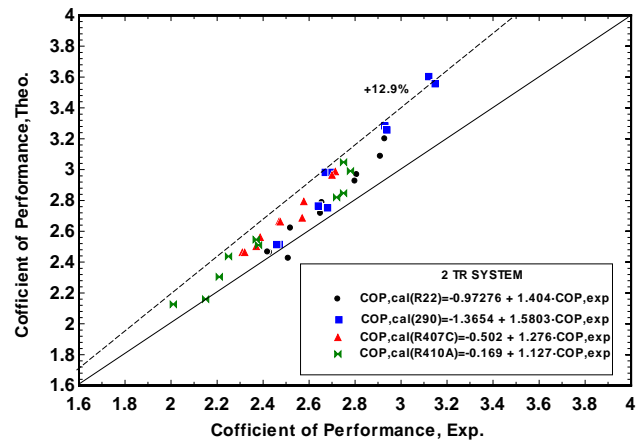


Fig.14 Comparison between theoretical and experimental coefficient of performance for system working with R22 and its alternative

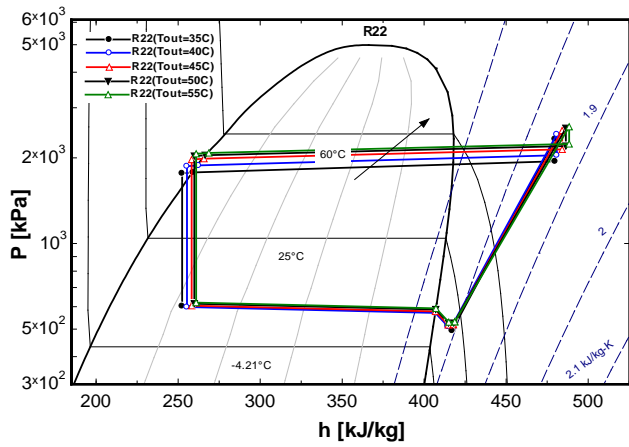


Fig.15 Pressure-enthalpy diagram of actual cycle for R22 under different outdoor air temperatures

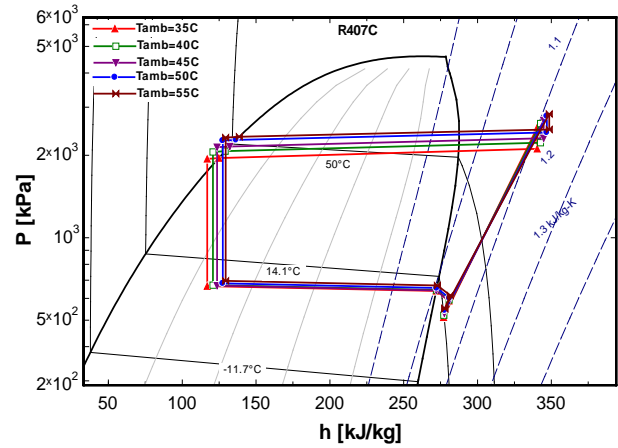


Fig. 17 Pressure-enthalpy diagram of actual cycle for R407C under different outdoor air temperatures

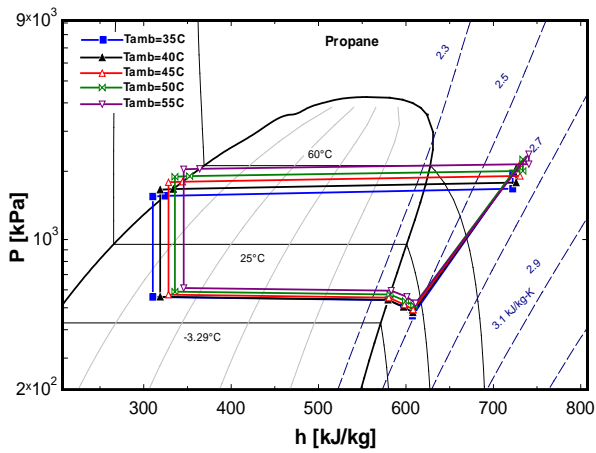


Fig. 16 Pressure-enthalpy diagram of actual cycle for R290 under different outdoor air temperatures

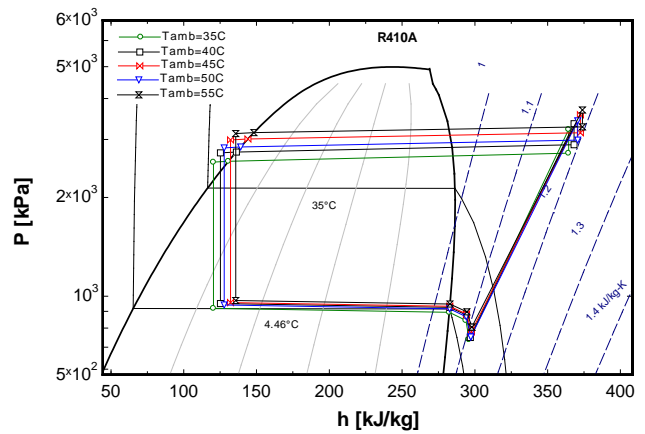


Fig.18 Pressure-enthalpy diagram of actual cycle for R22 under different outdoor air temperatures

# Analytical Solution of Transient Heat Conduction through a Hollow Spherical Thermal Insulation Material of a Temperature Dependant Thermal Conductivity

Dr. Mishaal Abdulameer Abdulkareem

Lecturer, Mechanical Engineering Department

College of Engineering, Al-Mustansiriyah University, Baghdad, Iraq

[dr.mishal04@gmail.com](mailto:dr.mishal04@gmail.com)

## ABSTRACT

The one-dimensional, spherical coordinate, non-linear partial differential equation of transient heat conduction through a hollow spherical thermal insulation material of a thermal conductivity temperature dependent property proposed by an available empirical function is solved analytically using Kirchhoff's transformation. It is assumed that this insulating material is initially at a uniform temperature. Then, it is suddenly subjected at its inner radius with a step change in temperature. Four thermal insulation materials were selected. An identical analytical solution was achieved when comparing the results of temperature distribution with available analytical solution for the same four case studies that assume a constant thermal conductivity. It is found that the characteristics of the thermal insulation material and the pressure value between its particles have a major effect on the rate of heat transfer and temperature profile.

**KEYWORDS:** Nonlinear differential equation, analytical solution, thermal conductivity, transient, Kirchhoff's transformation.

## حل تحليلي لتوصيل الحرارة المتغير مع الزمن خلال مادة كروية مجوفة عازلة للحرارة ذات توصيل حراري متغير مع درجة الحرارة

د. مشعل عبد الأمير عبد الكريم  
مدرس في قسم الهندسة الميكانيكية  
الجامعة المستنصرية / كلية الهندسة

### الخلاصة

تم حل المعادلة التفاضلية الغير خطية الأحادية البعد ذو الإحداثيات الكروية لانتقال الحرارة المتغير مع الزمن خلال مادة كروية مجوفة عازلة للحرارة ذات خاصية توصيل حراري متغير مع درجة الحرارة مأخوذة من معادلة مختبريه متوفرة باستخدام تحويل كرشوف. تم افتراض إن هذه المادة العازلة كانت في البداية بدرجة حرارة منتظمة وثابتة. ثم تعرضت إلى تغير مفاجئ في درجة الحرارة وبقيمة ثابتة عند نصف قطرها الداخلي. تم اختيار أربعة مواد عازلة مختلفة. تم التوصل إلى حل تحليلي مطابق عند المقارنة مع نتائج الحل التحليلي لتوزيع درجات الحرارة للحالات الأربعة بافتراض إن المادة العازلة للحرارة ذو خاصية توصيل حراري ثابتة ولا تتغير مع درجة الحرارة. تم استنتاج إن خواص المادة العازلة للحرارة وقيمة الضغط بين جزيئاتها له تأثير مباشر على مقدار كمية الحرارة المنتقلة وتوزيع درجات الحرارة.

الكلمات الرئيسية: معادلة تفاضلية غير خطية ، حل تحليلي ، توصيل حراري ، متغير مع الزمن ، تحويل كرشوف.

## 1. INTRODUCTION

The characteristics of the thermal insulating materials that are used in air separation plants, storage tanks, transfer lines and transport vessels for cryogenic liquids and liquefied hydrocarbons affect the performance of these applications. Most of these thermal insulations operate under atmospheric or medium vacuum pressure, and it use either Perlite (a loose granulated material of volcanic glass origin heated at 850-900 C° to vaporize the high water content that is trapped in its structure and allowing its volume to be porous and expanded up to 7–16 times its original volume), or mineral fibers in the form of shells or mats (Kropschot and Burges, 1962), (Kaganer, 1969) and (Verschoor and Greebler, 1952). For specific applications, when only a small space is available for thermal insulation, a system of multilayered foils is used in a high vacuum. It is preferred in the field of transfer lines of liquid hydrogen and liquid helium as well as components in the space technology and in the field of physical basic experimental research (Hoffman, 2006). A common property of all cryogenic thermal insulating materials is that it operates under high temperature deference between atmospheric air and cryogenic fluid temperatures. Therefore, filling it inside a vacuumed leak tight annular space separating the atmosphere from cryogenic fluid vessels is necessary to avoid the drop in its efficiency due to the penetration and freeze of water vapor and carbon dioxide.

The sudden filling of an empty cryogenic liquid storage tank initially at atmospheric temperature with a cryogenic liquid at its saturation temperature will initiate a sudden high temperature difference between the terminals of the annular space containing the thermal insulating material. This high temperature difference is behind the dependence of thermal conductivity of the thermal insulation material on its temperature. In addition, it will initiate a potential for the evaporation of cryogenic liquid due to the transient heat transfer

inside the cryogenic liquid storage tank. This energy loss is of a great economic interest especially when the size of cryogenic liquid storage tank is relatively big.

(Zivkovic et al, 2010) have used the PAK-T software package, which is based on the finite element method using the Galerkin approach to solve the non-linear transient two-dimensional heat conduction through an insulation wall of tank for transportation of liquid aluminum. The objective was to optimize, under certain boundary conditions, the thickness of the insulation material which its thermal properties is a temperature dependent.

(Singh, Jain and Rizwan-Uddin, 2008) presented an analytical double-series solution for transient heat conduction in polar coordinates (2-D cylindrical) for multi-layer domain in the radial direction with spatially non-uniform but time-independent volumetric heat sources. Inhomogeneous boundary conditions of the third kind are applied in the direction perpendicular to the layers. Only homogeneous boundary conditions of the first or second kind are applicable on  $\theta =$  constant surfaces.

(Jain, Singh and Rizwan-uddin, 2010) presented an analytical series solution for transient boundary-value problem of heat conduction in  $r - \theta$  spherical coordinates. The proposed solution is applicable in spherical or part-spherical multilayer geometries in which temperature does not depend upon the  $\phi$  direction such as: spherical cone, hemisphere, spherical wedge or full sphere. Spatially non-uniform, (only  $r$  and  $\theta$  -dependent), time independent volumetric heat sources may be present in the layers. Inhomogeneous, time independent,  $\theta$ -dependent boundary conditions of the first, second or third kind may be applied on the inner and outer radial boundaries, and only homogenous boundary conditions of the first or second kind may be applied on the  $\theta$ -direction boundary surfaces.

(Amiri, Kayhani and Norouzi, 2012) have investigated analytically the unsteady heat conduction in composite fiber winded cylindrical shape laminates. This solution is valid for the most generalized boundary conditions that combine the effects of conduction, convection and radiation both inside and outside the cylindrical composite laminates. The Laplace transformation has been used to change the problem domain from time into frequency. An appropriate Fourier transformation has been derived using the Sturm-Liouville theorem. Due to the difficulty of applying the inverse Laplace transformation, the Meromorphic function method is utilized to find the transient temperature distribution in laminate.

In this paper, the one-dimensional, spherical coordinate, non-linear partial differential equation of transient heat conduction through a hollow spherical thermal insulation material of a thermal conductivity temperature dependent property proposed by an available empirical function ( $k = a + bT^c$ ), (Hoffman, 2006), is solved analytically using Kirchoff's transformation. This insulating material is initially at a uniform temperature ( $T_i$ ). Then, it is suddenly subjected at its internal radius ( $r = R_1$ ) with a constant temperature ( $T_o$ ), ( $T_o < T_i$ ). Four thermal insulation materials were selected, (Hoffman, 2006), each of outside radius of (1m). The first is Perlite of thickness (500mm) with a characteristic mean particle diameter of ( $d_m = 0.5mm$ ) and density of ( $\rho = 64kg/m^3$ ) at ( $10^5 Pa$ ) atmospheric pressure. The second is Perlite of thickness (300mm) with a characteristic mean particle diameter of ( $d_m = 0.5mm$ ) and density of ( $\rho = 50kg/m^3$ ) at a gas pressure ( $\leq 0.1Pa$ ). The third is Microglass spheres of thickness (200mm) with a characteristic mean particle diameter of ( $d_m = 0.1mm$ ) and density of ( $\rho = 225kg/m^3$ ) at a gas pressure ( $\leq 1Pa$ ).

The fourth is micro fine Fiberglass mats of thickness (100mm) with a mean fiber diameter of ( $d_m = 1.143\mu m$ ) and density of ( $\rho = 240kg/m^3$ ) at a gas pressure ( $\leq 1Pa$ ). To validate the results, the temperature distribution will be compared with an available analytical solution for the same four case studies that assume a constant thermal conductivity. A summary table will present the general analytical solution for the history of temperature profiles and heat transfer rates of any size and type of thermal insulation material that is subjected at ( $r = R_1$ ) with a constant temperature ( $T_o$ ), ( $T_o < T_i$ ).

## 2. STATEMENT OF THE PROBLEM

Consider a spherical storage tank of liquefied cryogenic fluid is thermally insulated with a hollow spherical super insulating material of temperature dependent thermal conductivity proposed by an available empirical function ( $k = a + bT^c$ ), and of inside radius ( $R_1$ ) and outside radius ( $R_2$ ). This insulating material is initially at a uniform temperature ( $T_i$ ). Then, it is suddenly subjected at ( $r = R_1$ ) with a constant temperature ( $T_o$ ), ( $T_o < T_i$ ) as shown in **Fig. 1**. It is required to find the transient temperature distribution of the insulating material and the rate of heat transfer.

## 3. ANALYTICAL SOLUTION

To solve this problem, the following assumptions are considered:

1. The temperature is a function of ( $r, t$ ) only, (Transient, One-dimensional solution), and no heat transfer in ( $\theta$  and  $\phi$ ) directions.
2. The temperature dependant thermal conductivity of the insulating material is proposed by an available empirical function ( $k = a + bT^c$ ).

3. The mean specific heat capacity ( $C_m$ ) and the density ( $\rho$ ) of the insulating material are temperature independent properties.
4. The initial temperature of the insulating material is constant ( $T_i$ ).
5. The insulating material is suddenly subjected at ( $r = R_1$ ) with a constant temperature ( $T_o$ ) and held at its initial temperature value ( $T_i$ ) at its outside surface at ( $r = R_2$ ).
6. No convection or radiation heat transfer at the boundaries.
7. No internal heat generation.

Since all of the thermal properties of the insulating material are temperature independent except for the thermal conductivity, which is a temperature dependent property, and there is no heat generation and no convection or radiation heat transfer at the boundaries. Therefore, the spherical coordinates, one-dimensional, non-linear transient heat conduction partial differential equation, with its initial and Dirichlet boundary condition are given as follows:

$$\left. \begin{aligned} \rho C_m \frac{\partial T}{\partial t} &= \frac{1}{r^2} \frac{\partial}{\partial r} \left( r^2 k(T) \frac{\partial T}{\partial r} \right) \\ T(r,0) &= T_i \\ T(R_1,t) &= T_o \\ T(R_2,t) &= T_i \end{aligned} \right\} \quad (1)$$

To linearize the non-linear partial differential equation in system (1), a corrected Kirchoff's transformation in accordance to the zero lower limit of the absolute temperature scale, as shown in **Fig. 2**, is used as follows:

$$\psi = \int_0^{T^{**}} k(T) dT \quad (2)$$

Substituting eq. (2) into system (1) and rearranging yields;

$$\left. \begin{aligned} \rho C_m \frac{1}{k(T)} \frac{\partial \psi}{\partial t} &= \frac{1}{r^2} \frac{\partial}{\partial r} \left( r^2 \frac{\partial \psi}{\partial r} \right) \\ \psi(r,0) &= \psi_i \\ \psi(R_1,t) &= \psi_o \\ \psi(R_2,t) &= \psi_i \end{aligned} \right\} \quad (3)$$

$$\begin{aligned} \psi_i &= \int_0^{T_i} k(T) dT \\ \mu_i &= \int_{T_i}^{T_o} k(T) dT \\ \psi_o &= \psi_i + \mu_i \end{aligned}$$

To homogenize system (3), assume;

$$\beta = \psi - \psi_i \quad (4)$$

Substitute eq. (4) into system (3) and rearranging, yields;

$$\left. \begin{aligned} \rho C_m \frac{1}{k(T)} \frac{\partial \beta}{\partial t} &= \frac{1}{r^2} \frac{\partial}{\partial r} \left( r^2 \frac{\partial \beta}{\partial r} \right) \\ \beta(r,0) &= 0 \\ \beta(R_1,t) &= \mu_i \\ \beta(R_2,t) &= 0 \end{aligned} \right\} \quad (5)$$

To eliminate the ( $r^2$ ) term in system (5), assume;

$$\beta = \frac{\theta}{r} \quad (6)$$

Substitute eq. (6) into system (5) and rearranging, yields;



$$\left. \begin{aligned} \frac{1}{\alpha_m} \frac{\partial \theta}{\partial t} &= \frac{\partial^2 \theta}{\partial r^2} \\ \theta(r,0) &= 0 \\ \theta(R_1,t) &= R_1 \mu_i \\ \theta(R_2,t) &= 0 \end{aligned} \right\} \quad (7)$$

$$\alpha_m = \frac{k_m}{\rho C_m} \int_{T_i}^{T_o} k(T) dT$$

$$k_m = \frac{\int_{T_i}^{T_o} k(T) dT}{T_o - T_i} = \frac{\mu_i}{T_o - T_i}$$

$$C_m = \frac{\int_{T_i}^{T_o} C(T) dT}{T_o - T_i}$$

To solve system (7), assume the following:

$$\theta(r,t) = \theta_1(r) + \theta_2(r,t) \quad (8)$$

$$\theta_1(r) = c_1 r + c_2 \quad (9)$$

Substitute the boundary conditions of system (7) into eq. (9) and rearranging, yields;

$$\theta_1(r) = R_1 \mu_i \frac{R_2 - r}{R_2 - R_1} \quad (10)$$

Assume;

$$\theta_2(r,t) = R(r)\tau(t) \quad (11)$$

Substituting eq. (11) into system (7) and using the method of separation of variables, then rearranging, yields;

$$R(r) = c_1 \cos(\lambda r) + c_2 \sin(\lambda r) \quad (12)$$

$$\tau(t) = c_3 e^{-\lambda^2 \alpha_m t} \quad (13)$$

Substitute eq. (10), (12) and (13) into eq. (8), yields;

$$\theta(r,t) = R_1 \mu_i \left( \frac{R_2 - r}{R_2 - R_1} \right) + \quad (14)$$

$$[c_1 \cos(\lambda r) + c_2 \sin(\lambda r)] c_3 e^{-\lambda^2 \alpha_m t}$$

Substitute the boundary condition of system (7) into eq. (14) and rearranging, yields;

$$\theta(r,t) = R_1 \mu_i \left( \frac{R_2 - r}{R_2 - R_1} \right) - \quad (15)$$

$$\sum_{n=1}^{\infty} b_n \left\{ \frac{\sin[\lambda_n (r - R_1)]}{\sin(\lambda_n R_1)} \right\} e^{-\lambda_n^2 \alpha_m t}$$

$$\lambda_n = \frac{n\pi}{R_2 - R_1}, \quad n = 0, 1, 2, \dots, \infty \quad (16)$$

$$b_n = \frac{2R_1}{n\pi} \mu_i \sin\left(n\pi \frac{R_1}{R_2 - R_1}\right) \quad (17)$$

Substitute eq. (16) and (17) into eq. (15), yields;

$$\theta(r,t) = R_1 \mu_i \cdot$$

$$\left[ \left( \frac{R_2 - r}{R_2 - R_1} \right) - \sum_{n=1}^{\infty} \frac{2}{n\pi} \sin\left(n\pi \frac{r - R_1}{R_2 - R_1}\right) e^{-\left(\frac{n\pi}{R_2 - R_1}\right)^2 \alpha_m t} \right]$$

Since;

$$\beta(r,t) = \frac{\theta(r,t)}{r} = \psi(r,t) - \psi_i$$

$$\frac{\psi(r,t) - \psi_i}{\mu_i} = \frac{R_1}{r}$$

$$\left[ \left( \frac{R_2 - r}{R_2 - R_1} \right) - \sum_{n=1}^{\infty} \frac{2}{n\pi} \sin\left(n\pi \frac{r - R_1}{R_2 - R_1}\right) e^{-\left(\frac{n\pi}{R_2 - R_1}\right)^2 \alpha_m t} \right]$$

Assume;

$$\phi(r,t) = \frac{R_1}{r} \left[ \left( \frac{R_2 - r}{R_2 - R_1} \right) - \sum_{n=1}^{\infty} \frac{2}{n\pi} \sin\left(n\pi \frac{r - R_1}{R_2 - R_1}\right) e^{-\left(\frac{n\pi}{R_2 - R_1}\right)^2 \alpha_m t} \right]$$

The unsteady heat transfer through the spherical thermal insulation material is given as:

$$q(r,t) = -\left(-k(T)A_{(r)} \frac{\partial T(r,t)}{\partial r}\right) \quad (21)$$

$$\frac{\int_0^T k(T)dT - \int_0^{T_i} k(T)dT}{\int_{T_i}^{T_o} k(T)dT} = \frac{R_1}{r} \quad (18)$$

$$A_{(r)} = 4\pi r^2 \quad (22)$$

Differentiating eq. (18) and rearranging, yields:

$$\left[ \left( \frac{R_2 - r}{R_2 - R_1} \right) - \sum_{n=1}^{\infty} \frac{2}{n\pi} \sin\left(n\pi \frac{r - R_1}{R_2 - R_1}\right) e^{-\left(\frac{n\pi}{R_2 - R_1}\right)^2 \alpha_m t} \right]$$

$$\frac{\partial T(r,t)}{\partial r} = -\left(\frac{R_1}{r^2}\right) \cdot \left[ \frac{\int_{T_i}^{T_o} k(T)dT}{k(T)} \right]$$

To normalize eq. (18), assume the following:

$$\left. \begin{aligned} \xi &= \frac{R_2}{R_1} \\ r^* &= \frac{r - R_1}{R_2 - R_1} \\ Fo &= \frac{\alpha_m t}{R_1^2} \end{aligned} \right\} \quad (19)$$

$$\left[ \frac{R_2}{R_2 - R_1} + 2 \sum_{n=1}^{\infty} \left[ \frac{\cos\left(n\pi \frac{r - R_1}{R_2 - R_1}\right)}{\left(\frac{R_2 - R_1}{r}\right)} - \frac{\sin\left(n\pi \frac{r - R_1}{R_2 - R_1}\right)}{n\pi} \right] e^{-\left(\frac{n\pi}{R_2 - R_1}\right)^2 \alpha_m t} \right] \quad (23)$$

Substitute eq. (22) and (23) into eq. (21), and rearrange, yields:

Hence, substituting eq. (19) into eq. (18) and rearrange, yields the general analytical close form solution of unsteady temperature distribution through the spherical thermal insulation material as follows;

$$q(r,t) = -4\pi R_1 \cdot \left[ \int_{T_i}^{T_o} k(T)dT \right]$$

$$T^* = \frac{\int_0^T k(T)dT - \int_0^{T_i} k(T)dT}{\int_{T_i}^{T_o} k(T)dT} = \left[ \frac{-(r^* - 1)}{r^*(\xi - 1) + 1} \right] \quad (20)$$

$$\left[ \frac{R_2}{R_2 - R_1} + 2 \sum_{n=1}^{\infty} \left[ \frac{\cos\left(n\pi \frac{r - R_1}{R_2 - R_1}\right)}{\left(\frac{R_2 - R_1}{r}\right)} - \frac{\sin\left(n\pi \frac{r - R_1}{R_2 - R_1}\right)}{n\pi} \right] e^{-\left(\frac{n\pi}{R_2 - R_1}\right)^2 \alpha_m t} \right] \quad (24)$$

$$\left[ 1 + \sum_{n=1}^{\infty} \frac{2}{n\pi(r^* - 1)} \sin(n\pi r^*) e^{-\left(\frac{n\pi}{\xi - 1}\right)^2 Fo} \right]$$



To normalize eq. (24), substituting eq. (19) into (24) and rearrange, yields:

$$q = -4\pi R_1 \left[ \int_{T_i}^{T_o} k(T) dT \right] \left( \frac{2}{\xi - 1} \right) \left[ \frac{\frac{\xi}{2} + \sum_{n=1}^{\infty} \left[ \frac{(r^*(\xi - 1) + 1) \cos(n\pi r^*)}{\left( \frac{\xi - 1}{n\pi} \right) \sin(n\pi r^*)} \right] e^{-\left( \frac{n\pi}{\xi - 1} \right)^2 Fo}} \right] \quad (25)$$

And the heat transfer at the inner surface of the thermal insulation material ( $r^* = 0$ ) is given as:

$$q_o = -4\pi R_1 \left[ \int_{T_i}^{T_o} k(T) dT \right] \left( \frac{2}{\xi - 1} \right) \left[ \frac{\xi}{2} + \sum_{n=1}^{\infty} e^{-\left( \frac{n\pi}{\xi - 1} \right)^2 Fo} \right]$$

The general analytical close form solution of unsteady heat transfer through the spherical thermal insulation material is given as follows:

$$\frac{q}{q_o} = \frac{\frac{\xi}{2} + \sum_{n=1}^{\infty} \left[ \frac{(r^*(\xi - 1) + 1) \cos(n\pi r^*)}{\left( \frac{\xi - 1}{n\pi} \right) \sin(n\pi r^*)} \right] e^{-\left( \frac{n\pi}{\xi - 1} \right)^2 Fo}}{\frac{\xi}{2} + \sum_{n=1}^{\infty} e^{-\left( \frac{n\pi}{\xi - 1} \right)^2 Fo}}$$

**3.1 Case study (1):  $k(T) = k_m$**

**3.1.1 Temperature profile:**

Substitute the value of ( $k_m$ ) into eq. (20) and rearranging, yields;

$$\frac{T - T_i}{T_o - T_i} = \left[ \frac{-(r^* - 1)}{r^*(\xi - 1) + 1} \right] \left[ 1 + \sum_{n=1}^{\infty} \frac{2}{n\pi(r^* - 1)} \sin(n\pi r^*) e^{-\left( \frac{n\pi}{\xi - 1} \right)^2 Fo} \right]$$

**3.1.2 Heat transfer:**

Substitute the value of ( $k_m$ ) into eq. (25) and rearranging, yields;

$$q = 4\pi R_1 k_m (T_i - T_o) \left( \frac{2}{\xi - 1} \right) \left[ \frac{\xi}{2} + \sum_{n=1}^{\infty} \left[ \frac{(r^*(\xi - 1) + 1) \cos(n\pi r^*)}{\left( \frac{\xi - 1}{n\pi} \right) \sin(n\pi r^*)} \right] e^{-\left( \frac{n\pi}{\xi - 1} \right)^2 Fo} \right]$$

**3.2 Case study (2):  $k(T) = a + bT^c$**

**3.2.1 Temperature profile:**

Substitute the value of ( $k(T) = a + bT^c$ ) into eq. (20) and rearranging, yields;

$$\frac{\left[ aT + \frac{b}{c+1} T^{c+1} \right] - \left[ aT_i + \frac{b}{c+1} T_i^{c+1} \right]}{\left[ aT_o + \frac{b}{c+1} T_o^{c+1} \right] - \left[ aT_i + \frac{b}{c+1} T_i^{c+1} \right]} = \eta$$

Where:

$$\eta = \left[ \frac{-(r^* - 1)}{r^*(\xi - 1) + 1} \right] \left[ 1 + \sum_{n=1}^{\infty} \frac{2}{n\pi(r^* - 1)} \sin(n\pi r^*) e^{-\left( \frac{n\pi}{\xi - 1} \right)^2 Fo} \right] \quad (26)$$

To solve eq. (26), assume;

$$g(T) = aT + \frac{b}{c+1} T^{c+1} \quad f = [g(T) - g(T_i)] - \eta [g(T_o) - g(T_i)] \quad (27)$$

The root T of eq. (27) is found using the approximate numerical iterative Newton Method, (Gerald, 1989);

$$f' = \frac{df}{dT} = \frac{dg(T)}{dT} = k(T)$$

$$T_{new} = T_{old} - \frac{f_{old}}{f'_{old}}$$

$$T_{new} = T_{old} - \frac{[g(T_{old}) - g(T_i)] - \eta[g(T_o) - g(T_i)]}{k(T_{old})}$$

**3.2.2 Heat transfer:**

Substitute the value of  $(k(T) = a + bT^c)$  into eq. (25) and rearranging, yields;

$$q = 4\pi R_1 \cdot [g(T_i) - g(T_o)] \cdot \left(\frac{2}{\xi - 1}\right).$$

$$\left[ \frac{\xi}{2} + \sum_{n=1}^{\infty} \left[ \frac{(\xi - 1)}{n\pi} \sin(n\pi r^*) \right] \right] e^{-\left(\frac{n\pi}{\xi - 1}\right)^2 Fo}$$

**4. THERMAL CONDUCTIVITY**

The dependence of thermal conductivity on temperature is suggested by the empirical function  $(k = a + bT^c)$ , (Hoffman, 2006). The values of  $(a, b, c)$  for the four selected thermal insulation materials are given in **Table 1**. This empirical function is valid in a temperature range of  $(77 - 400 K)$ . The thermal conductivity of the first insulation material, Perlite in air at  $(10^5 Pa)$  atmospheric pressure, is linearly dependent on temperature, (Perlite Institute Thermal Data Sheet, 1970). In the literatures (Christiansen and Hollingworth, 1958) and (Christiansen, Hollingworth and Marsh, 1959), measurements of the thermal conductivity of micro fine Fiberglass mats are published. This material consists of fibers type ‘AA’ of Owens-Corning Fiberglass Corporation. The behavior of the thermal conductivity and its mean value for each of these thermal insulating materials for a temperature range of  $(77 - 300 K)$  is shown in **Fig. 3**.

**5. SPECIFIC HEAT CAPACITY**

Each of the four selected thermal insulation materials is originally made from

Quartz glass. Therefore, the temperature dependence of specific heat capacity of Quartz glass for a temperature range of  $(77 - 300 K)$  is given in **Table 2**, (Corruccini and Gniewek, 1960). In order to evaluate the mean value of specific heat capacity  $(C_m)$  of Quartz glass, its relation with temperature is represented using a 4<sup>th</sup> Degree polynomial fit as shown in **Table 3** and it is plotted with its mean value in **Fig. 4**.

**6. THERMAL DIFFUSIVITY**

The behavior of thermal diffusivity and its mean value for each of the four selected thermal insulation materials for a temperature range of  $(77 - 300 K)$  is shown in **Fig. 5**.

**7. RESULTS AND DISCUSSION**

Consider four empty spherical storage tanks of liquid nitrogen for instance. Each of these tanks is thermally insulated with a hollow spherical super insulating material of outside radius  $(R_2 = 1m)$  and initially at  $(T_i = 300 K)$ . The first thermal insulation material is Perlite of thickness  $(500mm)$  with a characteristic mean particle diameter of  $(d_m = 0.5mm)$  and density of  $(\rho = 64kg/m^3)$  at  $(10^5 Pa)$  atmospheric pressure. The second is Perlite of thickness  $(300mm)$  with a characteristic mean particle diameter of  $(d_m = 0.5mm)$  and density of  $(\rho = 50kg/m^3)$  at a gas pressure  $(\leq 0.1 Pa)$ . The third is Microglass spheres of thickness  $(200mm)$  with a characteristic mean particle diameter of  $(d_m = 0.1mm)$  and density of  $(\rho = 225kg/m^3)$  at a gas pressure  $(\leq 1 Pa)$ . The fourth is micro fine Fiberglass mats of thickness  $(100mm)$  with a mean fiber diameter of  $(d_m = 1.143\mu m)$  and density of

( $\rho = 240 \text{ kg/m}^3$ ) at a gas pressure ( $\leq 1 \text{ Pa}$ ). The thermal conductivity of the four selected thermal insulation materials is temperature dependent and is proposed by an available empirical function ( $k = a + bT^c$ ), (Hoffman, 2006). The values of ( $a, b, c$ ) are given in **Table 1**. Then, each of these tanks is suddenly filled with saturated liquid nitrogen at ( $T_o = 77 \text{ K}$ ). Therefore, each of the four selected thermal insulation materials is subjected at ( $r = R_1$ ) with a constant temperature of ( $T_o = 77 \text{ K}$ ).

**Fig. 6** shows the temperature profiles for each of the four selected thermal insulation materials for two case studies. The first considers a constant mean value of thermal conductivity ( $k_m$ ) for the temperature range ( $77 - 300 \text{ K}$ ). The general analytical close form solution of the first case study is identical to the solution of (Carslaw and Jaeger, 1959) using the same assumptions. Therefore, the validation of the analytical solution is accomplished perfectly. The second case study is for a temperature dependent thermal conductivity proposed by an available empirical function ( $k = a + bT^c$ ), (Hoffman, 2006). Each profile of the second case study was converged after a maximum of 5 iterations for a temperature residual value of ( $1 \times 10^{-6} \text{ C}^\circ$ ). **Table 4** shows the summary of the present work analytical solutions for both case studies.

**Fig. 7** shows the heat transfer profiles for each of the four selected thermal insulation materials. It is clear that the thermal insulation material that has the lowest value of thermal conductivity has the lowest heat transfer value. **Table 4** shows the summary of the present work analytical solutions.

For both **Fig. 6 and 7**, it is clear that the characteristics of the thermal insulation material and the pressure value between its particles have a major effect on the rate of heat transfer and consequently the temperature profile. For instance, the

dominant heat transfer mode when choosing Perlite at ( $10^5 \text{ Pa}$ ) atmospheric pressure is by heat conduction of the interstitial gas between the particles, whereas the heat transfer by radiation is negligible. When the pressure within a thermal insulation material is lowered to a value, the percentage of heat transfer by heat conduction of the interstitial gas between the particles becomes negligibly small when compared with the percentage heat transfer by radiation and conduction over the bulk material. The gas pressure, at which this is reached, depends on the characteristic diameter of the thermal insulation material. For Perlite with a characteristic mean particle diameter of ( $d_m = 0.5 \text{ mm}$ ), a gas pressure of ( $\leq 0.1 \text{ Pa}$ ) is sufficient, for Microglass spheres with a characteristic mean particle diameter of ( $d_m = 0.1 \text{ mm}$ ) and for micro fine Fiberglass with a mean fiber diameter of ( $d_m = 1.143 \mu\text{m}$ ), it is ( $\leq 1 \text{ Pa}$ ) respectively.

**Figures 8 and 9** shows the time history of temperature profiles and rate of heat transfer for each of the four selected thermal insulation materials for a temperature dependent thermal conductivity proposed by an available empirical function ( $k = a + bT^c$ ), (Hoffman, 2006).

The general analytical solution for the history of temperature profiles and heat transfer rates of any size and type of thermal insulation material that is subjected to the assumptions that are listed in article (3) is given in **Table 4** and is plotted in **Fig. 10 and 11** respectively.

## 8. CONCLUSIONS

The optimum selection of thermal insulating material for a specific spherical storage tank of liquefied cryogenic fluid is that with a minimum heat leakage (minimum boil off rate of cryogenic fluid), a minimum amount of insulating material (minimum cost) and a maximum storage capacity of the storage tank (minimum thickness of the thermal insulating material). This optimum selection is accomplished

when choosing the micro fine Fiberglass mats when compared with the three other thermal insulating materials. On the other hand, it is found that the characteristics of the thermal insulation material and the pressure value between its particles have a major effect on the rate of heat transfer and temperature profile. The dominant mode of heat transfer when choosing a specific thermal insulation material at atmospheric pressure is by heat conduction of the interstitial gas between its particles, whereas the heat transfer by radiation is negligible. When the pressure within a thermal insulation material is lowered to a vacuum level, the percentage of heat transfer by heat conduction of the interstitial gas between its particles becomes negligibly small when compared with the percentage heat transfer by radiation and conduction over the bulk material.

#### **ACKNOWLEDGEMENTS**

The author would like to thank Mr. Hofmann A., "A formerly Linde AG, Geschäftsbereich LE, Germany", for his valuable technical details during email communications. Without his contribution, this paper could not be done.

#### **REFERENCES**

Amiri D.A., Kayhani M.H., Norouzi M., Exact analytical solution of unsteady axisymmetric conductive heat transfer in cylindrical orthotropic composite laminates, International journal of heat and mass transfer, ELSEVIER, 55, 4427-4436, 2012.

Carslaw H.S. and Jaeger J.C., Conduction of Heat in Solids, 2<sup>nd</sup> ed., Oxford University Press, New York, 1959.

Christiansen R.M. and Hollingworth Jr.M., The performance of glass fiber insulation under high vacuum, Adv. Cryogen Eng., 1958(4):S141.

Christiansen R.M., Hollingworth Jr.M. and Marsh Jr.H.N., Low temperature insulation systems, Adv. Cryogen Eng., 1959(5).

Corruccini R.J. and Gniewek J.J., Specific Heats and Enthalpies of Technical Solids at Low Temperatures, NBS Monograph, 21, 1960.

Gerald C.F. and Wheatley P.O., Applied Numerical Analysis, 4<sup>th</sup> ed., Addison-Wesley, New York, 1989.

Hofmann A., The thermal conductivity of cryogenic insulation materials and its temperature dependence, Elsevier, Cryogenics, 46, 815-824, 2006.

Jain P.K., Singh S. and Rizwan-uddin, An exact analytical solution for two-dimensional, unsteady, multilayer heat conduction in spherical coordinates, International journal of heat and mass transfer, ELSEVIER, 53, 2133-2142, 2010.

Kaganer, Thermal Insulation in Cryogenic Engineering, Israel Program for Scientific Translations, 1969.

Kropschot R.H. and Burges R.W., Perlite for cryogenic insulation, Adv. Cryogen Eng., 1962(8):S425.

Perlite Institute New York, Thermal Data Sheet No. 2-4, 1970.

Singh S., Jain P.K., Rizwan-Uddin, Analytical solution to transient heat conduction in polar coordinates with multiple layers in radial direction, International journal of thermal sciences, ELSEVIER, 47, 261-273, 2008.

Verschoor and Greebler, Heat transfer by gas conduction and radiation in fibrous insulations, Transactions of ASME Paper No. 51-A54, 1952.



Zivkovic M.M., Nikolic A.V., Slavkovic R.B. and Zivic F.T., Non-Linear transient heat conduction analysis of insulation wall of tank for transportation of liquid Aluminum, Thermal Science, Vol. 14, Suppl., S299-S312, 2010.

### NOMENCLATURE

A	Cross section area, $m^2$
C	Specific heat Capacity, $kJ/kg.K$
d	Particle diameter, mm
Fo	Fourier number
k	Thermal conductivity, $W/m.K$
q	Rate of heat transfer, W
r	Distance along the r-direction, m
$R_1, R_2$	Inner, outer radius, respectively, m
T	Temperature, K
t	Time, second

### GREEK SYMBOLS

$\alpha$	Thermal diffusivity, $m^2/s$
$\beta$	Area under the Kirchhoff's transformation curve, $W/m$
$\phi$	Dimensionless parameter
$\eta$	Dimensionless parameter
$\lambda_n$	Root values of equation (16), $m^{-1}$
$\mu$	Area under the Kirchhoff's transformation curve, $W/m$
$\theta$	Parameter, W
$\rho$	Density, $kg/m^3$
$\xi$	Ratio of outer to inner radius
$\psi$	Area under the Kirchhoff's transformation curve, $W/m$

### SUBSCRIPTS

<i>i</i>	Initial
<i>m</i>	Mean
<i>o</i>	Inner surface

### SUPERSCRIPTS

*	Dimensionless sign
**	Arbitrary

**Table 1 Suggested empirical function and constant values for the selected thermal insulation materials, (Hoffman, 2006).**

Insulating material	Empirical function ( $k = a + bT^c$ ), (W/m.K)		
	<i>a</i>	<i>b</i>	<i>c</i>
Perlite in air $\rho = 64 \text{ kg / m}^3, d_m = 0.5 \text{ mm}, p = 10^5 \text{ Pa}$	$8.25 \times 10^{-3}$	$1.165 \times 10^{-4}$	1.0
Perlite - vacuum $\rho = 50 \text{ kg / m}^3, d_m = 0.5 \text{ mm}, p \leq 0.1 \text{ Pa}$	$1.9112 \times 10^{-4}$	$3.4757 \times 10^{-12}$	3.678
Microglass spheres – vacuum $\rho = 225 \text{ kg / m}^3, d_m = 0.1 \text{ mm}, p \leq 1 \text{ Pa}$	$3.7037 \times 10^{-4}$	$7.4041 \times 10^{-11}$	3.0158
Fiberglass – vacuum $\rho = 240 \text{ kg / m}^3, d_m = 1.143 \mu\text{m}, p \leq 1 \text{ Pa}$	$2.7074 \times 10^{-4}$	$3.083 \times 10^{-11}$	3.0

**Table 2 Data values of specific heat capacity for Quartz glass with temperature, (Corruccini and Gniewek, 1960).**

T (K)	50	100	150	200	250	300
C (J/g.K)	0.095	0.21	0.41	0.54	0.65	0.745

**Table 3 Data values for a 4<sup>th</sup> degree polynomial fit of specific heat capacity for quartz glass with temperature.**

$C(T) = \sum_{n=0}^4 \beta_n T^n$ , (J/kg.K)				
$\beta_0$	$\beta_1$	$\beta_2$	$\beta_3$	$\beta_4$
$2.16667 \times 10^2$	-6.485582	$9.92778 \times 10^{-2}$	$-3.9926 \times 10^{-4}$	$5.333 \times 10^{-7}$



Table 4 Summary of analytical solutions.

Case study	Thermal conductivity [W / m.K]	Temperature profile T, [K]	Heat transfer q, [W]
0	$k(T)$	$T^* = \frac{\int_0^r k(T)dT - \int_0^{T_i} k(T)dT}{\int_{T_i}^{T_o} k(T)dT} =$ $\left[ \frac{-(r^* - 1)}{r^*(\xi - 1) + 1} \right] \left[ 1 + \sum_{n=1}^{\infty} \frac{2}{n\pi(r^* - 1)} \sin(n\pi r^*) e^{-\left(\frac{n\pi}{\xi - 1}\right)^2 Fo} \right]$	$\frac{q}{q_o} = \frac{\frac{\xi}{2} + \sum_{n=1}^{\infty} \left[ (r^*(\xi - 1) + 1) \cos(n\pi r^*) - \left(\frac{\xi - 1}{n\pi}\right) \sin(n\pi r^*) \right] e^{-\left(\frac{n\pi}{\xi - 1}\right)^2 Fo}}{\frac{\xi}{2} + \sum_{n=1}^{\infty} e^{-\left(\frac{n\pi}{\xi - 1}\right)^2 Fo}}$
1	$k(T) = k_m$	$\frac{T - T_i}{T_o - T_i} =$ $\left[ \frac{-(r^* - 1)}{r^*(\xi - 1) + 1} \right] \left[ 1 + \sum_{n=1}^{\infty} \frac{2}{n\pi(r^* - 1)} \sin(n\pi r^*) e^{-\left(\frac{n\pi}{\xi - 1}\right)^2 Fo} \right]$	$q = 4\pi R_1 k_m (T_i - T_o) \left( \frac{2}{\xi - 1} \right).$ $\left[ \frac{\xi}{2} + \sum_{n=1}^{\infty} \left[ (r^*(\xi - 1) + 1) \cos(n\pi r^*) - \left(\frac{\xi - 1}{n\pi}\right) \sin(n\pi r^*) \right] e^{-\left(\frac{n\pi}{\xi - 1}\right)^2 Fo} \right]$
2	$k(T) = a + bT^c$	$\frac{\left[ aT + \frac{b}{c+1} T^{c+1} \right] - \left[ aT_i + \frac{b}{c+1} T_i^{c+1} \right]}{\left[ aT_o + \frac{b}{c+1} T_o^{c+1} \right] - \left[ aT_i + \frac{b}{c+1} T_i^{c+1} \right]} =$ $\left[ \frac{-(r^* - 1)}{r^*(\xi - 1) + 1} \right] \left[ 1 + \sum_{n=1}^{\infty} \frac{2}{n\pi(r^* - 1)} \sin(n\pi r^*) e^{-\left(\frac{n\pi}{\xi - 1}\right)^2 Fo} \right]$	$q = 4\pi R_1 \cdot \left\{ \left[ aT_i + \frac{b}{c+1} T_i^{c+1} \right] - \left[ aT_o + \frac{b}{c+1} T_o^{c+1} \right] \right\} \cdot \left( \frac{2}{\xi - 1} \right).$ $\left[ \frac{\xi}{2} + \sum_{n=1}^{\infty} \left[ (r^*(\xi - 1) + 1) \cos(n\pi r^*) - \left(\frac{\xi - 1}{n\pi}\right) \sin(n\pi r^*) \right] e^{-\left(\frac{n\pi}{\xi - 1}\right)^2 Fo} \right]$

Where:  $q_o = -4\pi R_1 \cdot \left[ \int_{T_i}^{T_o} k(T)dT \right] \cdot \left( \frac{2}{\xi - 1} \right) \left[ \frac{\xi}{2} + \sum_{n=1}^{\infty} e^{-\left(\frac{n\pi}{\xi - 1}\right)^2 Fo} \right]$  ,  $\xi = R_2 / R_1$  ,  $r^* = (r - R_1) / (R_2 - R_1)$  ,  $Fo = \alpha_m t / R_1^2$

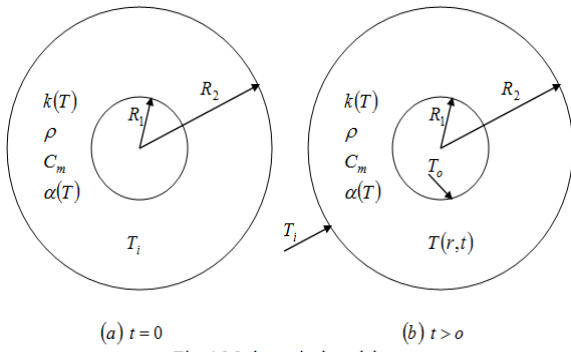


Fig. 1 Mathematical model.

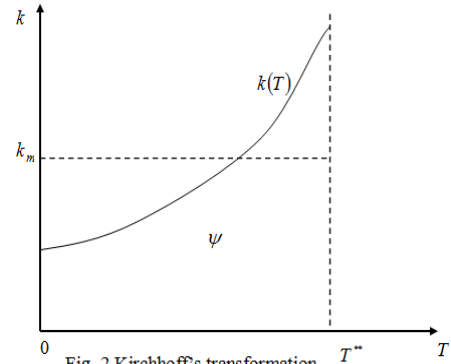


Fig. 2 Kirchhoff's transformation.

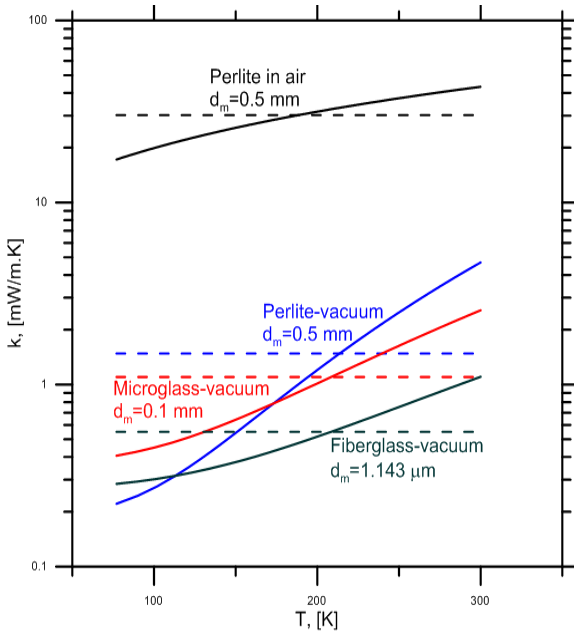


Fig. 3 Thermal conductivity, (Hoffman, 2006)  
 (i) Solid lines  $k(T)=a+bT^c$   
 (ii) Dashed lines  $k(T)=k_m$  (77-300 K)

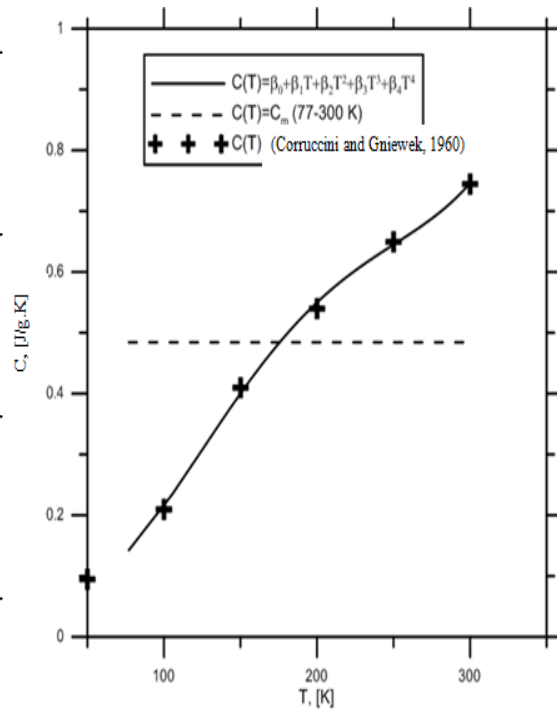


Fig. 4 Specific heat capacity for quartz glass.

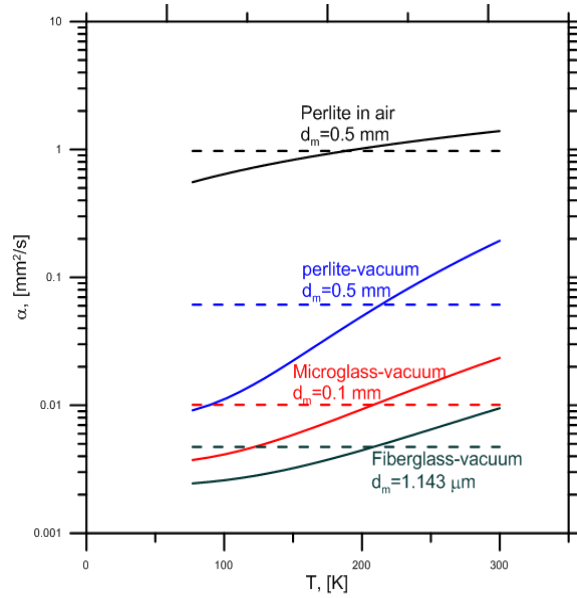


Fig. 5 Thermal diffusivity,  
 (i) Solid lines,  $\alpha(T)=k(T)/\rho C_m$   
 (ii) Dashed lines,  $\alpha(T)=\alpha_m (77-300 \text{ K})$

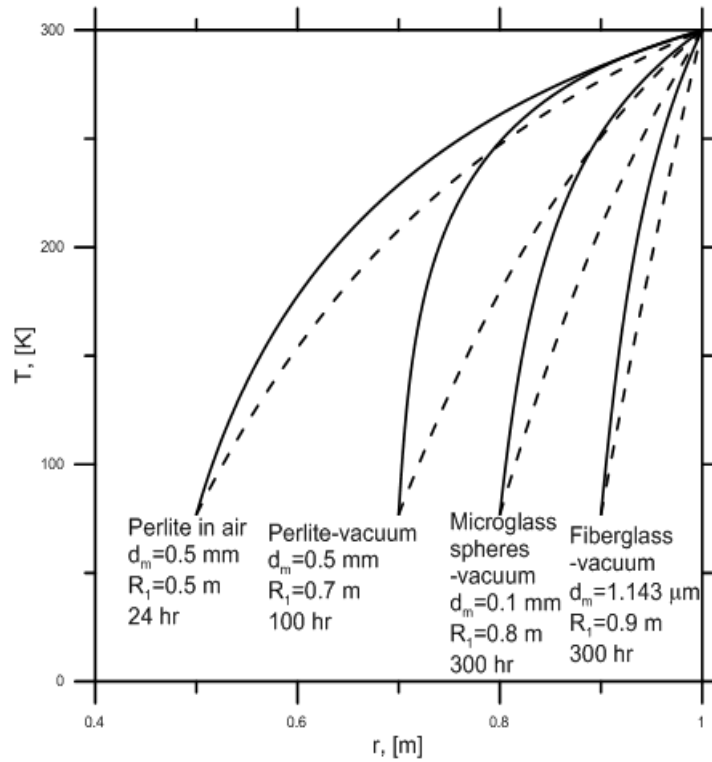


Fig.6 Temperature profiles.  
 (i) Solid lines (present work),  $k(T)=a+bT^c$   
 (ii) Dashed lines (present work and (Carlsaw and Jaeger, 1959)),  $k(T)=k_m (77-300 \text{ K})$ .

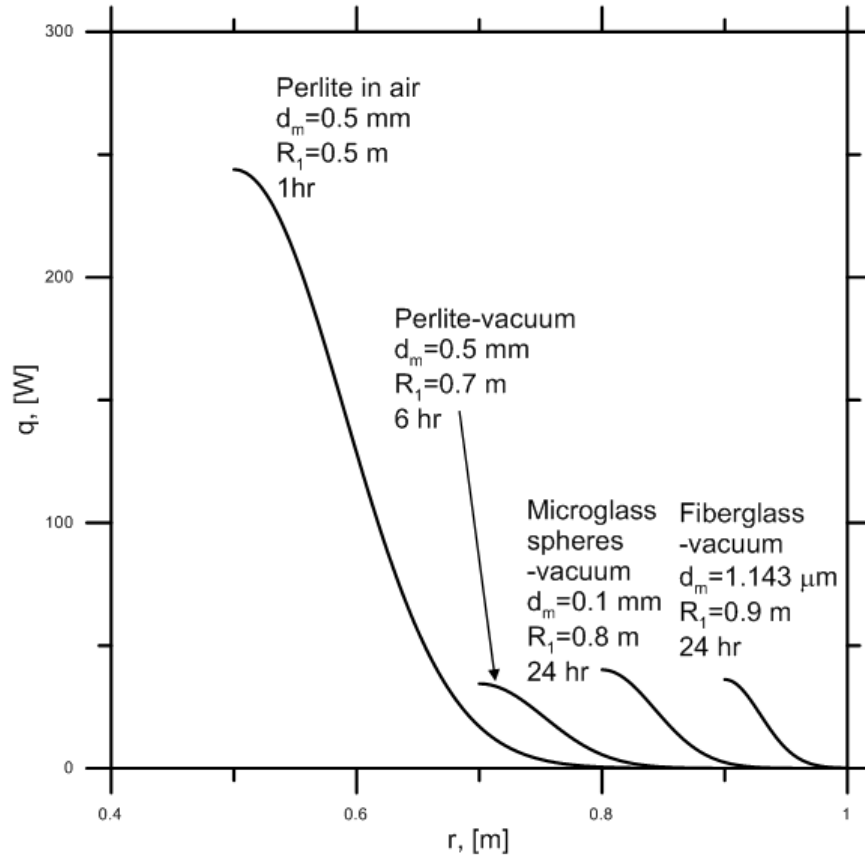


Fig. 7 Heat transfer profiles.

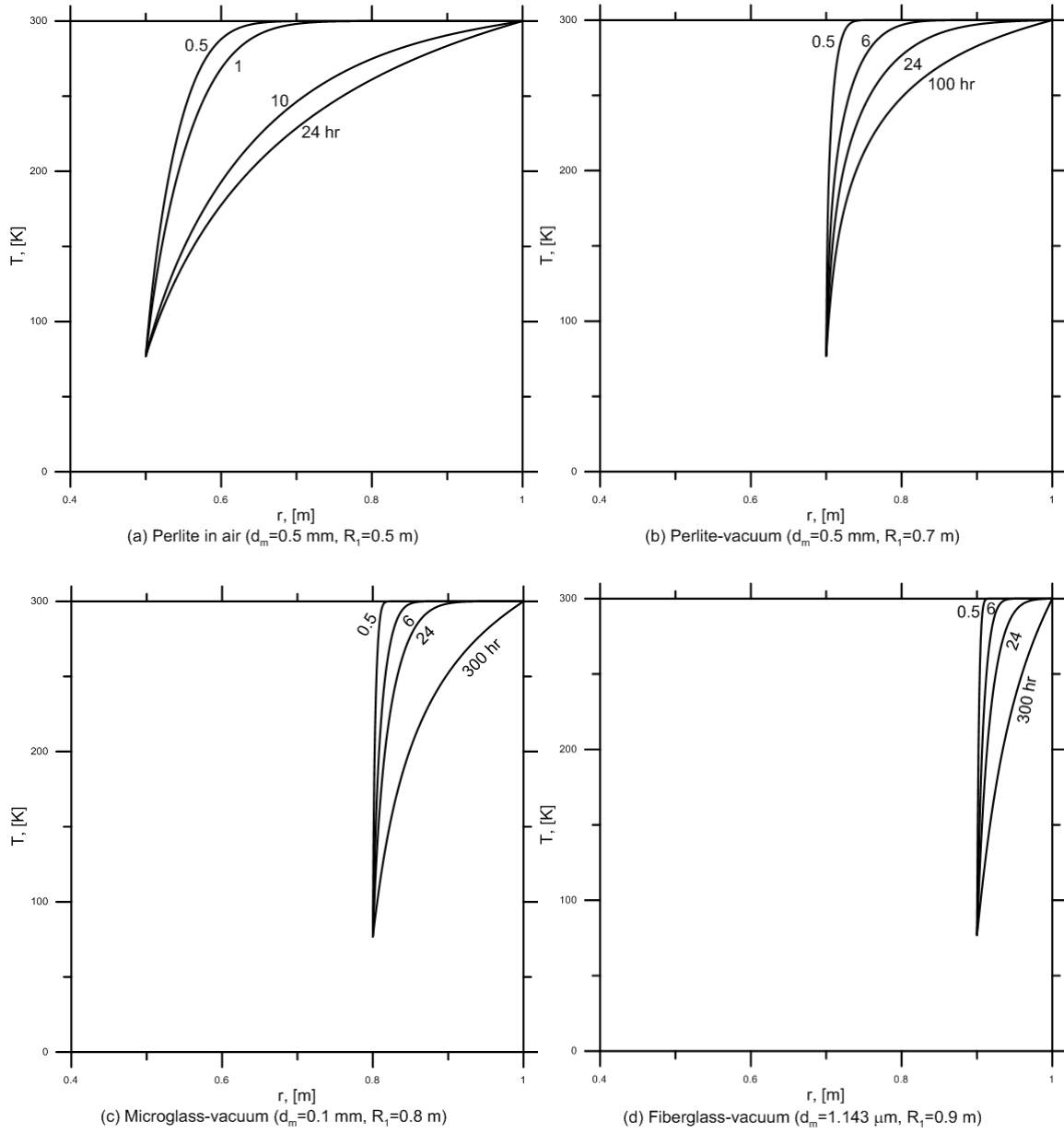
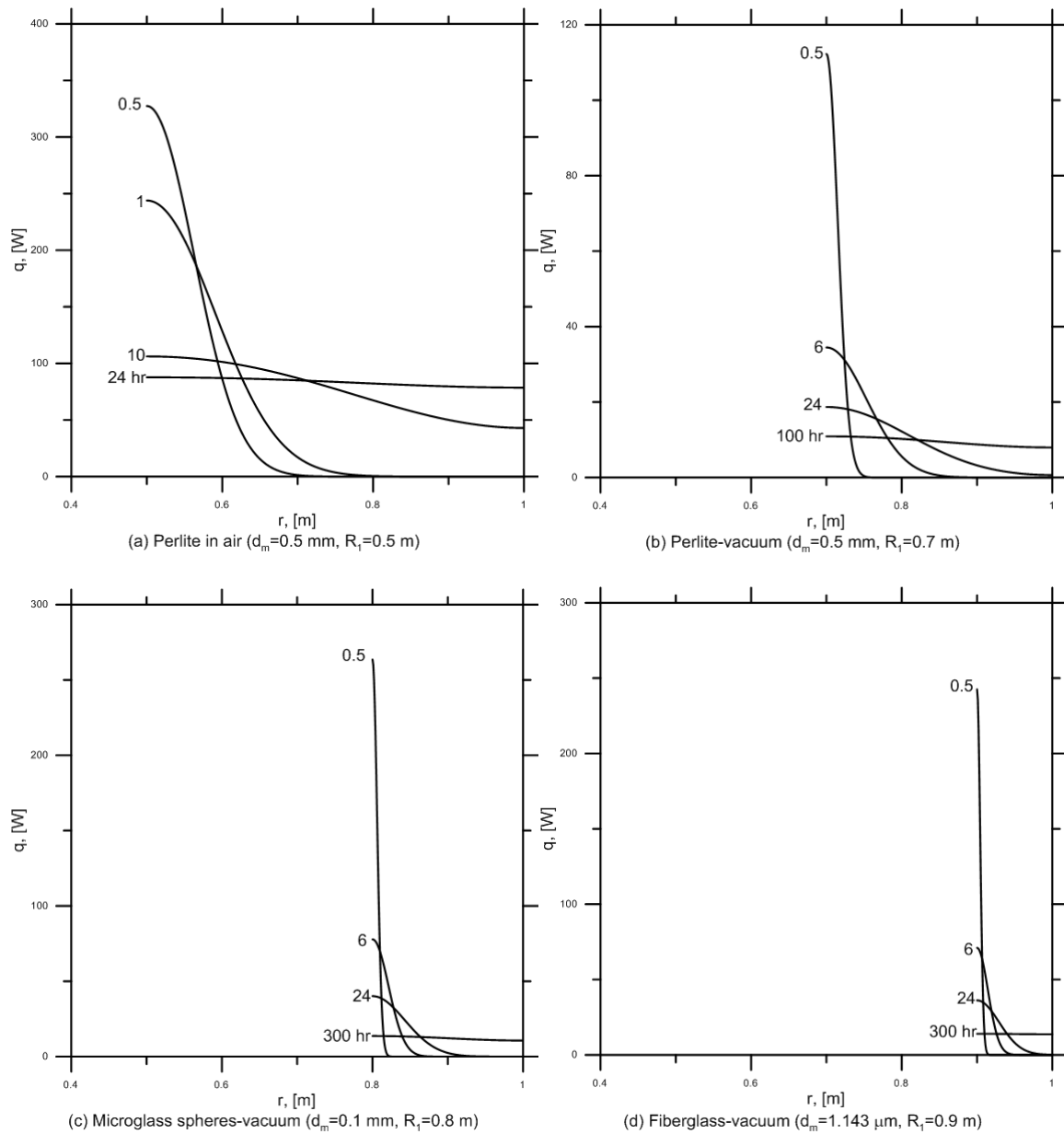


Fig. 8 History of temperature profiles.



**Fig. 9** History of heat transfer profiles.

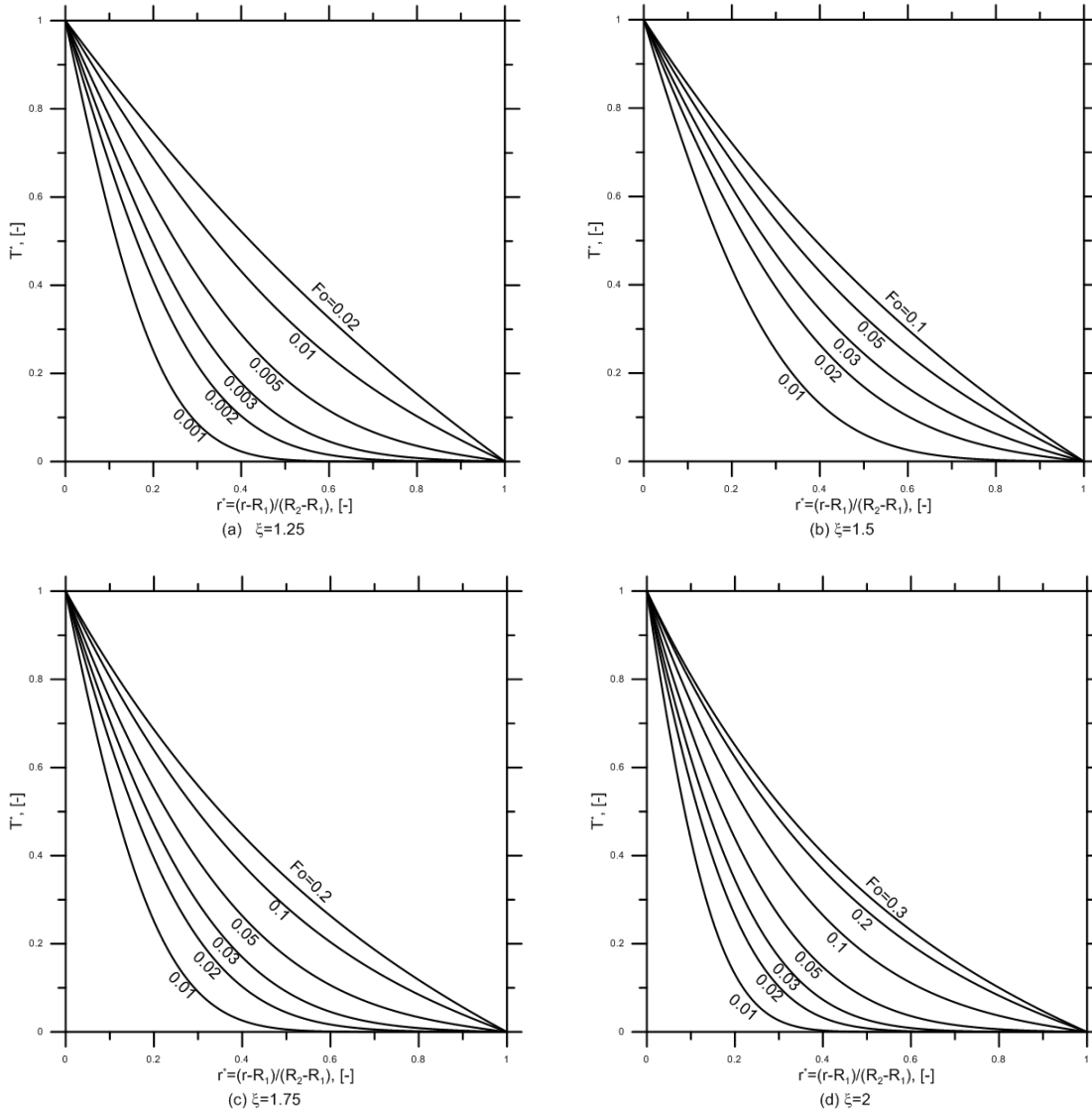


Fig. 10 History of temperature profiles.

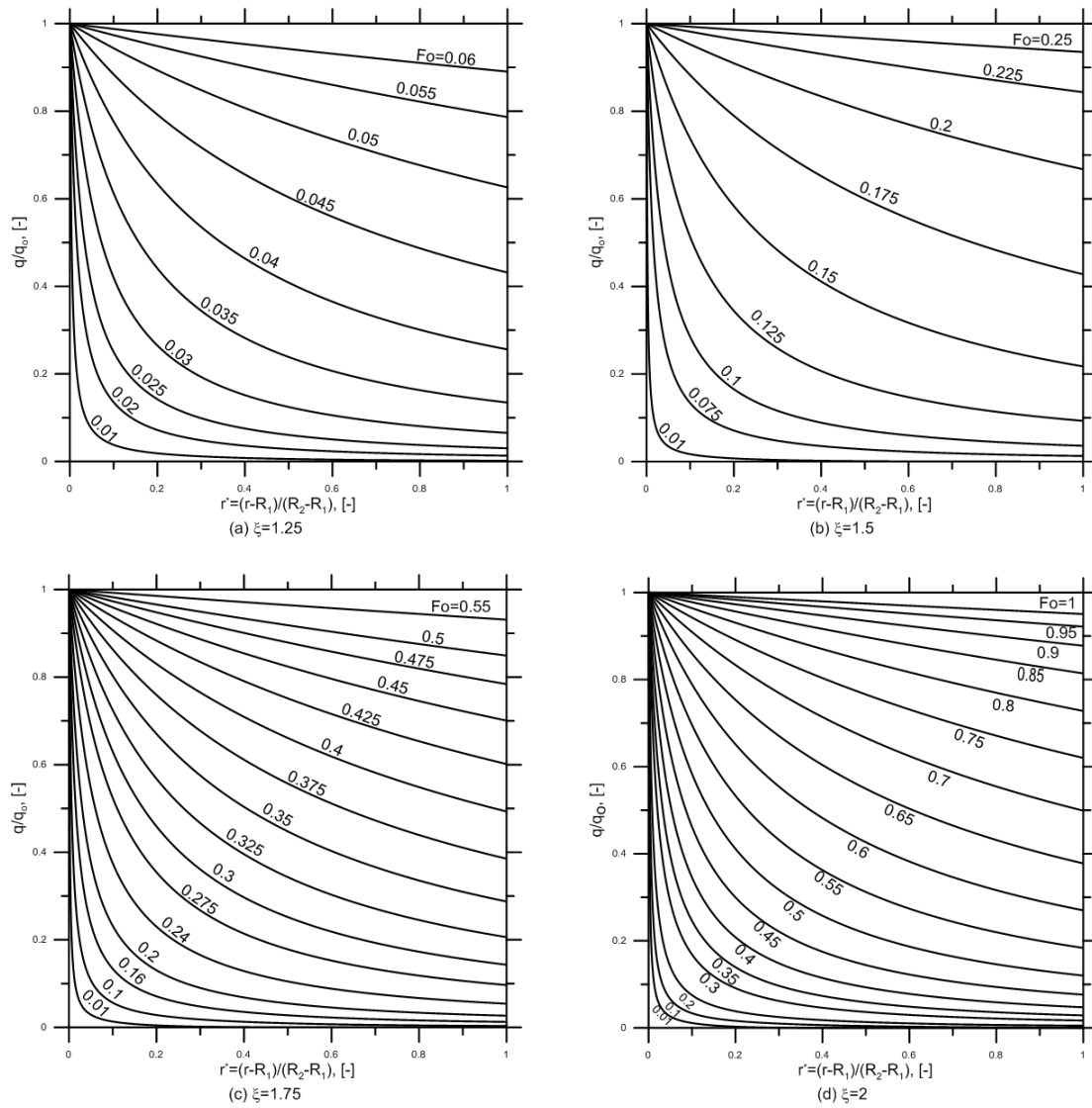


Fig. 11 History of heat transfer profiles.



## A Developed Model for Selecting Optimum Locations of Water Harvesting Dams Using GIS Techniques

**Dr.Prof.Rafa Hashim Al-Suhaili**  
Department of Civil Engineering  
College of Engineering  
Baghdad University  
Email:rafaalsuhili@yahoo.com

**Raghad Hadi Hassan**  
Department of surveying Engineering  
College of Engineering  
Baghdad University  
Email:raghad\_hd007@yahoo.com

### ABSTRACT

An integrated GIS-VBA (Geographical Information System – Visual Basic for Application), model is developed for selecting an optimum water harvesting dam location among an available locations in a watershed. The proposed model allows quick and precise estimation of an adopted weighted objective function for each selected location. In addition to that for each location, a different dam height is used as a nominee for optimum selection. The VBA model includes an optimization model with a weighted objective function that includes beneficiary items (positive) , such as the available storage , the dam height allowed by the site as an indicator for the potential of hydroelectric power generation , the rainfall rate as a source of water . In addition to that (negative) penalty items are also included such as surface area, evaporation rate.

In order to obtain precise results, an Artificial Neural Network (ANN) model was formulated and applied to correct the elevations of the Digital Elevation Model (DEM) map using real and DEM elevations of available selected control points.

The application of the model is tested using a case study of a catchment area in Diyala and Wasit Governorate. The DEM file was corrected for elevations, using the developed ANN model .This model is found using SPSS – software. The correlation coefficient of this model is found to be (0.97) , with 3- hidden nodes and hyperbolic tangent and identity activation functions. Different weight scenarios for the objective function of the optimization model were adopted. The results indicate that different optimum dam locations can be observed for each case. Results indicate also that sometimes equal objective can be obtained but each has different reservoir volume and surface area.

**KEY WORDS:** Water harvesting - Dam location- Geographical Information System – Visual Basic for Application – ANN model- DEM

### تطوير نموذج لاختيار المواقع المثلى لسدود حصاد المياه باستخدام تقنية نظم المعلومات الجغرافية

رغد هادي حسن  
قسم هندسة المساحة  
كلية الهندسة/جامعة بغداد

أ.د.رافع هاشم السهيلي.  
قسم الهندسة المدنية  
كلية الهندسة/جامعة بغداد

### الخلاصة:

تم بناء نموذج تكاملي باستخدام برامج نظم المعلومات الجغرافية وبرمجة فيجوال بيسك لاغراض التطبيق يمكن استخدامه لإيجاد المواقع الأمثل لسدود حصاد المياه من المواقع العديدة المحتملة في جابية معينة . يقوم النموذج بحساب دالة هدف موزونة باوزان معينة ولمواقع عديدة لوديان بالجابية وكذلك لعدة ارتفاعات للسدود في كل موقع بطريقة دقيقة وسريعة . يتضمن النموذج معايير ايجابية (موجبة) واخرى سلبية

(سالبية) موزونة باوزان يمكن للمستخدم ان يختارها حسب اهمية كل معيار . من هذه المعايير الموجبة قابلية الخزن المتوفرة ، ارتفاع السد الممكن كمؤشر لقابلية انتاج الطاقة الكهربائية ، معدلات الامطار كمصدر للمياه . ومن المعايير السالبة استخدمت كجزء مثل المساحة السطحية. وأوضحت النتائج بأن المواقع المثلى تتغير عند الاوزان المختلفة. احيانا يتوفر حلين مثاليين لدالة هدف واحدة متساوية رغم اختلاف قيم حجم الخزان والمساحة السطحية لغرض ان تكون النتائج اكثر دقة تم بناء نموذج اخر هو نموذج الشبكات العصبية الذي يجب تطبيقه على خارطة نموذج الارتفاعات الرقمية . لتصبح مناسب النقاط اعتمادا على العلاقة بين الارتفاعات الحقيقية والارتفاعات التي يعطيها نموذج الرقمية (DEM). الارتفاعات لنقاط الضبط الارضي المتوفرة في المنطقة.

الكلمات الرئيسية: حصاد المياه - مواقع السدود - نظم المعلومات الجغرافية - نموذج الارتفاعات الرقمية - نموذج الشبكات العصبية

## INTRODUCTION:

Our planet is known as the blue planet, due to its extensive reserves of water. The three fourth of the Earth's surface is covered by water. Unfortunately, 98% of this surface water is in the oceans, the remaining 2% accounts for the fresh water supplies of the world. More drastically, 90% of this fresh water supply is either in the poles or remains under the ground. As fresh water resources, humans make up only 0.26%, which is available to consumption. **Jhon, 2000.**

As it is well known now everywhere the water needs is growing up, coupled with the decrease of availability. This problem has an increased importance in arid and semi-arid regions. Rain-water harvesting dams is one of the solutions that could be adopted in such areas to store water during rainy season to be used later during dry season for agriculture, domestic and mini-power generation uses . For a large watershed different valleys may exist that could have a feasible potential for building a water harvesting dam. In such problem engineers or water resources planners may face the difficulty of selecting the proper location or locations of such dams that must be the most beneficiary for optimum storage and use of the harvested rain water. For such large watershed the use of Geographical Information System (Arc GIS ver.9.3) can simplify the process used to evaluate each valley and each location in this valley in the watershed and then to put these location in descending order according to it's evaluation score. This will be a useful tool for water recourse planners to use this evaluation process for deciding the optimum locations to build these dams ,with consideration to the available budget for building them.

**Weerasinghe et. al, 2010,** Had described a comprehensive and convenient method to optimize the locations of proposed dams, to implement integrated water management strategies efficiently and effectively. To illustrate this routine methodology, they develop a spatially explicit spatial analysis model: Geographic Water Management Potential (GWAMP). they focus on the aspect of using GIS, to find adaptation- and mitigation- strategic solutions for water management, by applying GWAMP at global scale. These solutions are important towards ensuring- and improving- agricultural land productivity at climate initiated water related drastic events. **Al-Ayyash et.al, 2012:** Had carried a major research project in the Jordanian Badia on site selection criteria for rain water harvesting systems based on the integration between indigenous knowledge and the use of Geo-infor- matics. This work was followed by conducting a geophysical and soil investigation for five potential sites. In this study, GIS was used to investigate the potential of having enough runoff in the five selected sites to establish water harvesting dams based on rainfall, evaporation data and catchments' areas for the selected sites. It was found that the estimated runoff that could be harvested on annual basis at these sites varies between 0.2 Million Cubic Meters (MCM) in Alaasra site to 0.82 MCM in Al-Manareh (Al-Ghuliasi) site. This indicates that these sites have the potential for small scale water harvesting that could be utilized by local livestock owners in the area.



## THE DEVELOPED MODELS.

The work in the research consists of two models which can be summarized as follows :

- 1- An Artificial Neural Network model For enhancement of the digital elevation model (Vertical accuracy enhancement)

## DIGITAL ELEVATION MODEL (DEM)

Digital Elevation Models are data files that contain the elevation of the terrain over a specified area, usually at a fixed grid interval over the surface of the earth. The intervals between each of the grid points will always be referenced to some geographical coordinate system. This is usually either latitude-longitude or UTM (Universal Transverse Mercator) coordinate systems. The closer together the grid points are located, the more detailed the information will be in the file. **Lynn,2009**

## WATER HARVESTING

Water harvesting means capturing rainwater where it falls or capturing the runoff. Measures should be taken to keep that water clean by not allowing polluting activities to take place in the catchment. Water harvesting can be undertaken through a variety of ways:

- Capturing runoff from rooftops.
- Capturing runoff from local catchments.
- Capturing seasonal floodwaters from local streams.
- Conserving water through watershed management.

These techniques can serve the following purposes:

- Provide drinking water.
- Provide irrigation water.
- Increase groundwater recharge.
- Reduce storm water discharges, urban floods and overloading of sewage treatment plants.

Rain is the first form of water that is known in the hydrological cycle, hence is a primary source of water. Rivers, lakes and groundwater are all

- 2- An optimization model to select the optimum locations of water harvesting dams, in a certain multi-valley, catchment.

These two developed models are used in conjunction with GIS software .as shown in **Fig.1** Schematic representation of the developed models.

secondary sources of water. In present times, human depend entirely on such secondary sources of water. In the process, the rain is the ultimate source that feeds all these secondary sources and remain ignorant of its value.**ER-ING,2008.**

## OPTIMIZATION PROCEDURE

Optimization means maximizing or minimizing an objective function which represents the criteria adopted to define *best dam's location*. Generally, the quality of a dam location is characterized by dam's height, reservoir volume and economy.....etc.

In the general view, optimization problems are made up of three basic items:

1. An objective function, which should be minimized or maximized. For instance in fitting experimental data to a user-defined model, we might minimize the total deviation of observed data from predictions based on the model.
2. A set of unknown or variables, which affect the value of the objective function. In fitting-the data problem, the unknowns are the parameters that define the model.
3. Sets of constraints that allow the unknowns to take on certain values but exclude others.

So generally the optimization problem defined as, finding values of the variables that minimize or maximize the objective function while satisfying the constraints, these variables are known as the decision variables. **Kiamehr, R.,2003.**

## STUDY AREA DESCRIPTION:

A DEM file has to be observed and prepared for application of case study, Diyala and Wasit Governorates extend to the north-east of Baghdad. They are cover an area of 34,838 square kilometers. Its location (32° 1' 10 " - 34° 54' 10 " N). (44° 16' 15 " - 46° 3' 51"E ) A large portion of Diyala is drained by the Diyala River, a major tributary of the Tigris river .The Hemrin Mountains pass through the governorate. Wasit Governorate location in the central part of Iraq,to the east lies Iraq's international border with Iran . **Fig.2**, shows the location of the case study.

### ENHANCEMENT OF THE DEM MODEL USING ANN MODELING.

Improvement of DEM means corrections of the elevations given by the DEM file using ground control points.

The procedure of the improvement of the digital elevation model contains the following phases:

- Conversion of the original digital elevation model from raster file system to shapefile feature class format, using Arc GIS 9.3 software.
- Locating the Ground Control points(164) on the study area.
- Calculation of the elevations ( Z values) from the original digital elevation model (Zdem) and (Ztrue) for the Ground Control points.
- Computation of a relationship between the (Zdem) and (Ztrue) , using Artificial Neural Network model,by using statistical program called Statistical Package for the Social Sciences (SPSS 16.0).
- Programming a software for computing the new corrected elevations (new Z value),using the matlab software .
- Conversion of new data (new Z) to a new Digital elevation model , using the Arc GIS V.9.3 program .

The architecture of the ANN model has three input nodes in the input layer and one output node in the output layer. The input nodes represent the coordinates (X,Y,Zdem) for Ground Control Points. The output node represented the (Ztrue)

for Ground Control Points, and three hidden node in this model as the required number of hidden nodes for the ANN model as obtained by the SPSS software .With single layer neural network.

### FORMULATION OF THE OPTIMIZATION MODEL FOR DAM LOCATION SITE SELECTION AND SOLUTION PROCEDURE.

The mathematical model of the optimum location of water harvesting dam's location can be formulated as follows:

select {X} = {dam location}

To maximize the objective function (F), which can be written as:

$$F(V,S,T,R,E,H) = (V/V_{max} * W_v) - (S/S_{max} * W_s) - (T/T_{max} * W_t) + (R/R_{max} * W_r) - (E/E_{max} * W_e) + (H/H_{max} * W_h) \quad (1)$$

Where :

F(V,S,T,R,E,H) = objective function of the benefits.

V = reservoir volume.

V<sub>max</sub> = maximum reservoir volume , given by a site .

S = reservoir surface area.

S<sub>max</sub> = maximum reservoir surface area, given by a site .

T = temperature, in the dam location .

T<sub>max</sub> = maximum temperature.

R = rainfall, in the dam location .

R<sub>max</sub> = maximum rainfall.

E = evaporation, in the dam location .

E<sub>max</sub> = maximum evaporation.

H = dams height.

H<sub>max</sub> = maximum height, given by a site .

W<sub>i</sub> = weights for each items, i= V,S,T,R,E,H.

The following constrains could be used:

$$H_{min} \leq H \leq H_{max}$$

Where :

H<sub>max</sub> : maximum elevation available in the valley.

H<sub>min</sub> : A selected minimum height by the user .

## THE DESIGNED (VBA) SOFTWARE FOR THE OPTIMIZATION MODEL.

The operation of the designed model is presented by the overall flow chart, which shows its components and its logic sequence of operations, as shown in **Fig.3**.

### MODEL DESCRIPTION.

The developed (VBA) code is inserted inside the active tool bar of the GIS software, as shown in **Fig.4**. Inside ArcMap operation window. The code item is shown in one of the tool bars of the GIS software.

The following steps should be performed; then.

- Open the ArcMap
- Clicking on the (VBA) code, the window shown in **Fig .5**, will appear to the user.

### MODEL OPERATION.

The developed software was applied using the explained case study. Different locations and Dam heights for each location were tried for purpose of presentation, one of the locations selected will be shown in the model operation. Starting the model operation using the VBA code shown in **Fig .5**, the software will analyze these data and **Fig.6**, appears which shows the first drainage point after which a dam was drawn manually, as a red line. shown in the **Fig.6**, Example of a dam drawn in a certain drainage point. The lake borders will appear immediately as shown in **Fig.7**, for the

maximum dam height. Entered in the VBA code input window. Then the internal code will start the estimation of the objective function variables. (volume , area , ... etc) , and the weighted objective function accordingly. There calculation will be adopted for the same dam location but for different heights, starting from the max. Height and down according to user selection. **Fig.8**, shows the calculations of the objective function for the selected dam with 3 – different heights (H = 20,18,16) .**Fig.8**, shows also the borders of the lake for the first height dam heights selection H = 20 (blue solid line) . As the user assign the mouse cursor to the sectional row and click it , the borders of the lake with the second height value will appear as shown in **Fig.9**, simitary for any height the lake border can be shown, as in **Fig.10** compare these **Figures.8,9,10**, shows the reduction in the lake area .

Then the procedure can be repeated for any other location as shown in **Fig.11**. In this figure, the green color indicate the lake and for the new location . The user can keep the layer of the first location for visual comparison (shown in blue.)

The procedure is further repeated for many locations for each location different dam height values are selected . All the results of the objective function of these locations and heights will be stored in descending order of the objective function as shown in **Fig.12**

## RESULTS PRESENTATION AND DISCUSSIONS.

The results obtained from different sites selection each with different dam heights varied from its minimum height to the maximum height offered by each locations are presented in tabulated view in descending order of the objective function as shown in **Fig .12**. Recalling that those results obtained are for equal weights values of each item of the presenta will be indicated later .

If the user select the first row its data can be presented in many ways, for example the dam profile can easily draw as shown in **Fig.13**.

The selected optimum dam location and the corresponding lake can be presented in the georeference map of the case study as shown in **Fig.14**.

To present changes in storage and surface area and/or height ws the storage and surface area and the objective function respectively for the list (33) site, with their location and heights shown in for equal weights.

In order to check the effect of items weights on the solution, different weight scenarios were used as shown in **Table .1**.

In general, changing the weights can affect the optimum solution as shown in **Table .2**. shows the first 3- optimum solution for each scenario. In order to simulate effect of weight the differences should be more than 1.

The objective function is plotted against location number for each scenario.

## CONCLUSIONS.

The following conclusions can be deduced from the work conducted in this research:

- 1- The best data division required for the ANN model used for elevations corrections is 67% ,18% ,15% for training, testing and holdout sub – sets respectively.
- 2- The required hidden nodes is (3) with a hyperbolic tangent and identity activation functions for the hidden and output layer respectively.
- 3- The ANN model can predict the corrected elevations with a correlation coefficient is (0.9).
- 4- The developed integrated GIS- optimization model can be used easily, and can produce the optimum results of many selected locations very quickly.
- 5- The results indicated that even though the differences in the objective functions of different locations are seemd to be small, the corresponding differences in storage and surface area are significantly different.
- 6- Among the 33-sites and heights combinations selected as a nominee for dam construction in the watershed case study, site number (6), followed by sites number (9) and (18) represent the most optimum locations with storage capacities of (150353686.466 , 2145519.15142, 46045984.5662 )m<sup>3</sup>, and surface areas (15743356.479, 499543.130235, 5366985.41692) m<sup>2</sup>, respectively. For the case of equal weights adopted for the different items of the objective function.
- 7- Adopting different weights for each items in the objective function have considerable effect on the optimum dam location.

8-In some weight scenarios, the models gives the maximum objective functions of the first two solution as an equal value.

8- However the storage and surface area are different. The first solution gives higher storage than the second one, but with lower surface area. This means that the benefits gained from the difference in storage, is equalized by the penalty of evaporation given by the increase in evaporation less due to increase in surface area. For example for scenario (A), the first two solutions gives both an objective function value  $f1=f2= 0.3333$ . but with  $S1 = 149177957.309$  ,  $S2 = 246679790.58 \text{ m}^3$  and  $A1 = 15651355.098$  ,  $A2 = 24065080.3 \text{ m}^2$ .

## REFERENCE.

AL-Ayyash, et,al. 2012 " Runoff Estimation for Suggested Water Harvesting Sites in the Northern Jordanian Badia" Journal of Water Resource and Protection,2012,4,127-132.

ER-Ing,2008."Water Harvesting". Web Page: <http://www.rainwaterharvesting.org/whatiswh.htm> . Accessed date: 5/5/2008.

Jhon R. Jensen, 2000,"Remote Sensing of Environment an Earth Perspective", Prentice-hall series., USA

Kiamehr, R., 2003," Multi Object Optimization of Geodetic Network",Department of Surveying Engineering, Zanjan University, Iran.

Lynn.E,Johnson,2009 "Geographic Information System in Water Resources Engineering " CRC. Tayler and Francis Group.LLC,ISBN978-1-4200-6913-6.

Weerasinghe et,al. 2010 "*Water Harvest- and Storage- Location Optimization Model Using GIS and Remote Sensing*" BALWOIS 2010 - Ohrid, Republic of Macedonia - 25, 29 May 2010.

**Table (1) Different weight scenarios**

scenarios	Volume weight	Dam height weight	Surface area weight	Rain & temp. & evap.
A	3	2	1	1
B	5	3	1	1
C	7	4	1	1
D	1	2	3	1
E	1	4	7	1
F	1	3	2	1
G	2	3	1	1

**Table (2) The first 3- optimum solution for each scenario.**

scenario	Equal weight	A	B	C	D	E	F	G
First 3- optimum Dams	6 9 18	6,21 22 7	6,15 16 7	6,21 22 7	9 24 12	24 9 25	24 9 12	6,21 22 0

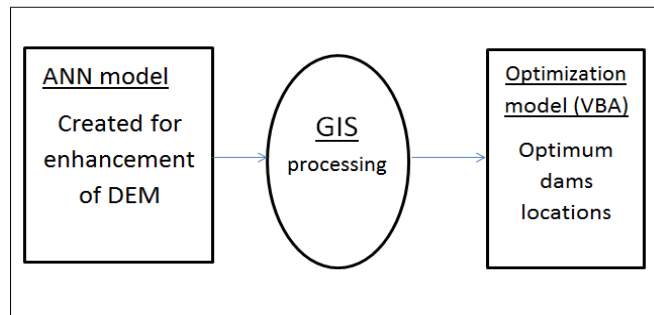


**Fig. (1) Schematic representation of the developed models**



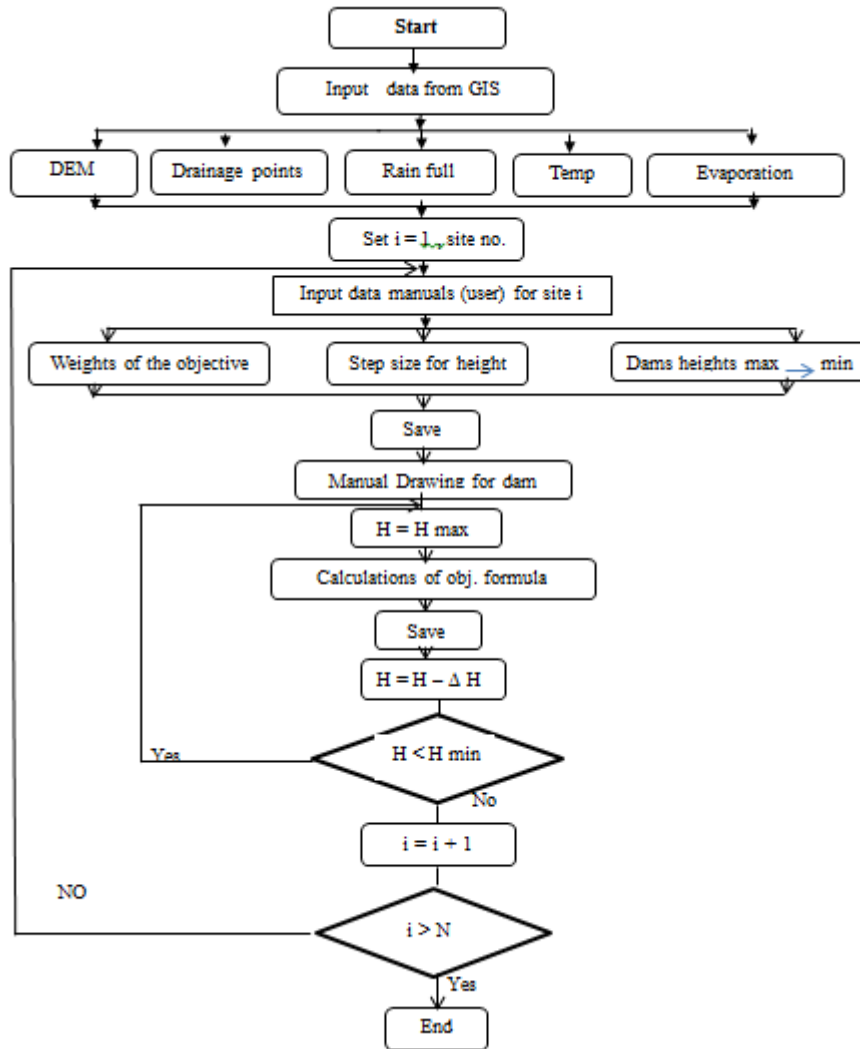


Fig.(3) Model flow chart.

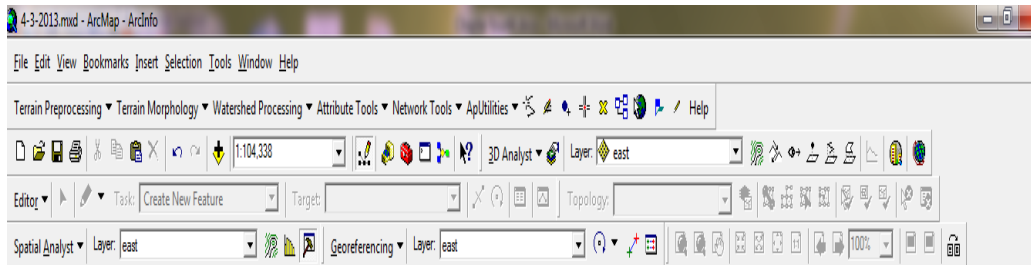


Fig.(4) VBA model code insertion in the active tool bar of the GIS software.

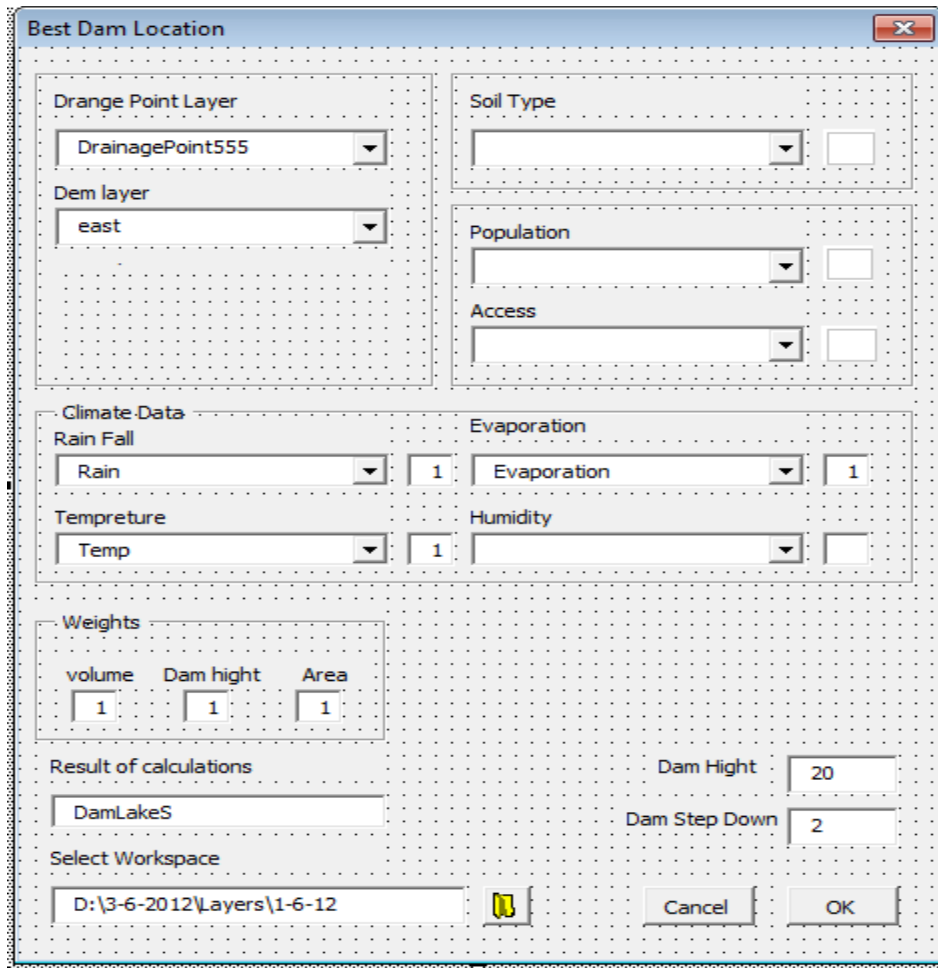


Fig. (5) Main VBA program window, Data inputs.

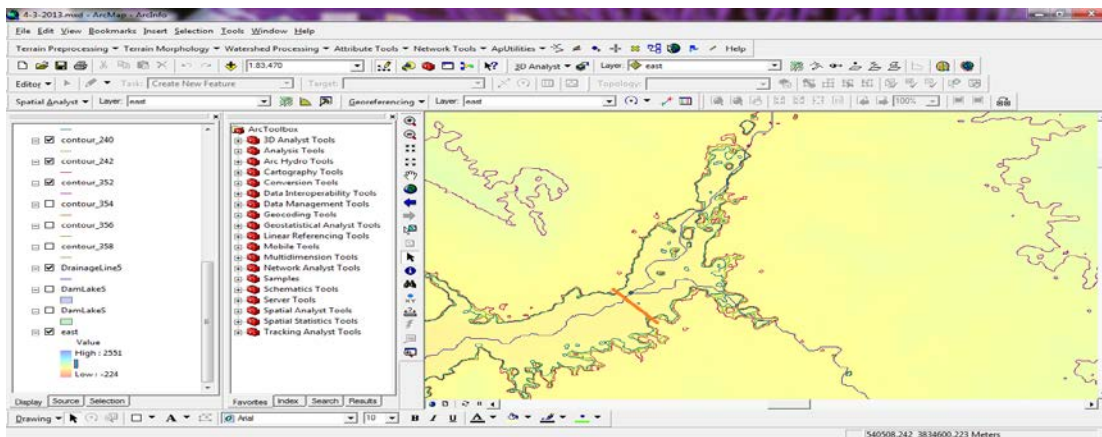


Fig. (6) Example of a dam drawn in a certain drainage point .

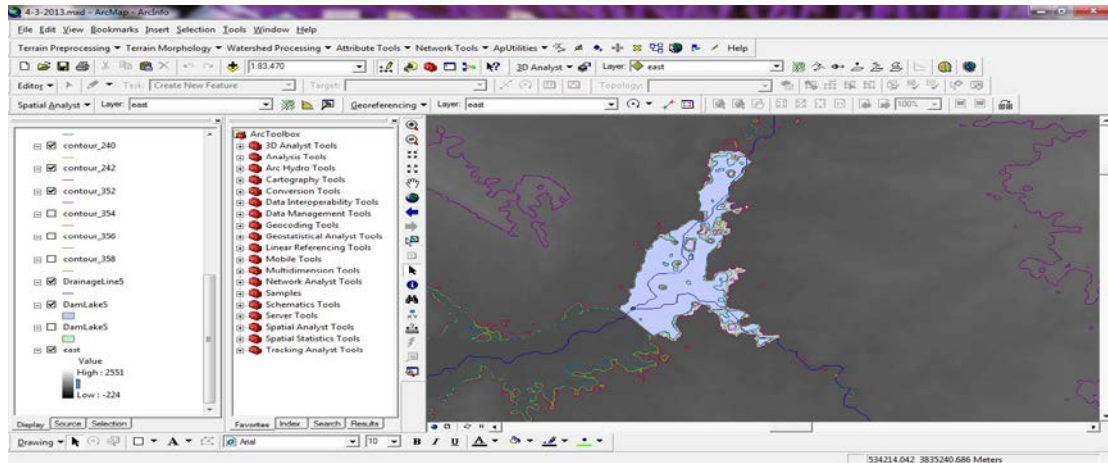


Fig. (7) The lake borders of the selected dam.

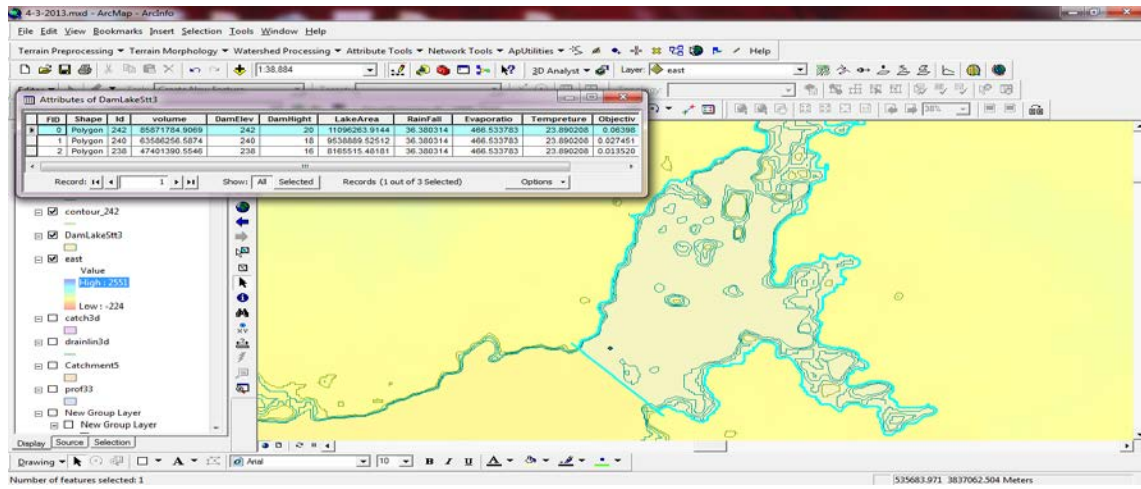


Fig. (8) The objective function calculation results for the selected dam.

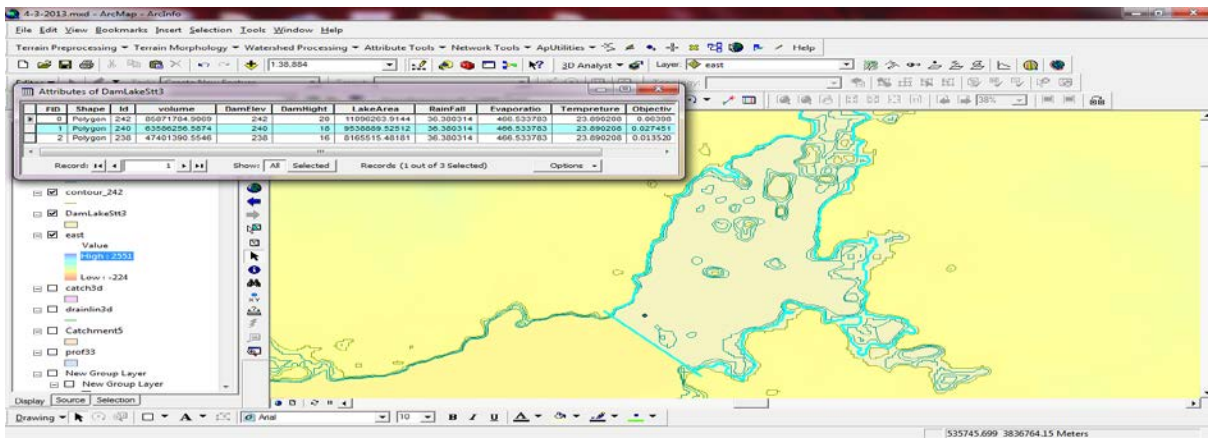


Fig. (9) Calculation for the second lower dam.

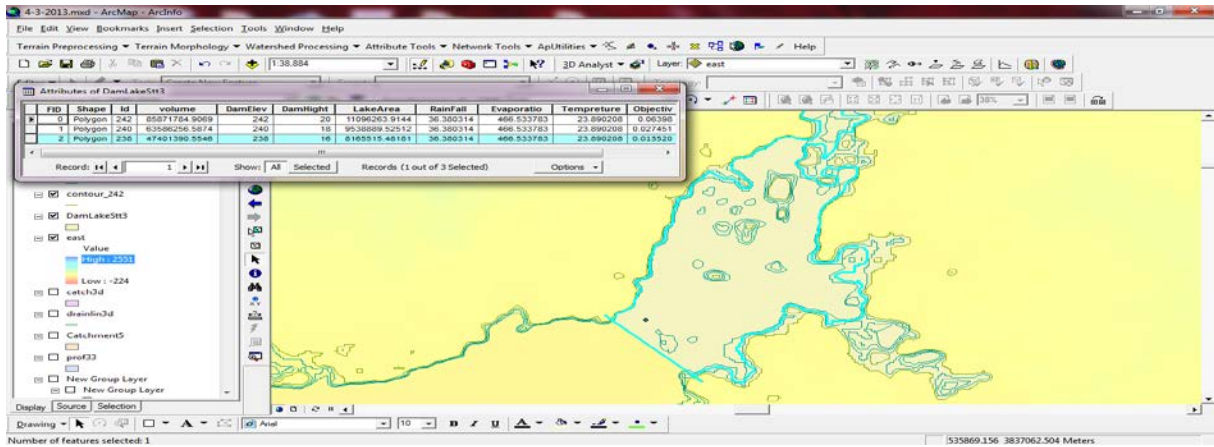


Fig.(10) Calculation for the third lower dam.

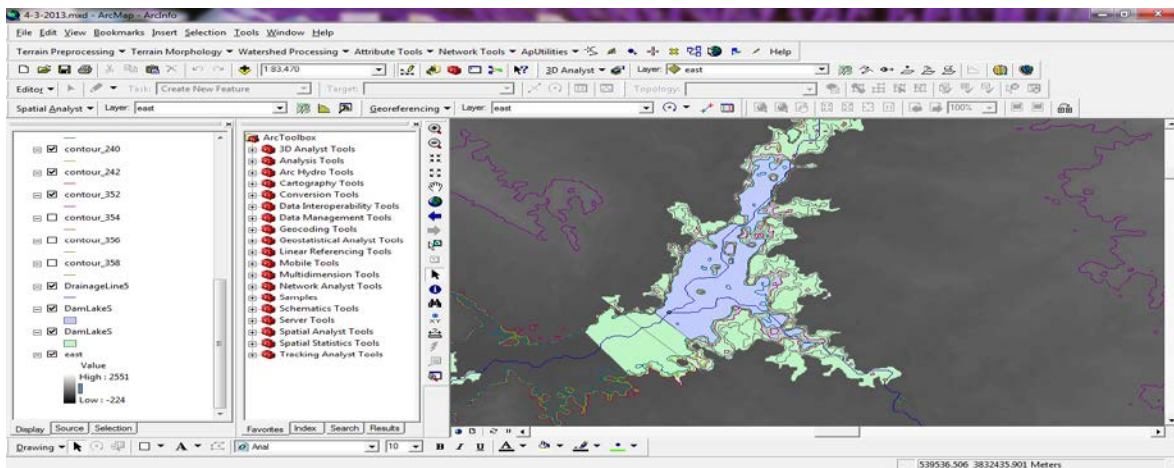


Fig. (11) Selection of another location.

Dam	* Shape	Id	volume	DamElev	DamHight	LakeArea	RainFall	Evaporatio	Tempreture	Objectiv
6	Polygon	242	150353686.466	242	20	15743326.479	36.380314	466.533783	23.890208	0.067128
9	Polygon	358	2145519.15142	358	20	499543.130235	36.380314	466.533783	23.890208	0.064218
18	Polygon	502	46045984.5662	502	20	5366985.41692	36.380314	466.533783	23.890208	0.061352
12	Polygon	502	2925708.54299	502	20	869370.617218	36.380314	466.533783	23.890208	0.061167
15	Polygon	502	12501221.3831	502	20	2040538.26184	36.380314	466.533783	23.890208	0.059383
10	Polygon	356	1266079.93782	356	18	401416.397122	36.380314	466.533783	23.890208	0.047615
13	Polygon	500	1543448.65197	500	18	556396.96759	36.380314	466.533783	23.890208	0.046282
0	Polygon	242	85821663.6326	242	20	11080888.7793	36.380314	466.533783	23.890208	0.044953
19	Polygon	500	35999801.6801	500	18	4328768.96663	36.380314	466.533783	23.890208	0.04454
16	Polygon	500	9081337.67657	500	18	1598791.97586	36.380314	466.533783	23.890208	0.043602
3	Polygon	242	73650224.9826	242	20	9973784.08164	36.380314	466.533783	23.890208	0.043182
21	Polygon	252	245333693.433	252	30	23980992.9241	36.380314	466.533783	23.890208	0.043131
24	Polygon	368	2309591.25902	368	30	577491.772973	36.380314	466.533783	23.890208	0.040687
7	Polygon	240	121138466.92	240	18	13802820.7226	36.380314	466.533783	23.890208	0.038619
30	Polygon	511	65272818.4152	511	30	7497552.23834	36.380314	466.533783	23.890208	0.035367
27	Polygon	511	21662804.089	511	30	3676492.60704	36.380314	466.533783	23.890208	0.032297
11	Polygon	354	609924.989408	354	16	250659.6917	36.380314	466.533783	23.890208	0.031817
14	Polygon	498	724190.77288	498	16	320944.165635	36.380314	466.533783	23.890208	0.0312
25	Polygon	366	1439641.17967	366	28	323015.586161	36.380314	466.533783	23.890208	0.030753
17	Polygon	498	6314775.71936	498	16	1246204.98523	36.380314	466.533783	23.890208	0.027601
20	Polygon	498	28785692.6999	498	16	3602571.18056	36.380314	466.533783	23.890208	0.027565
22	Polygon	250	198238184.777	250	28	20129901.9295	36.380314	466.533783	23.890208	0.026791
31	Polygon	509	52977208.0246	509	28	6346468.76845	36.380314	466.533783	23.890208	0.023903
28	Polygon	509	15324852.1367	509	28	2846152.48073	36.380314	466.533783	23.890208	0.022651
4	Polygon	240	54563682.6756	240	18	8495269.71454	36.380314	466.533783	23.890208	0.02101
1	Polygon	240	63541478.7038	240	18	9523865.51276	36.380314	466.533783	23.890208	0.020072
26	Polygon	364	862277.018689	364	26	282066.470836	36.380314	466.533783	23.890208	0.019535
29	Polygon	507	10397872.1941	507	26	2133718.62605	36.380314	466.533783	23.890208	0.013144
32	Polygon	507	41356100.9954	507	26	5319360.56601	36.380314	466.533783	23.890208	0.012035
8	Polygon	238	95395339.7267	238	16	12102526.7949	36.380314	466.533783	23.890208	0.011417

Fig. (12) The results of (33) locations selected , each of different dam height values .

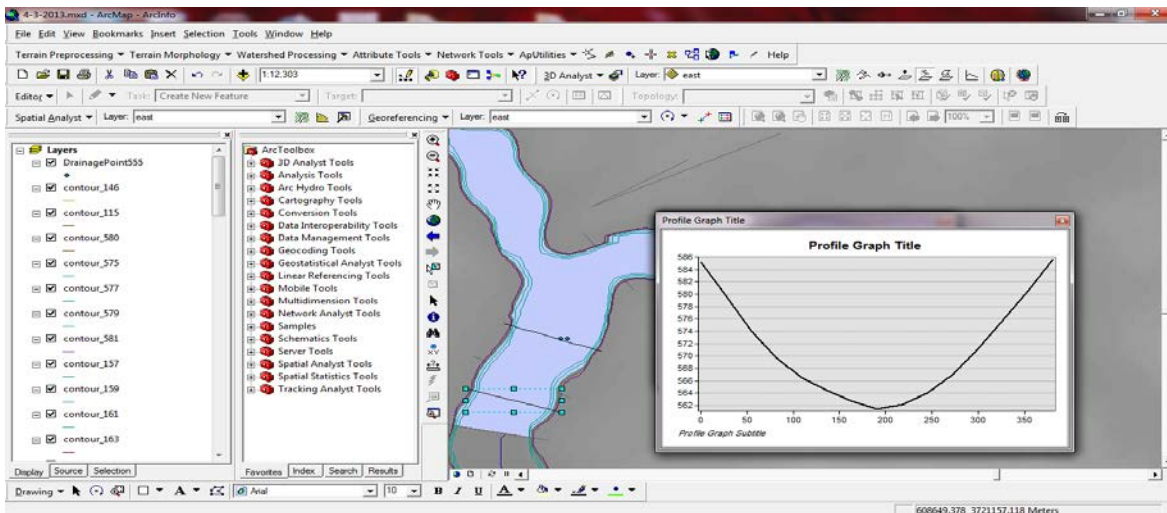


Fig. (13) The profile of the dam site.

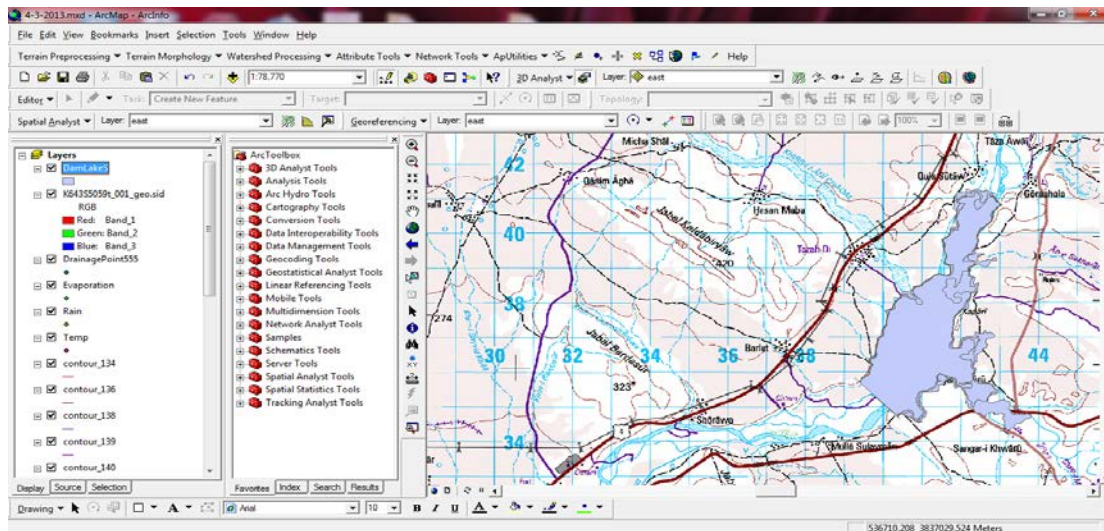


Fig (14) Selected optimum dam location and its corresponding lake present on the georeferenced map of the case study.

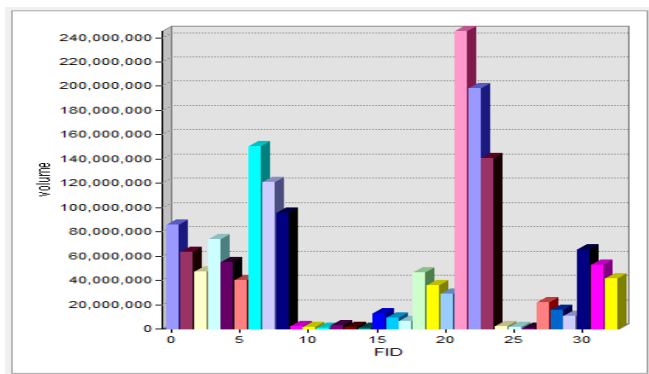


Fig.(15) Change in storage with the 33 sites

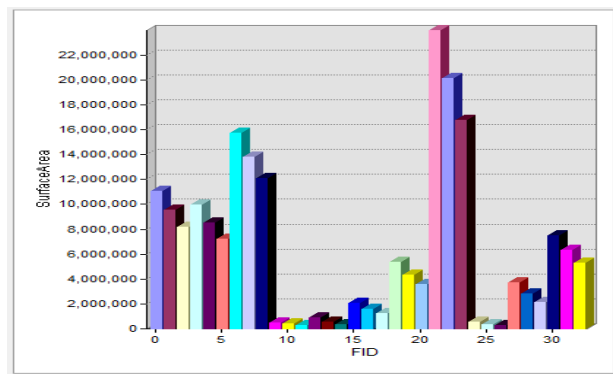


Fig (16) Change in surface area with the 33 sites

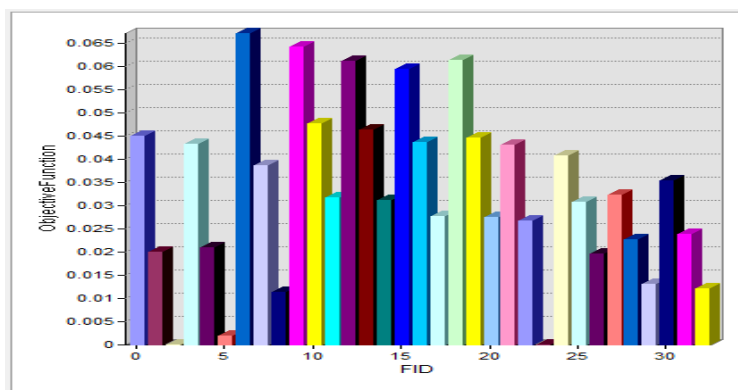


Fig. (17) Change in the objective function with the 33 sites.

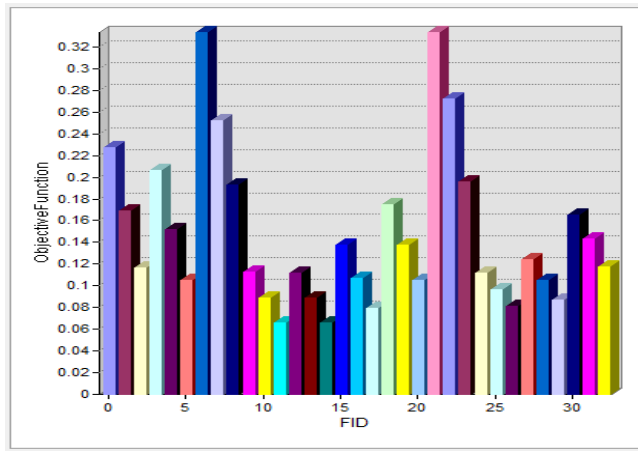


Fig.(18) Objective function and dams numbers for scenario (A).

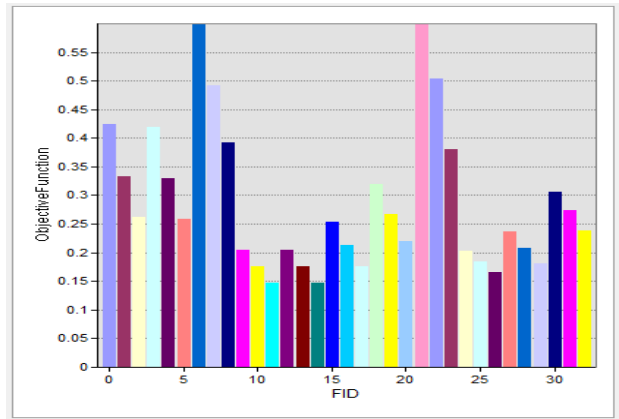


Fig.(20) Objective function and dams numbers for scenario (C).

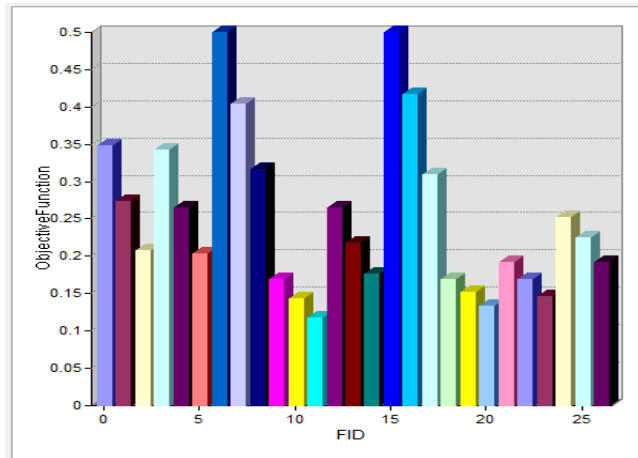


Fig.(19) Objective function and dams numbers for scenario (B) .

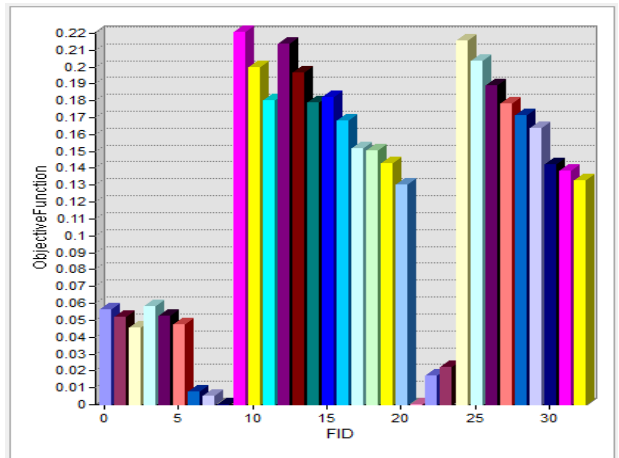


Fig.(21) Objective function and dams numbers scenario (D).

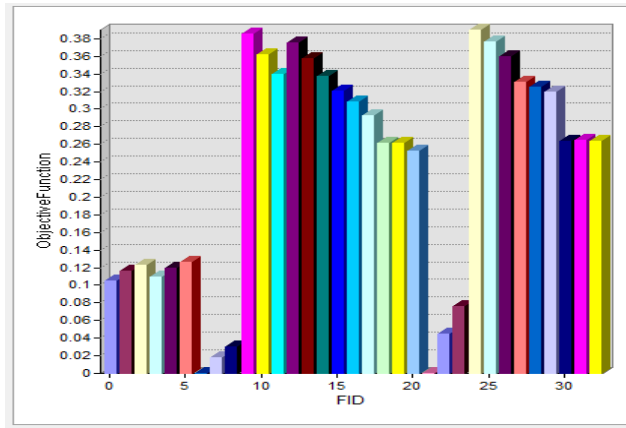


Fig.(22) Objective function and dams numbers for scenario (E).

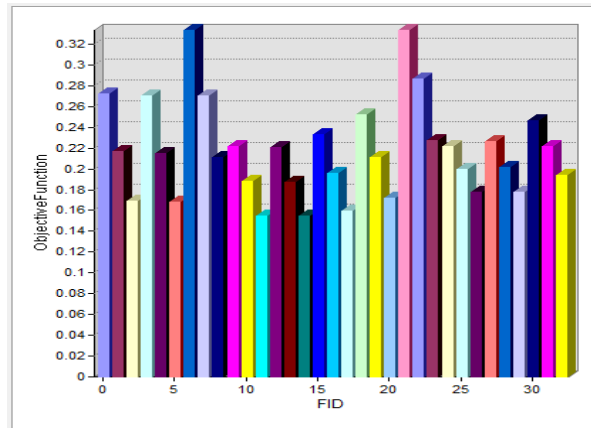


Fig.(24) Objective function and dams numbers for scenario (G).

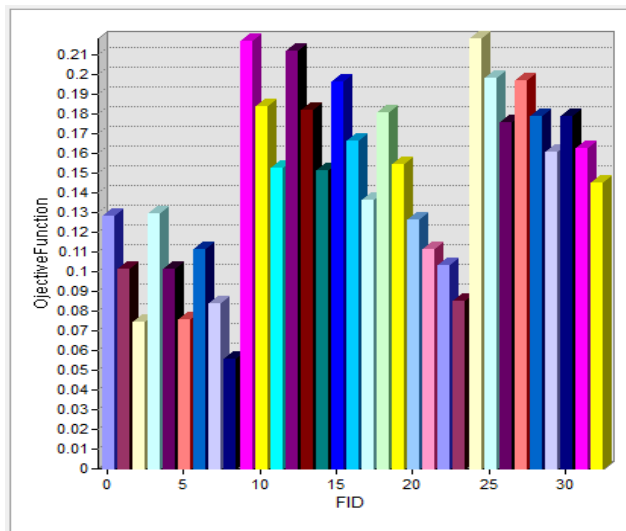


Fig.(23) Objective function and dams numbers for scenario (F).



# Construction Time-Cost Optimization Modeling Using Ant Colony Optimization

Mohammed Nooruldeen Azeez (1), Angham Alsaffar (2)

[mohammed.n.azeez@gmail.com](mailto:mohammed.n.azeez@gmail.com), [anghamalsaffar@yahoo.com](mailto:anghamalsaffar@yahoo.com)

M.Sc. Candidate Baghdad University/ Civil Eng. Dep. (1), Prof. Ph.D. Baghdad University/ Civil Eng. Dep. (2)

## ABSTRACT

In the field of construction project management, time and cost are the most important factors to be considered in planning every project, and their relationship is complex. The total cost for each project is the sum of the direct and indirect cost. Direct cost commonly represents labor, materials, equipment, etc.

Indirect cost generally represents overhead cost such as supervision, administration, consultants, and interests. Direct cost grows at an increasing rate as the project time is reduced from its original planned time. However, indirect cost continues for the life of the project and any reduction in project time means a reduction in indirect cost. Therefore, there is a trade-off between the time and cost for completing construction activities.

In this research, modeling of time-cost optimization, generating global optimum solution for time and cost problem, and lowering construction time and cost using ant colony optimization algorithm.

**KEYWORDS:** Time-Cost Optimization, Time-Cost Trade-off, Ant Colony Optimization.

## موديل رياضي لأمثلية الوقت والكلفة الانشائية باستخدام امثلية مستعمرة النمل

### الخلاصة

ان الوقت والكلفة هي اهم العوامل المأخوذة في تخطيط اي مشروع، في اختصاص ادارة المشاريع الانشائية. وان العلاقة بين الوقت والكلفة معقدة. فان الكلفة الكلية في اي مشروع تمثل مجموع الكلف المباشرة وغير المباشرة، وتمثل الكلف المباشرة كلف العمالة والمواد والمعدات، الخ

بينما الكلف غير المباشرة تمثل بصورة عامة مصاريف الاشراف و الاداريات والاستشارية اضافة الى الفوائد. الكلف المباشرة تزداد بنسبة كلما طال عمر المشروع عن عمره المقرر، بينما الكلف غير المباشرة تستمر طيلة عمر المشروع وان اي تقليل في مدة المشروع عن المدة المحددة تعني تقليل الكلف غير المباشرة، لذا فان هنالك مقايضة بين الكلفة والوقت في اكمال الفعاليات الانشائية.

في هذا البحث، سوف يتم انشاء موديل لحساب امثلية الوقت-الكلفة الانشائية. توليد حلول مثلى عالمية للوقت والكلفة، تقليل الوقت والكلفة باستخدام طريقة مستعمرة النمل.

## LITERATURE REVIEW

Time-cost trade-off analysis is as an important aspect of any construction project planning, and it is an interesting subject for both researchers and contractors, due to the academic / real field nature of the problem.

Construction time-cost problems were tackled repeatedly in the past decades using different methods and modeling techniques are classified

into three types heuristic, mathematical and evolutionary based algorithms.

Ant Colony Optimization (ACO) is introduced as a new approach for deriving approximate solutions for computationally sophisticated problems, using the Traveler Salesman Problem TSP as an example application (Dorigo et. al., 1991). Since that, ACO has been employed to solve various problems, such as no-wait flow shop scheduling routing problems, etc.

In addition, ACO Algorithms was and is still widely used to solve various discrete problems and still to date applied for solving complex optimization problems (**Blum, 2005**), ACO is also widely used in Civil Engineering and for different applications

Even though ACO algorithms were developed to solve TSP problems, the extensive use of ACO in

#### **Heuristic Models:**

(**Prager, 1963**) showed that Time-Cost algorithm can be given a structural interpretation, using concepts that are familiar to civil engineers.

(**Siemens, 1971**) introduced an algorithm (Siemens Approximate Algorithm) for efficiently shortening the duration of a project when the expected project duration exceeds a predetermined limit. The problem consists of determining which activities to expedite and by what amount. The objective is to minimize the cost of the project.

(**Goyal, 1975**) modified Siemens algorithm for shortening the duration of a project when the expected duration of the project exceeds a predetermined limit. Goyal redefined "effective cost slope", by selecting the activity with minimum effective cost slope, and simultaneously de-shortening appropriate activities on adequately shortened paths while shortening the selected activity,

(**Al-Samaraai, 2005**) used the typical cost slope approach that managers take in making time-cost trade-off and presented a crashing program.

Heuristic methods are widely used for their simplicity and general ability to produce good results, and they do not require a complicated calculations however they are problem dependent. Their results vary on different cases. In addition, despite the good solutions they provide, they do not guarantee optimality. Also most heuristic methods assume only linear time-cost relationships within activities. In addition, the solutions obtained by heuristic methods do not provide the range of possible solutions, making it difficult to experiment with different scenarios for what-if analyses (**Feng e. al., 1997**), (**Feng e. al., 2000**), and (**Hegazy, 2002**).

#### **Mathematical Models:**

(**Kelly, 1961**) established a mathematical basis For Crashing Cost in Critical-Path Scheduling Method. The essential ingredient of the technique is a mathematical model that incorporates

Civil Engineering and other sciences, and the outstanding performance of ACO algorithms provided the motive for applying ACO in TCO problems.

This research will use ACO searching behavior for developing a Time-Cost Optimization Model .

sequence information, durations, and costs for each component of the project by using linear programming.

(**Patterson et. al., 1974**) studied minimum duration schedules for the resource constrained by using bounding techniques in conjunction with zero-one programming to solve project scheduling problems. The developed algorithms consist of examining the feasibility of a series of zero-one programming problems.

(**Robinson, 1975**) presented a model that involves a dynamic-programming approach to determine the allocation which minimizes the duration of the project (critical path). They presented a model able to determine the optimum allocation for networks of activities with computational shortcuts for functions with special properties used to increase the efficiency of their model.

(**Hendrickson, et. al, 1989**) used linear programming, and presented many solved examples for their method; however, the model was suitable only for problems with linear time-cost relationships.

(**Liu et al, 1995**) provided a hybrid method to solve Time-Cost trade-off problems using mathematical models. Their method takes advantage of linear programming for efficiency, and integer programming to find the exact solutions.

(**Chassiakos et. al., 2005**) incorporated important characteristics such as precedence relationships between activities, external time constraints, activity planning constraints, and bonuses/penalties for early/delayed project completion projects, which provide more realistic representation of actual construction in the analysis and two solution methods (exact and approximate) are developed, The exact method utilizes a linear/integer programming model to provide the optimal project time-cost curve and the minimum cost schedule considering all activity time-cost alternatives together.

The main criticisms to mathematical programming models is their complex



formulations, computational-intensive nature, and applicability to small-size problems (Feng et. al., 1997), and (Feng et. al., 2000).

Although the heuristic methods and mathematical approaches have their specific strengths, their weaknesses are also obvious especially as both techniques may not always lead to optimal solutions. The future seems to favor EOAs (Zheng et. al., 2005), and (Ng. et. al, 2008).

Another major deficiency of those methods is their inability to handle more than one objective. In addition, these methods are built upon the hill climbing algorithms, which has only one randomly generated solution exposed to some kind of variation to create a better solution. Therefore, it is questionable as to whether the solution is a "Global" optimal one (Feng et. al., 1997), and (Feng et. al., 2000).

### **Evolutionary-Based Optimization Algorithm (EOA) Models :**

In an attempt to reduce processing time and improve the quality of solutions, particularly to avoid being trapped in local optima, EOAs have been introduced during the past 10 years (Elbeltagi et. al, 2005).

EOAs are stochastic search methods that mimic the metaphor of natural biological evolution and/or the social behavior of species. The behavior of such species is guided by learning, adaptation, and evolution (Hegazy, 2002), and (Ng. et. al, 2008).

(Feng et. al., 1997) presented an algorithm based on the principles of Genetic Algorithms (GAs) for construction time-cost trade-off, and a computer program that can execute the algorithm efficiently. The computer program used, TCGA, automates the execution of the new algorithm, and it provides a practical tool for practitioners to apply the algorithm in practice.

After that, (Feng et. al., 2000) developed their previous work by utilizing GAs with simulation techniques to imitate the probabilistic nature of project networks throughout the search of optimal solutions. The approach provides more realistic solutions for construction time-cost trade-off problem under uncertainty.

They also demonstrated that GAs can be integrated with simulation techniques to provide an efficient and practical means of assessing project time and cost risks.

(Li e. al., 1997) also introduced a genetic algorithm model to solve time-cost trade-off problems with less computation time of (Feng et. al., 1997)

(Hegazy, 2002) also developed GA model to solve time-cost trade-off problems and was able to minimize the number of calculation used to find the solution. Also he was able to present a computer program to solve TCT problems for both researchers and planners.

Despite its benefit, the time taken by a GA model to generate a near-optimum solution can be excessive. The main drawback of the GA-based applications is that they require large computational time for the search (Feng et. al., 1997), and (Ng. et. al, 2008).

Another major drawback of GAs have to do with genetic drift which is typified by the existence of multiple peaks of equal height. When genetic drift occurs, it will converge to a single peak due to the stochastic errors during processing, and this is undesirable for any multi-objective TCO problems (Feng e. al., 2000), and (Zheng et. al., 2004).

GAs have been used extensively in the last decade to solve the TCT problem as mentioned above but Except for GA, other EOA techniques were inspired by different natural processes including the Ant Colony Optimization (ACO), Memetic Algorithms (MA), Particle Swarm Optimization (PSO), and Shuffled Frog Leaping Approach (SFL) etc. that were employed by (Elbeltagi et. al, 2005) for solving discrete time-cost trade-off problems.

(Elbeltagi et. al, 2005) developed five TCT models using all types of EOAs and provided better optimal solutions. They also conduct benchmark comparisons among the five algorithms for discrete time-cost trade-off problem to check the algorithm efficiency, in terms of processing time, convergence speed, and quality of the results. Based on this comparative analysis, some guidelines for determining the best operators for each algorithm were presented.

Although TCT problem has been extensively examined, all the researchers' only focused on minimizing the total cost for an early completion. This does not necessarily convey any reward to the contractor. However, clients and contractors are more concerned about the combined benefits and opportunities of early completion as well as

cost savings. This has led to the development of the TCO concepts (Zheng et. al., 2005), and (Ng, et. al, 2008).

### **TIME-COST OPTIMIZATION:**

The time-cost optimization (TCO) problem is a multi-objective problem, which attempts to strike a balance between resource allocation costs and project schedule duration. TCO also is one of the greatest challenges in construction project planning, since the optimization of either time or cost would usually be at the expense of the other (Afshar, et. al, 2009), and (Kalhor et. al, 2011).

The goal of TCO is the same goal of any multi-objective optimization problems, which is to find the best compromise between multiple and conflicting objectives. In multi objective optimization, there is more than one solution which optimizes simultaneously all the objectives and there is no distinct superiority between these solutions. Therefore, we face a set of non-dominated solutions in these problems called Pareto optimal. Among the feasible solutions, a solution is identified as dominant if it is better than all other solutions in all of the considered objectives simultaneously. Among the feasible solutions, those belonging to Pareto front are known as non-dominated solutions, while the remainder solutions are known as dominated. Since none of the Pareto set solutions is absolutely better than the other non-dominated solutions, all of them are equally acceptable as regards the satisfaction of all the objectives (Feng et. al., 2000), (Zheng et. al., 2005), and (Kasaeian, et. al, 2007).

### **Time-Cost Optimization Models:**

There are only few researches on TCO subject and they are summarized as follows:

(Zheng et. al., 2004) used GA and Pareto front approach; they developed a new algorithm for optimizing construction time-cost decisions. Their algorithm shows its efficiency by searching only a small fraction of the total search space. Its accuracy was verified by only small problems.

(Zheng et. al., 2004) compared their multi-objectives modified adaptive weight approach model with the previous single-objective models (Hegazy, 2002); The test results of the deterministic scenario confirm that the new model can correctly locate the non-replaceable points on

the segment of Pareto front within the limitation of time and cost.

They revealed that the model provides managers with greater flexibility to analyze their decisions in a more realistic manner.

Later on (Zheng et. al., 2005) applied a fuzzy sets theory to the original model to simulate uncertainty and produces better results especially as the risk increases, though it is not without weaknesses

Their model has significantly reduced the number of solutions generated for decision support, which is essential to multi-objective optimization, they proposed further refinements that are necessary to improve its efficiency when applied to large and complicated projects.

(Kasaeian, et. al, 2007) introduced a TCO model using Gas and a novel technique called Non-dominated Archiving to find the optimal solutions. Their model presented better solutions when compared to (Zheng et. al., 2005) with relatively higher computations.

(Xiong, et. al, 2008) presented a multi-objective TCO model using ACO as a searching tool, optimal solutions were generated, and outperformed (Zheng et. al., 2004) GA model results.

(Ng, et. al, 2008) also used ACO to find Time and cost optimality, the model was formulated and implemented on a commercial planning software. When performance compared with (Zheng et. al., 2005) model on large scale problems, results revealed better solutions for ACO model.

(Afshar, et. al, 2009) Adopted (Kasaeian, et. al, 2007) Non-Dominated Archiving technique and developed TCO model using multi colony ant algorithm. Results comparison with (Ng, et. al, 2008) model favored Non-dominant model, but no improvement in the solution from the original GA model, with the same calculation time.

Time-Cost Models can be summarized in **Table 1**

### **MODELING TCO**

To solve the TCO problem, project network for TCO must be considered as a graphic network. Firstly the project is converted to an Activity-On-Arrow (AOA) network as shown in Fig. (1). The performance of ACO algorithms in TSP can be seen as a reference for ACO-based TCO model.

In this network, the events (1, 2, 3... etc.) could be regarded as nodes and the different options for

each activity linking them would be the “distance” between these nodes.

Activity B in Fig. (1) could be taken as an example, there are three method options to complete this activity and they could be marked as B1, B2 and B3, and they are the different “distance” from event ① to event ④. Therefore, in ACO, the ants will travel from the first event ① to the event ⑦ with proper options selected for each activity.

Like the shortest tour being set as the objective in TSP, the objectives for TCO would be the minimal time and lowest cost. On the other hand, there are many differences between TSP and TCO, for example, ants should not come back to the starting points in TCO which is otherwise necessary in TSP; despite the numerous differences, ACO could competently handle TCO problems.

### MODEL DEVELOPMENT

To create an efficient optimization tool for Time and Cost and by considering the needs of the decision maker an evolutionary based model is created and developed, taking into account the strength and weaknesses of previous methods stated in the literature review for making this proposed model.

The developed model will transform time and cost from single option in an activity to optimum solutions that a construction project could be executed.

The model development process is divided into five important parts

- (i) Fitness function.
- (ii) Time and cost functions
- (iii) Ant Colony Solution Algorithm ACSA
- (iv) Pareto Front

#### • Fitness Function

Fitness Function (F.F.) represents planners and decision maker’s goal or what their needs are. To address a multi-objective optimization problem such as time, cost and to properly evaluate the solutions generated by the ACO, the fitness function consider both objectives and must be calculated during the ant colony solution algorithm part.

The FF. used is called Modified Adaptive Weight Approach (MAWA) which integrates both time

and cost into one single function and prioritize the time and cost according to the solutions found by the ant colony solution algorithm part, accordingly to be used again in the algorithm for evaluating these solutions and finding the best ant in any iteration of the model calculation.

This approach is effective and able to optimize time and cost concurrently and generate optimal solution (Zheng et. al., 2004), and (Kalhor et. al., 2011).

The weights can be calculated using (Zheng et. al., 2005) equations :

- If  $Z_t^{\max} = Z_t^{\min}$  and  $Z_c^{\max} = Z_c^{\min}$ :

Where:

$Z_t^{\max}, Z_c^{\max}$  : maximal value for the objective of time and total cost in the current iteration.

$Z_t^{\min}, Z_c^{\min}$  : minimal value for the objective of time and total cost in the current iteration.

$$W_t = W_c = 0.5 \text{ (eq.1)}$$

Where:

$W_t, W_c$ : the adaptive weight for the objective of time and total Cost.

- If  $Z_t^{\max} = Z_t^{\min}$  and  $Z_c^{\max} \neq Z_c^{\min}$ :

$$W_t = 0.1, W_c = 0.9 \text{ (eq.2)}$$

- If  $Z_t^{\max} \neq Z_t^{\min}$  and  $Z_c^{\max} = Z_c^{\min}$ :

$$W_t = 0.9, W_c = 0.1 \text{ (eq.3)}$$

- if  $Z_t^{\max} \neq Z_t^{\min}$  and  $Z_c^{\max} \neq Z_c^{\min}$ :

$$V_t = \frac{Z_t^{\min}}{Z_t^{\max} - Z_t^{\min}}, V_c = \frac{Z_c^{\min}}{Z_c^{\max} - Z_c^{\min}} \text{ (eq.4)}$$

$$V = V_t + V_c \text{ (eq.5)}$$

$$W_t = \frac{V_t}{V}, W_c = \frac{V_c}{V} \text{ (eq.6)}$$

Where:

$V_t, V_c, V$  represent Time, Cost, and project Value respectively.

This approach will generate optimal solution and will optimize both time and cost simultaneously.

The F.F. for any ant (k) in any given iteration will be:

$$f(k) = W_t \frac{Z_t^{\max} - Z_t(k) + R}{Z_t^{\max} - Z_t^{\min} + R} + W_c \frac{Z_c^{\max} - Z_c(k) + R}{Z_c^{\max} - Z_c^{\min} + R}$$

$$\text{(eq.7) (Zheng et. al., 2005)}$$

Where:

$Z_t(k)$  and  $Z_c(k)$  is the time and cost function for ant (k) in the current iteration.

R is a positive random number between 0 and 1.

This approach imparts the ACO with greater freedom to search in the multi-objective space that overcomes the drawbacks of single objective and hill-climbing algorithms.

These weights will guide the algorithms to search through a wider range against the objectives that have a relatively small exploration space in previous generation.

### • Time and cost Functions

To calculate  $Z_t(k)$  &  $Z_c(k)$  and prepare the necessary data to find the Non-dominant solution using Pareto front, two objectives were used for time and the total cost **designed for this purpose**

#### Time objective function

$$Z_t(k) = \text{Max}_{P_p \in P} \left[ \sum_{i \in P_p} t_{ij}^{(k)} x_{ij}^{(k)} \right] \text{ (eq. 8)}$$

(Researcher)

Where:

$t_{ij}^{(k)}$  : Execution time of option j in the activity i selected by ant k.

$x_{ij}^{(k)}$  : Index used to verify which option the ant selected to execute, if ant k selects option No. 4 then  $x_{ij}^{(k)} = 1$ , if not  $x_{ij}^{(k)} = 0$ .

$P_p$ : Activity Sequence of certain path.

P: All the Paths in the network.

#### Cost Objective Function

$$Z_c(k) = \left[ \sum_{i \in L} c_{ij}^{(k)} x_{ij}^{(k)} + Z_t(k)(IC) \right] \text{ (eq. 9)}$$

(Researcher)

Where:

$c_{ij}^{(k)}$  : Execution direct cost of option j in the activity i selected by ant k.

IC: project indirect cost rate.

L: number of project total activities.

### • Ant Colony Solution Algorithm

This process is the key to find the optimal solutions and the beating heart (core) of the developed model that the decision makers need. It transforms the time and cost from being a single option in one activity to an optimal solution consisted of set of best options to execute the project with, throughout a sequence of intelligent and efficient steps to select the best option combinations and constantly update the resulted best solution found yet.

The closed cycle of searching, communicating, evaluating, and learning is the reason of solution continuous improvement. it is in a sensible

balance between exploration of other solutions and exploitation of existing ones.

The Algorithm used in this model is ACS, due to its robustness in finding the shortest path and its low deviation from the optimal solution.

The ant colony solution algorithm is based upon (Dorigo et. al. 2004) ACS algorithm modified and developed to deal with construction projects networks ant to solve TCO

The ant colony solution algorithm contains four main steps :

- 1- Initiating ACS parameters
- 2- Creating the solutions
- 3- Path retracing and pheromone updating,

Figure (2) shows how and where the model development steps proceeds and interacts with each other

#### 1- Initialization of ACSA parameters

Depending on (Dorigo et. al., 2004) and after conducting Parameter Sensitivity Analysis the necessary parameters are set to start ACSA:

m: is the number of ants in each iteration

t: no. of iterations in the model (optional)

L: no. of activities the user input

n: no. of options in each activity the user input

$\alpha$ : Coefficient represent the importance of the pheromone value ( $\tau$ )

$\beta$ : Coefficient represent the importance of the heuristic value ( $\eta$ )

$\tau_0$ : initial pheromone value

$\rho$ : global pheromone evaporation rate ( $0 < \rho < 1$ )

$\epsilon$ : local pheromone evaporation rate ( $0 < \epsilon < 1$ )

q0: factor of the pseudorandom proportional action choice rule ( $0 < q_0 < 1$ )

Table (4.1) represents the parameters set by the researcher as the optimum parameter between exploration and exploitation; other parameters are variables and depend upon time-cost data that the user inputs (user oriented).

#### 2- Creating the Solution

The strategy of the algorithm is to exploit information gathered from pervious iteration (pheromone trails) ( $\tau_{ij}$ ) and heuristic information ( $\eta_{ij}$ ) calculated from input variables (option constructional properties) to construct candidate solutions and fold the information learned from constructing solutions again.

This step of the modeling starts by randomly generating solution using the first iteration (colony) to explore the environment and starts

learning what a good solution is. By evaluating the outcome of this iteration using MAWA to find the best solution, and then direct the next iteration (colony) towards the best solution found so far.

Fig. (2) shows that projects will have L activities where each activity has nL possibilities (construction options). To execute the selected activity, the model will have t number of iterations (colonies). In any colony there are m ants which will travel through the network to generate optimum solutions, This is the model complexity where Ant Colony Solution Algorithm can manage it efficiently yet it is easy for any user to use.

The bold line in fig. (3) represent the path taken by ant (K) selections and when the ant reaches the finishing point it will have a discrete time-cost solution. ACSA choices will be compared with other ants that crossed different paths to finish the project (each ant represents a candidate solution). it can be seen that the ant does not travel from an activity to the next activity according to the network dependency no matter what they are (finish to start, start to start, start to finish, finish to finish). Ants travel in a numerical order, the model manage the ant solutions and transform the ant selected option to a candidate solution with respect to the activity relationships that the project is subjected to.

Ants select an option from n options by performing pseudorandom proportional rule , when the ant travel throughout the project network it will perform the same rule for every activity until all the activities have been passed.

**Pseudorandom proportional rule:**

$$Option_j = \begin{cases} Max. \{ [\tau_{ij}]^\alpha [\eta_{ij}]^\beta \} & \text{if } q \leq q_0; \\ J & \text{otherwise,} \end{cases}$$

(eq.10)

Where:

- q : random variable between [0,1]
- q0 : tunable parameter.
- J: variable generated using random proportional rule (eq.12).

$\tau_{ij}$ : pheromone value of activity i option j .

$\eta_{ij}$ : heuristic value of activity i option j and calculated according to this equation :

$$\eta_{ij} = \frac{1}{Cost_{ij} * time_{ij}} \quad \text{(eq.11)}$$

Fig. (4) depicts the variables in one single option (J) to execute an activity in a project, the figure also shows the variables that are subjected to change during model calculations from those which will not change. The construction variables (time and cost entered by user for this option) generates the ACSA (heuristic value and the pheromone value will be generated by the algorithm according to equations 11, 13, and 15) respectively.

**Random proportional rule:**

$$P_{ij}^k = \frac{[\tau_{ij}]^\alpha [\eta_{ij}]^\beta}{\sum_{j \in n_k} [\tau_{ij}]^\alpha [\eta_{ij}]^\beta} \quad \text{(eq. 12)}$$

Ant selects an option by generating a random No. (q) uniformly distributed between [0,1] where it is compared to q0 (0 ≤ q ≤ 1).

If q ≤ q0, the ant selects the option with the higher value of both pheromone and heuristic value (using eq. 4.10); otherwise, the ant selects option from probability distribution created using (eq. 12)

### 3- Path Retracing and Pheromone Updating

This step contains two of the most important concepts in ACO (learning and communicating), which will contribute in improving the solution and exploring the solution environment, either by increasing the confidence in an option to become the most desirable choice or decrease it. This option will be the less desirable and almost neglected, without this step the solution will not change or improve.

The updating and evaporating occur only for the options selected by at least an ant, otherwise no changes will occur.

Pheromone Updating is divided in two types:

1- **Local pheromone update:** It retraces the ant k path and updates the pheromone value of the ant selection by applying equation (13). The importance of the local updating lies in using local evaporation rate to minimize the pheromone value of this option. To make this option less desirable for the ants in the same iteration, so they will not follow this ant directly to avoid premature convergence of the solution.

Therefore, achieving the maximum exploration possible in each iteration to and seek other options.

$$\tau_{ij}(t) = (1 - \varepsilon)\tau_{ij} + \varepsilon.\tau_0 \text{ (eq.13)}$$

Where:

$\varepsilon$ : local evaporation rate (factor used to minimize the pheromone value of the selected option)

$\tau_0$ : initial pheromone value of activity i and calculated by applying this equation:

$$\tau_0 = \frac{1}{L * \min(\text{time}_j * \text{cost}_j)} \text{ (eq.14)}$$

The activity option which have min. (time \* cost) will be selected to calculate the initial pheromone value because it has a rough estimation of the good solution.

$\tau_{ij}$ : pheromone trail of activity i option j in the previous iteration.

$\tau_{ij}(t)$ : pheromone value of activity i option j in this iteration (t).

2- Global pheromone update: When all the ants of the colony (in single iteration) travel the network and generate discrete solutions, the algorithm points the ants of the next colony (iteration) to the path that achieved the best outcome so far by updating only the path of this ant, the so called iteration best solution or the iteration best ant which got the lowest value in the F.F.

The global pheromone updating is done according to the following equation:

$$\tau_{ij}(t) = (1 - \rho)\tau_{ij} + \rho.\Delta\tau \text{ (eq.15)}$$

Where:

$\rho$ : global evaporation rate

$\Delta\tau$ : pheromone updating value for the option selected by the best ant in this activity and this iteration, calculated according to the following equation:

$$\Delta\tau = \frac{1}{F.F_{BS} \text{ value}} \text{ (eq.16)}$$

F.F.<sub>BS</sub> value: result of the best ant Fitness function calculation.

This step is repeated for each activity until finishing the best ant traveling throughout its project path. When the next iteration starts the pheromone value in this option combination will be relatively higher and will lead to more ants selecting these options.

### • Optimal Non-Dominant Solution(s) Using Pareto Front

In this step of the model development, the solution will be classified into optimum and not

optimum to give the decision maker only the optimum solutions to be used. A solution pool created to contain the outcome of the Ant colony solution algorithm, as shown in Fig.(5).

In each iteration ten solutions will be generated (if the recommended parameter setting used) and these solutions will be added to the solution pool and then by applying Pareto front only the optimum solution will be selected.

For the next iteration there will be ten more options, If any new solution ( $x^*$ ) is better than that exists Pareto Front solution( $x$ ) with at least one objective, then the solution will be compared according to the performance of the other objective; otherwise, the new solution will be sent to the solution pool so as to reduce the unnecessary calculations.

But when a new solution is better than an existing PF selected solution for both objectives (time and cost) the inferior solution will be sent back to the solution pool. When the model stops, there will be only dominant optimal solutions left in the PF Pareto Front constraints are:

If ( $x^*$ ) cost  $\geq$  ( $x$ ) cost and ( $x^*$ ) time  $\leq$  ( $x$ ) time  $\rightarrow$   
add  $x^*$  to Pareto front

If ( $x^*$ ) cost  $\leq$  ( $x$ ) cost and ( $x^*$ ) time  $\geq$  ( $x$ ) time  $\rightarrow$   
add  $x^*$  to Pareto front

If ( $x^*$ ) cost  $\geq$  ( $x$ ) cost and ( $x^*$ ) time  $\geq$  ( $x$ ) time  $\rightarrow$   
add  $x^*$  to solution pool

If ( $x^*$ ) cost  $\leq$  ( $x$ ) cost and ( $x^*$ ) time  $\leq$  ( $x$ ) time  $\rightarrow$   
add  $x^*$  to Pareto front  
add  $x^*$  to solution pool

### MODEL EVALUATION

Model outcome tested and compared with credible and reliable references to confirm and validate the performance with other models.

This problem first will be applied to test the performance of the developed model, including seven activities problem presented by (Feng, et. al., 1997), Table (3) represents the construction values of the problem, containing time and cost for each alternative option in every activity, and Fig. (6) represent the network of this problem, and the indirect cost was 1500\$/day.

The activities contains 3 to 5 possible options (alternative), so the problem complexity will be  $[(3^5) * 4 * 5] = 4860$  possible solutions. Although the project activities are only 7 but the



problem complexity is considered as medium for civil engineering problems.

The project critical path calculated first to find the normal duration and for that the options selected were the normal time/normal cost, and the project time was 105 days, and 253700 \$.

And after using TCO model the highest value of time was 68 days, and the cost was 220500\$.

From the total cost 0.15%, and 54.4% of the project time were saved by using optimized values. This is achieved by using the saved the indirect cost to use more advanced equipment and increase the number of the crews or labors in the construction work, or a different construction method may be used.

As we can see from Table (4), the maximum possible total cost reached was 233500\$ and it remains below both time and cost of the normal duration.

The comparison of the developed model solutions with two TCO models presented by (Zheng, 2004) using GA and (Xiong, 2008) using AS algorithm, is shown in Table (5).

By comparing the solutions of this problem with other reference solutions, the developed model shows the ability to generate global optimal solutions with an incredibly small time of 1 sec.

using only 10 ants in 20 iterations while Xiong ACO model used 40 ants and 40 iterations to achieve the same solution, and Zheng used 5 as a population size in each of the 5 generations (iterations).

The developed model efficiency showed by searching only 4% of the possible solution [200/4860] and generated the global optimal solutions.

## CONCLUSIONS

Ant Colony Optimization was able to generate optimal solutions in a fast and accurate way.

The developed model was able to generate global optimum solutions with less iterations and faster time compared to well-known time-cost optimization models.

Time and cost was optimized without dominating to only one function.

Time was saved by 54.4% while cost was 15% saved using the developed model.

Time-Cost Optimization Have A Great Effect On Lowering The Construction Time And Cost Of Construction Project In And Overcome The Delays And Cost Excess That Could Occurs During The Execution Of Any Construction Project

## REFERENCES:

Afshar, A.; Ziaraty, A.; Keveh, A.; and Sharifi, F. , (2009) " Non-dominated Archiving Multi-colony Ant Algorithm in Time-Cost Trade-Off Optimization "Journal of Construction Engineering and Management, Vol. 135, No. 7, July 1, pages 668-674 ASCE,.

Al-Samaraai, H. Fulla (2005) "Developing Computer Program To Implement Time-Cost Relationship For Planning Construction Projects In Iraq" M.Sc. thesis submitted to the Civil Engineering Department, Al-Mustansria University.

Chassiakos A. P. and Sakellariopoulos S. P. (2005) "Time-Cost Optimization of Construction Projects with Generalized Activity Constraints" Journal of Construction Engineering and Management, Vol. 131, No. 10, October 1, 1115–1124 ASCE.

Dorigo M. and T. Stützle (2004). "Ant Colony Optimization". London, England, The MIT Press.

Dorigo M. and V. Maniezzo (1991). "Positive feedback as a search strategy". Dipartimento Di Elettronica - Politecnico Di Milano, pages 91-116.

Elbeltagi, E.; Hegazy, T. and Grierson, D. (2005), "Comparison among Five Evolutionary-Based Optimization Algorithms " Advanced Engineering Informatics, 19 , pages 43–53, Elsevier Ltd.

Feng C.-W. Liu L., and Burns S. A. (1997), "Using Genetic Algorithms To Solve Construction Time-Cost Trade-Off Problems", Journal of Computing in Civil Engineering, Vol. 11, No.3, July, Pages 184-189, ASCE.

Feng C.-W. Liu L., and Burns S. A. (2000) "Stochastic Construction Time-Cost Trade-Off Analysis" Journal Of Computing In Civil Engineering. - April 2000. - pp. 117-126 ASCE.

Goyal S. K. (1975), " A Note on A Simple CPM Time-Cost Tradeoff Algorithm" Management Science, Feb., Vol. 21, No. 6, Application Series jstor.

Hegazy, T. (2002). "Computer-based Construction Project Management" Upper Saddle River, NJ, Prentice Hall.

Hendrickson C. and Au T. (1989), "Project Management for Construction Fundamental Concepts for Owners, Engineers, Architects and Builders" first edition Prentice Hall.

Kalhor E., Khanzadi M., Eshtehardian E., Afshar A. (2011), "Stochastic time-cost optimization using non-dominated archiving ant colony approach", Automation in Construction. Elsevier.

Kasaieian, A.; Shoghli, O., and Afshar, A. (2007), "Non-dominated Archiving Genetic Algorithm for Multi-objective Optimization of Time-Cost Trade-off" Proceedings of the 8th WSEAS International Conference on Evolutionary Computing, Vancouver, British Columbia, Canada, June 19-21 Pages 241-246.

Kelley J. E. (1961), "Critical-Path Planning and Scheduling: Mathematical Basis" Operations Research, May - Jun., Vol. 9, No.3 jstor

Li H., and Love P. (1997) "Using Improved Genetic Algorithms to Facilitate Time-Cost Optimization" Journal of Construction Engineering and Management, Vol. 123 September, No.3. , 0233-0237, ASCE.

Liu L, Burns S. A. and Feng C.-W. (1995) "Construction Time-Cost Trade-Off Analysis Using Lp/Ip Hybrid Method" Journal of Construction Engineering and Management, Vol. 121, No.4, 0446-0454 December, ASCE,

Ng. Thomas S., and Zhang Y., (2008) "Optimizing Construction Time and Cost



Using Ant Optimization” *Journal of Construction Engineering and Management*, Vol. 134, No. 9, September 1, pages 721–728, ASCE.

Patterson J. H and Huber W. D. (1974) “A Horizon-Varying, Zero-One Approach to Project Scheduling”. *Management Science*, Vol. 20, No. 6, Application Series, Feb., pp. 990-998 jstor.

Prager W. (1963) “A Structural Method of Computing Project Cost Polygons” *Management Science*, Vol. 9, No. 3 (Apr., 1963), pp. 394-404 jstor.

Robinson D. R. (1975), “A Dynamic Programming Solution to Cost-Time Tradeoff for CPM” *Management Science*, Oct., Vol. 22, No. 2 pp. 158-166Published

Siemens N. (1971) “A Simple CPM Time-Cost Tradeoff” *Management Science*, Vol. 17,

No. 6, Application Series Feb., pp. B354-B363 jstor.

Xiong, Y.; and Kuang, Y. (2008), “Applying an Ant Colony Optimization Algorithm-Based Multi-objective Approach for Time–Cost Trade-Off”, *Journal of Construction Engineering and Management*, Vol. 134, No. 2, February 1, Pages 153-156, ASCE.

Zheng, D.; Ng, T.; and Kumaraswamy. M. (2004),” Applying a Genetic Algorithm-Based Multi-objective Approach for Time-Cost Optimization” *Journal of Construction Engineering and Management*, Vol. 130, No. 2, April 1, pages 168-176, ASCE.

Zheng, D.; Ng, T.; and Kumaraswamy. M. (2005),” Applying Pareto Ranking and Niche Formation to Genetic Algorithm-Based Multi-objective Time–Cost Optimization” *Journal of Construction Engineering and Management*, Vol. 131, No. 1, January 1, pages 81–91, ASCE.

### LIST OF ABBREVIATIONS

ACO:	Ant Colony Optimization
ACS:	Ant Colony System
ACSA:	Ant Colony Solution Algorithm
AOA:	Activity on Arrow
DC:	Direct Cost
FF:	Fitness Function
GA:	Genetic Algorithm
IC:	indirect cost rate.
MA:	Memetic algorithms
MAWA:	Modified Adaptive Weight Approach
PF:	Pareto Front
PSO:	Particle Swarm optimization
SFL:	Shuffled Frog Leaping
TCO:	Time-Cost Optimization
TCT:	Time-Cost Trade-off
$C_{ij}^{(k)}$ :	Execution of direct cost of option j in activity i selected by ant (k)
J:	Variable generated using random proportional rule
K:	Random ant
L:	Total number of project activities
m:	The number of ants in each iteration
n:	No. of options in each activity the user input
P:	All the Paths in the network
$P_p$ :	Activity Sequence of certain path
q:	Random variable between $[0 < q < 1]$
q0:	Factor of the pseudorandom proportional action choice rule $[0 < q0 < 1]$
R:	Positive random number between $[0 < R < 1]$
S:	Total number iterations
T:	No. of iterations in the model (optional)
$t_{ij}^{(k)}$ :	Execution time of option j in activity i selected by ant (k)
$V_t, V_c, V$ :	Value of Time, Cost, and Project, respectively
$W_t, W_c$ :	Adaptive weight for the objective of time and total cost
$x_{ij}^{(k)}$ :	Index used to verify which option the ant selected to execute
$Z_c(k)$ :	Objective function of cost for ant (k) in the current iteration
$Z_t(k)$ :	Objective function of time for ant (k) in the current iteration
$Z_t^{max}, Z_c^{max}$ :	Maximal value for objective of time and total cost in current iteration
$Z_t^{min}, Z_c^{min}$ :	Minimal value for objective of time and total cost in current iteration
$\alpha$ :	Coefficient represents the importance of the pheromone value ( $\tau$ )
$\beta$ :	Coefficient represents the importance of the heuristic value ( $\eta$ )
$\Delta\tau$ :	Best ant pheromone updating value
$\epsilon$ :	Local pheromone evaporation rate $[0 < \epsilon < 1]$
$\eta_{ij}$ :	Heuristic value of activity i option j
$\rho$ :	Global pheromone evaporation rate $[0 < \rho < 1]$



$\tau_0$ : Initial pheromone value

$\tau_{ij}$ : Pheromone value of activity i option j

TSP: Traveler salesman problem

### FIGURES

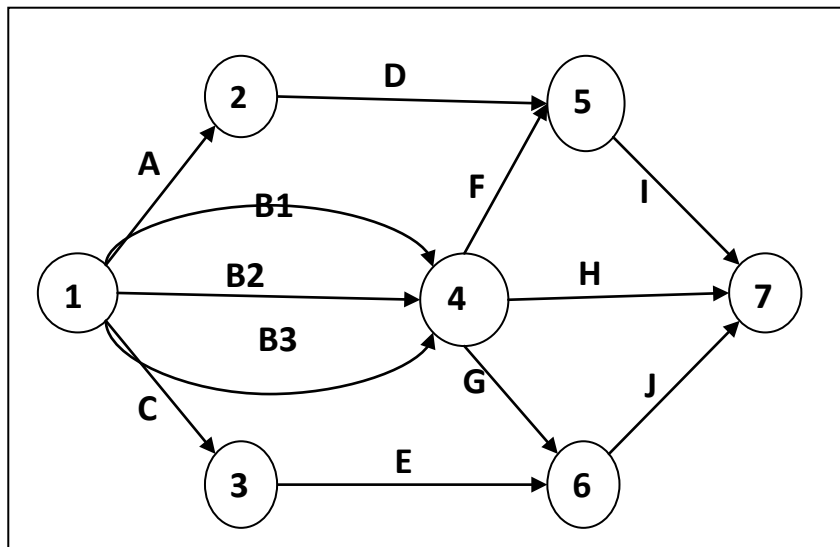


Fig. (1): TCO Project (AOA Network).

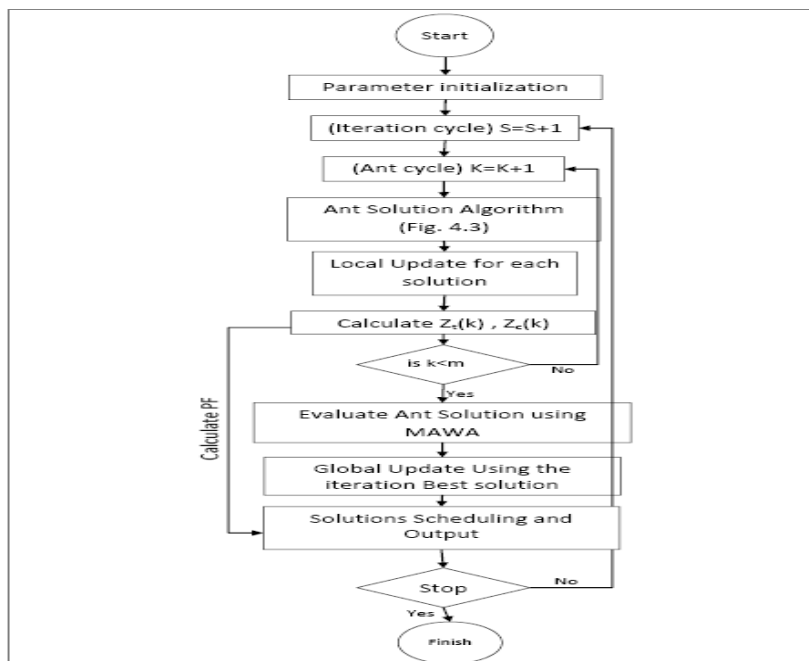
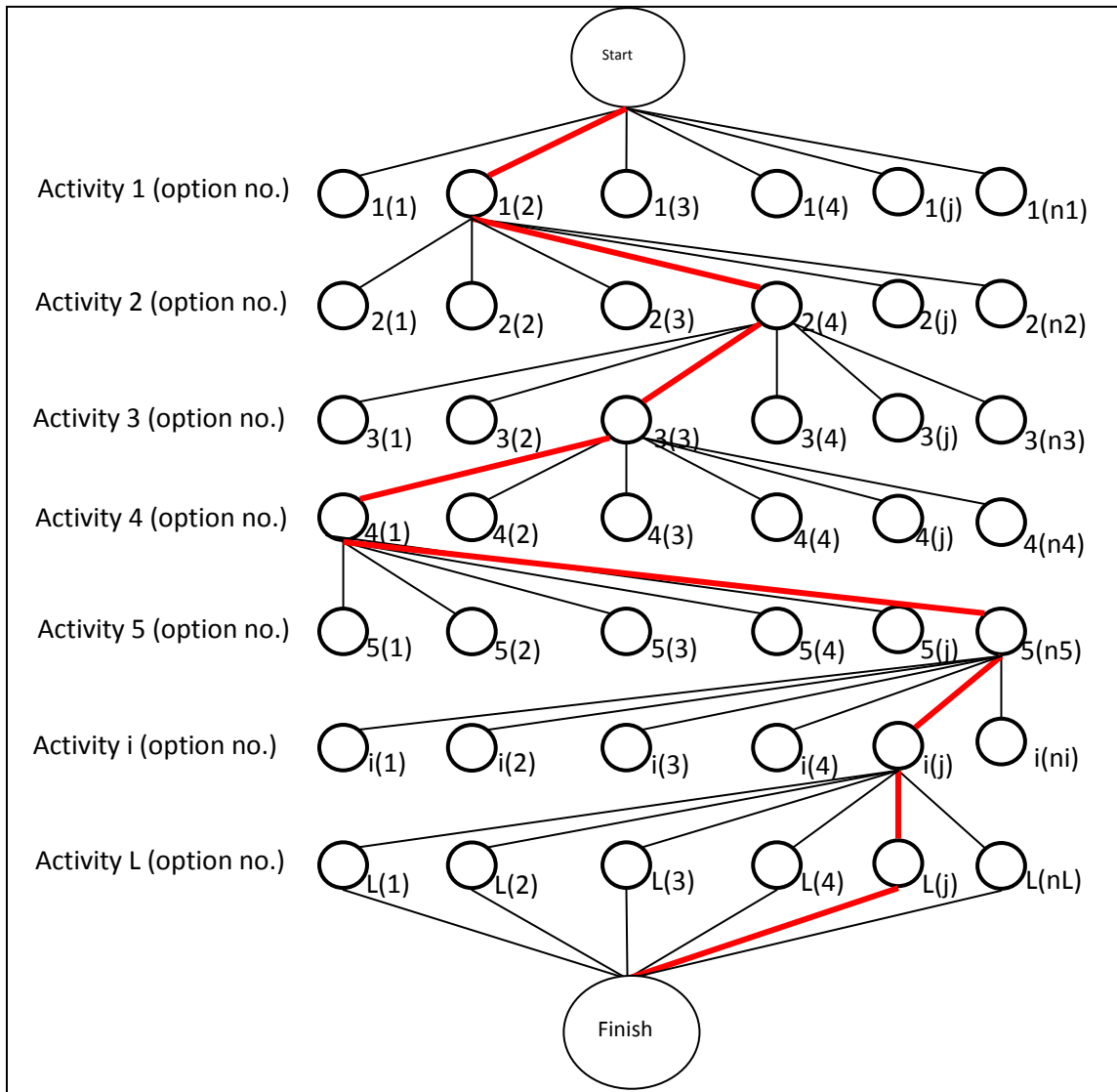
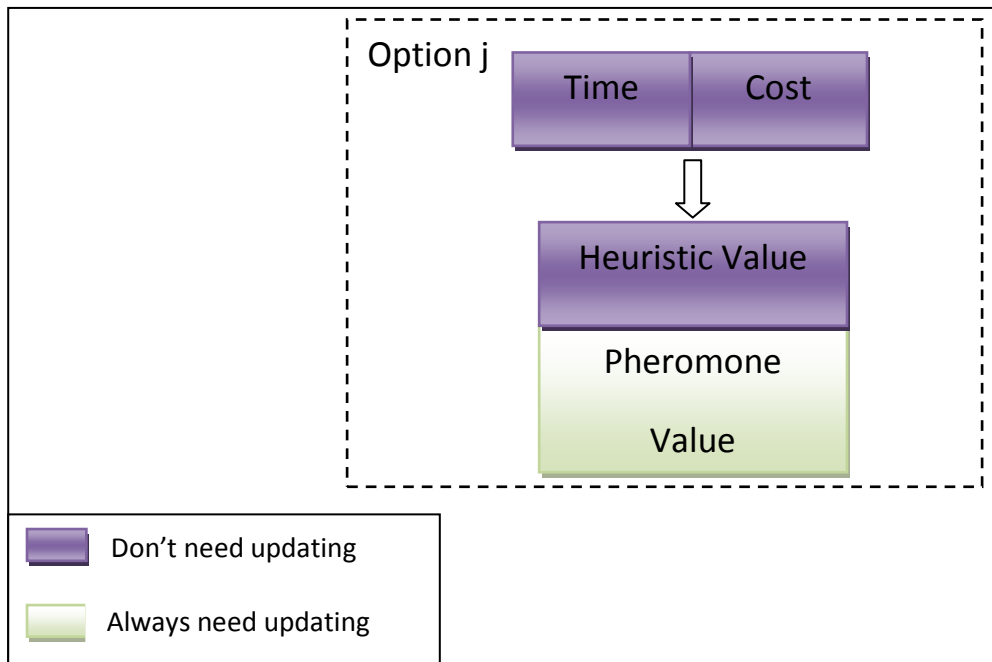


Fig (2): Developed Model Flowchart.



**Fig. (3): Graphical Representation of Ants' traveling through construction projects Activities (Researcher).**



**Fig. (4): Option  $j$  Variables (Researcher).**

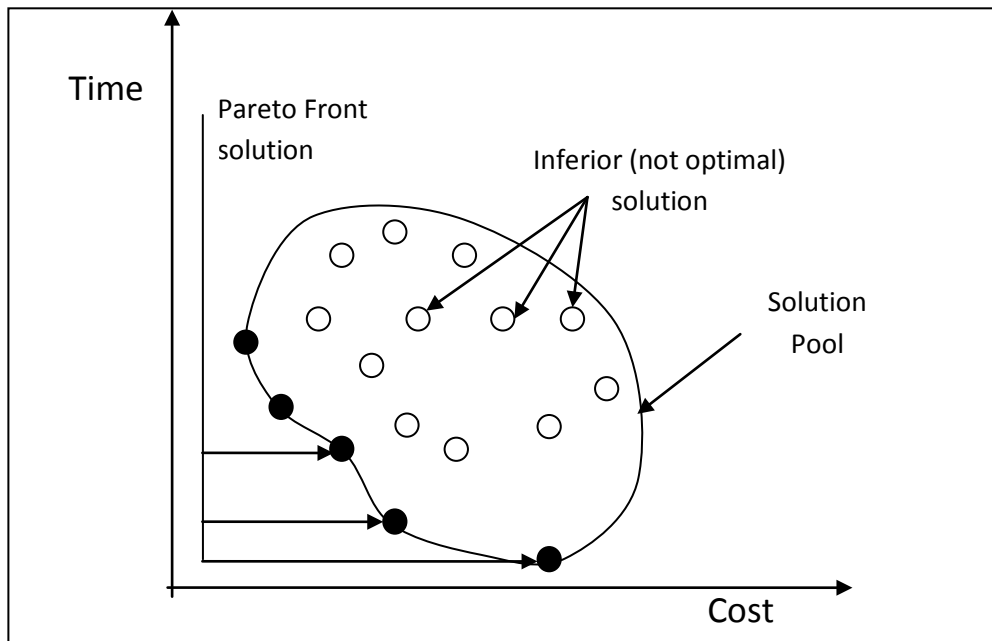


**Fig.(5): Pareto front and solution pool.**

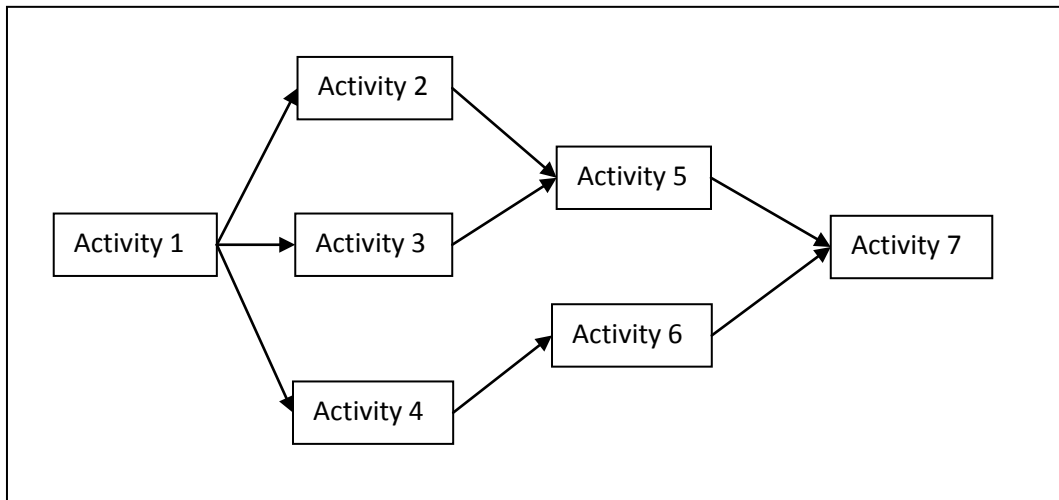


**Fig. (6):** Network representation of the 7 activity reference problem.

**Table (1) Time-Cost Models (Researcher)**

Time-Cost Trade-off			Time-Cost Optimization
Heuristic Models	Mathematical Models	Evolutionary-Based Optimization Algorithm Models	Evolutionary-Based Optimization Algorithm Models
Structural Interpretation (Prager, 1963)	Linear Programming (Kelly, 1961)	Genetic Algorithms (Feng et. al. 1997)	Genetic Algorithms (Zheng et. al. 2004)
	Zero-One Programming (Patterson, 1974)	Genetic Algorithms (Feng et. al. 2000)	Genetic Algorithms (Zheng et. al. 2005)
Cost Slope (Siemens, 1971)	Dynamic Programming (Robinson, 1975)	Genetic Algorithms (Li et. al. 1997)	Genetic Algorithms (Kasaeian et. al. 2005)
Effective Cost Slope (Goyal, 1975)	Linear Programming (Handrickson, 1989)	Genetic Algorithms, Particle Swarm, Ant Colony, Shuffled Frog Leaping and Mimetic Algorithms (Elbaltagi, et. al 2005)	Ant Colony Optimization (Xiong, et. al. 2008)
Cost Slope (Al-Samaraai, 2005)	Linear/Integer Programming (Lui, et. al. 1995)		Ant Colony Optimization (Ng, et. al. 2008)
	Linear Programming (Chassiakos et. al. 2005)		Ant Colony Optimization (Afshar, et. al. 2008)

**Table (2): Model recommended parameters (Researcher)**

<i>Parameter</i>	<i>Value</i>	<i>Parameter</i>	<i>Value</i>
$m$	10	$\rho$	0.002
$\alpha$	1	$\varepsilon$	0.1
$\beta$	2	$q_0$	0.4

**Table (3): Reference Problem (7 Activity) (Feng, et. al., 1997)**

Activity	Precedence	Option No.1		Option No.2		Option No.3		Option No.4		Option No.5	
		Time (Days)	Cost (\$)								
1-Site Preparation	-	14	23,000	20	18,000	24	12,000	-	-	-	-
2-Forms and rebar	1	15	3,000	18	2,400	20	1,800	23	1,500	25	1,000
3-Excavation	1	15	4,500	22	4,000	33	3,200	-	-	-	-
4-Precast concrete girder	1	12	45,000	16	35,000	20	30,000	-	-	-	-
5-Pour foundation and piers	2.3	22	20,000	24	17,500	28	15,000	30	10,000	-	-
6-Deliver PC concrete	4	14	40,000	18	32,000	24	18,000	-	-	-	-
7-Erect girders	5.6	9	30,000	15	24,000	18	22,000	-	-	-	-

**Table (4): Option selection and solution generated for the 7 activity reference problem (indirect cost is 1500\$/day)**

Solution	Project Time (Days)	Project Total Cost (\$)	Options selected by the model to execute the corresponding activity						
			1	2	3	4	5	6	7
1	60	233500	1	1	1	1	1	3	1
2	62	233000	1	1	1	3	2	2	1
3	63	225500	1	1	1	2	2	3	1
4	67	224000	1	1	1	3	3	3	1
5	68	220500	1	1	1	3	4	3	1

**Table (5): Solution comparison of (7activity) reference problem**

Zheng Model 2004		Xiong Model		Developed Model	
Time (Days)	Total cost (\$)	Time (Days)	Total cost (\$)	Time (Days)	Total cost (\$)
66	236500	60	233500	60	233500
73	251500	62	233000	62	233000
84	251000	63	225500	63	225500
-	-	67	224000	67	224000
-	-	68	220500	68	220500



## Study of the Friction Stir Welding For A516 Low Carbon Steel

Prof. Dr. Qasim Mouhamed Doos  
Department of Mechanical Engineering  
College of Engineering - Baghdad University  
E- mail : [Kasim\\_daws@yahoo.com](mailto:Kasim_daws@yahoo.com)

Riyadh F. Farhan  
Department of Mechanical Engineering  
College of Engineering - Baghdad University  
E-mail: [riadh\\_engineer81@yahoo.com](mailto:riadh_engineer81@yahoo.com)

### ABSTRACT

The main objective of present work is to describe the feasibility of friction stir welding (FSW) for joining of low carbon steel with dimensions (3 mm X 80 mm X 150 mm). A matrix (3×3) of welding parameters (welding speed and tool rotational speed) was used to see influence of each parameter on properties of welded joint .Series of (FSW) experiments were conducted using CNC milling machine utilizing the wide range of rotational speed and transverse speed of the machine. Effect of welding parameters on mechanical properties of weld joints were investigated using different mechanical tests including (tensile and microhardness tests ). Micro structural change during (FSW) process was studied and different welding zones were investigated using optical microscope. The stir welding experiments conducted that show the low carbon steel can be welded using (FSW) process with maximum welding efficiency (100.02%) in terms of ultimate tensile strength using best result of welding parameters (700 RPM, 25 mm/min, tool rotational speed and welding speed respectively and 0.2 mm plunging depth of welding tool) ,there is afirst time that we obtain the efficiency reach to 100.02 % to weld this type of low carbon steel by FSW. The corrosion resistance was measure which is the new test on the welding by this way and we obtained different result from the result on traditional welding processes and the result that obtained show the corrosion resistance for this welding plate better than the base metal. Maximum temperature has been calculated numerically by using the ANSYS program. The obtained peak temperature is 1102°C, A percentage minimum of the melting point .

**KEYWORDS :** FSW, Mechanical properties, FEM simulation .

### دراسة اللحام بالخلط الاحتكاكي للفولاذ الواطيء الكاربون A516

م.م. رياض فرع فرحان  
قسم الهندسة الميكانيكية  
كلية الهندسة / جامعة بغداد

أ.د. قاسم محمد دوس  
قسم الهندسة الميكانيكية  
كلية الهندسة / جامعة بغداد

#### الخلاصة

اللحام بالخلط الاحتكاكي هي احدى عمليات اللحام الحديثة ، اللحام بالخلط الاحتكاكي هي احدى طرق لحام الحالة الصلبة التي بها يتم دوران اداة الخلط وتجير القطعتان على الترابط بتأثير مركب من الحرارة والجهد الميكانيكي . ان الغرض الرئيسي من هذا العمل هو لبيان امكانية طريقة اللحام بالخلط الاحتكاكي من ربط قطعتان من الفولاذ المنخفض الكربون ذات ابعاد (150 ملم × 80 ملم × 3 ملم ) . تم استخدام مصفوفة (3×3) من متغيرات اللحام والتي تمثل ( السرعة الدورانية لعدة اللحام والسرعة الخطية للحام) لدراسة تأثير كل متغير من هذه المتغيرات بشكل منفصل على خواص وصلات اللحام . تم القيام بسلسلة من تجارب اللحام باستعمال ماكينة تفريز الميكانيكي المبرمجمة ( CNC ) ذات المدى الواسع من

السرعة الدورانية والسرعة الخطية لهذه الماكينة. تأثير متغيرات اللحام على الخواص الميكانيكية لوصلات اللحام تم دراستها بالأعتماد على الفحوصات الميكانيكية المختلفة (فحص الشد ، فحص الصلادة) . كما تم دراسة التغيرات الميتالورجية خلال عملية اللحام ودراسة مناطق اللحام المختلفة بأستعمال المجهر الضوئي . بناءاً على التجارب المختلفة في هذه الدراسة أتضح من النتائج بأن الفولاذ المنخفض الكربون قابل للحام بهذه الطريقة مع الحصول على اقصى كفاءة لحام وصلت الى (2,100%) بدلالة مقاومة الشد بأستخدام متغيرات اللحام المثلى (700 دورة بالدقيقة سرعة دورانية ، 25 ملم / دقيقة سرعة لحام ، 0,2 ملم عمق عدة الغرز ) تم حساب اقصى درجة حرارة عددياً"بأستعمال برنامج (ANSYS) . وكانت اقصى درجة حرارة حصلنا عليها هي (1102 درجة سيليزية ) التي كانت اقل بكثير من درجة حرارة انصهار الفولاذ الكربوني

**كلمات رئيسية : لحام بالخلط الاحتكاكي ، الخواص الميكانيكية ، المحاكاة باستخدام طريقة العناصر المتناهية**

## 1 INTRODUCTION

Exploration for welding process is expanding , one of the welding process is (FSW) , It is a modern method to joint parts as a solid state welding process , anon consumable tool used . The tool have large diameter called shoulder and small diameter called pin . And by the friction between the piece and shoulder the heat will be generated. There is some of advantages in welding rejoin such as reduced of porosity, lower distortion and shrinkage. (Thomas 1991). ( Scott M. 2005 ) present tool geometry and process parameters for PCBN tool . (Thomas 1991) describe the tool and equipment required to study FSW . (Naiyi 2004) study the FSW of Mg alloy . (Takehito 2006) tried to joint dissimilar metal such as Al to steel. (Tery and 2003) focused on heat flow in FSW tool. (X.K.Zhn 2003) simulated temperature and stresses in FSW for stainless steel . ultrahigh carbon steel during FSW was applied by (Y.S. Sato 2007). ( T. Saeid 2008) focused on the welding speed and it is effected on the properties of stir zone .

## 2 EXPERIMENTAL PROCEDURES

An overview of the used FSW tool is shown in figure 1 quantitative information can be illustrated in Table 1. The tool is fitted into a tool holder and linked to the machine spindle. The tool is rotated clockwise as seen from above the weld.

(FSW) were produced on plates A516 low carbon steel (3 mm thick). The plates of Low Carbon Steel were prepared with the dimensions (160mmx80mmx3mm) as shown in figure 2 .Each

two plates were joining with the friction stir welding.

The plates were manufactured to get minimum faults which affect on the quality of welding.

Chemical analysis has been conducted in the Specialized Institute for Engineering Industries for these plates.

The table 2 shows the chemical composition for the Steel plate that used in present work.. Welds were made in the butt-joint configuration on samples typically. The dimensions 150 mm length and 80 mm width. The shoulder diameter used (16 mm), The length of the pin was approximately (2.6 mm). A Tungsten carbide (WC) tool was used. Table 2 gives the FSW parameters for low carbon steel. The Vickers microhardness of the weld have been measured in the center of the thickness in the advancing side. Tensile specimens were prepared accordance to ASTM E8.

## 3 RESULTS AND DISCUSSION

### 3.1 Fsw Joint

It is clearly seen that sound joints are obtained up to the welding speed of 50 mm/min. However, at a higher speed of 150 mm/min, a groove-like defect is observed in the joint advancing side figure 3. This defect can seriously degrade the mechanical properties of the weld metal. Previous studies revealed that groove-like defects are primarily formed when the heat input during FSW is insufficient. In this situation, the material could not easily flow to fill up the gap generated by the tool pin. As will be described in subsequent section, one of the key parameters that have an essential influence on the heat input is the welding speed.



With increasing the welding speed, the heat input would be decreased gradually up to a limit that the generated frictional heat is insufficient to allow viscoplastic material flow and therefore, the groove-like defect is more likely to occur.

### 3.2 The Weld Thermal

The temperature distribution varies in time and space; hence a three-dimensional, transient, isotropic solid with moving heat source model was used to simulate FSW thermal process. The conservation of energy in a differential form can be written as (ANSYS v.10),(John 2005).

$$\rho c_p(T) \frac{\partial T}{\partial t} = k(T) \left( \frac{\partial^2 T}{\partial x^2} + \frac{\partial^2 T}{\partial y^2} + \frac{\partial^2 T}{\partial z^2} \right) + \dot{Q} \quad (1)$$

Where:  $\rho$  : density  
 $c_p(T)$  : specific heat  
 $T$  : temperature  
 $t$  is time  
 $k(T)$  : temperature

$\dot{Q}$  is rate of heat generation

Temperature dependent thermal properties. Three boundary conditions associated with equ. (1) as shown in figure (4 ). The first is the energy loss by heat convection which is defined by

$$Q_{conv} = h_c (T - T_a) \quad (2)$$

Where:  
 $Q_{conv}$ : energy loss of by convection per unit area.  
 $h_c$ : coefficient of the heat transfer ( $h=30 \text{ W/m}^2 \text{ }^\circ\text{C}$ )  
 $T$ : absolute surface temperature.  
 $T_a$ : absolute ambient temperature ( $T_a=298 \text{ }^\circ\text{K}$ ).  
 The equivalent convection coefficient for the workpiece/backing plate interface is calculated by (Frigaard 2001),(Hwanga 2008)

$$Q_b = h_b (T - T_a) \quad (3)$$

Where:  $Q_b$ : energy loss of by convection per unit area.  
 $h_b$ : convection heat transfer coefficient. ( $h=350 \text{ W/m}^2 \text{ }^\circ\text{C}$ ).

The third type is the radiation heat loss which is defined by

$$Q_{rad} = eF\sigma_{SB} (T^4 - T_a^4) \quad (4)$$

Where:  $Q_{rad}$ : energy loss of by radiation per unit area.

$e$ : effective emissivity of radiant surface ( $e=0.5$ ).

$F$ : radiation view factors ( $F=1$ ).

$\sigma_{SB}$ : Stefan-Boltzman constant  
 ( $\sigma_{SB}=5.67 \times 10^{-8} \text{ W/m}^2 \text{ }^\circ\text{K}^4$ ).

The heat generation during friction- stir is difficult. And in general we note that the total heat generated from the shoulder may be used to compensate for deformation heat generation; this could be done by an adjusting coefficient of friction. Friction is a complex physical phenomenon that depends on parameters like material, surface roughness, lubrication, temperature and pressure Frictional heat generated by the shoulder face may be derived, where area element on shoulder face is:

$$dA = 2 \pi r dr \quad (5)$$

Frictional torque required is given by:

$$dM = \mu P r dA = 2 \pi \mu P r^2 dr \quad (6)$$

Where:  $M$  : torque

$\mu$  is the friction coefficient

$P$  is the interfacial pressure

Frictional heat for the shaft rotating at rubbing angular speed of  $(1-\delta)\omega$  is:

$$dQ_s = (1 - \delta) \omega dM = 2 \pi (1 - \delta) \omega \mu P r^2 dr \quad (7)$$

where  $\delta$  is the slip factor that compensate for tool/material relative velocity. Typical values for slip factor found in literature ranges between 0.6, 0.85 (Takehiko 2006). Total frictional heat of shoulder will be:

$$Q_s = \int_0^{R_s} dQ_s = \frac{2}{3} \pi (1-\delta) \omega \mu P R_s^3 \quad (8)$$

In similar concept, heat generated by lateral surface of the pin is :

$$Q_p = 2 \pi (1-\delta) \omega \mu P L_p R_p^2 \quad (9)$$

Total frictional heat generated by the tool is the summation of equ. (9) and equ. (10) which is:

$$Q_t = 2 \pi (1-\delta) \omega \mu P \left( \frac{R_s^3}{3} + L_p R_p^2 \right) \quad (10)$$

During the process the tool travels at a constant speed (Vt). This motion was simulated by changing heat source location, as shown in Figure 5. according to the following equation:

$$X_{i+1} = X_i + V_t \Delta t \quad \text{for} \quad L_i \leq X \leq L_w \quad (11)$$

Where  $\Delta t$  is the time required for the tool to travel from location  $X_i$  to  $X_{i+1}$ , (i.e. element size) and  $V_t$  is the tool traveling speed

$L_i$  : Welding Starting position =  $2 * R_s$ .

$L_w$ : Weld length

.Final comments may be mentioned regarding ANSYS program description. The three dimensional element "SOLID70", shown in Figure (6), selected in the thermal model. "SOLID70" has a 3-D thermal conduction capability. The nodes has asingle degree of freedom and each element has 8 nodes . The applicable is 3D transient , steady state analysis. In order to include radiation heat transfer, the element "SURF152", Figure(7), was used with extra node option. It simulates radiation heat loss to a space node and is applicable to 3-D thermal analyses.

One of the two classes of radiation systems must be specified in ANSYS, either open radiation system or closed one. In case of an open radiation system (in contrast with closed radiation system), in which no surfaces that receive the radiated energy can be specified, a space node should be defined. Space node serves to absorb all radiated energy (ANSYS v.10). Space node temperature was used same as the ambient temperature. Element type "SURF152" was used to simulate

radiation and convection heat loss, where it was overlaid on the free faces of element "SOLID70". The peak temperature obtained is 1102°C as shown in figure 8 , The material properties as shown in table (3).

### 3.3 Tensile Test

To investigate the effect of different welding parameters on tensile strength of welded joint, tensile tests have been conducted using specimen for each of the welded joints. Tensile specimens were machined from the welds according to the ASTM sub-size specimen geometry shown in figure (9), such that the weld nugget was positioned in the middle of the specimen gage length (transverse specimen).

The test results have been compared with the base metal .The competence for friction stir welding have been calculated for each experiment as follows:

Joint Efficiency = test of tensile strength / ultimate tensile strength (Base metal).

Frome the results noticed that the mechanical properties affected by welding parameters (rotational speed and welding speed) for welded plates.

On my view to obtain high quality of (FSW) welded joints with high mechanical properties i.e. high welding efficiency; the main welding parameters(rotational speed, welding speed) must be carefully selected to obtain high efficiency as shown in table (3), the tensile tests strength and its efficiency are decreased directly with increasing of welding speed.

In this work the selcted metal gives high welding efficiency when welded using (700 RPM rotational speed, 25 mm/min welding speed) that get (100.02%) welding joint efficiency. There is afirst time that we obtain the efficiency reach to 100.02 % to weld steel by FSW. Frome Figure (19-12) which explain the relation between the welding speed of welding tool and tensile strength for the same rotational speed ,as welding speed increase(more than 25 mm/min) the tensile strength decrease for the same rotational speed due to decrease in heat generation.

### 3.4 Corrosion Resistance Test.

The current and potential had passed (-309.4 mV) and (565.91 nA/cm<sup>2</sup>) are respectively. The experiment had required to 15 minutes. The electrochemical cell show that the penetration loss for welded plate are less than the base metal see table 5. So The corrosion resistance of base metal is less than stir zone. There are two reasons to interpret these results. Firstly, because there is a change in microstructure and the grain size of stir zone is finer than that of base metal. Secondly, the temperature of friction stir welding is less than the melting point so this degree make a heat treatment (stress release) to the welded plate. The results that appear in the form of a curves in the computer as shown in figure (13) and figure (14).

### 3.5 Microhardness Results

The microhardness was measured from center of welding to the base metal at a spacing of (1mm). Microhardness results show that an increase in hardness values in the stir zone. The increased values are probably because of to the dislocation density of the weld nugget. Another reason to increase the hardness because of the small grain size of pearlite phases in the stir zone. For each set of measurement (see Table 6) the microhardness is decreased with increasing the welding speed because the peak temperature decreased with welding speed increasing. Hardness profiles for each welded samples are shown in Figs.(15-22).

### 3.6 Microstructure Results

The effect of friction stir welding on the material combines heat flow and plastic strain. The heat generated by friction between the tool shoulder and the top of the sheets, and plastic flow by the rotation of the pin tool. These thermo-mechanical condition vary through the joint. The weld region displayed several microstructurally distinct regions including the stir zone (nugget zone), (along the weld centerline), a grain-coarsened region (surrounding the stir zone), a grain-refined region (encompassing the grain-coarsened region). The figures (23,24 and 25) show that there is no change in the phases. In other words the nugget zone and

base metal have the same phase (pearlite+ferrite). But the difference is in the grains size, shapes and distribution which gives the difference in mechanical properties. The pearlite has yarn shape with homogeneous distribution in the base metal, while it has different sizes masses and nonhomogeneous distribution in nugget zone. In heat affected zone the particles of pearlite as form homogeneous masses

### CONCLUSIONS

According to results of the present study of (FSW) process on selected steel, several conclusions can be writing regarding alloy weldability, mechanical, microstructural and modeling.

- Low alloy steel with (0.13% C) is weldable using different (FSW) parameters giving different welding efficiencies.
- The maximum weld strength obtained in this study was (437.09 MPa) or (100.02%) weld efficiency with (14.20 %) elongation is recorded in the weld.
- The weld region displayed several microstructurally distinct regions, But there is no change in the phases, In other words the nugget zone and base metal have the same phase (pearlite+ferrite), But the difference is in the grains size, shapes and distribution.
- FSW defects are related to welding parameters, defect free (FSW) welds can be obtained using best main welding parameters (700 RPM + 25mm/min).
- FSW for steel gives a very good corrosion resistance with respect to the base metal.
- The peak temperature theoretically obtained was 1102°C, which was less than the melting point of low carbon steel.

## REFERENCES

ANSYS v.10 help, "ANSYS Theory reference".

Hwanga ,Yeong-Haw Hawang,Zong –Wei kang,yuang-cherng chiou and Hung Hsion Hsu, 2008. "Experimental Study on Temperature Distributions within the Workpiece during Friction Stir Welding of Aluminum Alloys." International Journal of Machine Tools and Manufacture, No. 48, pp 778–787.

John A. Goldak and 2005 Mehdi Akhlaghi, "Computation Welding Mechanics" Springer Science and Business Media, Inc.

Naiyi Li,Tsung-Yu,Ronald P. Cooper,Dan Q. Houston,Zhili Feng and Michael L. Santella. 2004. FRICTION STIR

Thomas WM, Nicholas ED, Needham JC, Church MG, Templesmith P., Dawes C. Intl. 1991 Patent Application no PCT/GB92/02203 and GB Patent Application no. 9125978.9,.

T. Saeid ,A. Abdoollah zadeh ,H.Assadi and F. Malek Ghaini. 2008 Effect of friction stir welding speed on the microstructure and mechanical properties of a duplex stainless steel , Materials Science and Engineering A 496 pp 262–268

WELDING OF MAGNESIUM AM60 ALLOY. Magnesium Technology Edited by A. Lou

Scott M. Packer ,Tracy W. Nelson,Russell J. Steel and Murray Mahoney.2005. Tool Geometries and Process Parameters Required to Friction Stir Weld High Melting Temperature Materials

Takehiko Watanabe ,Hirofumi Takayama and Atsushi Yanagisawa 2006" Joining of aluminum alloy to steel by friction stir welding" Journal of Materials Processing Technology 178 pp. 342–349.

Terry Dickerson ,Qing-yu Shi and Hugh Shercliff.2003. HEAT FLOW INTO FRICTION STIR WELDING TOOLS , 4th International Symposium on Friction Stir Welding.

X.K. Zhu, Y.J. Chao 2004. Numerical simulation of transient temperature and residual stresses in friction stir welding of 304L stainless steel 146 pp 263–272

Y.S. Sato ,H. Kokawa and T. Furuhashi. 2007. Microstructural evolution of ultrahigh carbon steel during friction stir welding 57 pp 557–560



NOMENCLATURE

- A : Cross section area of the tool (mm<sup>2</sup>)
- C<sub>p</sub> : The specific heat (J/Kg.K)
- F<sub>f</sub> : Friction force (N).
- F<sub>n</sub> : Normal force (N).
- k : Heat conductivity (W/m.k)
- T : Temperature (K or °C).
- FSW : Friction stir welding

Greek Symbols

- $v$  : Welding speed (mm/min).
- $\omega$  : Rotational speed (rev/min)
- $\rho$  : Density (Kg/m<sup>3</sup>).
- $\mu$  : Coefficient of friction.



Fig. 1 Welding Tool

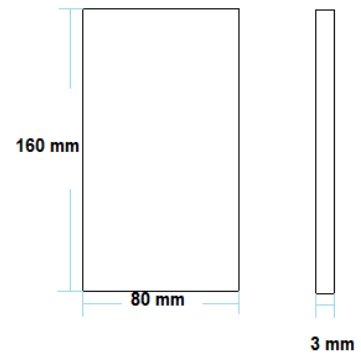


Fig. 2 welding plate

Table 1 Details of the tool used in friction stir welding.

Tool Feature		Tool Detaile
Shoulder	Diameter	16 mm
	Material	WC
Probe	Base Diameter	4mm
	Top Diameter	2mm
	Length	2.6mm
	Material	WC

Table (2): The chemical composition of Plates A516 ASTM.

Sample	C %	Si%	Mn%	P%	S%	Cr%	Mo%	Ni%	Cu%	Al%	Fe%
Chemical composition	0.130	0.003	0.496	0.008	0.003	0.007	0.002	0.042	0.036	0.040	Bal.



Fig. 3 a groove-like defect

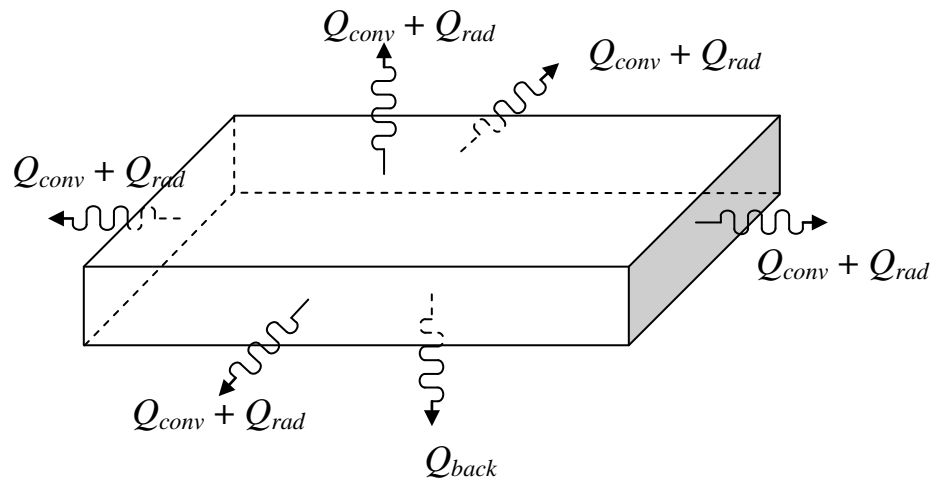


Fig.4 Thermal Boundary Conditions.

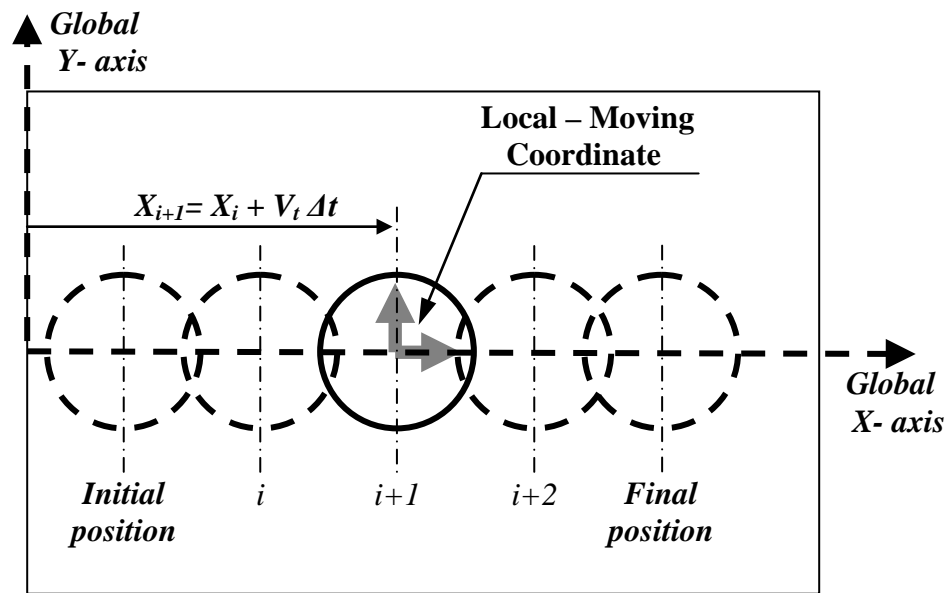


Fig. 5 Modeling of Heat Source Movement at Different Time

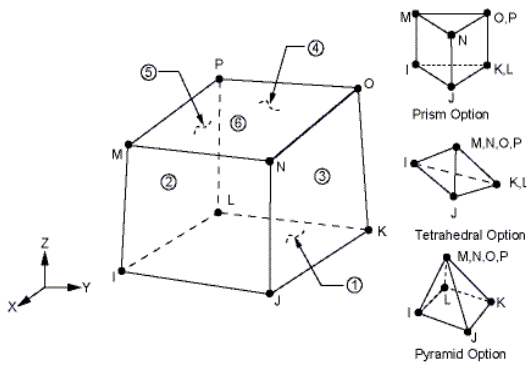


Fig. 6 Geometry of Element “SOLID70” (ANSYS v.10)

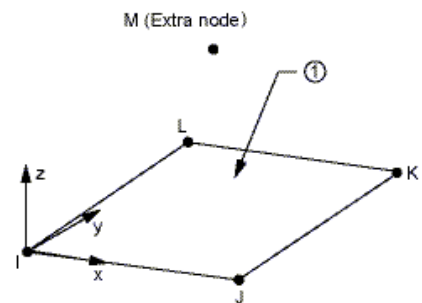


Fig. 7 Geometry of Element “SURF152” (ANSYS v.10)

Table 3 material properties for low carbon steel

Sl. No	Temperature (°C)	Thermal conductivity (W/m°C)	Specific heat (J/Kg° C)
1	0	16	500
2	200	19	540
3	400	21	560
4	600	24	590
5	800	29	600
6	1000	30	610

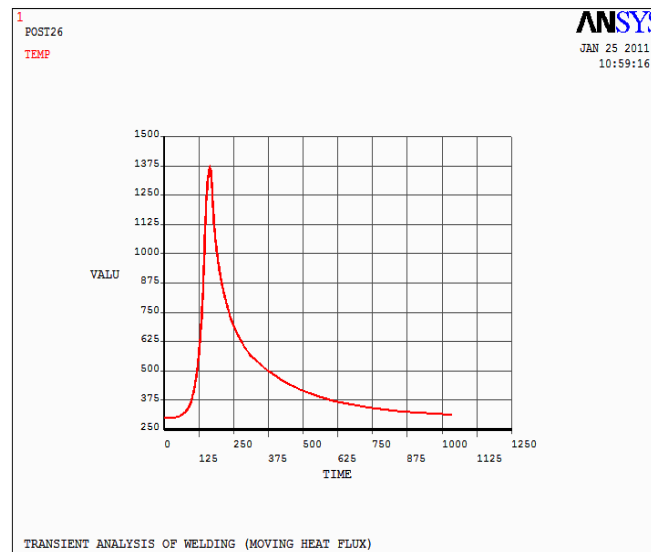


Fig.8 maximum temp. (K°) in center of welded line at(700 RPM+25 mm/min)

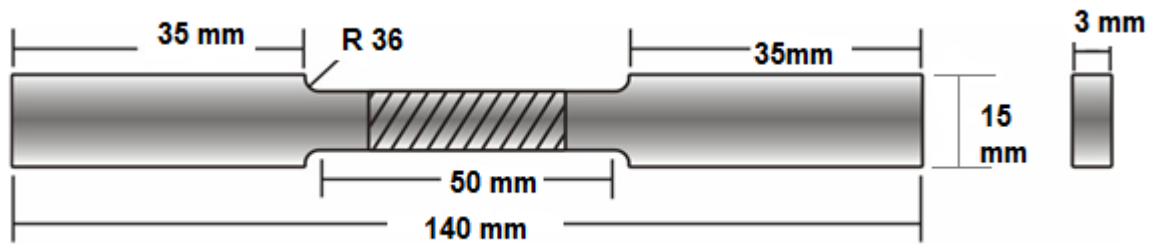


Fig.9 ASTM (E8) Sample for Tensile Test .

Table 4 Tensile test results

	Fsw Exp.	Rotational speed (RPM)	Welding speed (mm/min)	Tensile strength (N/mm <sup>2</sup> )	Elongation(%)	Joint efficiency in terms of tensile strength (%)
	Base metal	-	-	427.29	14.75	-
Set 1	FSW1	450	25	354.64	3.55	82.99
	FSW2	450	50	141.54	1.43	33.12
	FSW3	450	150	Fail	Fail	Fail
Set 2	FSW4	700	25	437.09	14.20	100.02
	FSW5	700	50	397.00	4,29	92.29
	FSW6	700	150	220	2.06	51.48
Set 3	FSW7	900	25	384.72	4.95	90.03
	FSW8	900	50	325.56	5.03	76.19
	FSW9	900	150	267.44	2.24	62.58

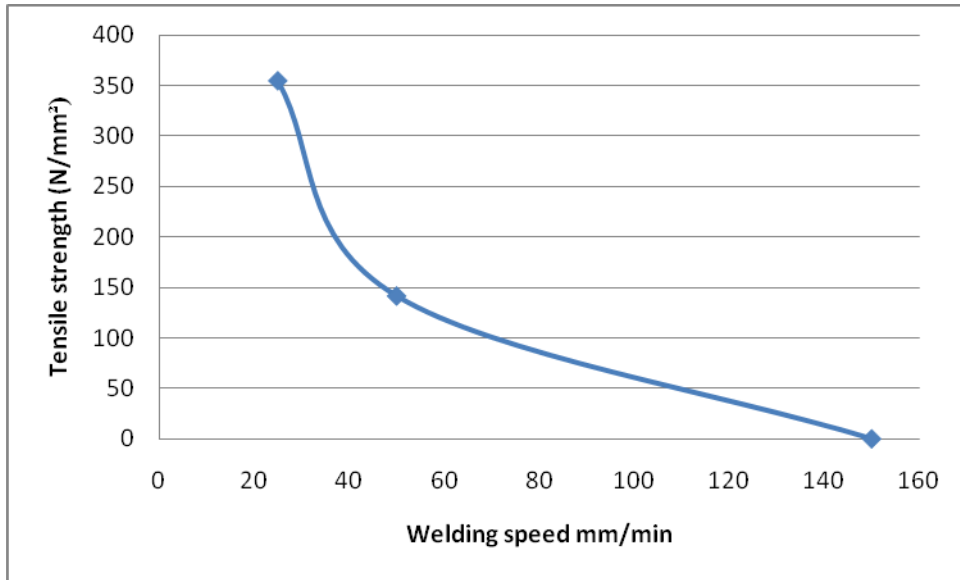


Fig. 10 Relation between welding speed and tensile strength at 450 rpm.

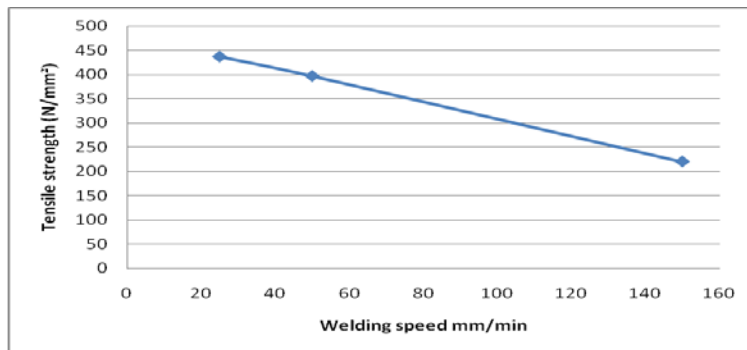


Fig. 11 Relation between welding speed and tensile strength at 700rpm.

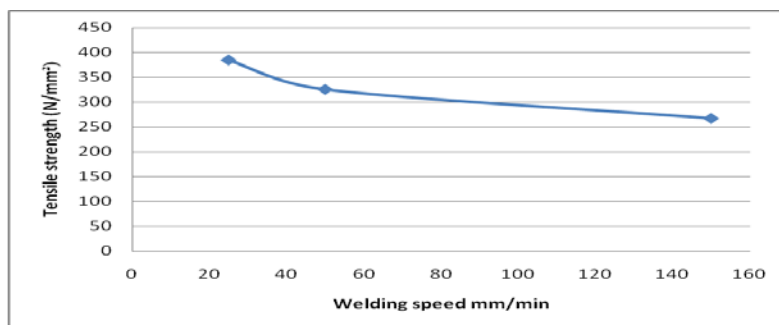


Figure 12 Relation between welding speed and tensile strength at 900rpm.

**Table 5 Results of corrosion tests**

<b>Exp. NO.</b>	<b>Weight loss (g/m<sup>2</sup> *d)</b>
<b>Base metal</b>	4.07E.001
<b>Welded plate</b>	1.41E.001

**Table 6 Results of Microhardness test for FSW Joints**

<b>FSW NO.</b>		<b>Microhardness in the center welding (HVN)</b>
<b>BASE METAL</b>		183
<b>Set 1</b>	<b>FSW1</b>	255
	<b>FSW2</b>	224
	<b>FSW3</b>	FAIL
<b>Set 2</b>	<b>FSW4</b>	276
	<b>FSW5</b>	210
	<b>FSW6</b>	172
<b>Set 3</b>	<b>FSW7</b>	291
	<b>FSW8</b>	280
	<b>FSW9</b>	258

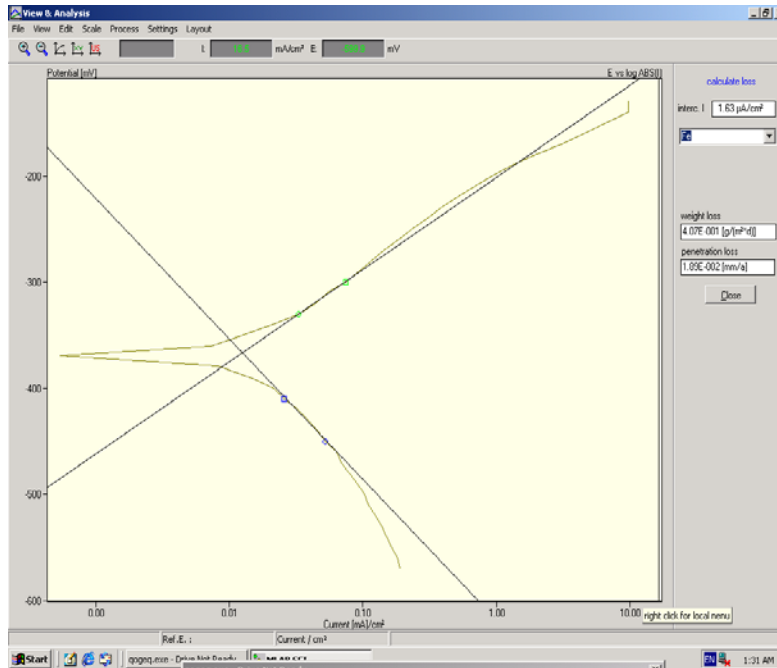


Fig. 13 current-potential curve for base metal.

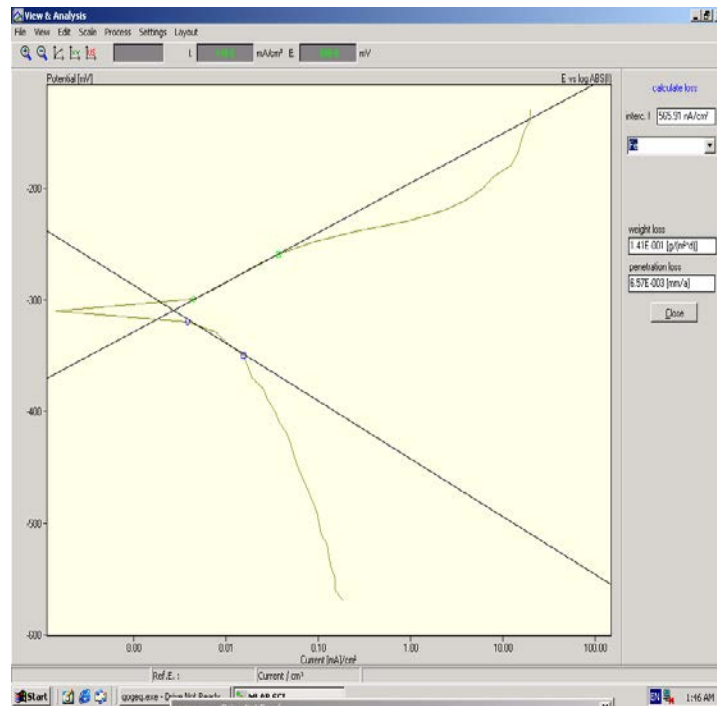


Fig.14 current-potential curve for welded region.

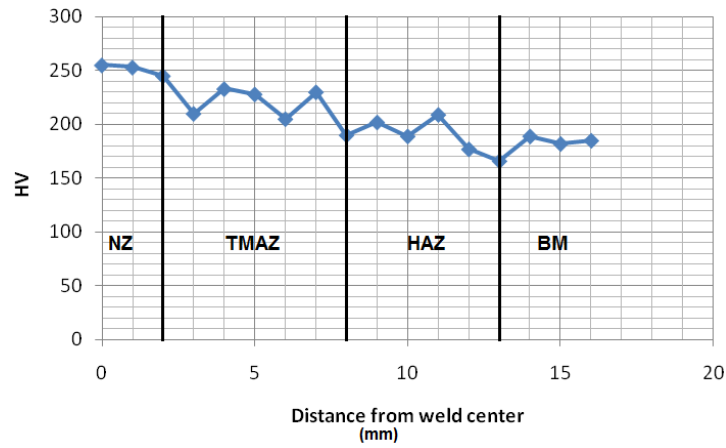


Fig.15 Microhardness Profile in FSW1

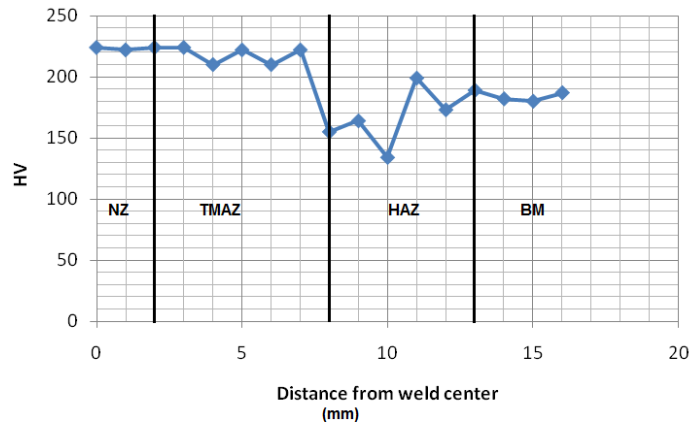


Fig.16 Microhardness Profile in FSW2

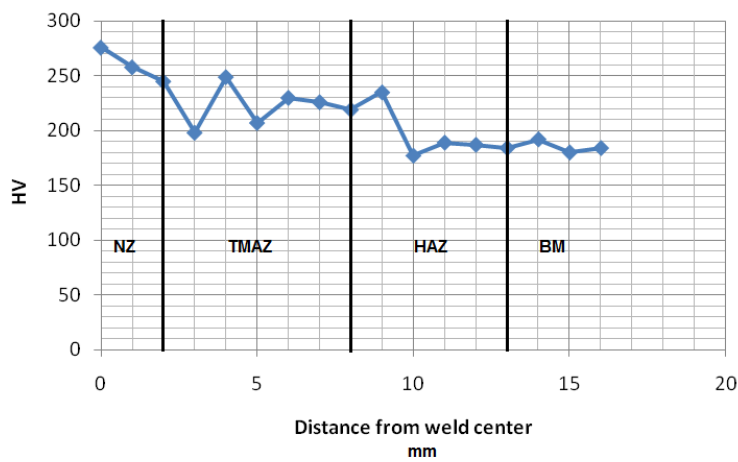


Fig.17 Microhardness Profile in FSW4

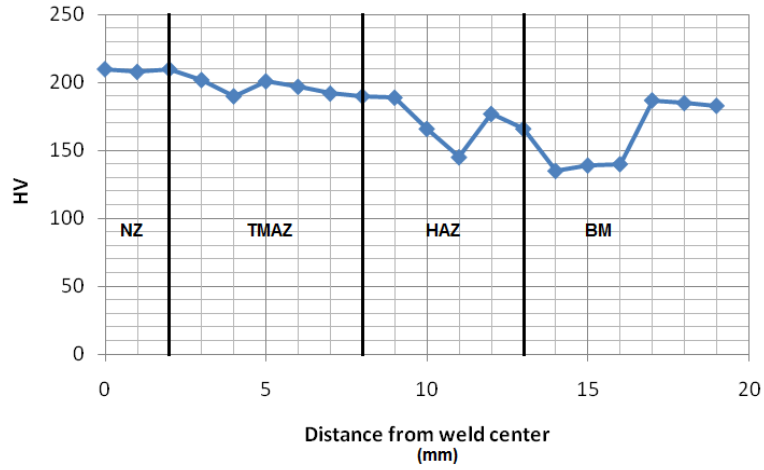


Fig.18 Microhardness Profile in FSW5

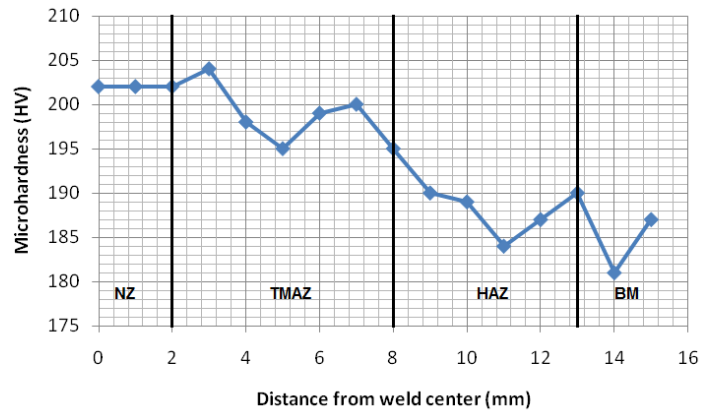


Fig.19 Microhardness Profile in FSW6

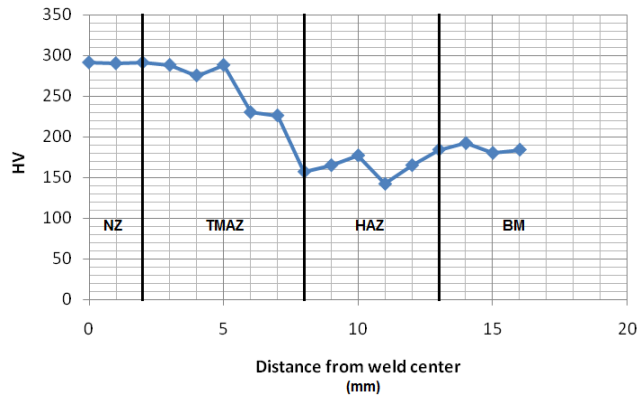
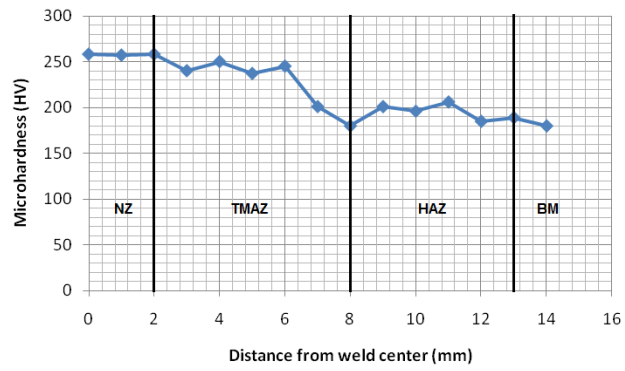
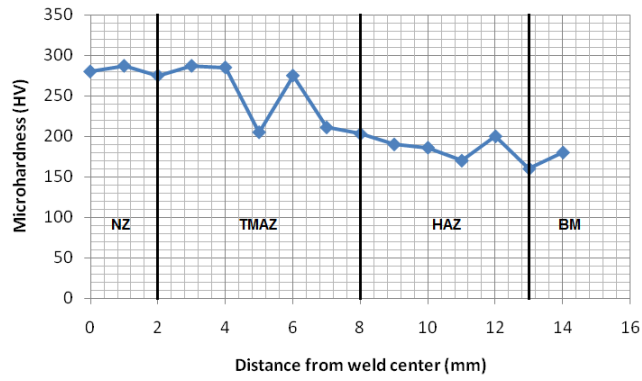


Fig.20 Microhardness Profile in FSW7



**Fig.21 Microhardness Profile in FSW8**



**Fig.22 Microhardness Profile in FSW9**

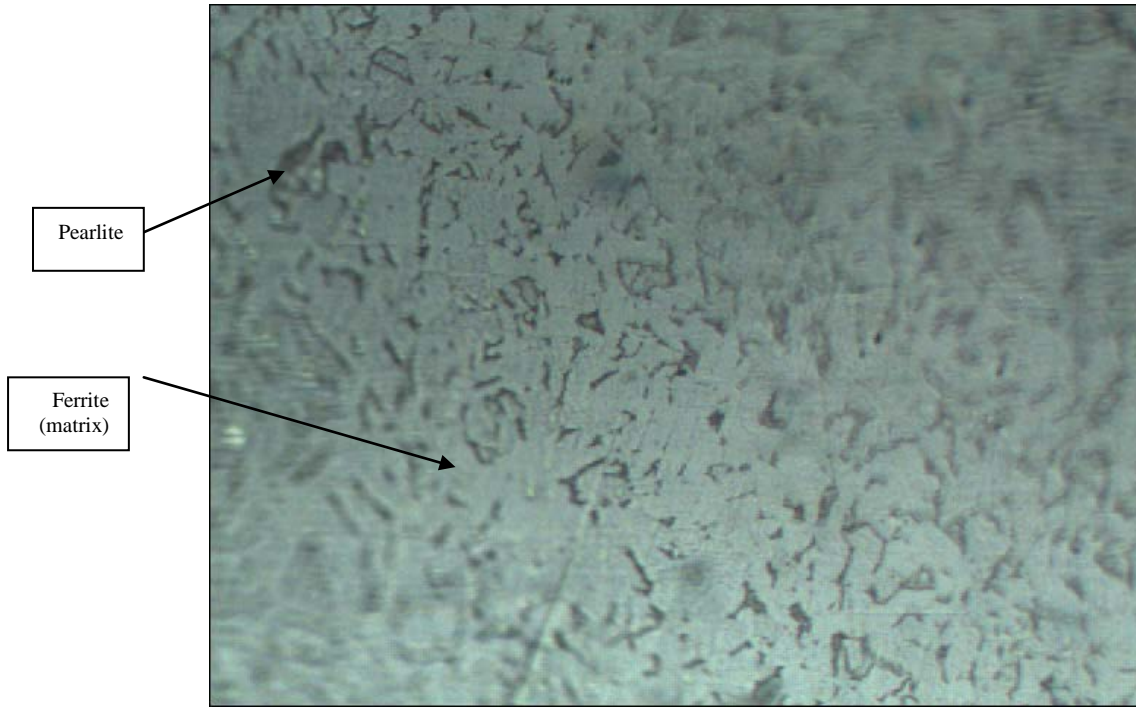


**Fig. 23 Base metal structure (X40)**

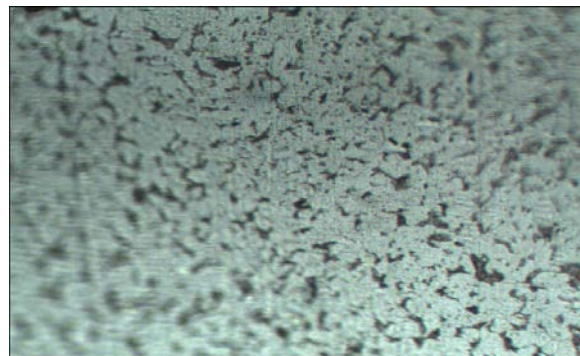


**Fig. 24 Nugget structure zone. (X40)**

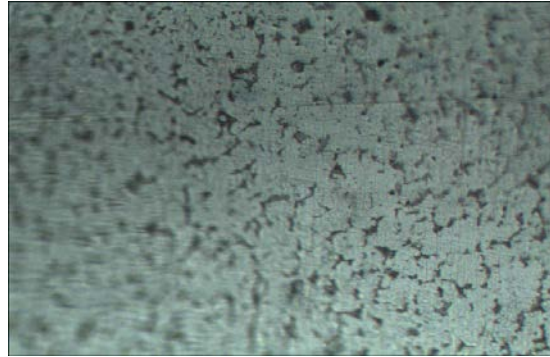


**Fig. 25 Heat effected structure zone. (X40)**



(a) FSW4



(b) FSW5



(c) FSW7



(d) FSW1



(e) FSW8



(f) FSW9



(g) FSW6



(h) FSW2



(i) FSW3

**Fig 26 Welding plates**